SCUOLA DI DOTTORATO
UNIVERSITÀ DEGLI STUDI DI MILANO-BICOCCA

Department of School of Medicine and Surgery

PhD program in Translational and Molecular Medicine

Cycle XXXVIII

Curriculum in Cellular and Molecular Mechanisms

Molecular and functional determinants of arrhythmias in genetic heart diseases: PLN-R14del cardiomyopathy and Long QT Syndrome

Dr. Eskandr Marem

Registration number: 810685

Tutor: Prof. Zaza Antonio

Supervisor: Dr. Sala Luca

Coordinator: Prof. Francesco Mantegazza

ACADEMIC YEAR 2024/2025

To my family…
To my mom, this milestone is for her.
Even though she's no longer here with us,
I hope she's proud of me.
To my dad, my anchor and safe harbor.

To my love, thank you for your endless support,
patience, and for believing in me every step of the way.

And to my lifelong friends,
thank you for being there and for sharing every joy
and every difficult moment with me.

Table of content

Chapter 1: Introduction 5

1.1. Acronyms 6

1.2. Arrhythmogenic Heart Diseases 7

1.3. Cardiomyopathies 7

1.3.1. Dilated Cardiomyopathy (DCM) 8

1.3.2. Arrhythmogenic cardiomyopathy 8

1.4. Channelopathies 10

1.4.1. LQTS 10

1.5. Aim 13

1.6. References 15

Chapter 2: Early consequences of the phospholamban mutation PLN-R14del+/− in a transgenic mouse model 17

2.1. Acronyms 18

2.2. Abstract 20

2.3. Background 21

2.3.1. Cardiac excitation–contraction coupling (E–C coupling) 22

2.3.2. SERCA2a: structure and function 23

2.3.3. PLN: structure and function 23

2.3.4. The interaction between SERCA and PLN 24

2.3.5. PLN R14-del 24

2.3.6. The role of Ca^{2+} in mitochondrial metabolism 25

2.4. Methods 27

2.4.1. Experimental model 27

2.4.2. Cardiomyocyte isolation 27

2.4.3. Preparation of cardiac homogenate 28

2.4.4. Electrophysiological recordings 29

2.4.5. Intracellular Ca^{2+} recordings 30

2.4.6. Energy metabolism 31

2.4.7. mRNA extraction and qRT-PCR assay 33

2.4.8. Protein Extraction and Western Blot Analysis 34

2.4.9. Statistical analysis 35

2.5. Results 35

2.5.1. SERCA2a ATPase activity 35

2.5.2. Intracellular Ca^{2+} dynamics 36

2.5.3. Effect PST-3093 on intracellular Ca^{2+} dynamics 43

2.5.4. Energy metabolism 46

2.5.5. Transcript and protein analysis 54

2.6. Discussion 58

2.6.1. Intracellular Ca^{2+} dynamics 58

2.6.2. Energy metabolism 60

2.6.3. Coupling between Ca^{2+} dynamics and energy metabolism 62

2.6.4. Transcript and protein analysis 62

2.7. Limitations 63

2.8. Conclusions 64

2.9. Therapeutic implications 64

2.10. References 66

Chapter 3: Genetic variants risk assessment for Long QT Syndrome through machine learning and multielectrode array recordings 74

3.1. Acronyms 75

3.2. Abstract 77

3.3. Background 79

3.3.1. Genetic insights and limitations 79

3.3.2. hiPSC-CM 79
3.3.3. Objectives of the study 80
3.4. Methods 80
3.4.1. Ethical statement 80
3.4.2. Patient-specific hiPSC lines included in the study 80
3.4.3. Cardiac events frequency assessment 81
3.4.4. hiPSC culture and differentiation to hiPSC-CMs 84
3.4.5. Patch-clamp 86
3.4.6. MultiElectrode Arrays 87
3.4.7. Drug testing 88
3.4.8. Field Potential analysis 89
3.4.9. Data Analysis and Statistics 89
3.5. Results 90
3.5.1. Patient cohort characteristics 90
3.5.2. Genetic variant risk level assignment 91
3.5.3. In vitro characterization of genetic variants selected for the study 93
3.5.4. Baseline electrophysiology of hiPSC-CM cohort 95
3.5.5. HiPSC-CMs from High Risk and Low Risk groups demonstrate distinct drug responses to ion channel blockers 97
3.5.6. HiPSC-CMs carrying High Risk and Low Risk P/LP variants demonstrate distinct drug responses to proarrhythmic drugs 102
3.5.7. Gene-specific drug response differences between in hiPSC-CMs carrying High Risk and Low Risk P/LP variants 104
3.5.8. Machine learning model stratifies P/LP variant risk from hiPSC-CM multielectrode array data 104
3.5.9. Machine learning validation confirmed model accuracy for predicting individual variant risk 104
3.6. Discussion 108

3.7. Study limitations 111

3.8. References 112

Chapter 4: Summary and Conclusions 126

4.1. References 130

Chapter 5: Papers 133

Chapter 1:

Introduction

1.1. Acronyms

ACM: arrhythmogenic cardiomyopathies

AHD: arrhythmogenic heart disease

BrS: brugada syndrome

CMR: cardiac magnetic resonance

CPVT: catecholaminergic polymorphic ventricular tachycardias

DCM: dilated cardiomyopathy

ECG: electrocardiogram

HCM: hypertrophic cardiomyopathy

hiPSC-CMs: human induced pluripotent stem cell-derived cardiomyocytes

ICD: implantable cardioverter-defibrillator

IKs: slow component of the delayed rectifier potassium current

IKr: rapid component of the delayed rectifier potassium current

LCSD: left Cardiac sympathetic denervation

LQTS: Long-QT Syndromes

LVNC: left ventricular noncompaction cardiomyopathy

NaV1.5: cardiac sodium channel

OCR: Oxygen Consumption Rate

PLN: phospholamban

PLN-R14del: deletion of arginine at position 14 in phospholamban.

SCD: sudden cardiac death

SCN5A: sodium channel, Voltage-gated, type V alpha subunit

SQTS: Short QT Syndrome

1.2. *Arrhythmogenic Heart Diseases*

Arrhythmogenic heart diseases (AHDs) comprise a heterogeneous group of conditions marked by a high risk of malignant ventricular arrhythmias and sudden cardiac death (SCD). Despite this shared arrhythmogenic propensity, they fall into two broad categories: arrhythmogenic cardiomyopathies (ACM) and channelopathies.

From a clinical standpoint, genetic AHDs are especially challenging because of their heterogeneity and the difficulty of predicting who is at greatest risk of life-threatening events. Two paradigmatic examples across this spectrum are Long QT Syndrome (LQTS) and ACM linked to the PLN-R14del mutation.

ACM denotes myocardial diseases that typically result from mutations in sarcomeric, cytoskeletal, or desmosomal proteins and lead to progressive structural remodeling of the heart [1]. In contrast, channelopathies arise in structurally normal hearts, where electrical dysfunction stems from pathogenic variants in ion channels or their regulators, classically LQTS, Brugada syndrome (BrS), and catecholaminergic polymorphic ventricular tachycardia (CPVT). Distinguishing these categories is clinically relevant because it guides diagnostic pathways, risk stratification, and therapy [2].

At the genetic level, both ACM and channelopathies are largely monogenic disorders, although their primary molecular substrates differ [1]. Nevertheless, accumulating evidence reveals substantial genetic and pathophysiological overlap: genes such as SCN5A, RYR2, PLN, and HCN4 are implicated both in inherited arrhythmia syndromes and in cardiomyopathies including DCM, ACM, and Left Ventricular Noncompaction (LVNC.) This convergence blurs the traditional boundary between “structural” and “electrical” disease and supports viewing AHDs as a continuum rather than strictly separate entities [1].

1.3. *Cardiomyopathies*

Within the broader spectrum of arrhythmogenic heart diseases, cardiomyopathies represent a major group in which structural remodeling of the myocardium provides the substrate for arrhythmias and sudden death.

Arrhythmias and sudden cardiac death (SCD) also occur in the context of hereditary cardiomyopathies, including hypertrophic cardiomyopathy (HCM), dilated cardiomyopathy (DCM), arrhythmogenic cardiomyopathy (ACM), and left ventricular noncompaction cardiomyopathy (LVNC). These entities are primarily linked to mutations in sarcomeric proteins (HCM), cytoskeletal proteins (DCM), or desmosomal proteins (ACM). The mechanisms underlying their arrhythmogenic potential include ventricular hypertrophy and dilatation, interstitial fibrosis, remodeling of ion channels and connexins, and disturbances of intracellular calcium homeostasis [1].

Cardiomyopathies are a heterogeneous group of pathologies characterized by structural and functional alterations of the heart [3].

Cardiomyopathies often lead to progressive heart failure with significant morbidity and mortality. Cardiomyopathies may be primary (i.e., genetic, mixed, or acquired) or secondary (e.g., infiltrative, toxic, inflammatory).

Although cardiomyopathy is asymptomatic in the early stages, symptoms are the same as those characteristically seen in any type of heart failure and may include shortness of breath, fatigue, cough, orthopnea, paroxysmal nocturnal dyspnea, and edema [4].

Diagnostic studies include B-type natriuretic peptide levels, baseline serum chemistries, electrocardiography, and echocardiography. Treatment is targeted at relieving the symptoms of heart failure and reducing rates of heart failure related hospitalization and mortality. Treatment options include pharmacotherapy, implantable cardioverter-defbrillators, cardiac resynchronization therapy, and heart transplantation. Recommended lifestyle changes include restricting alcohol consumption, losing weight, quitting smoking, and eating a low-sodium diet [4].

1.3.1. Dilated Cardiomyopathy (DCM)

Among the different cardiomyopathy subtypes, dilated cardiomyopathy stands out as a prototypical example of contractile dysfunction associated with arrhythmogenic risk.

Dilated cardiomyopathy is typically characterized by dilatation and impaired function of one or both ventricles. Patients may develop heart failure, and the presenting symptoms often include atrial or ventricular arrhythmias and sudden cardiac death. This disease can be classified as either primary or secondary DCM [3].

1.3.2. Arrhythmogenic cardiomyopathy

In contrast to the dilated form, arrhythmogenic cardiomyopathy is characterized not only by impaired systolic function but also by a distinctive arrhythmic phenotype driven by fibro-fatty myocardial replacement. Arrhythmogenic cardiomyopathy is defined as an arrhythmogenic heart muscle disorder [5].

Arrhythmogenic cardiomyopathy has a genetic basis and is characterized by the progressive replacement of the myocardium with fibrofatty tissue that starts from the epicardium and becomes transmural [4].

Clinical Manifestation

Arrhythmogenic cardiomyopathy shows variable phenotypic expression, from completely asymptomatic subjects to the development of ventricular arrhythmias that can be fatal and lead to sudden cardiac death. The most typical clinical presentation relates to arrhythmias that cause palpitations, syncope (often during exercise), and cardiac arrest. The ACM phenotype overlaps with other cardiomyopathies, particularly dilated cardiomyopathy with arrhythmia presentation that may be associated with ventricular dilatation and/or impaired systolic function [4].

ACM may present clinically with atrial fibrillation, conduction disease, and/or right or left ventricular arrhythmias; although initially considered to affect predominantly the right ventricle, it is now understood that the left ventricle may be equally involved or even predominant [4, 5].

Diagnosis of arrhythmogenic cardiomyopathy

In patients with suspected ACM, the initial evaluation includes clinical history, physical examination, detailed family history, 12-lead electrocardiogram (ECG), 2D echocardiography, ambulatory ECG monitoring, and Cardiovascular Magnetic Resonance (CMR). Most patients with suspected ACM presenting with arrhythmia can be diagnosed using noninvasive imaging and electrocardiographic assessment [5].

Management

The goal in the management of arrhythmogenic cardiomyopathy is to prevent sudden cardiac death. The first step is to impose lifestyle change. During exercise the risk of developing ventricular arrhythmias increases; therefore, patients with arrhythmogenic cardiomyopathy should be prohibited from competitive or endurance sport activity. The pharmacological approach involves the use of beta-blockers that reduce adrenergic activity and therefore the risk of developing arrhythmias [4].

PLN-R14-del

Among these cardiomyopathies, the PLN-R14del mutation represents a paradigmatic case that bridges structural and electrical disease. Mutations in PLN can cause cardiomyopathies, either arrhythmogenic (ACM) or dilated (DCM). Among these, the PLN-R14del mutation is particularly debated because its pathogenic mechanism remains unclear[6, 7].

1.4. Channelopathies

Channelopathies represent the other major category of inherited arrhythmogenic diseases, arising in the absence of overt structural abnormalities. Channelopathies predispose individuals to disturbances of normal cardiac rhythm. If the heart beats too slowly (bradyarrhythmia) or so rapidly that it cannot fill adequately (tachyarrhythmia), circulatory collapse may ensue and eventually lead to sudden death [8]

Repolarization heterogeneity is a strong risk predictor in arrhythmogenic conditions and is likely to provide a pivotal arrhythmogenic substrate in many cardiac channelopathies. The inherent stability of cardiac repolarization is compromised when action potentials are prolonged, a condition manifest at the surface ECG as prolongation of the rate-corrected QT interval (QTc). Thus, the ‘long-QT syndrome’ takes its name from the distinctive abnormality of the electrocardiogram in affected individuals [8].

1.4.1. LQTS

The term congenital long-QT syndromes (LQTS) denotes hereditary conditions in which QTc prolongation is associated with syncopal episodes and/or sudden death without evidence of structural heart disease. The syndrome’s phenotype is caused by ventricular arrhythmias, which entail a high risk of cardiac arrest and therefore represent a major cause of sudden death in the young. In LQTS symptoms are often (but not always) precipitated by emotional or physical stress [9].

The electrocardiographic QT interval represents the repolarization phase of the cardiac action potential. The interplay of several ion channels determines the action potential duration. Decreases in repolarizing outward potassium currents or increases in depolarizing inward sodium or calcium currents can lead to prolongation of the QT interval, thus representing a pathophysiological substrate for LQTS. The QT interval is physiologically rate-dependent. Therefore, to define whether its value falls within normal limits, the QT interval needs to be corrected for heart rate (QTc); several empirical formulas (Bazett, Fredericia etc.) have been developed for this purpose.

Sixteen genes have been identified as either responsible for or associated with LQTS [10]. By far, KCNQ1 (LQT1), KCNH2 (LQT2), and SCN5A (LQT3) are the most common LQTS genes, accounting for ≈90% of all genotype-positive cases.

KCNQ1 encodes the α-subunit of the K^+ channel Kv7.1, generating I_{Ks}, which, being physiologically increased by sympathetic activation, is essential for QT adaptation to increases in heart rate. When I_{Ks} is defective because of loss-of function mutations, the QT interval fails to shorten appropriately during tachycardia, thus creating a highly arrhythmogenic condition [9].

The second most common gene harboring LQTS mutations is KCNH2, encoding the α-subunit of the K^+ channel responsible for the rapid component of the delayed rectifier current (I_{Kr}). Together with the slow component (I_{Ks}, conducted by KCNQ1), I_{Kr} contributes to the overall delayed rectifier K^+ current (I_K), with I_{Kr} playing a predominant role in phase 3 repolarization of the cardiac action potential. Loss-of-function mutations in KCNH2 reduce I_{Kr}, either by impairing channel trafficking to the plasma membrane (trafficking-deficient variants) or by altering channel gating properties (e.g., shifts in activation, inactivation, or deactivation kinetics). These mechanisms parallel those observed in KCNQ1 mutations affecting I_{Ks}, ultimately diminishing repolarization reserve and predisposing to arrhythmogenesis [9].

The third major LQTS gene is SCN5A, which encodes the α-subunit of the cardiac sodium channel conducting the depolarizing sodium inward current. SCN5A gain-of function mutations produce the LQTS phenotype by increasing the "late Na^+ current (I_{NaL}) which contributes an inward current component to repolarization [10].

Most events in LQT1 occur during exercise or stress, with swimming representing a highly specific trigger. Many events in LQT2 occur during arousal, especially from auditory stimuli such as sudden noises and telephone ringing, particularly at rest. Most events in LQT3 occur while patients are asleep or at rest [9].

Clinical Manifestation

The clinical manifestations of LQTS vary according to the genetic background. The disease-causing gene is the main determinant of the clinical phenotype, but the position of the mutation in the protein and the specific disease-causing mutation also contribute to clinical severity.

The arrhythmogenic events characteristic of LQTS are most often caused by torsades de pointes (TdP), a distinctive type of polymorphic ventricular tachycardia in which the QRS axis gradually shifts over time, mimicking a “torsion of the cardiac apex”. TdP episodes are often self-terminating, typically resulting in only transient loss of consciousness (syncope); however, the arrhythmia can degenerate into sustained ventricular fibrillation, leading to sudden cardiac death. Understanding the factors that determine whether TdP terminates spontaneously or progresses to a fatal arrhythmia remains a critical challenge [9]. Beyond these clinical manifestations, an additional layer of complexity arises from the remarkable phenotypic heterogeneity observed even among carriers of the same pathogenic variant. As emphasized by Crotti et al., this variability is best explained by the dual concepts of incomplete penetrance and variable expressivity [11]. This inter-individual variability is strongly influenced by modifier alleles, which act as genetic cofactors capable of either amplifying or attenuating the phenotypic consequences of a given mutation. These insights highlight that LQTS results from intricate genetic interactions in which pathogenic variants, modifier alleles, and the broader genomic background collectively shape phenotypic penetrance and arrhythmic susceptibility.

Diagnosis

Given this genetic and phenotypic variability, accurate diagnosis of LQTS requires a structured approach that integrates clinical, electrocardiographic, molecular, and genetic data. The diagnostic criteria for LQTS proposed in 1985 remain essentially valid for a quick assessment; however, a more quantitative approach to diagnosis becomes possible with the presentation of a diagnostic score in 1993 that is known as the Schwartz score, updated in 2006. This score tabulates elements of the personal history, family history, and ECG QTc values to qualitatively frame an index of suspicion for LQTS and is helpful for the assessment of the index case and of family members [10].

As the score gives importance to the degree of QTc prolongation, it is evident that it does not help in the identification of electrocardiographically silent mutation carriers. A practical approach consists of using the Schwartz score to select patients who should undergo molecular screening (everyone with a score ≥3.0) and of using cascade screening to identify all affected family members, including silent mutation carriers [9].

Notably, the clinical risk associated with pathogenic or likely pathogenic (P/LP) variants in LQTS is not uniform, with some variants conferring a much higher incidence of cardiac events than others and modifier genes contributing to the picture. This heterogeneity poses significant challenges for patient management. Recent studies demonstrate that combining patient-specific induced pluripotent stem cell-derived cardiomyocytes (hiPSC-CMs, hosting the entire patient's genotype) with multielectrode array recordings and machine learning (ML) provides genotype-specific electrophysiological profiles and drug-response signatures, enabling improved discrimination between high- and low-risk genotypes. In a proof-of-concept study, ML classifiers trained on hiPSC-CM electrophysiological data achieve nearly 90% accuracy in stratifying P/LP variants, offering a scalable and innovative tool for predicting arrhythmic risk and supporting precision medicine in LQTS [12].

Management

Beyond diagnosis, the ultimate challenge lies in tailoring management strategies to each patient's genetic profile and arrhythmic risk.

The key elements of management of LQTS patients are β-adrenergic blocking agents, left cardiac sympathetic denervation (LCSD), the ICD, and common sense. These established strategies are now complemented by emerging gene-specific approaches, both pharmacological and behavioral [9]. While β-blockers are pharmacological and relatively noninvasive, both LCSD and ICD implantation are invasive procedures associated with perioperative risks, device-related complications, and significant impact on quality of life. For this reason, accurate risk stratification is crucial to identify those patients who will most benefit from such interventions, while sparing low-risk individual unnecessary invasive therapies.

1.5. Aim

The aim of this thesis is to advance the understanding of the molecular and functional determinants of arrhythmic risk in genetic heart diseases, focusing on two paradigmatic conditions that exemplify manifestations of inherited arrhythmogenic disorders: the arrhythmogenic cardiomyopathy associated with the PLN-R14del mutation and the Long QT Syndrome (LQTS).

- The first part focuses on the PLN-R14del mutation. By using a transgenic mouse model of the mutation, this work investigates its early consequences, i.e. those occurring before the onset of overt cardiomyopathy. This aims to distinguish primary mutation-induced abnormalities from those secondary to myocardial remodeling, eventually caused by a maladaptive response to hemodynamic impairment. Particular attention has been devoted to calcium handling, energy metabolism, and stress signaling pathways, to determine which of these may primarily contribute to pathogenesis [13].

- The second part focuses on the development and validation of an exploratory approach for risk stratification in Long QT Syndrome, using patient-specific hiPSC-derived cardiomyocytes coupled with multielectrode array recordings and machine learning, with the goal of discriminating high- from low-risk genetic variants and providing a basis for future improvements in risk assessment [12].

By integrating animal models for mechanistic insights and cellular/computational models for risk assessment, my doctoral work aims to contribute to a deeper, translationally relevant understanding of inherited arrhythmogenic disorders, ultimately supporting the future development of targeted preventive and therapeutic strategies.

1.6. References

1. Priori, S.G., Remme, C.A.: Inherited conditions of arrhythmia: translating disease mechanisms to patient management. Cardiovasc Res. 116, 1539–1541 (2020). https://doi.org/10.1093/cvr/cvaa150.
2. Priori, S.G.: Inherited Arrhythmogenic Diseases. Circ Res. 94, 140–145 (2004). https://doi.org/10.1161/01.RES.0000115750.12807.7E.
3. Ciarambino, T., Menna, G., Sansone, G., Giordano, M.: Cardiomyopathies: An Overview. Int J Mol Sci. 22, 7722 (2021). https://doi.org/10.3390/ijms22147722.
4. Wexler, R.K., Elton, T., Pleister, A., Feldman, D.: Cardiomyopathy: an overview. Am Fam Physician. 79, 778–84 (2009).
5. Towbin, J.A., McKenna, W.J., Abrams, D.J., Ackerman, M.J., Calkins, H., Darrieux, F.C.C., Daubert, J.P., de Chillou, C., DePasquale, E.C., Desai, M.Y., Estes, N.A.M., Hua, W., Indik, J.H., Ingles, J., James, C.A., John, R.M., Judge, D.P., Keegan, R., Krahn, A.D., Link, M.S., Marcus, F.I., McLeod, C.J., Mestroni, L., Priori, S.G., Saffitz, J.E., Sanatani, S., Shimizu, W., van Tintelen, J.P., Wilde, A.A.M., Zareba, W.: 2019 HRS expert consensus statement on evaluation, risk stratification, and management of arrhythmogenic cardiomyopathy. Heart Rhythm. 16, e301–e372 (2019). https://doi.org/10.1016/j.hrthm.2019.05.007.
6. Vafiadaki, E., Glijnis, P.C., Doevendans, P.A., Kranias, E.G., Sanoudou, D.: Phospholamban R14del disease: The past, the present and the future. Front Cardiovasc Med. 10, (2023). https://doi.org/10.3389/fcvm.2023.1162205.
7. Stege, N.M., de Boer, R.A., Makarewich, C.A., van der Meer, P., Silljé, H.H.W.: Reassessing the Mechanisms of PLN-R14del Cardiomyopathy. JACC Basic Transl Sci. 9, 1041–1052 (2024). https://doi.org/10.1016/j.jacbts.2024.02.017.
8. Marbán, E.: Cardiac channelopathies. Nature. 415, 213–218 (2002). https://doi.org/10.1038/415213a.
9. Schwartz, P.J., Crotti, L., Insolia, R.: Long-QT Syndrome. Circ Arrhythm Electrophysiol. 5, 868–877 (2012). https://doi.org/10.1161/CIRCEP.111.962019.
10. Schwartz, P.J.: Practical issues in the management of the long QT syndrome: focus on diagnosis and therapy. Swiss Med Wkly. 143, w13843 (2013). https://doi.org/10.4414/smw.2013.13843.

11. Crotti, L., Lahtinen, A.M., Spazzolini, C., Mastantuono, E., Monti, M.C., Morassutto, C., Parati, G., Heradien, M., Goosen, A., Lichtner, P., Meitinger, T., Brink, P.A., Kontula, K., Swan, H., Schwartz, P.J.: Genetic Modifiers for the Long-QT Syndrome. Circ Cardiovasc Genet. 9, 330–339 (2016). https://doi.org/10.1161/CIRCGENETICS.116.001419.
12. Khudiakov, A., Mura, M., Giannetti, F., Leonov, V., Alberio, C., Eskandr, M., Brink, P.A., Crotti, L., Gnecchi, M., Schwartz, P.J., Sala, L.: Genetic variants risk assessment for Long QT Syndrome through machine learning and multielectrode array recordings, (2025).
13. Maniezzi, C., Eskandr, M., Florindi, C., Ferrandi, M., Barassi, P., Sacco, E., Pasquale, V., Maione, A.S., Pompilio, G., Teixeira, V.O.N., de Boer, R.A., Silljé, H.H.W., Lodola, F., Zaza, A.: Early consequences of the phospholamban mutation PLN-R14del in a transgenic mouse model. Acta Physiologica. 240, (2024). https://doi.org/10.1111/apha.14082.

Chapter 2

Early consequences of the phospholamban mutation PLN-R14del+/− in a transgenic mouse model.

Claudia Maniezzi[1], Marem Eskandr[1], Chiara Florindi[1], Mara Ferrandi[2], Paolo Barassi[2], Elena Sacco[1], Valentina Pasquale[1], Angela S. Maione[3], Giulio Pompilio[3,4] , Vivian Oliveira Nunes Teixeira[5] , Rudolf A. de Boer[6], Herman H. W. Silljé[5], Francesco Lodola[1*], Antonio Zaza[1*]

1. Department of Biotechnology and Bioscience, University of Milano-Bicocca, Milan, Italy
2. Windtree Therapeutics Inc., Warrington, Pennsylvania, USA
3. Unit of Vascular Biology and Regenerative Medicine, Centro Cardiologico Monzino IRCCS, Milan, Italy
4. Department of Biomedical, Surgical and Dentist Sciences, University of Milano, Milan, Italy
5. Department of Cardiology, University Medical Center Groningen, University of Groningen, Groningen, Netherlands
6. Department of Cardiology, Erasmus University Medical Center, University of Rotterdam, Rotterdam, Netherlands

***Correspondence**

Francesco Lodola and Antonio Zaza,
Department of Biotechnology and
Bioscience, University of Milano-Bicocca,
P.za della Scienza 2, Milan 20126, Italy.
Email: francesco.lodola@unimib.it and antonio.zaza@unimib.it

[published; *Acta Physiologica.*2024;240:e14082DOI: 10.1111/apha.14082]

2.1. Acronyms

ACM: Arrhythmogenic Cardiomyopathy
ADP: Adenosine Diphosphate
AMPK: AMP-activated Protein Kinase
ATP: Adenosine Triphosphate
BAPTA(-AM): 1,2-Bis(o-aminophenoxy)ethane-N,N,N′,N′-tetraacetic acid acetoxymethyl ester)
CaD: Diastolic Calcium
CaMKII: Calcium/Calmodulin-dependent Protein Kinase II
CaSR: Sarcoplasmic Reticulum Calcium Content
CaT: Calcium Transient
CICR: Calcium-induced Calcium Release
CMs: Cardiomyocytes
DCM: Dilated Cardiomyopathy
DCFDA: 2′,7′-Dichlorodihydrofluorescein Diacetate
DMSO: Dimethyl Sulfoxide
E-C coupling: Excitation–Contraction coupling
EHT(s): Engineered Heart Tissue(s)
ER: Endoplasmic Reticulum
ET(C): Electron Transport (Chain)
FCCP: Carbonyl cyanide p-trifluoromethoxyphenylhydrazone
GAPDH: Glyceraldehyde 3-Phosphate Dehydrogenase
GLIBE: Glibenclamide
hiPSC(s): Human Induced Pluripotent Stem Cell(s)
hiPSC-CM(s): Human Induced Pluripotent Stem Cell–derived Cardiomyocyte(s)
IKATP: ATP-sensitive Potassium Current
Im: Membrane Current
INCX: Sodium-Calcium Exchanger Current
INaL: Late Sodium Current
IP3R: Inositol 1,4,5-Trisphosphate Receptor
LV: Left Ventricle
MCU: Mitochondrial Calcium Uniporter

MERCS: Mitochondria–Endoplasmic Reticulum Contact Sites

Mut: Mutant

NCX: Sodium-Calcium Exchanger

NCXm: Mitochondrial Sodium-Calcium Exchanger

OCR: Oxygen Consumption Rate

Oligo: Oligomycin

PER: Proton Efflux Rate

PKC: Protein Kinase C

PKA: Protein Kinase A

PLN: Phospholamban

PP1: Protein Phosphatase 1

qRT-PCR: quantitative Reverse Transcription Polymerase Chain Reaction

ROS: Reactive Oxygen Species

RV: Right Ventricle

SERCA2a: Sarco/Endoplasmic Reticulum Calcium ATPase isoform 2a

SR: Sarcoplasmic Reticulum

TG: Transgenic

TMRE: Tetramethylrhodamine, Ethyl Ester

UPR: Unfolded Protein Response

V-clamp: Voltage Clamp

VDAC1: Voltage-dependent Anion Channel 1

WT: Wild Type

Ψm: Mitochondrial Membrane Potential

2.2. Abstract

Aims: The heterozygous phospholamban (PLN) mutation R14del (PLN-R14del+/−) is associated with a severe arrhythmogenic cardiomyopathy (ACM) developing in the adult. “Superinhibition” of SERCA2a by PLN- R14del is widely assumed to underlie the pathogenesis, but alternative mechanisms such abnormal energy metabolism have also been reported. This work aims to (1) to evaluate Ca^{2+} dynamics and energy metabolism in a transgenic (TG) mouse model of the mutation prior to cardiomyopathy development; (2) to test whether they are causally connected.

Methods: Ca^{2+} dynamics, energy metabolism parameters, reporters of mitochondrial integrity, energy, and redox homeostasis were measured in ventricular myocytes of 8–12 weeks-old, phenotypically silent, TG mice. Mutation effects were compared to pharmacological PLN antagonism and analyzed during modulation of sarcoplasmic reticulum (SR) and cytosolic Ca^{2+} compartments. Transcripts and proteins of relevant signaling pathways were evaluated.

Results: The mutation was characterized by hyperdynamic Ca^{2+} handling, compatible with a loss of SERCA2a inhibition by PLN. All components of energy metabolism were depressed; myocyte energy charge was preserved under quiescence but reduced during stimulation. Cytosolic Ca^{2+} buffering or SERCA2a blockade reduced O_2 consumption with larger effect in the mutant. Signaling changes suggest cellular adaptation to perturbed Ca^{2+} dynamics and response to stress.

Conclusions: (1) PLN R14del+/− loses its ability to inhibit SERCA2a, which argues against SERCA2a super inhibition as a pathogenetic mechanism; (2) depressed energy metabolism, its enhanced dependency on Ca^{2+} and activation of signaling responses point to an early involvement of metabolic stress in the pathogenesis of this ACM model.

2.3. Background

Phospholamban (PLN) is a small protein which restrains SERCA2a operation, thus limiting Ca^{2+} uptake by the sarcoplasmic reticulum (SR) under resting conditions. Receptor triggered phosphorylation (e.g., by PKA) positively regulates SERCA2a by relieving inhibition by PLN.

The heterozygous deletion of arginine 14 in PLN (PLN R14del+/−) is associated with a form of arrhythmogenic dilated cardiomyopathy (ACM), characterized by PLN aggregate formation, myocardial fibrosis, and heart failure, with typical onset at middle age [1]. PLN R14del+/− is among the prevailing cardiomyopathy-related mutations, particularly in the Netherlands [2] and currently lacks a specific treatment.

More than a decade ago, the pioneering work of Haghighi et al. [3] ascribed PLN R14del+/− phenotype to a "super inhibitory" effect on SERCA2a detected, in a heterologous expression system, as a decrease in sensitivity of pump function to $Ca^{2+.}$ Several subsequent studies, inspired by this interpretation, provided more or less indirect support [4–6] but also conflicting results [7–9]. At any rate, even among the supporting studies, the mechanisms proposed to account for the super inhibitory effect were inconsistent and remain debated.

The "super inhibition" theory motivated us to test reversal of PLN R14del+/− phenotype by a recently developed compound (PST-3093) that selectively stimulates SERCA2a by antagonizing its interaction with PLN [10]. Unexpectedly, human iPS cardiomyocytes (hiPS-CMs), derived from a heterozygous human mutation carrier, displayed a hyperdynamic Ca^{2+} handling instead, a phenotype that is obviously incompatible with SERCA2a "super inhibition". Notably, PST-3093 mimicked the effect of the mutation when applied to the WT hiPS-CMs but was ineffective in mutant ones [11]. Studies on contracting engineered tissues (EHT), obtained from the same hiPS-CMs, detected a major decrease in force development and energy metabolism derangements, but no clear abnormalities in intracellular Ca^{2+} dynamics [12]. Nonetheless, being such studies based on immature cells from a single mutation carrier, caution is warranted in generalization of these results, particularly in light of the wide acceptance of the super inhibition hypothesis.

We have developed and characterized a PLN-R14del+/− transgenic (TG) mouse model which closely recapitulates the human ACM phenotype, including lack of cardiac abnormalities at young age [13]. The present work characterizes cardiomyocytes (CMs) obtained from this disease model in terms of mutation effect on intracellular Ca^{2+} dynamics and energy metabolism. This with the aim of testing the “super inhibition” theory in native mature CMs and compare them to hiPS-CMs for metabolic derangements, thus providing cross-validation of experimental models of the disease.

Evaluation of primary pathogenetic mechanisms in mutations leading to contractile deficit is complicated by overlap with the etiology-unspecific maladaptive process induced by the deficit itself, in which SERCA2a loss of function dominates [14]. To minimize this potential confounder, we selected an animal age at which cardiac contraction is still normal in the PLN R14del+/− TG mice [13].

2.3.1. Cardiac excitation–contraction coupling (E–C coupling)

E–C coupling is the process that links the excitation of cardiomyocytes to the contraction of the whole heart. Contraction is finely regulated by intracellular Ca^{2+} concentration ($[Ca^{2+}]_i$) and can be influenced by changes in the amplitude and duration of the Ca^{2+} transient or by alterations in myofilament affinity for the ion [15].

Systole is triggered by an increase in $[Ca^{2+}]_i$: Ca^{2+} enters the cells through voltage-dependent L-type Ca^{2+} channels located in the sarcolemma, generating I_{CaL} [15–17]. I_{CaL} undergoes Ca^{2+}-dependent inactivation, a negative feedback mechanism that prevents Ca^{2+} overload and cell death. The entry of Ca^{2+} into the dyadic space activates ryanodine receptors (RyR2) on the SR, leading to Ca^{2+} release from the SR, a phenomenon known as Ca^{2+}-induced Ca^{2+} release (CICR) [16, 17]. The combined contribution of external Ca^{2+} influx and SR release raises $[Ca^{2+}]_i$ from ~100 nM to ~10 μM.

Cardiomyocyte contraction is sustained by the sarcomere, where thin filaments (actin, troponin C, troponin I, troponin T, and tropomyosin) interact with thick filaments (myosin). In the resting state, troponin I inhibits actin–myosin interaction. The rise in $[Ca^{2+}]_i$ allows Ca^{2+} binding to the N-terminal domain of troponin C, increasing its affinity for troponin I and displacing it from the myosin-binding site. This promotes actin–myosin cross-bridge formation. The subsequent transition of myosin from a high-energy, ATP-hydrolyzed state to a lower-energy state produces filament sliding. Global sarcomere shortening results from repeated cross-bridge cycles, each coupled to ATP hydrolysis [15, 17].

During diastole (relaxation), $[Ca^{2+}]_i$ decreases due to the combined action of SERCA2a and the Na^+/Ca^{2+} exchanger (NCX) [18]. The quantitative contribution of these transporters varies by species: in humans, SERCA2a accounts for ~70% and NCX for ~28% of Ca^{2+} removal; in mice, ~92% and ~7%, respectively [19].

At steady state, the amount of Ca^{2+} entering the cell during systole must equal the amount extruded during diastole. Any imbalance in these fluxes alters the intracellular Ca^{2+} content, thereby modulating contractile strength.

2.3.2. SERCA2a: structure and function

SERCA is a 110 kDa transmembrane protein belonging to the family of P-type ATPases. Three genes (SERCA1, 2, and 3) encode for approximately ten different isoforms.

Within the transcript of the SERCA2 gene, three alternative splicing events have been identified that affect the C-terminal portion of the protein and give rise to the isoforms SERCA2a, 2b, and 2c. SERCA2a is mainly expressed in cardiac muscle, and to a lesser extent in skeletal muscle. SERCA2b is expressed in smooth muscle and in non-muscle tissues. SERCA2c is expressed at comparable levels in both cardiac muscle and non-muscle tissues such as epithelium [20, 21]

The primary function of the protein is to actively transport Ca^{2+} into the SR. This activity is coupled to ATP hydrolysis, whereby one molecule of ATP is consumed for every two Ca^{2+} ions translocated, along with three protons (H^+) transported in the opposite direction [22]. The transport process thus generates a net charge movement, which must be compensated by separate shunt mechanisms (ion channels). SERCA2a is finely regulated by PLN.

2.3.3. PLN: structure and function

PLN is a small protein of approximately 52 amino acid residues located in the SR membrane. The protein is organized into three domains: two hydrophilic cytosolic domains (Ia and Ib) and one transmembrane inhibitory domain (II). Domain Ia contains residues Ser16 and Thr17, which are phosphorylated by protein kinase A (PKA) and Ca^{2+}/calmodulin-dependent protein kinase II (CaMKII), respectively. Domain Ib modulates the interactions between domains Ia and II. Finally, the inhibitory domain II includes several amino acids that are essential for the stabilization of the oligomeric pentameric structure, such as leucine/isoleucine clusters [13, 18, 23]. PLN is present in both monomeric (10–20%) and homo-pentameric (80–90%) forms. The monomeric form is functionally active, whereas the pentameric form acts as a reserve pool [12, 18, 23].

2.3.4. The interaction between SERCA and PLN

PLN is a crucial regulator of Ca^{2+} cycling in cardiomyocytes. In its non-phosphorylated state (monomeric PLN), it inhibits SERCA2a, which mediates Ca^{2+} removal from the cytosol and determines the degree of SR Ca^{2+} loading [18]. Conversely, phosphorylation of PLN by PKA at the Ser16 residue in the cytosolic domain relieves this inhibition, favoring the pentameric conformation of PLN and thereby accelerating Ca^{2+} reuptake by SERCA2a.

PLN can be phosphorylated at Ser16 by PKA, at Thr17 by CaMKII, or at Ser10 by protein kinase C (PKC); each of these phosphorylation events contributes to Ca^{2+} handling. PLN is subsequently dephosphorylated by protein phosphatase 1 (PP1) [18, 23].

The interaction between SERCA and PLN is essential for both systole and diastole and is subject to β-adrenergic regulation. Two models have been proposed: according to the first, PLN dissociates from SERCA following phosphorylation, thereby restoring its activity. Alternatively, it has been suggested that phosphorylation induces a conformational change in the cytoplasmic domain Ia of PLN, reversing inhibition without requiring dissociation [7, 22]. The existence of the pentameric form of PLN nevertheless suggests that dissociation may occur, even if not directly related to the inhibitory mechanism.

2.3.5. PLN R14-del

Several PLN mutations have been closely linked to ACM and DCM. Among them PLN-R14del mutation, consists of the deletion of the nucleotide triplet AGA (positions 40–42) in the coding region of the PLN gene. This alteration results in the synthesis of a protein lacking the arginine residue at position 14. The mutation was first described in a Greek family in 2006 and was later identified in the United States, Canada, China, Germany, Spain, and the Netherlands. It is particularly prevalent in the northern part of the Netherlands, especially in the Friesland region [24]. Indeed, it has been reported that 10–15% of Dutch patients affected by dilated cardiomyopathy (DCM) are heterozygous carriers of the mutation [2, 13]. Notably, the homozygous form of the mutation has not been observed in humans [3].

At present, no specific treatments are available for DCM associated with the PLN-R14del mutation. The therapeutic approach is limited to slowing disease progression through drugs commonly used for the treatment of heart failure, particularly antifibrotic agents such as aldosterone antagonists. However, current therapies are not able to reverse the pathological phenotype. This highlights the importance of understanding the pathophysiological mechanisms underlying PLN-R14del–associated DCM, in order to develop novel therapeutic strategies aimed at halting or reducing the severity of the disease.

More than a decade ago, Haghighi and co-workers have defined the PLN-R14del as a "super inhibitory" [3] mutation. The underlying mechanisms have been related to an imbalance between the pentameric and monomeric structure of PLN, resulting in increased PLN monomers concentration, thus increased SERCA2a inhibition. Nevertheless, it remains unclear how the mutation leads to the severe phenotype (biventricular dysfunction, arrhythmias, fibrofatty replacement and interstitial fibrosis), observed in ACM and DCM patients.

Nonetheless, this theory is not fully supported by more recent experimental evidence, which instead suggests that the mutation results in a "SERCA gain of function" / "PLN loss of function" [7, 9, 11].

These additional findings open the possibility to consider different mechanisms involved in the pathophysiology of this PLN mutation.

More recently, two parallel lines of evidence support an alternative pathogenesis for PLN-R14-del cardiomyopathies: i) hyperdynamic EC-coupling, not further improved by pharmacological PLN antagonists, was first described in patient-derived hiPS-CMs [11] and then confirmed by two studies in a murine model of the mutation [25, 26]; ii) intracellular PLN "clusters" were reported to perturb the organelle structure of mutant human and murine CMs, with overt signs of endoplasmic/sarcoplasmic reticulum (E/SR) stress being detected in patient-derived hiPS-CMs [12]. The former evidence is incompatible with the super-inhibition hypothesis; the latter suggests that "toxicity" of mutant PLN protein might be involved in the pathogenesis of ACM/DCM.

2.3.6. The role of Ca^{2+} in mitochondrial metabolism

In adult cardiomyocytes, mitochondria occupy approximately one-third of the total cell volume, underscoring the essential role of oxidative phosphorylation in meeting the high energetic demand associated with contraction. Under working conditions, the two principal ATP consumers are SERCA2a and the NCX. About 95% of ATP is generated by oxidative phosphorylation, whereas only ~5% derives from glycolysis [27–29].

In eukaryotic cells, oxidative phosphorylation takes place within mitochondria, double-membrane organelles with distinct permeability properties. The outer mitochondrial membrane is permeable to small molecules and ions through transmembrane channels, while the inner membrane is impermeable to most ions and solutes, including protons. Only metabolites with dedicated transporters can cross it [28]. The inner membrane also contains invaginations, termed cristae, which significantly expand its surface area and host the electron transport chain (ETC).

Oxidative phosphorylation couples the reduction of O_2 to H_2O with the transfer of electrons (e^-) donated by NADH and $FADH_2$ along the ETC, embedded in the cristae of the inner membrane. Electron transfer is coupled to proton (H^+) pumping, generating an electrochemical gradient across the inner mitochondrial membrane that drives ATP synthesis by the ATP synthase [27]. Mitochondrial ATP production is tightly regulated by several factors, including substrate and product availability (e.g., ADP/ATP ratio), the abundance of NADH and $FADH_2$, and mitochondrial Ca^{2+} levels. The close spatial relationship between mitochondria and the SR ensures that Ca^{2+} released from the SR produces a steep local increase in Ca^{2+} concentration at the SR–mitochondria interface, rising from 100–200 nM up to ~500 nM [27, 30–33] Ca^{2+} crosses the outer mitochondrial membrane via voltage-dependent anion channels (VDAC1), which preferentially transport anions but also contribute to Ca^{2+} fluxes [34, 35]. Once in the intermembrane space, Ca^{2+} enters the matrix through the mitochondrial Ca^{2+} uniporter (MCU), located in the inner membrane [36]. Because MCU has low Ca^{2+} affinity, it becomes active only when cytosolic Ca^{2+} reaches ~500 nM [16, 37]. Under physiological conditions, mitochondrial [Ca^{2+}] remains low (~0.1 μM), but during MCU activation it can transiently rise to ~10 μM due to the steep electrochemical gradient across the inner membrane [37].

Mitochondrial Ca^{2+} homeostasis requires that, at steady state, Ca^{2+} influx during each cycle is balanced by efflux before the next cycle begins. Ca^{2+} extrusion is mediated primarily by the mitochondrial Na^+/Ca^{2+} exchanger (NCXm), located in the inner membrane [16]. Importantly, mitochondrial Ca^{2+} directly regulates ATP production in response to cellular energy demand [16]. Ca^{2+} activates key dehydrogenases in the tricarboxylic acid cycle, including pyruvate dehydrogenase, α-ketoglutarate dehydrogenase, and NAD-dependent isocitrate dehydrogenase. Their activation enhances the supply of reducing equivalents (NADH and $FADH_2$) to the ETC, thereby boosting the proton gradient and ATP synthesis [37, 38]. Additionally, Ca^{2+} can directly modulate ATP synthase activity by regulating phosphorylation of its γ subunit [39].

Perturbations in intracellular Ca^{2+} homeostasis can profoundly affect mitochondrial Ca^{2+} uptake, oxidative phosphorylation, and the generation of reactive oxygen species (ROS). Mitochondrial Ca^{2+} overload, especially when combined with excessive ROS production, induces opening of the mitochondrial permeability transition pore (MPTP). This event disrupts inner membrane integrity, collapses the proton gradient, and leads to mitochondrial failure. Release of pro-apoptotic factors such as cytochrome C subsequently activates programmed cell death pathways [38].

Pathological conditions, such as heart failure, are characterized by progressive mitochondrial remodeling and impaired oxidative capacity. This remodeling includes reduced transcription of key enzymes for fatty acid oxidation as well as downregulation of components of the ETC and oxidative phosphorylation machinery [27, 36].

2.4. Methods

2.4.1. Experimental model

Development of the PLN R14del TG mouse is described by Eijgenraam et al.[13]. The studies were performed on tissues from PLN-R14del heterozygous (Mut) mice and WT controls aged 8 to 12 weeks. In this age range, the animals are healthy; overt physical or echocardiographic signs of chamber remodeling or contractile dysfunction are present in this model at 18 months of age. This is crucial to the interpretation of the observed changes as directly resulting from the mutation, rather than secondary to aspecific myocardial remodeling.

2.4.2. Cardiomyocyte isolation

All experiments involving animals confirmed to the guidelines for Animal Care endorsed by the Milano-Bicocca and to the Directive 2010/63/EU of the European Parliament on the protection of animals used for scientific purposes.

Mut mice and WT controls were intraperitoneally anesthetized with Chloral hydrate ($ClCCH(OH)2$, Sigma - Aldrich) in 200 μL of Seleparina (Nadroparina Calcica 9500 U.I, ItalFarmaco) and 200 μL of physiological solution (0.9% NaCl 1M in MilliQ). After anesthesia, evidenced by absence of movements and reflexes, animals were sacrificed by cervical dislocation and ventricular cardiomyocytes (CMs) were isolated by using a manual perfusion method [40].

Briefly, while the heart was still in situ, the right ventricle (RV) was injected with 7 mL of EDTA buffer solution (130 mM NaCl, 5 mM KCl, 0.5 mM NaH_2PO_4, 10 mM HEPES, 10 mM Glucose, 10 mM 2,3-Butanedione Monossime, BDM, 10 mM Taurine, 5 mM EDTA; pH=7.8 with NaOH); the ascending aorta was then clamped and the heart was transferred to a dish containing EDTA buffer solution.

Digestion was achieved by sequential injections into the left ventricle (LV) of 10 mL EDTA buffer solution, 6 mL of perfusion buffer solution (130 mM NaCl, 5 mM KCl, 0.5 mM NaH_2PO_4, 10 mM HEPES, 10 mM Glucose, 10 mM 2,3-Butanedione Monossime, BDM, 10 mM Taurine, 1 mM $MgCl_2$; pH=7.8 with NaOH) and 20 to 30 mL of Liberase buffer solution (0.1 mg/ml Liberase in Perfusion Buffer + 0.02 mg/ml Trypsin EDTA and 6.25 μM $CaCl_2$).

Cellular dissociation was completed by gentle trituration, while enzyme activity was quenched by adding 10 mL of stop buffer solution (perfusion Buffer + 10% FBS). The resulting suspension was filtered, centrifuged and resuspended in calcium free solution (130 mM NaCl, 5.4 mM KCl, 0.4 mM NaH_2PO_4, 0.5 mM $MgCl_2$, 25 mM Hepes, 22 mM Glucose; pH=7.4 with NaOH). Finally, the physiological extracellular Ca^{2+} concentration (2 mM) was gradually reestablished by adding to the cell suspension small volumes at increasing $CaCl_2$ concentration.

2.4.3. Preparation of cardiac homogenate

For each group of tissues, the hearts were divided into two pools to be processed separately, in order to get two different preparations.

The hearts were thawed, weighed, dissected by surgical scissor, and homogenized 4 times (20 seconds for each period) with IKA Ultra Turrax at 4°C in homogenization buffer (ratio 1g / 4 ml) containing 50 mM Potassium Phosphate, 300 mM Sucrose, Sodium Fluoride 10 mM, pH 7 plus 0.3 mM PMSF and 0.5 mM DTT. The total homogenate was centrifuged at 17000 rpm for 30 minutes at 4°C (Beckman); the final pellet was resuspended in 2.5 volumes of homogenization buffer.

SERCA2a ATPase measurements in cardiac homogenates

The measurement was performed as previously described [41]. Briefly, SERCA2a ATPase activity was measured in homogenates as the rate of P-ATP hydrolysis and identified as the fraction inhibited by 10 μM cyclopiazonic acid (CPA). The ATPase activity was measured at multiple Ca^{2+} concentrations; data points were fitted to a sigmoidal (Hill) function, from which the maximum velocity (V_{max}) and Ca^{2+} affinity [Kd_{Ca}] parameters were estimated.

2.4.4. Electrophysiological recordings

Ruptured-patch recordings

Except for IK_{ATP} measurements, V-clamp was performed by the ruptured-patch version of the whole-cell mode. Cells were perfused (at 36 °C) with an extracellular solution containing (in mM): 154 NaCl, 4 KCl, 5 HEPES NaOH, 1 mM $CaCl_2$, 1 mM $MgCl_2$, 5.5 glucose; pH=7.35 with NaOH. Patch pipettes (tip resistance of 1.5-2.5 MΩ) were filled with an intracellular solution containing (in mM): 110 K-aspartate, 23 KCl, 3 $MgCl_2$, 0.04 $CaCl_2$, 0.1 EGTA KOH (10-7 Ca^{2+}-free), 5 Hepes KOH, 0.4 Na^+-GTP, 5 Na^+-ATP, 5 Na^+-phosphocreatine; pH=7.3 with KOH. Membrane capacitance and series resistance (<10 MΩ) were measured in every cell but left uncompensated. The V protocols were applied, and the recorded signals amplified by MultiClamp 700B (Molecular Devices, Sunnyvale, CA, United States), digitized at 20 kHz (Axon Digidata 1440A, Molecular Devices), and filtered at 10 kHz. As validated in previous work, membrane current (I_m) recorded during steps from -40 to 0 mV in the presence of 2 mM 4-aminopyridine and 0.1 mM $BaCl_2$ are largely representative of I_{CaL}; intracellular K^+ was not substituted to avoid interference with SR function. The change in I_m induced by caffeine challenge (at Vm = -40 mV) was taken as a measure of Na^+/Ca^{2+} exchanger current (I_{NCX}) [42].

Perforated-patch recordings

I_{KATP} was recorded using amphotericin-perforated patch technique, aimed to prevent intracellular contamination by the pipette solution [43]. Briefly, a stock solution was prepared by sonicating 3 mg amphotericin B (Merck) in 50 μl dimethylsulphoxide (DMSO). Prior to each experiment, 3.33 μl amphotericin stock was added to 1 ml of intracellular solution. To enhance seal formation, the pipette tip was dipped in amphotericin-free intracellular solution for 20 s prior to backfilling with the amphotericin containing one. Following seal formation, small depolarizing pulses (10 mV from -80 mV) were applied and overall "access resistance" was computed from the capacitive current transients. The latter became stable after about 10 min; poration was considered satisfactory when access resistances fell below 25 MΩ.

I_{KATP} was evaluated at a holding potential of -120 mV as the difference ($I_{CTRL} – I_{GLIBE}$) between the current recorded in control (CTRL) and during steady-state perfusion with the selective blocker glibenclamide (GLIBE, 5 μM). I_{KATP} was normalized to membrane capacitance to obtain current density.

2.4.5. Intracellular Ca^{2+} recordings

Intracellular Ca^{2+} measurements were performed at 36°C. Cytosolic Ca^{2+} was optically measured in ventricular CMs loaded with the probe Fluo-4 AM (10 μM) by 30 min incubation at room temperature. During the recording, cells were perfused with an extracellular solution containing (in mM): 154 NaCl, 4 KCl, 5 HEPES NaOH, 2 mM $CaCl_2$, 1 mM $MgCl_2$, 5.5 glucose; pH=7.35 with NaOH.

Calcium transients (CaT) were recorded as Fluo-4 signal, collected at 40X magnification (oil immersion) through a 535 nm band pass filter, converted to voltage, low-pass filtered (10 kHz) and digitized at 20 kHz. To compensate for potential differences in probe loading, all fluorescence (F) values were normalized to F0, which was recorded during prolonged quiescence.

Ca^{2+} transients (CaT) were measured either under field-stimulation (1 Hz) or V-clamp, as specified in the results section. The following parameters were extracted from CaT: Ca^{2+} transient amplitude (CaT amplitude), Ca^{2+} transient decay kinetics (τ decay), Ca^{2+} transient rise-time (tpeak), diastolic Ca^{2+} (CaD). Rate-dependency of CaT properties was tested by stepwise increments in pacing rate (to 1, 1.3, 1.7, and 2 Hz). Under V-clamp, simultaneous measurement of I_{CaL} allowed to estimate the "gain" of Ca^{2+}-induced Ca^{2+} release (CICR) as the Ca^{2+} release/influx ratio [44].

The sarcoplasmic reticulum (SR) Ca^{2+} content was estimated as the integral of the I_m (mostly representing I_{NCX}) elicited by a caffeine (10 mM) pulse applied after a loading train of V steps (−40 to 0 mV at 1 Hz). To avoid Ca^{2+} influx during the SR emptying, caffeine was dissolved in Ca^{2+}-free solution (containing 1 mM EGTA CsOH).

The fraction of SR Ca^{2+} content released by membrane excitation (fractional release) was calculated as the ratio between the amplitudes of V- and caffeine-triggered CaT. The "gain" of Ca^{2+} -induced Ca^{2+} release (CICR) was measured as the ratio between Ca^{2+} influx through I_{CaL} and the resulting increase in cytosolic Ca^{2+}.

Information on NCX function was obtained by linear fitting of the trailing branch of the I_{NCX}/[Ca^{2+}] loops, recorded during caffeine-induced transients. The slope coefficient and the 0 I_{NCX} intercept were used as surrogate of NCX "conductance" and cytosolic [Ca^{2+}] at electrochemical equilibrium, respectively.

The Ca^{2+} uptake function of the SR was evaluated through a dedicated "SR reloading" protocol, applied under V-clamp [45]. The SR was initially emptied by a caffeine pulse and reloaded by a train (0.25 Hz) of 200 ms V steps from −40 to 0 mV. CaT and I_{CaL} were simultaneously recorded during the reloading protocol. The following parameters were analyzed from each step of the protocol: i) CaT amplitude, ii) CICR gain, iii) CaT decay kinetics (τ decay), iv) diastolic Ca^{2+} (CaD). The rate of increment of the former two parameters during the loading protocol reports the rate of SR refilling. τ decay reports the rate of cytosolic Ca^{2+} clearance (the faster Ca^{2+} removal, the smaller τ decay) within each step, i.e. at varying SR filling levels. CaD course reports the rate of cytosolic Ca^{2+} accumulation, expectedly reduced by enhancement of SR uptake function.

2.4.6. *Energy metabolism*

Analysis of mitochondrial respiration (OCR) and anaerobic glycolysis

Oxygen consumption rate (OCR) and Proton Efflux Rate (PER) were measured within each plate in quiescent CMs (Seahorse XFe96 Extracellular Flux Analyzer, Agilent) by using the Mito Stress Test and the Glycolytic Rate Assay protocols, in order to determine respiratory and glycolytic bioenergetics respectively. To minimize measurement stray variability, both experimental groups were represented within the same multiwell plate; furthermore, the position of each treatment within the plate was changed in each session. To prevent cell displacement, plate wells were coated with the adhesive agent Cell-Tak (22.4 μg/ml, Corning). Cell concentration in the CMs suspension was preliminarily analyzed (Operetta CLS™– Perkin Elmer). Viable cells per unit volume were counted as the difference between number of nuclei (stained by Hoechst 0.5 μg/ml) and of dead cells stained with Propidium Iodide (PI 0.5 μg/ml). Based on the count, CMs suspension (Agilent Seahorse XF DMEM Medium pH=7.4, # 103575-100, supplemented with 2mM L-glutamine, 10mM glucose and 1 mM sodium pyruvate) was seeded into each well to obtain a density of 2.5×10^3 cells/well.

OCR was measured under basal conditions and after injection of oligomycin (Oligo; 1.5, 3 μM), carbonyl cyanide p-trifluoromethoxyphenylhydrazone (FCCP; 0.5, 1, 2 μM) and Rotenone/Antimycin A (Rot/Ant; 0.5, 1, 3 μM). The minimal doses of drugs causing the maximal response were determined for each experimental group in preliminary measurements.

OCR parameters were calculated as follows: i) mitochondrial basal respiration = OCR before Oligo (1.5 μM) – OCR after Rot/Ant (3 μM); ii) mitochondrial maximal respiration = OCR after FCCP (0.5 μM) − OCR after Rot/Ant (3 μM); iii) spare respiratory capacity = mitochondrial maximal respiration – mitochondrial basal respiration; iv) non-mitochondrial respiration = OCR after Rot/Ant (3 μM).

PER was measured under basal conditions and after injection of 1.5 μM Oligo, 3 μM Rot/Ant and 50 mM 2-deoxy-D-glucose (2-DG) to assess anaerobic glycolysis. The 2-DG concentration was 5-fold that of glucose (the natural substrate), as required to block its metabolism.[46]

Glycolytic parameters were calculated as follows: i) basal glycolysis = PER before Oligo – PER after 2DG); ii) compensatory glycolysis = PER after Rot/Ant − PER after 2-DG; iii) glycolytic reserve = compensatory glycolysis – basal glycolysis; iv) non-glycolytic acidification = PER after 2-DG.

At the end of the experiment, measured OCR and PER values were normalized to the number of viable cells in each well, again quantified as above.

To assess the influence on OCR of cytosolic and SR Ca^{2+} respectively, a subset of cells was pre-incubated for 30 minutes with BAPTA-AM (BAPTA; 5 μM) or Thapsigargin (THAPSI; 5 μM). Vehicle (DMSO) was present at the same concentration in all the experimental solutions.

ROS quantification

To evaluate intracellular content of reactive oxygen species (ROS), quiescent CMs were stained with 2’7’-dichclorofluorescin diacetate (DCFDA; 20 μM) for 10 minutes at 37°C and 5% CO2. Stained cells were seeded, at the concentration of 2.5×10^3 per well, in 96-wells plates (Perkin Elmer). DCFDA was excited at 485 nm and ROS levels were estimated as fluorescence emission at 535 nm. Automated (unbiased) confocal single-cell fluorescence measurement was performed by Operetta CLS™ (Operetta– Perkin Elmer) at 40× magnification.

Mitochondrial Membrane Potential evaluation

To evaluate mitochondrial membrane potential (Ψm), cells were stained with 100 nM Tetramethylrhodamine, Ethyl Ester (TMRE) for 10 min at 37 °C and 5% CO_2. Stained cells were seeded at the concentration 7.5×10^3 per well. TMRE fluorescence was analyzed by confocal imaging at 63× magnification (Operetta CLS™). At the concentration used in the present study, TMRE works in "quenching mode", i.e. emission increases as Ψm depolarizes [47]. At any rate, TMRE fluorescence signal was calibrated in each measurement by short-circuiting mitochondrial electron transport with FCCP (0.02 μM).

2.4.7. mRNA extraction and qRT-PCR assay

After collection, RV bioptic samples from WT and Mut mice were mechanically disrupted using metallic beads by a TissueLyser (Qiagen, Milan, Italy) in an appropriate amount of RL lysis buffer (Norgen Biotek corp., Thorold, Canada). RNA was extracted by using a total RNA purification kit (Norgen Biotek corp., Thorold, Canada) and quantified by a NanoDrop spectrophotometer (ND-1000, EuroClone, Milan, Italy). Reverse transcription was conducted with SuperScript III (Invitrogen, Carlsbad, CA, USA), following manufacturer's instructions. qRT-PCR was performed with the iQTM SYBR Green Super Mix (Bio-Rad Laboratories, Hercules, CA, USA) reagent and specific primers (reported in Table 1). All reactions were performed in a 384-well format with the 7900HT Fast Real-Time PCR System (Thermo Fisher Scientific, Massachusetts, USA). The relative quantities of specific mRNAs were obtained by the comparative Ct method and normalized to the housekeeping gene glyceraldehyde 3-phosphate dehydrogenase (GAPDH).

Gene	**Forward primer**	**Reverse primer**
Eif2ak3	CACGCAGATCACAGTCAGG	GTGGGGCTGAGGATGGAAAA
Hspa5	GGGTCAGGGAGAGGAGGAAT	CCAAGGTGAACACACACCCT
Atf6	TGGAAGCCTAAAGAGGACCTG	CGTGGGAGGACAGAGAAACAA
Ern1	GAGACAGATTGTCAGGGCCA	CCTACAAAGTCTGTGGTAGCCT
Pink1	GATGGCTCTGTGCTCCAGTT	CCCTCCCTCTACTCCAGCTT
Parkin	GGGATTCAGAAGCAGCCAGA	GAGGGTTGCTTGTTTGCAGG
Map1lc3b	CCAAGCCTTCTTCCTCCTGG	TTGCTGTCCCGAATGTCTCC
Vdac1	CGGCCACACATGATCACAGA	ACCAGTCTCGGGGTCTTCTT
Itp3r 1	GTTGGACGAGGCTGGAAATG	GGCCAGCATTGACAGGATTC
Itp3r 2	GGGAGAAATCGTGAAATACAGCA	CATCCAGTGACACTCGCATG
Itp3r 3	CTCTGTCAACTGCAACACCA	TTGCCCCTGTACTCATCACA
Hspa9	AGGTTTCCAGAAGCGTAGCC	GGTTACGAGGGCAAGAACCA

Mfn2	GCTTGGACAGGTGGAGTCAA	GGACTCGAGGTCTCCTCTGT
Gpx3	GTGAACGGGGAGAAAGAGCA	CAGGAGTTCTGCAGTGGGAG
Sod2	GTAGGGCCTGTCCGATGATG	CGCTACTGAGAAAGGTGCCA
Nqo1	GCTCCACGAGGATGGGAAAA	TGCCCTGAGGCTCCTAATCT
Ho1	CCTCACAGATGGCGTCACTT	TGGGGGCCAGTATTGCATTT
Gclc	GCTTTGGGTCGCAAGTAGGA	GCGTCCCGTCCGTTCC
Ptgs2	CTTCGGGAGCACAACAGAGT	AAGTGGTAACCGCTCAGGTG
Camk2a	ATCGTCCACTTCCACAGA	CCACATTCCACGGACAAA
Camk2b	GCATTCCAACATTGTACGC	CTTGCCACGATGTCTTCA
Camk2g	TGATGCCAGCCACTGTA	GCAAGTTCTCAGGCTTCA
Camk2d	TGTTCACTTTCACCGTTCG	GCCTTGAGGACAGAATGAAG
Prkaa1	AAAGTGAAGGTGGGCAAGCA	CAGATGGTGTACTGATGACCTGG
Prkaa2	TCGCAGTTTAGATGTTGTTGGA	CTTCAACCCGCCCATGTTTG
Prkab1	CCTTGTGTCCCTGCAGATTCC	CATGAGGATCTTGGGCCTGTC
Prkab2	CGACCCCAGCGTCTTCAG	CAAATCCTGCTGCCAGGGTA
Prkag1	GCTTTCCAAGCTGAGGAACT	ACCAACTTGGAACTTGTGGG
Prkag2	TGCCTACTTAAGGACAGGCG	CCCTGAGACTCCTGAGAAAGC
Prkag3	CCATGGCTACCAGCTCCAAA	CTCTGCTTCTTGCTGTCCCA
Gapdh	ACCACAGTCCATGCCATCAC	TCCACCACCCTGTTGCTGTA

Table 1. *Primer sequences 5’ - 3’*

2.4.8. Protein Extraction and Western Blot Analysis

RV samples were chopped using metallic-beads by a Tissue Lyser (Qiagen, Milan, Italy) in cell lysis buffer (Cell Signaling Technology, Danvers, MA, USA) supplemented with protease- and phosphatase-inhibitor cocktails (Sigma-Aldrich, Saint Louis, MO, USA). Protein lysate was then quantified, and equal amounts of total protein extracts were subjected to SDS-PAGE and transferred onto a nitrocellulose membrane (Bio-Rad, California, USA). The membranes were blocked for 1 hour at room temperature in 5% non-fat dry milk added to Wash Buffer (Tris Buffer Sulfate, 0.1% Tween-20) and then incubated overnight at 4°C with the appropriate primary antibodies (reported in Table 2). Peroxidase-conjugated secondary antibodies (GE Healthcare, Chicago, IL, USA) were then applied for 1 hour. Peroxidase signal was visualized using the LiteUP Western Blot Chemiluminescent Substrate (EuroClone, Milan, Italy). Images were acquired with the ChemiDocTM MP Imaging System (Bio-Rad, California, USA), and blot densitometric analysis was performed (ImageJ software, National Institutes of Health, Bethesda, MD, USA). Protein signals were normalized to GAPDH and TUBULIN based on the gel gradient used.

Protein	Clonality/Code	Source	Company	Diluition
phospho-CaMKII (T286)	Polyclonal, ab32678	Rabbit	Abcam	WB: 1:1000
CaMKII	Monoclonal, ab52476	Rabbit	Abcam	WB: 1:1000
phospho-AMPK	Monoclonal, #2535	Rabbit	Cell Signaling	WB: 1:1000
AMPK	Polyclonal, #2532	Rabbit	Cell Signaling	WB: 1:1000
SERCA2 ATPase	Monoclonal, ab2861	Mouse	Abcam	WB: 1:1000
GAPDH	Polyclonal, sc-25778	Rabbit	Santa Cruz	WB: 1:1000

Table 2. Primary antibodies.

2.4.9. Statistical analysis

GraphPad Prism 8 (GraphPad software, San Diego, CA, USA) was used for statistical analysis. Normality of distribution was assessed using D'Agostino-Pearson's normality test. To compare two sample means, either the Student's t-test and the Mann-Whitney U-test were used for continuous or categorical data, respectively. To compare more than two sample means, one-way ANOVA (with Tukey correction) or Kruskal-Wallis (with Dunn's correction) were used for continuous or categorical data, respectively. In the case of repeated measurements (e.g. rate-dependency and SR loading) a Mixed-effects model containing "Treatment" (WT vs Mut, PST-3093 vs Control) and "Variable" (rate or step #) factors was used. As reported for each result, the significance of "Treatment X Variable interaction" (i.e. difference between Treatments in their response to the Variable) was first tested; in its absence, significance of difference between Treatments at all Variable values was tested.

In figures, whenever feasible, individual data points were plotted, to illustrate dispersion, along with the sample mean ± SEM. Whenever the threshold for statistical significance ($p<0.05$) was achieved, the actual p-value for the comparison was reported as an index of robustness. For each experiment, the number of preparations or cells (n) and the number of animals from which they were obtained (N) are indicated in the respective figure legend.

2.5. Results

2.5.1. SERCA2a ATPase activity

SERCA2a ATPase activity correlates with Ca^{2+} transport rate [48], its measurement in myocardial homogenates provides direct information on the transporter function in a simplified (cell-free) system. Ca^{2+}-sensitivity of SERCA2a activity is mostly determined by SERCA2a-PLN interaction and is therefore suitable to detect its abnormalities [48]. In Mut homogenates, the Ca^{2+} dissociation constant (Kd_{Ca}) for SERCA2a ATPase activity was decreased by 21% compared with WT (unpaired Student's t-test, p = 0.0005), reflecting an increased apparent Ca^{2+} affinity. The maximum velocity of SERCA2a ATPase activity was similar between Mut and WT preparations. Mut SERCA2a ATPase activity exceeded WT one above 300 nM Ca^{2+} (Figure 1). This observation suggests reduced inhibition of SERCA2a by PLN in Mut preparations.

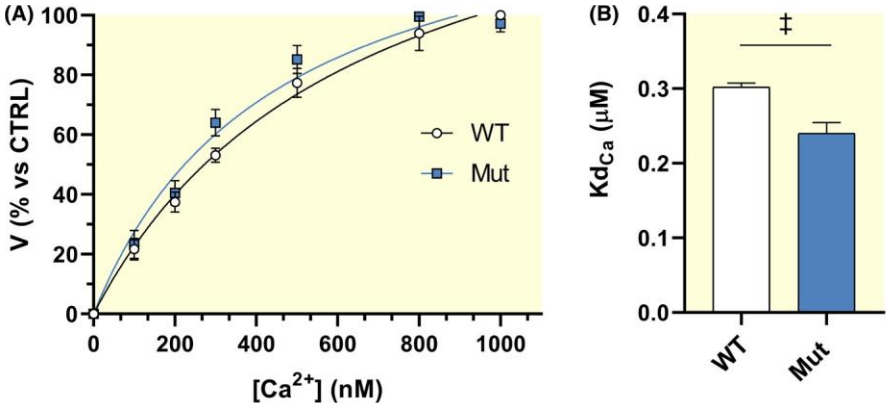

FIGURE 1. Ca^{2+}-dependent activation of SERCA2a ATPase in ventricular homogenates. (A) SERCA2a (CPA-sensitive) ATPase activity as function of medium Ca^{2+} concentration; solid lines obtained by fitting with Hill functions. (B) Ca^{2+} dissociation constant (Kd_{Ca}, lower values reflect increased affinity) estimated from the fitting (WT: 0.30 ± 0.01, *n* = 10; Mut: 0.24 ± 0.01, *n* = 8). WT: *N* = 2 preparations (4–5 technical replicates each); Mut: *N* = 2 preparations (4 technical replicates each). Data are expressed as mean ± SEM. Unpaired Student's *t*-test.

2.5.2. Intracellular Ca^{2+} dynamics

Next, SERCA2a function was assessed in intact cardiomyocytes to capture its contribution within the physiological cellular environment. To improve mechanistic interpretation of the mutation effect, parallel experiments were performed with a pharmacological agent known to enhance SERCA2a activity by disrupting its inhibitory interaction with PLN [10]. As the functional impact of SERCA2a on intracellular Ca^{2+} handling is influenced by pacing frequency, we further examined the rate dependency of Ca^{2+} dynamics by stimulating cardiomyocytes at four frequencies ranging from 1 to 2 Hz. Since these experiments aim to compare the rate- dependency of effect, statistical significance refers to the Treatment × Rate interaction.

Steady-state stimulation (1 Hz)

The impact of the mutation on intracellular Ca^{2+} dynamics was evaluated in intact cardiomyocytes under steady-state field stimulation at 1 Hz (Figure 2). Calcium transient (CaT) parameters were quantified as previously described. In Mut CMs τdecay (Figure 2E) was shorter by 43% (Mann–Whitney *U*-test, $p < 0.0001$ vs. WT), indicating accelerated cytosolic Ca^{2+} clearance. Diastolic Ca^{2+} (CaD, Figure 2F) was 5% lower (Mann–Whitney *U*-test, $p = 0.0002$ vs. WT) and remarkably less variable. CaT amplitude (Figure 2C) and rise-time (*t*peak, Figure 2D) were comparable between the two genotypes, indicating preserved Ca^{2+} release and upstroke kinetics.

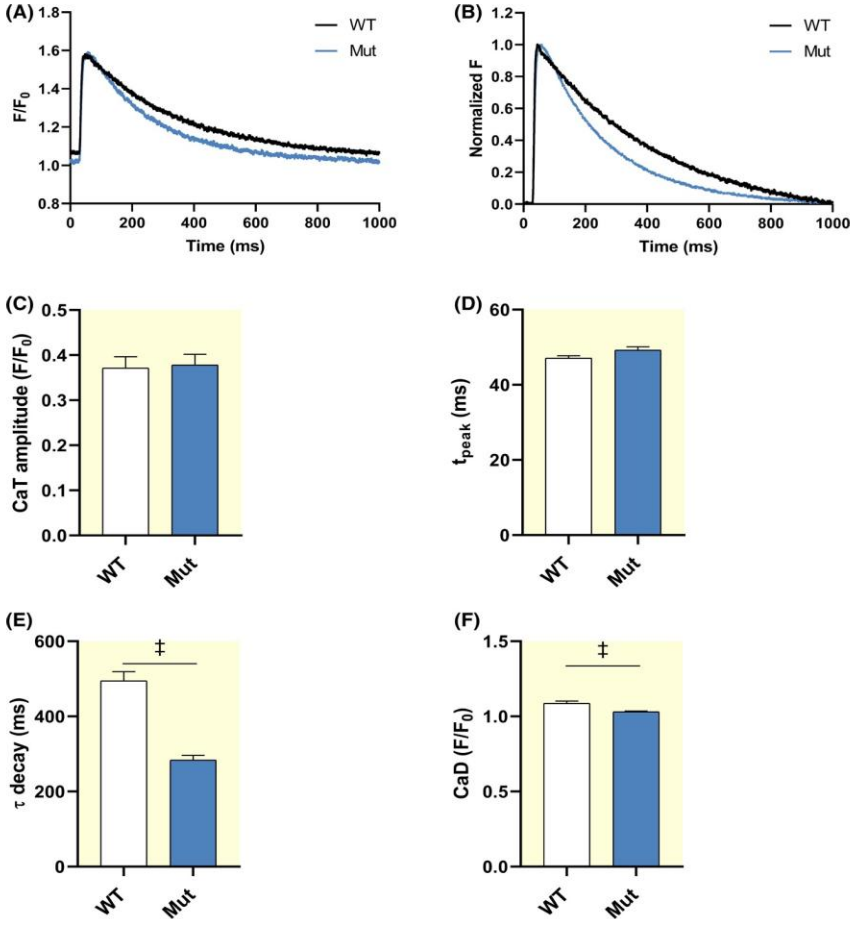

FIGURE 2. Parameters of calcium transients. (A) Representative Ca^{2+} transients (CaT). (B) CaT normalized to peak amplitude to illustrate changes in kinetics. (C) CaT amplitude (WT: 0.37 ± 0.03, $n = 32$; Mut: 0.38 ± 0.02, $n = 27$). (D) CaT time to peak, t_{peak} (WT: 47.1 ± 0.56, $n = 30$; Mut: 49.2 ± 0.94 $n = 27$). (E) Ca^{2+} transient decay kinetics, $τ_{decay}$ WT: 495 ± 24.1, $n = 32$; Mut 284 ± 12.2, $n = 27$). (F) Diastolic Ca^{2+}, CaD (WT: 1.09 ± 0.02, $n = 31$; Mut: 1.03 ± 0.01, $n = 27$). WT: $N = 4$; Mut: $N = 4$. Data expressed mean ± SEM; *p* by Mann– Whitney *U*-test

Rate-dependency

Since SERCA2a function influences the force–frequency relationship of cardiomyocytes [49], we hypothesized that the mutation might affect the frequency dependence of intracellular Ca^{2+} dynamics. To test this, cells were field-stimulated at progressively increasing frequencies between 1 and 2 Hz.

In wild-type cardiomyocytes, calcium transient parameters exhibited the expected rate dependency (Figure 3): *t*peak (inverse, $p < 0.0001$), τdecay (inverse, $p < 0.0001$) decreasing as frequency increased and CaD (direct, $p < 0.0001$) rising proportionally. Compared to WT, Mut CMs displayed a significantly shallower rate dependency of τdecay (Figure 3C, Mixed-effects model, Treatment × Rate, $p = 0.0015$ vs. WT), largely attributable to preferential shortening at slow stimulation rates. Consistent with faster SR Ca^{2+} uptake, frequency-dependent accumulation of CaD was less pronounced in CMs (Figure 3D, Mixed-effects model, Treatment × Rate, $p = 0.0114$ vs. WT). Rate dependency of the remaining CaT parameters did not differ significantly between genotypes.

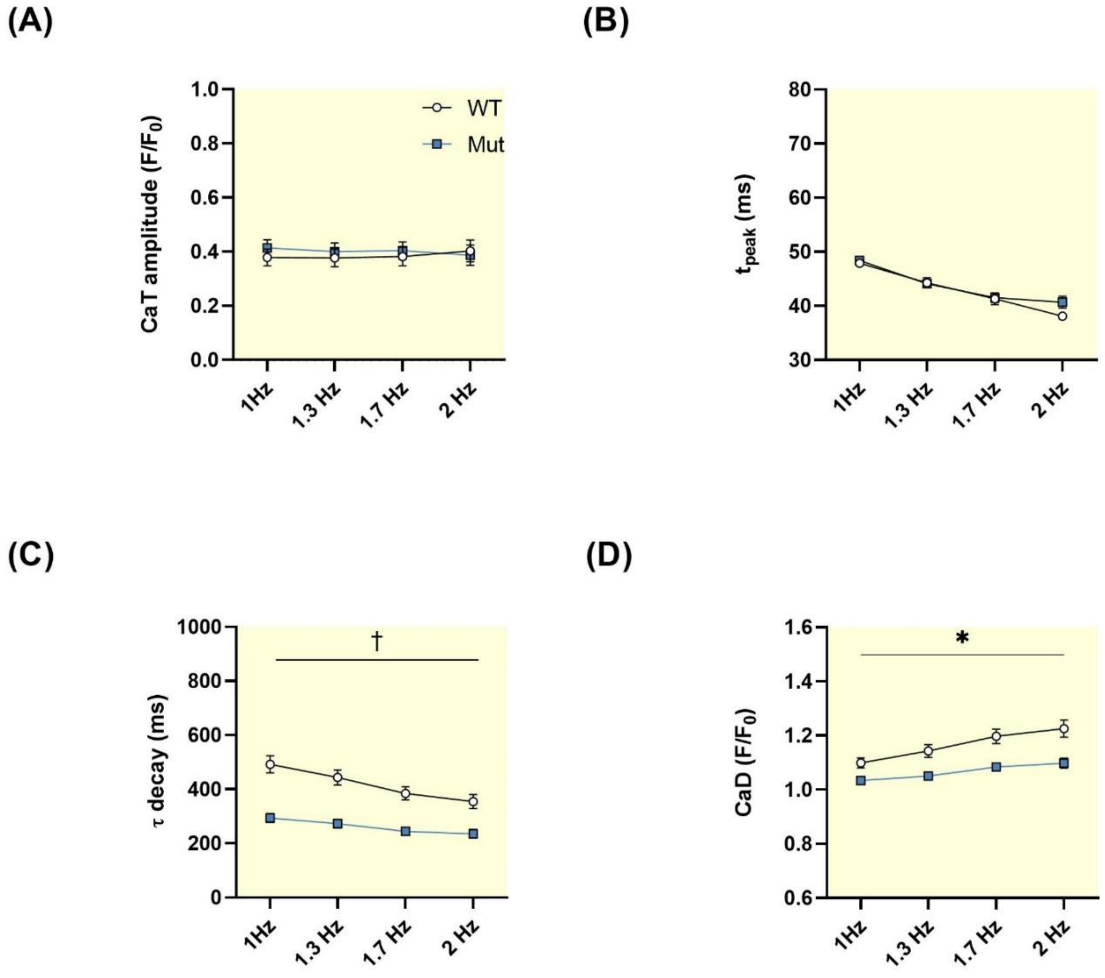

Figure 3. Rate dependency of CaT parameters in WT and Mut. Rate-dependency was tested by stepwise increments in pacing rate (1, 1.3, 1.7, and 2 Hz). (A) Ca^{2+} transient amplitude. (B) CaT time to peak, tpeak. (C) Ca^{2+} transient decay kinetics, τ decay. (D) Diastolic Ca^{2+}, CaD. WT: n=25, N=4; Mut: n=17, N=3. Data are expressed as mean ± SEM. Mixed-effects model, Treatment X Rate.

SR reloading rate and steady-state SR Ca^{2+} content

SR Ca^{2+} uptake function was assessed in V-clamped CMs by the “SR reloading” protocol and by measuring caffeine-releasable SR Ca^{2+} content (CaSR) (Figure 4A). The difference between Mut and WT CMs in the behavior of CaT parameters during SR reloading (from step 1 to 15) is reported below (Figure 4).

As expected, CaT amplitude progressively increased during SR reloading (Figure 4C); both the rate of increment and the final amplitude were larger for Mut CMs (Mixed-effects model, Treatment × Step, $p < 0.0001$ vs. WT). A similar trend was observed when normalizing CaT amplitude to Ca^{2+} influx through I_{CaL} (CICR gain, Figure 4F), although the larger variance in Mut data, for this parameter statistical significance was not achieved. The τdecay progressively decreased during SR reloading (Figure 4D). In Mut CMs τdecay values were markedly lower at baseline but exhibited a shallower decline across the protocol (Mixed-effects model, Treatment × Step, $p < 0.0001$ vs. WT). CaD started off from a lower value in Mut CMs (unpaired Student's *t*-test, $p = 0.0085$), but the difference decreased thereafter (Figure 4E, Mixed-effects model, Treatment × Step, $p = 0.0061$ vs. WT). Under these conditions, SR Ca^{2+} content (CaSR) was significantly larger in Mut CMs (Figure 4H, unpaired Student's *t*-test, $p = 0.0003$ vs. WT); while the fractional release of SR Ca^{2+} was comparable between groups (Figure 4I).

In summary, Mut CMs exhibited a “hyperdynamic” Ca^{2+} handling, consistent with reduced inhibition of SERCA2a rather than the proposed superinhibition. This pattern was observed both in intact CMs during field-stimulation and in V-clamp experiments assessing SR reloading.

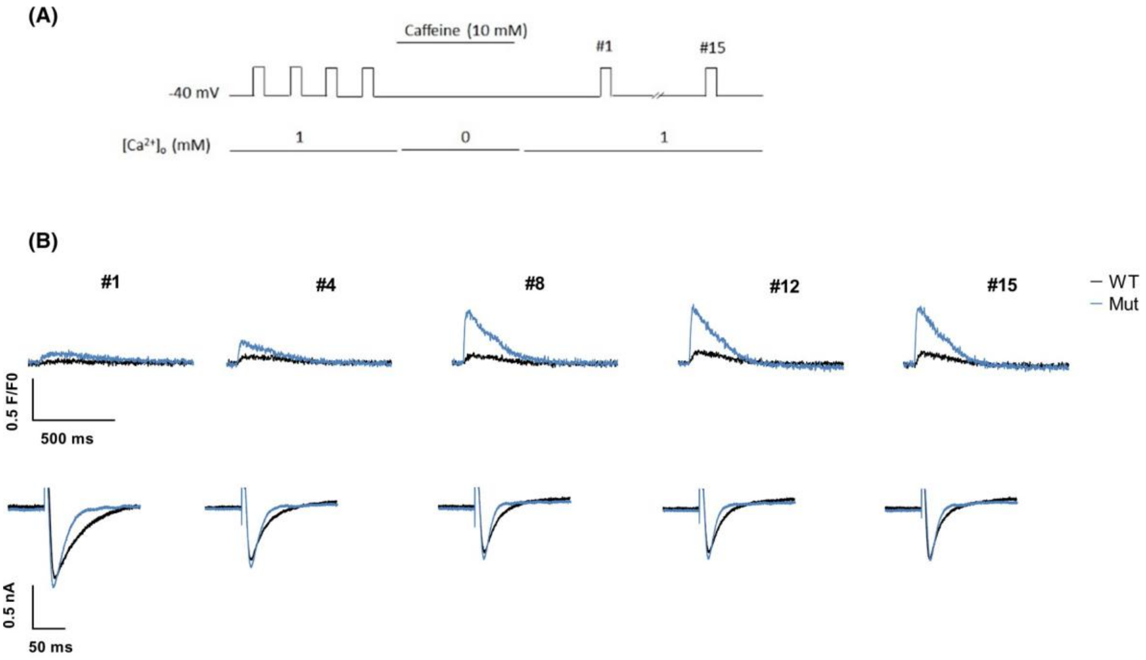

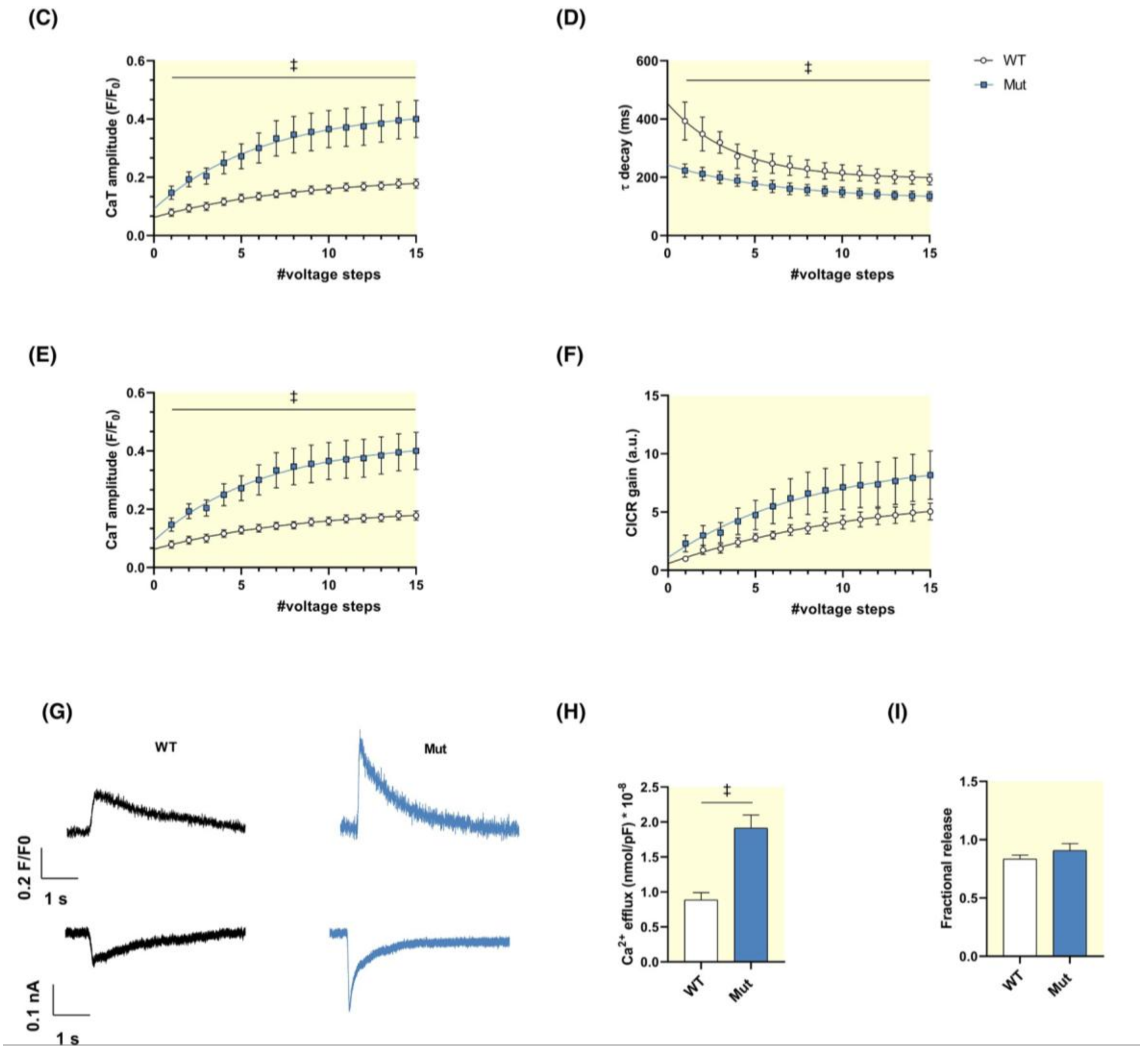

FIGURE 4. SR Ca^{2+} uptake and content. (A) Experimental protocol. (B) Representative Ca^{2+} transients (CaT, upper panels) and voltage-dependent calcium currents (I_{CaL}) (lower panels) recorded during SR reloading after caffeine-induced depletion. WT (black) and Mut (green) traces are superimposed for comparison. (C–F) Mean values of CaT parameters measured during each voltage step (1–15) of the loading train. WT: $n = 9$, $N = 7$; Mut: $n = 11$, $N = 6$; p by Mixed-effects ANOVA for loading rate. (G) Representative traces of Ca^{2+} transients (upper panels) and membrane currents, I_m (lower panels) recorded during caffeine-induced SR release. H) SR Ca^{2+} content (CaSR) estimated from the integral of I_m (representative of I_{NCX}) (WT: 0.89 ± 0.11, n = 9; Mut: 1.91 ± 0.19, n = 11). (I) Fractional SR Ca^{2+} release (WT: 0.83 ± 0.04, n = 9; Mut: 0.91 ± 0.06, n = 11). WT: N = 7; Mut: N = 6. Data expressed as mean ± SEM; p by unpaired Student's t-test.

NCX "conductance" and equilibrium

NCX functional parameters were measured during the caffeine pulse, a condition that bypasses SR transport activity (Figure 5). In Mut CMs NCX "conductance" was significantly decreased compared WT (Figure 5B, Mann–Whitney *U*-test, $p = 0.02$ vs.

WT); by contrast, the Ca^{2+} concentration corresponding to the extrapolated 0 I_{NCX} value (transport equilibrium point) did not differ significantly between the two groups (Figure 5C).

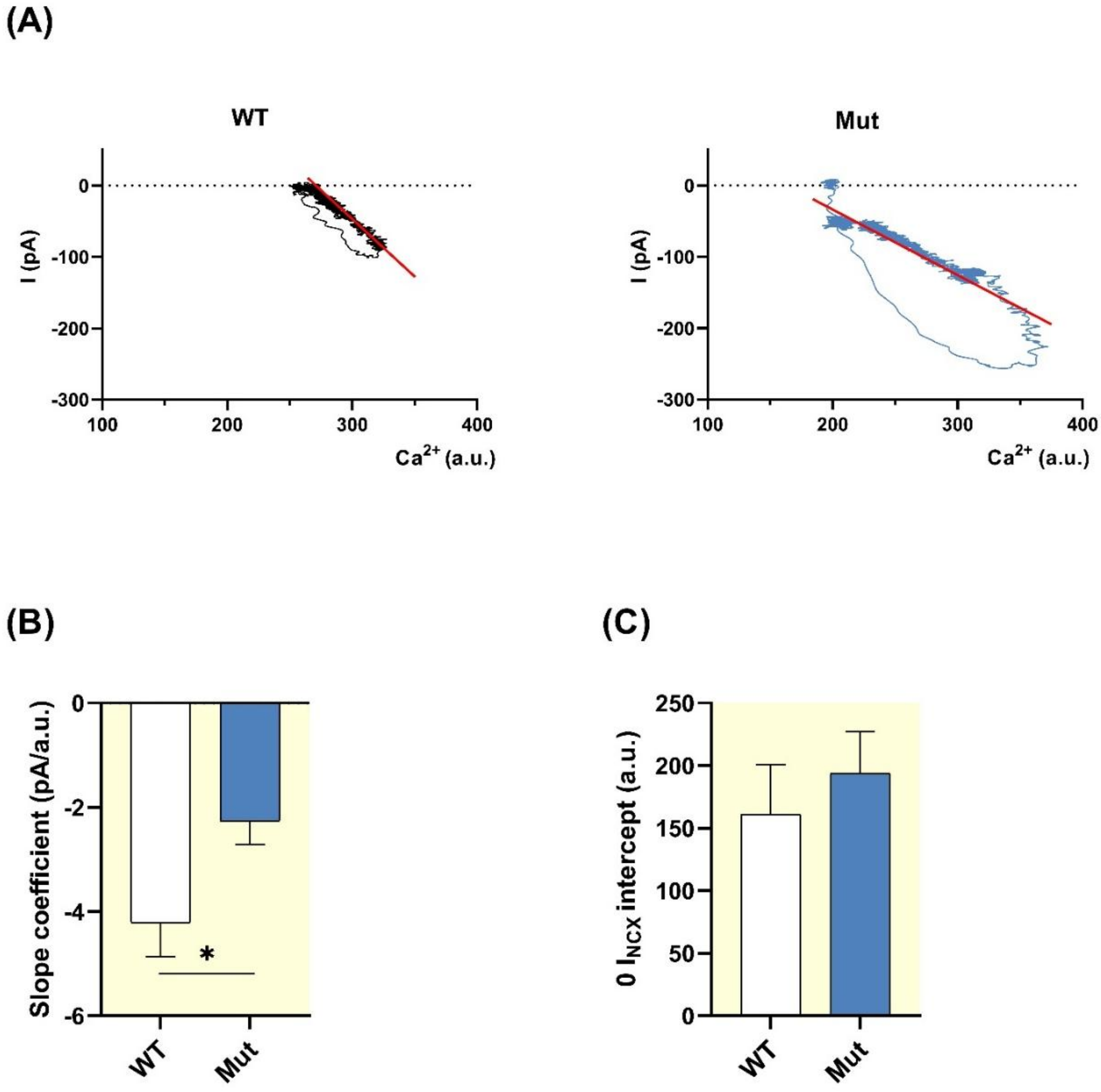

Figure 5. Relationship between I_{NCX} and $[Ca^{2+}]$ in WT and Mut. (**A**) Representative $I_{NCX}/[Ca^{2+}]$ loops during caffeine pulse. A linear regression (red solid line) has been drawn through the trailing branch of the loop. (**B**) Line slope coefficient used to define NCX “conductance” (WT: -4.2 ± 0.65, n=9; Mut: -2.3 ± 0.46, n=10). (**C**) 0 I_{NCX} intercept indicating cytosolic $[Ca^{2+}]$ at electrochemical equilibrium (WT: 161 ± 40, n=9; Mut: 194 ± 34, n=10). WT: N=7; Mut: N=6. Data are expressed as mean ± SEM. Mann-Whitney U-test.

2.5.3. *Effect PST-3093 on intracellular Ca^{2+} dynamics*

Steady state stimulation (1 Hz)

The effect of PLN antagonism by PST-3093 on intracellular Ca^{2+} dynamics was evaluated in intact WT and MUT CMs during steady-state field stimulation at 1 Hz. CaT parameters were quantified as previous described.

In WT CMs, PST-3093 significantly accelerated Ca^{2+} clearance, reducing τdecay by 24% (Figure 6E, One-way ANOVA, post-hoc $p = 0.0209$ vs. Control); the remaining parameters were unaffected (Figure 6). In contrast, in Mut CMs were insensitive to PST-3093, with no significant effect observed on any CaT parameter, including τdecay (Figure 6E).

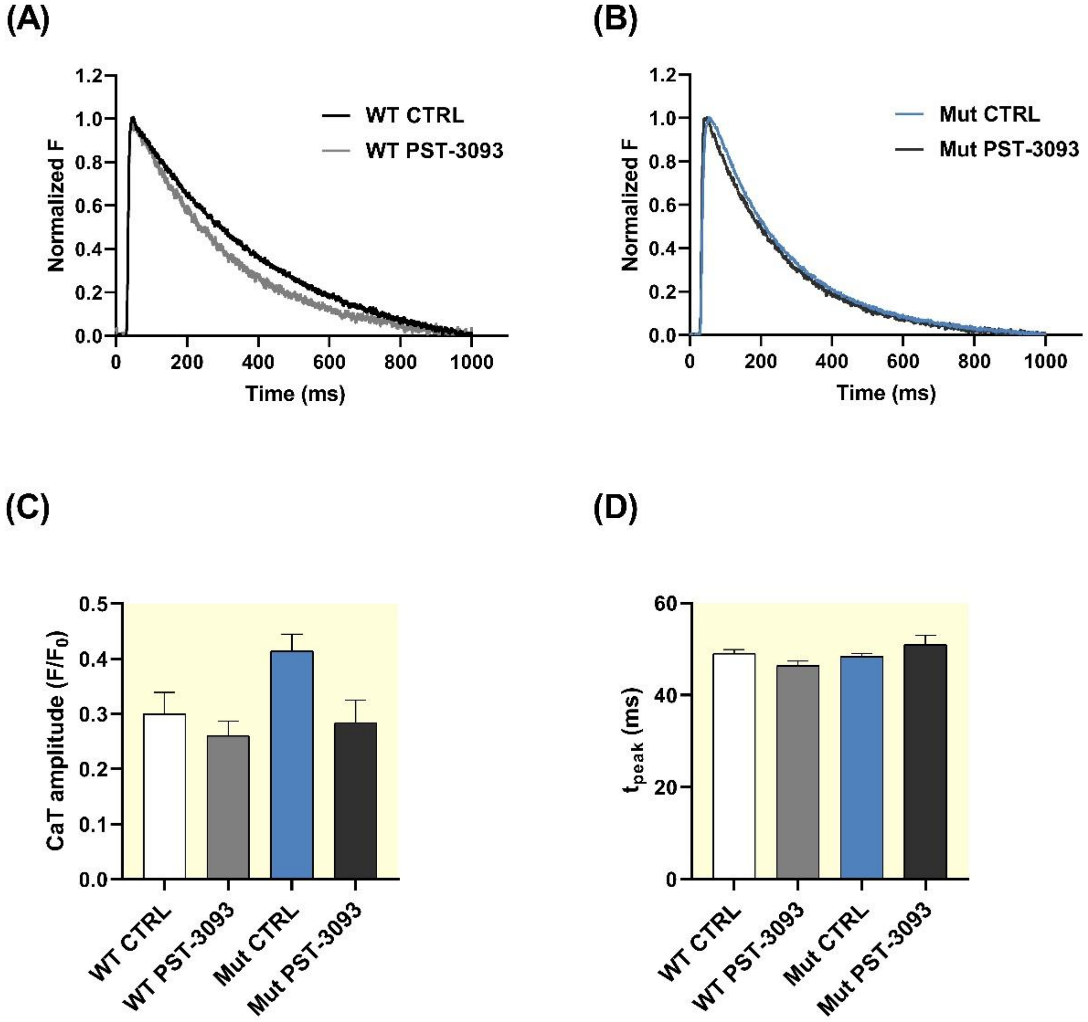

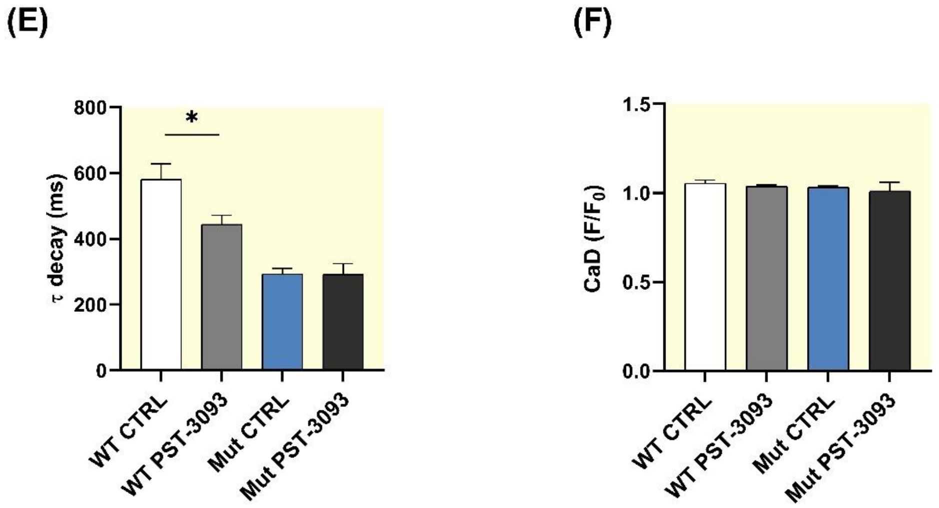

Figure 6. PST-3093 (1µM) effect on CaT parameters in WT and Mut. (**A-B**) Representative Ca^{2+} transient traces. (**C**) Ca^{2+} transient amplitude (WT CTRL: 0.30 ± 0.04, n=14; WT PST-3093: 0.26 ± 0.03, n=12; Mut CTRL: 0.41 ± 0.03, n=17; Mut PST-3093: 0.28 ± 0.04, n=9). (**D**) CaT time to peak (WT CTRL: 49 ± 0.89, n=14; WT PST-3093: 46.4 ± 1.05, n=12; Mut CTRL: 48.4 ± 0.66, n=17; Mut PST-3093: 50.9 ± 2.05, n =10). (**E**) Ca^{2+} transient decay kinetics, τ_{decay} (WT CTRL: 580 ± 48, n=12; WT PST-3093: 444 ± 27.7, n=12; Mut CTRL: 293 ± 16.5, n=17; Mut PST-3093: 291 ± 33.1, n=10). (**F**) Diastolic Ca^{2+}, CaD (WT CTRL: 1.05 ± 0.02, n=14; WT PST-3093: 1.04 ± 0.01, n=12; Mut CTRL: 1.03 ± 0.01, n=17; Mut PST-3093: 1.01 ± 0.05, n=9). WT: N=3; WT PST-3093: N=3; Mut: N=3; Mut PST-3093: N=4. Data are expressed as mean ± SEM. One-way ANOVA.

Rate dependency

Under control conditions, both WT and Mut CMs exhibited significant rate dependency of several CaT parameters: *t*peak (inverse, $p < 0.0001$), τdecay (inverse, $p < 0.0001$) and CaD (direct, $p < 0.0001$) (Figures 7 and 8).

In Mut CMs, PST-3093 enhanced rate-dependent accumulation of CaD (Figure 8D, Mixed-effects model, Treatment × Rate, $p = 0.004$ vs. Control). Rate dependency of all the remaining parameters was not significantly affected by PST-3093 in both genotypes (Figures 7 and 8).

In summary, PST-3093 in WT CMs produced effects compatible with SERCA2a activation (hyperdynamic Ca^{2+} handling), albeit quantitatively smaller than that induced by the mutation itself. By contrast, in Mut CMs the compound failed to exert any effect, and in some cases displayed an opposite trend.

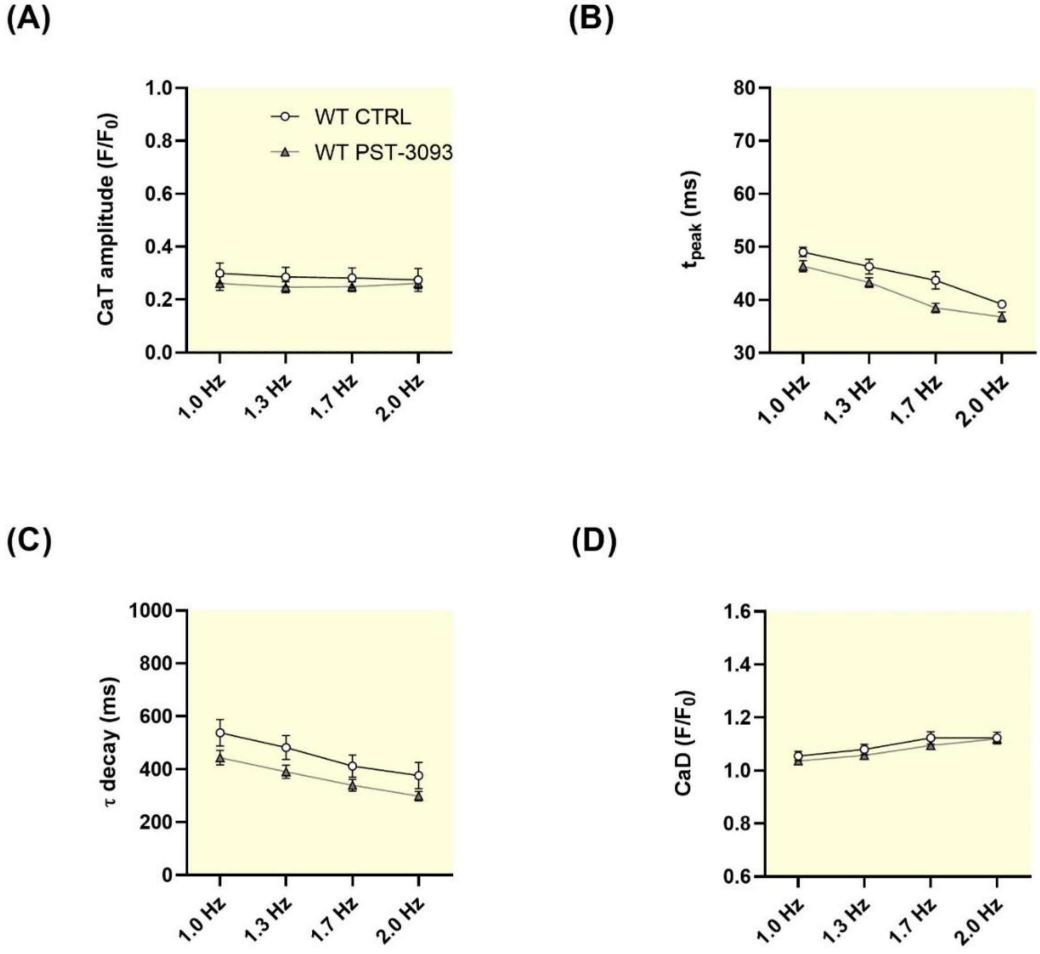

Figure 7. PST-3093 1µM effect on rate dependency of CaT parameters in WT. Rate-dependency was tested by stepwise increments in pacing rate (1, 1.3, 1.7, and 2 Hz) and it was significant ($p<0.05$) for t_{peak}, ${}_{decay}$ and CaD, as reported in the manuscript (**A**) Ca^{2+} transient amplitude. (**B**) CaT time to peak, t_{peak}. (**C**) Ca^{2+} transient decay kinetics, τ decay. (**D**) Diastolic Ca^{2+}, CaD. WT CTRL: n=14, N=3; WT PST-3093: n=12, N=2. Data are expressed as mean ± SEM. Mixed-effects ANOVA.

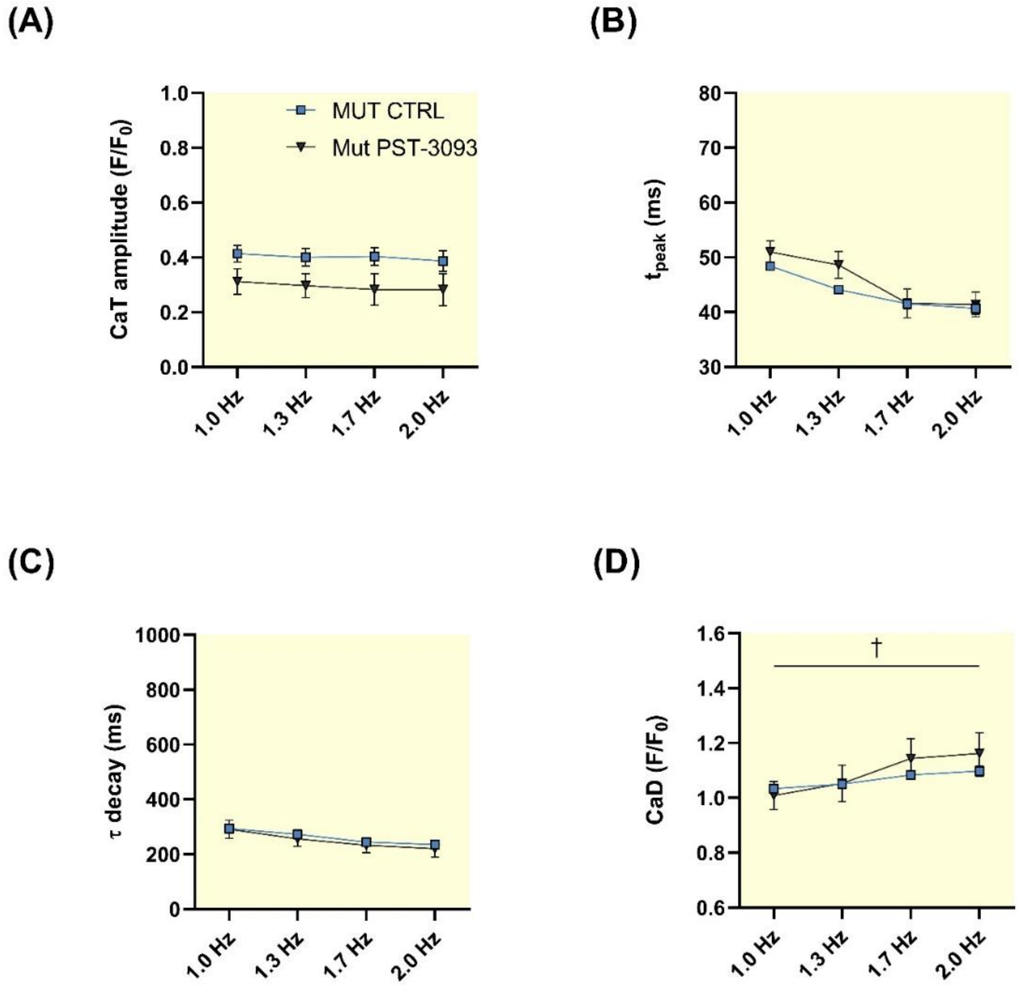

Figure 8. PST-3093 1µM effect on rate dependency of CaT parameters in Mut. Rate-dependency was tested by stepwise increments in pacing rate (1, 1.3, 1.7, and 2 Hz). (**A**) Ca^{2+} transient amplitude. (**B**) CaT time to peak, t_{peak}. (**C**) Ca^{2+} transient decay kinetics, τ decay. (**D**) Diastolic Ca^{2+}, CaD. Mut CTRL: n=17, N=3; Mut PST-3093: n=10, N=4. Data are expressed as mean ± SEM. Mixed-effects model.

2.5.4. Energy metabolism

Mitochondrial dysfunction is a well-recognized feature of secondary remodeling, arising from impaired intracellular Ca^{2+} handling and ultimately contributing to the development of heart failure. Here, we investigated whether energy metabolism is already altered in Mut CMs before the onset of overt contractile failure, which would suggest a primary pathogenic role. Notably, for technical reasons, all metabolic measurements were performed in unstimulated (quiescent) CMs.

Oxygen consumption rate

Oxygen consumption rate (OCR) was assessed in quiescent WT and Mut CMs plated in parallel within the same multiwell plate (Figure 9). OCR values were normalized to the number of cells per well. The mitochondrial respiration profile, from which respiration parameters were derived, was obtained by sequential modulation of specific functions using pharmacological agents, as detailed in the methods. The pattern observed in Mut CMs is reported below as relative to that of WT ones. Overall, OCR was markedly reduced in Mut CMs (Figure 9A), a finding consistently reproduced across all preparations examined. The most pronounced difference was observed in maximal OCR (Figure 9C, −36%; Mann–Whitney *U*-test, $p < 0.0001$); However, both basal OCR (Figure 9B, −39%; unpaired Student’s t test, $p = 0.0006$) and spare respiratory capacity (Figure 9D, −35%; Mann–Whitney U test, $p < 0.0001$) were likewise significantly diminished. Notably, the non-mitochondrial component of OCR was also significantly reduced (Figure 9E, −38%; unpaired Student’s t test, $p = 0.0003$). The modulation of OCR by cytosolic Ca^{2+}, and specifically by the sarcoplasmic reticulum (SR) compartment, was examined in a subset of samples. For this purpose, cytosolic Ca^{2+} was chelated with BAPTA-AM (BAPTA) (Figure 10 A, B, C, E), and SERCA2a activity was inhibited by thapsigargin (THAPSI) treatment, thereby functionally removing the SR contribution (Figure 10 A, B, D, F). Both interventions significantly reduced basal OCR; however, the effect of THAPSI did not differ significantly between WT and Mut CMs (Figure 9, middle panels). Maximal OCR was unaffected by THAPSI in WT CMs but was significantly reduced in Mut CMs (Figure 10, bottom panels). No clear difference was observed between the effects of BAPTA and THAPSI on OCR. Interestingly, the vehicle control (DMSO) unexpectedly increased OCR in Mut myocytes only. Importantly, the same DMSO concentration was applied across all experimental groups; however, the effect of THAPSI did not differ significantly between WT and Mut CMs (Figure 10, middle panels).

(A)

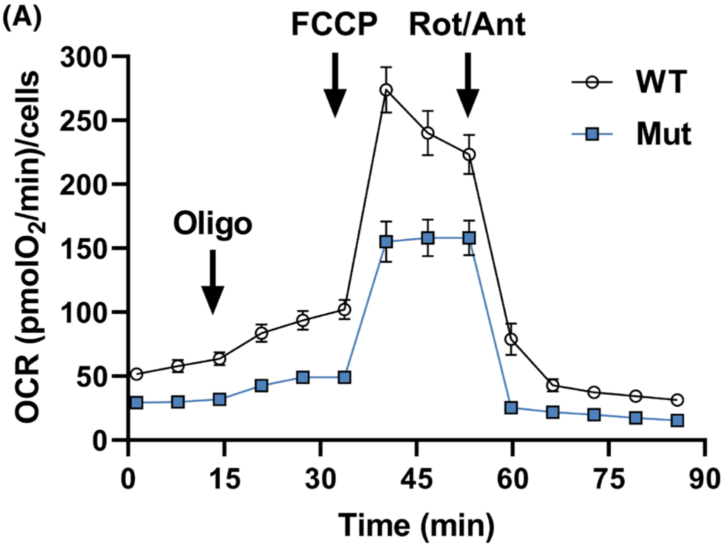

(B) Basal respiration

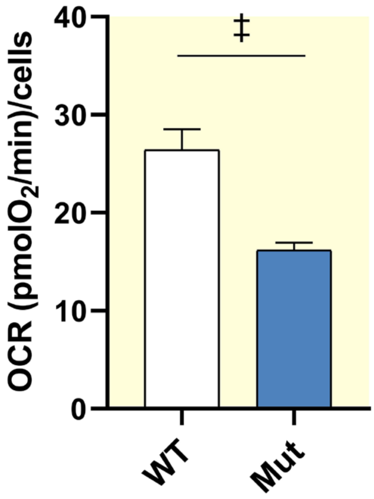

(C) Maximal respiration

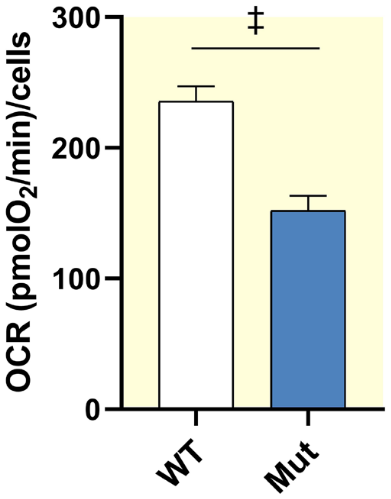

(D) Spare capacity

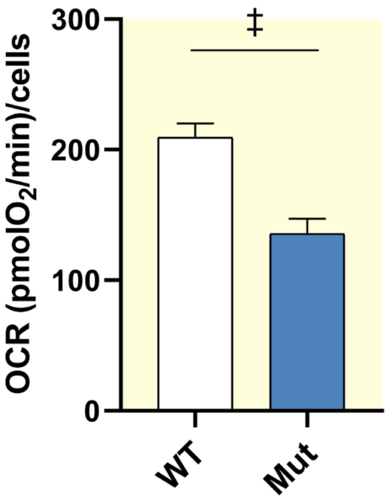

(E) Non-mitochondrial respiration

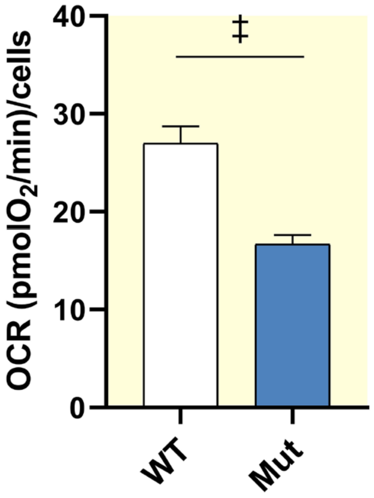

FIGURE 9. Parameters of mitochondrial respiration. (A) Oxygen consumption rate (OCR) profiles of WT and Mut CMs subjected to sequential injections of 1.5 µM Oligo, 0.5 µM FCCP and 3 µM Rot/Ant A (XF Mito Stress Test protocol). (B) Basal OCR (WT: 26.40 ± 2.13, *n* = 31; Mut: 16.20 ± 0.76, *n* = 19). (C) Maximal OCR (WT: 235 ± 11.46, *n* = 31; Mut: 151 ± 11.54, *n* = 19). (D) Spare respiratory capacity (209 ± 10.76, *n* = 31; Mut: 129 ± 12.6, *n* = 17). (E) Non-mitochondrial OCR (WT: 26.97 ± 1.74, *n* = 31; Mut: 16.68 ± 0.94 *n* = 19). WT: *N* = 3; Mut: *N* = 3. Data are expressed as mean ± SEM; *p* by unpaired Student's *t*-test and Mann–Whitney *U*-test.

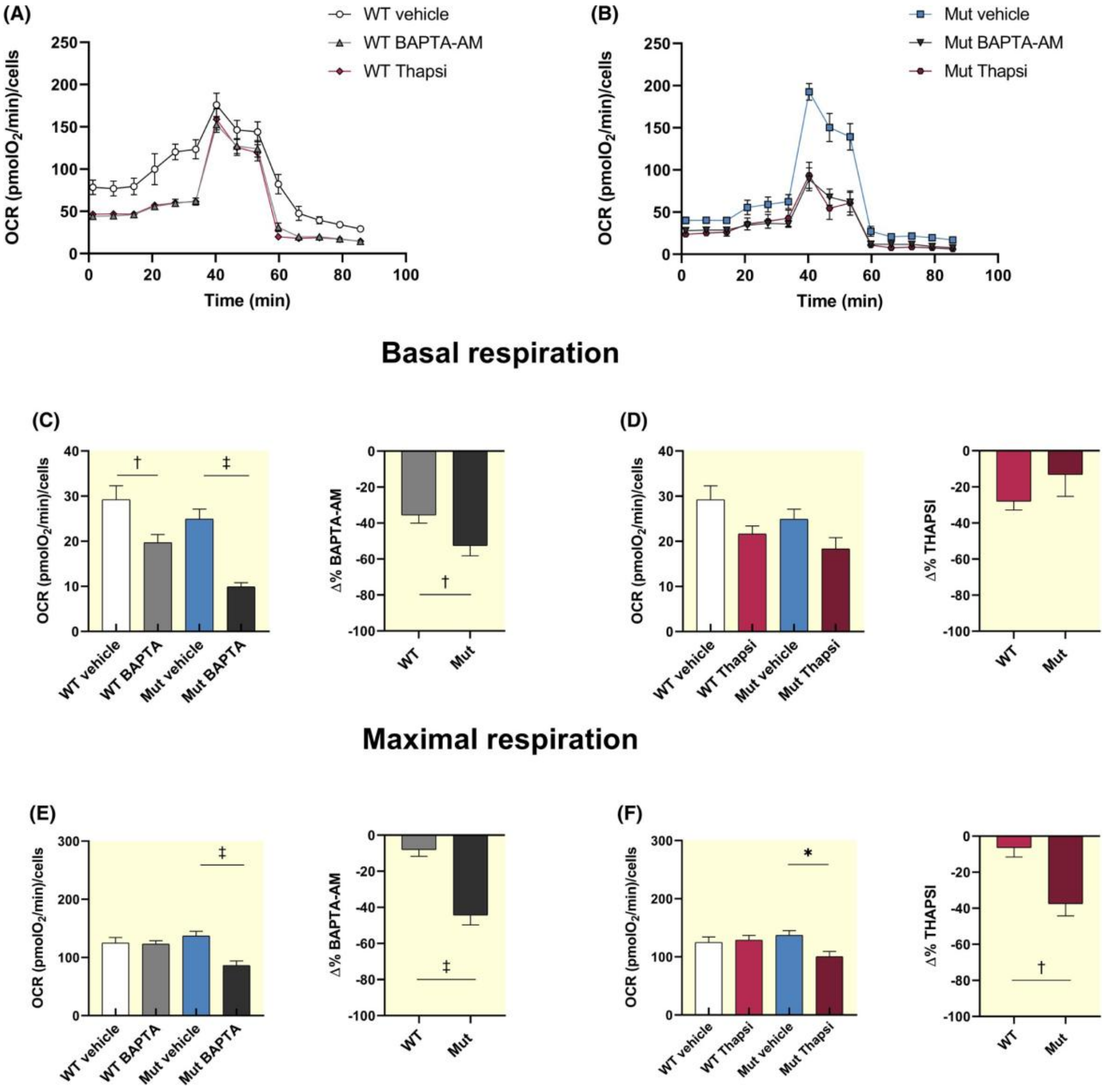

FIGURE 10. Effect of BAPTA-AM and Thapsigargin on oxygen consumption rate (OCR). (A, B) OCR profiles of WT and Mut CMs (protocol as in Figure 4) treated with BAPTA-AM (BAPTA, 5 µM) or thapsigargin (THAPSI, 5 µM). (C, D) Treatment Effect on basal OCR (WT vehicle: 29.22 ± 3.04, *n* = 19 wells; WT BAPTA: 19.69 ± 1.79, *n* = 35 wells; Mut vehicle: 24.92 ± 2.20, *n* = 15 wells; Mut BAPTA: 9.89 ± 0.93, *n* = 26 wells); (WT vehicle: 29.22 ± 3.04, *n* = 19 wells; WT THAPSI: 21.67 ± 1.71, *n* = 30 wells;

Mut vehicle: 24.92 ± 2.20, *n* = 15 wells; Mut THAPSI: 18.32 ± 2.51, *n* = 24 wells). (E, F) Treatment effect on maximal OCR (WT vehicle: 125 ± 9.42, *n* = 18 wells; WT BAPTA: 123 ± 5.61, *n* = 35 wells; Mut vehicle: 137 ± 8.00, *n* = 15 wells; Mut BAPTA: 86.43 ± 7.63, *n* = 27 wells); (WT vehicle: 125 ± 9.42, *n* = 18 wells; WT THAPSI: 129 ± 7.97, *n* = 31 wells; Mut vehicle: 137 ± 8.00, *n* = 15 wells; Mut THAPSI: 100 ± 9.08, *n* = 24 wells). WT: *N* = 3; Mut: *N* = 3. Data are expressed as mean ± SEM. One-way ANOVA and Kruskal–Wallis test for % data.

Glycolysis

Anaerobic glycolytic metabolism was evaluated in the same plates used for OCR measurements, by assessing the proton efflux rate (PER) (Figure 11). PER values were normalized to the number of cells per well in the Seahorse plate. Measurements were obtained under basal conditions, after inhibition of mitochondrial respiration with rotenone/antimycin A to assess compensatory glycolysis and following blockade of glycolysis with 2-deoxy-D-glucose (2DG) to quantify non-glycolytic acidification. Anaerobic glycolysis was depressed in Mut CMs compared with WT controls (Figure 11 A). Basal glycolysis showed only a non-significant trend toward reduction (Figure 11 B, −23%; unpaired t test, p = 0.0882), whereas both compensatory glycolysis (Figure 11C, −47%; unpaired Student's t test, p = 0.0005) and glycolytic reserve (Figure 11D, −58%; unpaired Student's t test, p = 0.0015) were markedly decreased. Non-glycolytic acidification was slightly (−23%), but still significantly, reduced (Figure 11 E, Mann–Whitney U-test, p = 0.0089).

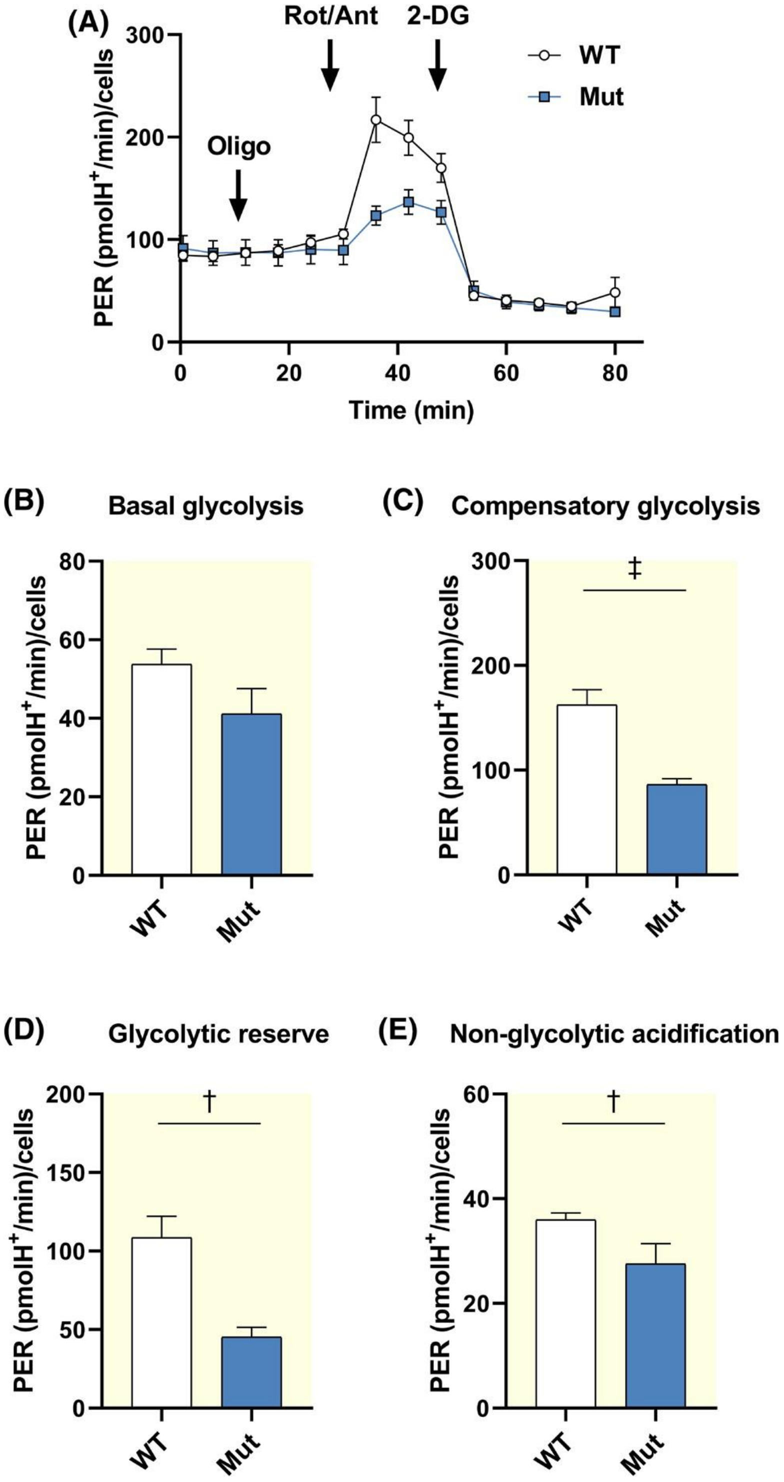

FIGURE 11. Parameters of anaerobic glycolysis. (A) Proton efflux rate (PER) profile of WT and Mut CMs subjected to sequential injections of 1.5 µM Oligo, 3 µM Rot/Ant and 50 mM 2-DG. (B) Basal glycolysis (WT: 53.77 ± 3.84, *n* = 13; Mut: 41.15 ± 6.42, *n* = 9). (C) Compensatory glycolysis (WT: 162 ± 14.52, *n* = 13; Mut: 86.34 ± 5.48, *n* = 9). (D) Glycolytic reserve (WT: 109 ± 13.58, *n* = 13; Mut: 45.19 ± 6.23, *n* = 9). (E) Non-glycolytic acidification (WT: 36 ± 1.29, *n* = 13; Mut: 27.56 ± 3.84, *n* = 9). WT: *N* = 3; Mut: *N* = 3. Data expressed as mean ± SEM; *p* by unpaired Student's *t*-test or Mann–Whitney *U*-test.

Cell energy charge

To assess whether the reduction in energy metabolism of Mut CMs leads to energy starvation, we measured the current carried by the glibenclamide-sensitive K^+ channel (I_{KATP}), whose conductance is sensitive to the ADP/ATP ratio [50]. This surrogate measurement was adopted because, in preliminary experiments, we found bulk fluorescence ATP assays to be confounded by unusually large number of dead CMs in the preparations.

To avoid intracellular dialysis by the pipette content, measurements were performed with the perforated-patch technique. I_{KATP} was recorded at −120 mV, membrane potential at which K^+ currents are expectedly inward (i.e., a positive current shift reflects a decrease in I_{KATP}). I_{KATP} was normalized to membrane capacitance to obtain current density. Under quiescence, no significant difference in mean I_{KATP} density was observed between WT and Mut CMs; nonetheless, very large I_{KATP} values were occasionally recorded in Mut CMs (Figure 12 A,B). Immediately after stimulation, mean I_{KATP} density was approximately 3-fold larger in Mut CMs than in WT ones (Figure 12C, D).

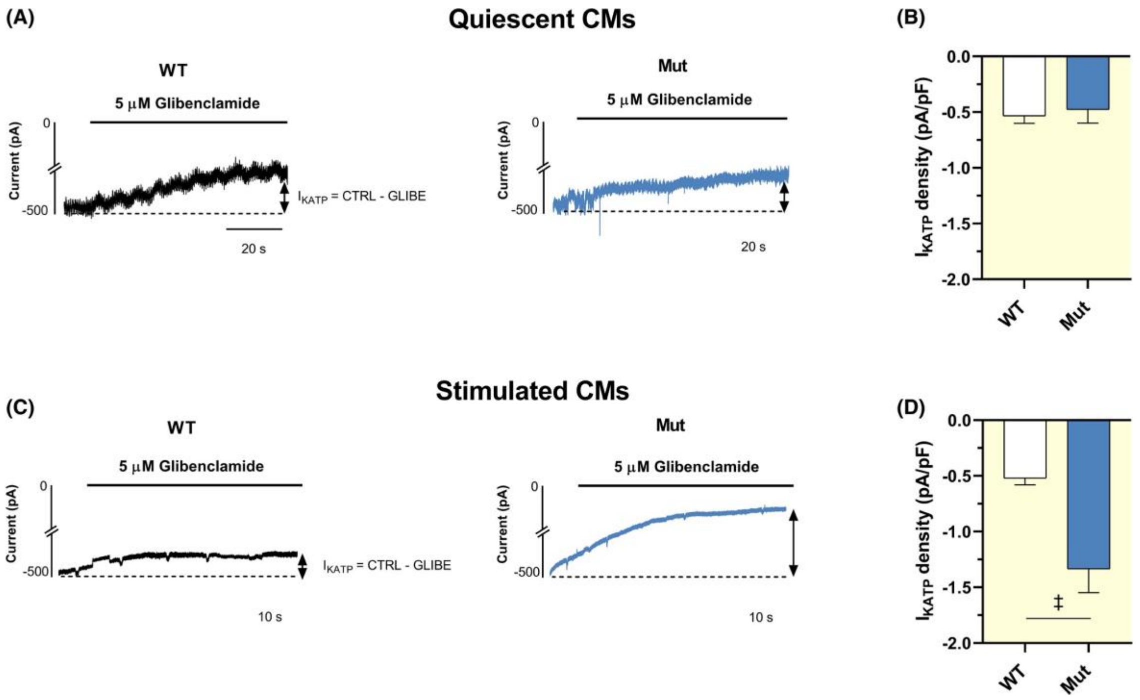

FIGURE 12. Energy charge in quiescent and paced CMs. Energy charge was estimated from the conductance of ATP-sensitive K^+ current (I_{KATP}), which is proportional to the ADP/ATP ratio. (A) Representative current traces recorded in quiescent CMs (holding potential −120 mV), in control conditions and during perfusion with 5 μM glibenclamide; I_{KATP} was calculated as the current difference (control –

glibe) normalized to membrane capacitance to obtain current density. (B) Statistics of I_{KATP} density in quiescent CMs (WT: −0.53 ± 0.07, $n = 9$; Mut: −0.47 ± 0.12, $n = 8$). WT: $N = 7$; Mut: $N = 6$. (C) Representative current traces recorded after pacing (2 Hz) in control conditions and during perfusion with 5 μM glibenclamide. (D) Statistics of I_{KATP} density after pacing (WT: −0.52 ± 0.06, $n = 12$; Mut: −1.34 ± 0.21, $n = 10$). WT: $N = 3$; Mut: $N = 4$. Data expressed as mean ± SEM; p by unpaired Student's t-test.

Intracellular ROS and mitochondrial membrane potential (Ψm)

Intracellular radical oxygen species (ROS) content was estimated in quiescent CMs by measuring 2-7-dichclorofluorescin diacetate (DCFDA) fluorescence; confocal images were automatically analyzed to quantify the signal from individual vital cells. In Mut CMs, DCFDA signal was marginally, but significantly, lower than in WT CMs (Figure 13A, −5%; unpaired Student's t-test, $p = 0.0115$ vs. WT), to indicate a slight reduction in ROS content. Mitochondrial membrane potential (Ψm) was evaluated by the fluorescent probe tetramethylrhodamine, ethyl ester (TMRE). TMRE signal was similar between Mut and WT CMs (Figure 13B). In the same CMs of both groups, short-circuit of mitochondrial membrane by FCCP significantly increased TMRE signal, thus confirming responsiveness of the probe to Ψm changes (Figure 13 B-inset).

In summary, despite the absence of overt mitochondrial damage (i.e., preserved ROS levels and membrane polarization), both oxidative and glycolytic components of energy metabolism were impaired in Mut CMs. Whereas OCR was sensitive to interventions affecting cytosolic Ca^{2+}, only the response of maximal OCR differed between WT and Mut CMs. Finally, a defect in cellular energy charge in Mut CMs, undetectable under quiescent conditions, became evident upon stimulation.

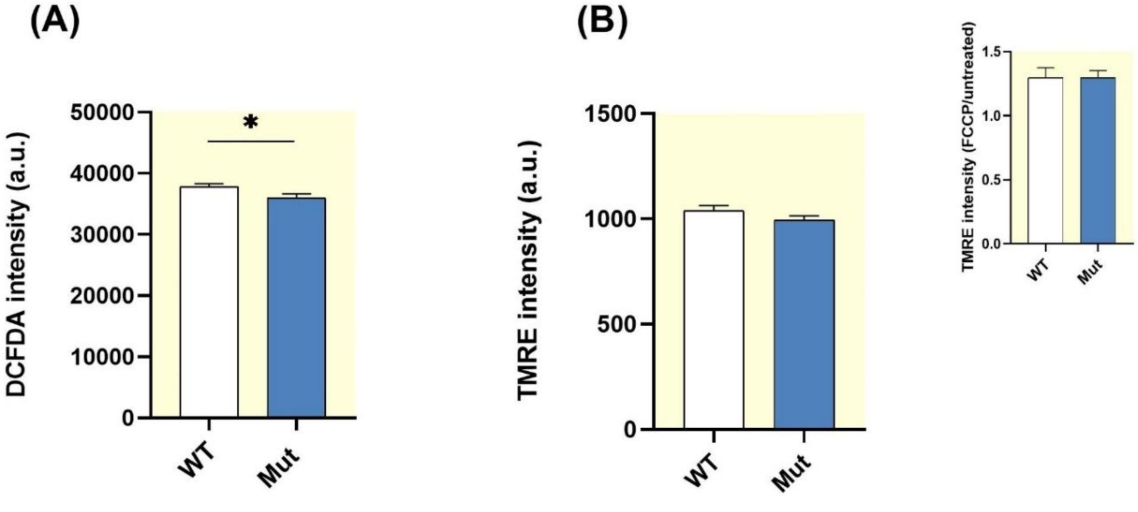

Figure 13. ROS quantification and evaluation of Ψ_m in WT and Mut. (**A**) DCFDA Fluorescence intensity (WT: 37827 ± 500, n=761, N=4; Mut: 35969 ± 672, n=430, N=4). (**B**) TMRE fluorescence intensity (WT: 1039 ± 24, n=311, N=4; Mut: 994 ± 21, n=305, N=4). **Inset**: TMRE fluorescence intensity after the incubation with FCCP normalized to fluorescence measured in control conditions (WT: 1.29 ± 0.07, n=11 wells, N=4; Mut: 1.29 ± 0.05, n=10 wells, N=4). Data are expressed as mean ± SEM. Unpaired Student's t-test

2.5.5. Transcript and protein analysis

The functional derangements described above may reflect profound alterations in the biology of Mut CMs, potentially arising from disrupted Ca^{2+} handling or direct toxicity of mutant PLN. To identify specific processes underlying the cellular response to the mutation, we analyzed transcriptional expression of genes and corresponding proteins across several functional categories: (1) mitochondrial remodeling (mitophagy) and their contact sites with the SR (MERCS); (2) antioxidant defense (DETOX); (3) energy starvation response (AMPK); (4) endoplasmic reticulum (ER) stress response (UPR); and (5) CaMKII signaling (Figure 14). Protein expression was further examined by Western blot for pErk/Erk (Figure 15 A), Bax (Figure 15 B), IP3R and pAMPK/AMPK (Figure 15 C), pCaMKII/CaMKII (Figure 15 D), and SERCA2 (Figure 15 E).

Transcription of genes related to UPR and mitophagy was unchanged (Figure 14). Nevertheless, protein analysis revealed a trend toward activation of ER-stress pathways, as suggested by elevated pErk/Erk and Bax levels (Figure 15 A, B). Genes encoding AMPK isoforms were upregulated 1.5–2-fold (Figure 14); however, the pAMPK/AMPK protein ratio instead showed a trend toward reduction, arguing against activation of energy-starvation signaling under quiescent conditions (Figure 15 C). Although IP3R transcripts were unaltered, IP3R protein levels were significantly increased (Figure 15 C), possibly reflecting a compensatory adaptation to the increased OCR dependence on Ca^{2+}. Genes encoding CaMKII were unchanged, and the pCaMKII/CaMKII protein ratio was not elevated (Figure 15 D), indicating that CaMKII signaling is unlikely to be activated at this disease stage. SERCA2 expression showed a nonsignificant trend toward upregulation in Mut myocardium (Figure 15 E).

In summary, transcript and protein analyses largely yielded negative results regarding activation of energy starvation, CaMKII signaling, or ROS detoxification. The limited positive findings instead point toward activation of ER-stress responses and altered functional interactions between the SR and mitochondria.

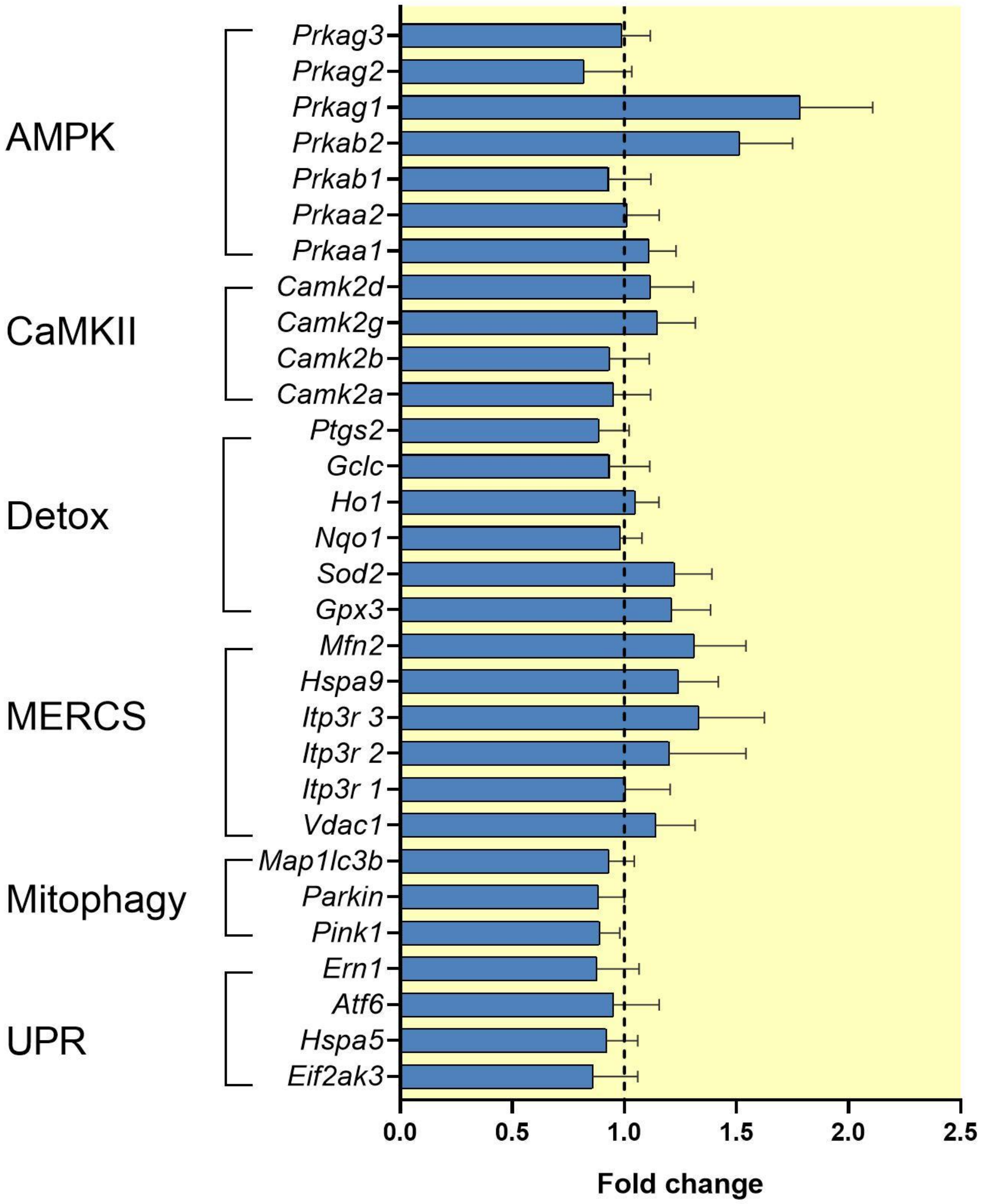

Figure 14. Transcript analysis in WT and Mut. Expression of AMPK (*Prkaa1*, *Prkaa2*, *Prkab1*, *Prkab2*, *Prkag1*, *Prkag2*, *Prkag3*), CaMKII isoforms (*Camk2a*, *Camk2b*, *Camk2g*, *Camk2d*) and genes associated to detoxification (*Ptgs2*, *Gclc*, *Ho1*, *Nqo1*, *Sod2*, *Gpx3*), mitochondria-ER contact sites (MERCS; *Mfn2*, *Hspa9*, *Itp3r1*, *Itp3r2*, *Itp3r3*, *Vdac1*), mitophagy (*Map1lc3b*, *Parkin*, *Pink1*) and unfolded protein response (UPR; *Ern1*, *Atf6*, *Hspa5*, *Eif2ak3*) in total RNA extracts of RV bioptic samples from WT and Mut mice. GAPDH was used as house-keeping gene and qRT-PCR data is shown as the fold change of target gene expression in Mut mice respect to WT mice (dotted blue line). Unpaired Student's t-test.

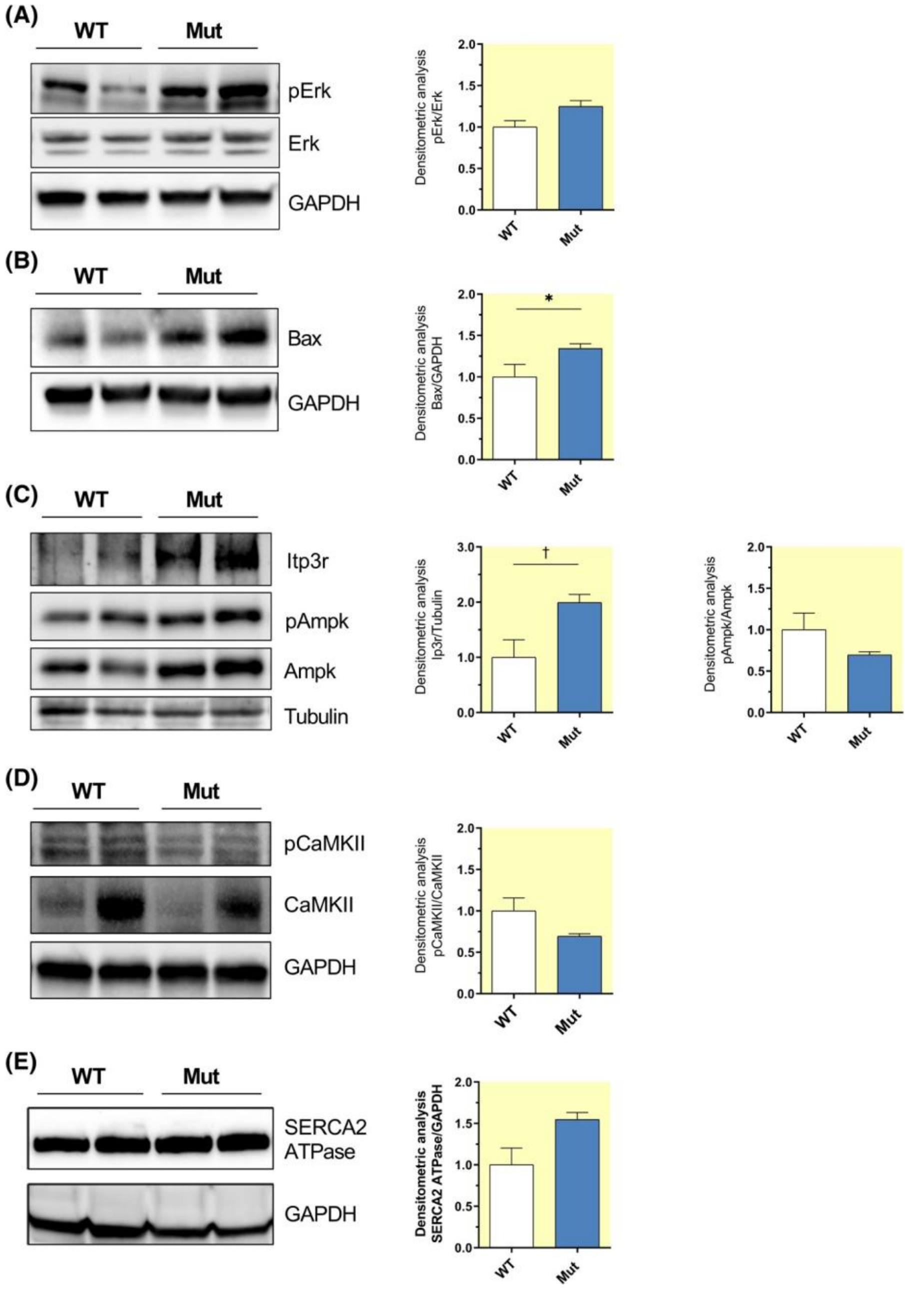

FIGURE 15. Protein analysis in myocardial homogenates. *Left panels*: representative Western Blots of proteins extracted from RV samples of WT and Mut mice (GAPDH or Tubulin included as housekeeping for normalization); *Right panels*: blot quantification by densitometric analysis normalized to housekeeping. (A) Erk and pErk (WT: 1.0000 ± 0.0777, *N* = 4; Mut: 1.2493 ± 0.0691, *N* = 4). (B) Bax (WT: 1.0000 ± 0.1506, *N* = 5; Mut: 1.3475 ± 0.0529, *N* = 8). (C) Ip3r (WT: 1.0000 ± 0.3180, *N* = 5; Mut: 1.9938 ± 0.1457; *N* = 8), total Ampk and pAmpk; densitometry shows pAmpk/ total Ampk (WT: 1.0000 ± 0.2013, *N* = 5; Mut: 0.6950 ± 0.0396, *N* = 8). (D) CaMKII and pCaMKII; densitometry shows the pCaMKII/total CaMKII ratio (WT: 1.0000 ± 0.1566, *N* = 4; Mut: 0.6936 ± 0.0309, *N* = 4). (E) SERCA2 (WT: 1.0000 ± 0.2026, *N* = 3; Mut: 1.5468 ± 0.0861, *N* = 3). Data expressed as mean ± SEM; *p* by unpaired Student's *t*-test.

2.6. Discussion

The main findings of this study are as follows. As compared to WT ones, Mut hearts were characterized by:

1) a lower Kd_{Ca} (higher Ca^{2+} affinity) of SERCA2a ATPase (Figure 1B);
2) intracellular Ca^{2+} dynamics consistent with enhanced SR Ca^{2+} uptake evidenced by accelerated decay kinetics and lower diastolic Ca^{2+} with preserved release amplitude and upstroke (Figure 2);
3) insensitivity of Ca^{2+} dynamics to PLN antagonism by PST-3093 (Figures 6–8);
4) lower NCX conductance (Figure 5).

All these findings point to diminished SERCA2a inhibition by Mut PLN, resulting in increased Ca^{2+} cycling by the pump.

5) These changes in intracellular Ca^{2+} handling were accompanied by an overall depression of energy metabolism, consisting in a parallel reduction of OCR and anaerobic glycolysis (Figures 9 and 11).
6) Notwithstanding this metabolic downshift, ROS content and mitochondrial membrane polarization were remarkably normal in Mut CMs (Figure 13).
7) The Ca^{2+}-dependency of maximal OCR was increased in Mut CMs (Figure 9).
8) Under quiescence, cell energy charge and energy starvation signaling (pAMPK/AMPK) were unperturbed (Figure 15); nonetheless, the pacing-induced reduction of cell energy charge was larger in Mut CMs (Figure 12).

2.6.1. Intracellular Ca^{2+} dynamics

The mutation-associated changes in intracellular Ca^{2+} dynamics observed in intact CMs corroborate the hyperdynamic state previously observed in patient-derived hiPSC-CMs carrying the PLN-R14del mutation [11], thus allowing generalization of that observation. If the hypothesis of SERCA2a super inhibition by mutant PLN were correct, one would expect to observe a prolongation of τdecay. By contrast, our data demonstrated a shortening of this parameter, consistent with enhanced SERCA2a function, that is, a loss of PLN's inhibitory effect.

Multiple lines of evidence reinforce the interpretation that this hyperdynamic behavior reflects enhanced SERCA2a activity: (1) increased Ca^{2+} sensitivity (lower Kd_{Ca}) of SERCA2a ATPase in myocardial homogenates; and (2) the close resemblance to the effects of PST-3093, a SERCA2a stimulator that acts by weakening the inhibitory SERCA2a–PLN interaction [10]. The latter observation implicates reduced SERCA2a affinity as a plausible mechanism of PLN-R14del behavior.

PST-3093 enhances SERCA2a activity by interfering with the PLN–SERCA2a interaction (acting as a PLN antagonist). When PST-3093 was applied to WT cardiomyocytes, a reduction in τdecay was observed, as expected. This finding confirms that the parameter reliably reflects SERCA2a activity.

If the hypothesis of SERCA2a super inhibition by mutant PLN were correct, PST-3093 would be expected to retain some efficacy by displacing residual WT PLN. However, in both the PLN-R14del mouse (present study) and in heterozygous PLN-R14del+/− patient hiPSC-CMs [11], PST-3093 completely lost its stimulatory effect on SERCA2a (Figures 6-8). This pattern may suggest negative dominance of the mutant allele, potentially via increased trapping of PLN in the non-inhibitory pentameric form [51].

The present findings of hyperdynamic Ca^{2+} handling contrast with the depressed SR function reported in a heterozygous PLN-R14del knock-in model expressing human PLN [52, 53]. The development of cardiac abnormalities has a rather different time-course in the two models: whereas in the former signs of depressed contractility appear at 18–20 months of age,13 clear-cut chamber dilatation and electrical remodeling were already present at 3 months in the latter [52, 53]. Importantly, both studies examined myocytes at 2–3 months of age, is in a markedly different relationship with the development of a failing phenotype. Given that impaired SR function is a hallmark of maladaptive remodeling [54], this might explain the different Ca^{2+} handling phenotypes observed in the two models. Indeed, SERCA2a downregulation is a well-established consequence of pathological remodeling and a key driver of contractile dysfunction and arrhythmogenesis in heart failure. By analogy, enhanced SERCA2a inhibition would easily explain the PLN-R14del+/− ACM phenotype, as previously claimed [3]. In contrast, the present results indicate that PLN-R14del+/− is unable to inhibit SERCA2a, yielding a “hyperdynamic” phenotype which may seem, at first, counterintuitive as a substrate for contractile impairment.

Evidence from other models provides important context. PLN knockout, which also produces hyperdynamic Ca^{2+} handling, is tolerated in transgenic mice [55], but in hiPSC-CMs it ultimately progresses to cardiomyopathy over longer durations [56]. In that setting, pathological remodeling was accompanied by increased late sodium current (I_{NaL})

[56], although it remained uncertain whether this represented a primary mutation effect. The present results show, the absence of increased ROS production or CaMKII activation, two well-established enhancers of I_{NaL}, at the presymptomatic stage suggests that hyperdynamic Ca^{2+} handling alone is insufficient to drive I_{NaL} enhancement. Nonetheless, the possibility that loss of PLN function exerts deleterious long-term effects is reinforced by its consistent association with human ACM mutations [57], by hypertrophic remodeling observed in PLN sarcolipin double knockouts [58], and by the profound derangements developing within two months of PLN knock-out in hiPS-CMs [56]. Altogether, these findings suggest that chronically unrestrained SERCA2a activity may, over time, destabilize myocyte biology. Notably, clinical ACM is indeed of late onset in PLN-R14del+/− carriers [1].

The discussion thus far assumes that PLN R14del detrimental effects depend on the impact of SERCA2a dysregulation on intracellular Ca^{2+} dynamics; however, this is not necessarily the case. For example, in the case of the PLN-R9C mutation, late-onset ACM developed independently of the specific direction of change in SERCA2a activity [59]. This highlights the possibility that alternative mechanisms, perhaps unrelated to Ca^{2+} handling, may contribute to cellular dysfunction in PLN-R14del. Unfortunately, this considerably broadens the array of mechanisms to be considered and, eventually, to be targeted with therapy (other than mutation reversal). For this reason, we performed a preliminary analysis of additional cell dysfunctions, potentially involved in the ACM of the PLN-R14del+/− TG mouse. Although admittedly far from exhaustive, this analysis may provide relevant clues.

2.6.2. Energy metabolism

Recent work on contracting hiPS-CMs organoids (EHTs) from a PLN-R14del+/− carrier detected abnormalities of the ER/mitochondrial compartment, reduced mitochondria number and function [12].

Despite preserved SR function, contractile force was reduced by approximately 50% in these preparations. Motivated by these findings, we investigated whether the PLN-R14del+/− mutation affects energy metabolism in our transgenic mouse model, specifically at a presymptomatic stage, before overt contractile dysfunction emerges (i.e., as a primary abnormality). Under quiescent conditions, PLN-R14del+/− cardiomyocytes displayed a profound depression of energy metabolism, including both oxidative phosphorylation and anaerobic glycolysis (Figures 9 and 11).

The most pronounced differences between WT and Mut cells were detected in maximal respiration and spare respiratory capacity, both markedly reduced in Mut. These parameters are measured following exposure to the uncoupler FCCP, which drives the electron transport chain to its maximal operating capacity. Because FCCP acts upstream of complex V (ATP synthase), the observed respiratory defect is likely independent of ATP synthase activity or ATP consumption. The reduction in maximal respiration may reflect either a lower mitochondrial content, due to enhanced mitophagy or intrinsic mitochondrial dysfunction associated with structural abnormalities of the cristae. Consistent with this, electron microscopy studies on PLN-R14del+/− hiPSCMs have documented a reduced mitochondrial number in dilated cardiomyopathy linked to PLN-R14del [12].

Compatibility of overall depression of energy metabolism with grossly normal cardiac function in-vivo is more surprising[13]. Either function is maintained despite energy starvation, or ATP demand is reduced (at least at rest) in PLN-R14del+/− CMs. To discriminate between these possibilities, we measured the I_{KATP} conductance (Figure 12), a surrogate of the ADP/ATP ratio, and activation of AMPK a major "energy starvation" signal. Albeit some heterogeneity was observed in I_{KATP} density, neither of the two measurements points to a mismatch between ATP production and demand under resting conditions. Why should PLN-R14del+/− CMs consume significantly less ATP than WT ones?

The two principal consumers of ATP in cardiomyocytes are SERCA2a and NCX, which differ in their stoichiometry of ATP utilization for an equivalent amount of Ca^{2+} transported: SERCA2a hydrolyzes one ATP molecule per two Ca^{2+} ions, whereas NCX requires the energetic equivalent of two ATP molecules [60]. Consequently, SERCA2a represents a more energy saving mechanism compared with NCX. Under quiescence the Na^+/K^+ pump dominates as energy consumer [61]. Therefore, lowering of SERCA2a Kd_{Ca}, as in PLN-R14del+/− CMs, might theoretically alleviate the load on the NCX pump and be energy saving. The reduction in NCX conductance (Figure 5), possibly an adaptation to SERCA2a dominance, would contribute to limit energy consumption.

Importantly, the presence of metabolic depression despite preserved mitochondrial membrane polarization and normal ROS levels (Figure 13) suggests that, at this stage, the former may reflect mitochondrial dysregulation, as opposed to overt damage. The heightened dependence of OCR on cytosolic Ca^{2+} (Figure 10) may be one mechanistic correlate of this dysregulation. However, when cardiomyocytes were paced, thereby increasing ATP demand to support contraction, PLN-R14del+/− cells manifested clear energetic incompetence. This indicates that hyperdynamic Ca^{2+} handling, while potentially energy-saving at rest, becomes insufficient to sustain metabolic requirements during increased workload, ultimately destabilizing the balance that preserves cellular energy charge under basal conditions.

2.6.3. Coupling between Ca^{2+} dynamics and energy metabolism

Mitochondrial Ca^{2+} plays a pivotal role in the regulation of oxidative phosphorylation and ATP synthesis. To investigate whether altered Ca^{2+} dynamics contribute to the reduction of resting oxygen consumption rate (OCR), we measured OCR following cytosolic Ca^{2+} chelation (BAPTA) or functional depletion of sarcoplasmic reticulum (SR) Ca^{2+} stores (thapsigargin, THAPSI). Both interventions reduced OCR (Figure 10), confirming that Ca^{2+}, and specifically the SR, play a key role in sustaining mitochondrial respiration. Interestingly, maximal, but not basal-OCR, was differentially regulated in Mut versus WT CMs. This can be tentatively interpreted by considering that, whereas basal OCR responds to multiple Ca^{2+}-sensitive factors (including extra-mitochondrial ones), maximal OCR should depend exclusively on the intrinsic electron transport (ET) rate. ET rate is expectedly sensitive to matrix $Ca^{2+,}$ required to support the production of reduced substrates fueling the ET reactions. This considered, the stronger sensitivity of maximal-OCR to BAPTA and THAPSI peculiar of Mut CMs may reflect increased Ca^{2+} requirements of the reactions fuelling ET, or of ET reactions themselves. While such a phenotype could represent an adaptation to hyperdynamic Ca^{2+} handling, the impaired energetic response of Mut cells upon pacing suggests a genuine defect in ATP production. The link between Ca^{2+} handling and energy metabolism abnormalities is still elusive. In hiPSC-CMs, PLN knock-out initially enhances OCR, with mitochondrial impairment emerging only at later stages [56]. This argues against hyperdynamic Ca^{2+} handling while both PLN-R14del+/− and PLN knock out induce a hyperdynamic state, in the latter PLN protein is missing. This may point to an additional pathogenetic mechanism in ACM caused by PLN-R14del+/− but perhaps independent from changes in SERCA2a function.

2.6.4. Transcript and protein analysis

Cell damage might be caused, independent of SERCA2a dysregulation, by direct toxicity of the mutant protein (ER-stress) and the resulting activation of the “unfolded protein response” (UPR) [62]. ER-stress activation and reduced mitochondria abundance were indeed the main derangement detected in PLN-R14del+/− [12]. In the present study, transcript and protein analysis (Figure 14; Figure 15) mainly yielded negative results, which may nonetheless be informative. Failure to detect activation of energy starvation signaling under rest is in line with unchanged cell energy charge (normal resting I_{KATP} density, Figure 12). Lack of activation of ROS scavenging genes, along with normal ROS content and mitochondrial membrane potential, stand for the absence of major mitochondrial damage under quiescence. Similarly, lack of CaMKII activation argues against early involvement of Ca^{2+} decompartmentalization in disease pathogenesis.

2.7. Limitations

Because of technical limitations, energy production and signaling were assessed in quiescent CMs. In this condition, SERCA2a is expected to be only marginally active, and the modest trend toward reduced OCR after THAPSI treatment (Figure 10 D) supports this interpretation. The metabolic state would clearly be different in contracting myocytes, so each result must be interpreted in relation to the condition (resting or contracting) in which it was obtained, as specified throughout the manuscript. Some speculation is necessarily involved in translating the study outcome to the contracting heart.

This study was designed to investigate early mechanisms by examining the effects of the mutation before the onset of overt cardiac abnormalities. As commonly occurs in cardiac remodeling, additional mechanisms may contribute to myocardial dysfunction at later stages.

The choice of sex uniformity reduced variability but did not take into account possible sex-specific differences of mutation manifestations.

Finally, because of the limited availability of samples, SERCA ATPase activity (Figure 1) was measured from only two hearts per group. However, multiple technical replicates were obtained from each sample, and this analysis represents only one element of the overall evidence supporting the conclusion that the mutation enhances SERCA2a function.

2.8. Conclusions

The present findings extend our previous observations in patient-derived hiPS-CMs [11] showing that PLN R14del$^{+/-}$ may upregulate SERCA2a activity and promote hyperdynamic Ca^{2+} handling in native mature CMs of the TG mouse. The mutation also results in a substantial downregulation of energetic metabolism at rest, not associated with signs of overt mitochondrial damage, but leading to energetic incompetence during pacing. Downregulation of energy production in resting mutant CMs might be seen as the "physiological" response to reduced ATP demand, expected from switch to SERCA2a dominance in Ca^{2+} handling. Nonetheless, increased OCR dependency on Ca^{2+} and pacing-induced energetic incompetence point to genuine mitochondrial dysfunction in Mut CMs.

Hyperdynamic Ca^{2+} handling is therefore unlikely to represent the primary cause of the metabolic defect at this disease stage. I previous work suggests that toxicity of the mutant protein may be involved. In fact, pronounced ER stress has been reported in PLN R14del$^{+/-}$ hiPS-CMs [12], and even at this early stage of disease, the present study detected activation of some markers of the unfolded protein response (UPR). Once initiated, UPR may trigger a range of cellular abnormalities, including extensive mitochondrial remodeling and SR damage [62]. Since many of these processes are Ca^{2+}-dependent, the idea that ACM pathogenesis may involve mechanisms independent of hyperdynamic Ca^{2+} handling is not incompatible with the finding that strong Ca^{2+} buffering can prevent phenotype development [12].

Last but not least, the cellular mutation phenotype of the TG mouse described in the present study is mostly consistent with that of patient-derived hiPS-CMs [11, 12], thus providing cross-validation of these experimental models.

2.9. Therapeutic implications

The initial hypothesis of SERCA2a super inhibition by PLN-R14del+/− pointed to the therapeutic potential of PLN-displacing SERCA2a activators, now available as drugs [10, 63, 64]. The loss of SERCA2a function detected in the zebrafish TG model of the mutation, was indeed reversed by one of these compounds (istaroxime) [5]. However, consistent with a loss of SERCA2a inhibition by PLN R14del+/−, the prototypical selective SERCA2a activator PST-3093, was totally ineffective in patient-derived hiPS-

CMs [11] and TG mouse CMs (present results). This, and the likely involvement of pathogenetic mechanisms beyond SERCA2a dysregulation, may suggest investing on mutation reversal [65], or at least on improvement of mutant protein processing (e.g. by "chaperone" molecules), or reducing the impact of pathogenic PLN protein [13, 25] as the most logical mechanism-based therapeutic approaches. Speaking of more generic approaches, countering the enhancement of sustained Na^+ current (a common response to cell stress) has proven effective in preventing the consequences of chronic upregulation of Ca^{2+} cycling in hiPS-CMs [56].

2.10. References

1. van der Zwaag, P.A., van Rijsingen, I.A.W., Asimaki, A., Jongbloed, J.D.H., van Veldhuisen, D.J., Wiesfeld, A.C.P., Cox, M.G.P.J., van Lochem, L.T., de Boer, R.A., Hofstra, R.M.W., Christiaans, I., van Spaendonck-Zwarts, K.Y., Lekanne dit Deprez, R.H., Judge, D.P., Calkins, H., Suurmeijer, A.J.H., Hauer, R.N.W., Saffitz, J.E., Wilde, A.A.M., van den Berg, M.P., van Tintelen, J.P.: Phospholamban R14del mutation in patients diagnosed with dilated cardiomyopathy or arrhythmogenic right ventricular cardiomyopathy: evidence supporting the concept of arrhythmogenic cardiomyopathy. Eur J Heart Fail. 14, 1199–1207 (2012). https://doi.org/10.1093/eurjhf/hfs119
2. van der Zwaag, P.A., van Rijsingen, I.A.W., de Ruiter, R., Nannenberg, E.A., Groeneweg, J.A., Post, J.G., Hauer, R.N.W., van Gelder, I.C., van den Berg, M.P., van der Harst, P., Wilde, A.A.M., van Tintelen, J.P.: Recurrent and founder mutations in the Netherlands-Phospholamban p.Arg14del mutation causes arrhythmogenic cardiomyopathy. Netherlands Heart Journal. 21, 286–293 (2013). https://doi.org/10.1007/s12471-013-0401-3
3. Haghighi, K., Kolokathis, F., Gramolini, A.O., Waggoner, J.R., Pater, L., Lynch, R.A., Fan, G.-C., Tsiapras, D., Parekh, R.R., Dorn Ii, G.W., Maclennan, D.H., Kremastinos, D.T., Kranias, E.G.: A mutation in the human phospholamban gene, deleting arginine 14, results in lethal, hereditary cardiomyopathy. (2006)
4. Stroik, D.R., Ceholski, D.K., Bidwell, P.A., Mleczko, J., Thanel, P.F., Kamdar, F., Autry, J.M., Cornea, R.L., Thomas, D.D.: Viral expression of a SERCA2a-activating PLB mutant improves calcium cycling and synchronicity in dilated cardiomyopathic hiPSC-CMs. J Mol Cell Cardiol. 138, 59–65 (2020). https://doi.org/10.1016/j.yjmcc.2019.11.147
5. Kamel, S.M., van Opbergen, C.J.M., Koopman, C.D., Verkerk, A.O., Boukens, B.J.D., de Jonge, B., Onderwater, Y.L., van Alebeek, E., Chocron, S., Polidoro Pontalti, C., Weuring, W.J., Vos, M.A., de Boer, T.P., van Veen, T.A.B., Bakkers, J.: Istaroxime treatment ameliorates calcium dysregulation in a zebrafish model of phospholamban R14del cardiomyopathy. Nat Commun. 12, (2021). https://doi.org/10.1038/s41467-021-27461-8
6. Vafiadaki, E., Haghighi, K., Arvanitis, D.A., Kranias, E.G., Sanoudou, D.: Aberrant PLN-R14del Protein Interactions Intensify SERCA2a Inhibition, Driving Impaired

Ca2+ Handling and Arrhythmogenesis. Int J Mol Sci. 23, 6947 (2022). https://doi.org/10.3390/ijms23136947

7. Ceholski, D.K., Trieber, C.A., Young, H.S.: Hydrophobic imbalance in the cytoplasmic domain of phospholamban is a determinant for lethal dilated cardiomyopathy. Journal of Biological Chemistry. 287, 16521–16529 (2012). https://doi.org/10.1074/jbc.M112.360859
8. Hughes, E., Middleton, D.A.: Comparison of the Structure and Function of Phospholamban and the Arginine-14 Deficient Mutant Associated with Dilated Cardiomyopathy. PLoS One. 9, e106746 (2014). https://doi.org/10.1371/journal.pone.0106746
9. Vostrikov, V. V., Soller, K.J., Ha, K.N., Gopinath, T., Veglia, G.: Effects of naturally occurring arginine 14 deletion on phospholamban conformational dynamics and membrane interactions. Biochim Biophys Acta Biomembr. 1848, 315–322 (2015). https://doi.org/10.1016/j.bbamem.2014.09.007
10. Arici, M., Ferrandi, M., Hsu, S.-C., Torre, E., Barassi, P., Luraghi, A., Ronchi, C., Chang, G.-J., Peri, F., Ferrari, P., Bianchi, G., Rocchetti, M., Zaza, A.: Istaroxime metabolite PST3093 selectively stimulates SERCA2a and reverses disease-induced changes in cardiac function Corresponding authors. https://doi.org/10.1101/2021.08.17.455204
11. Badone, B., Ronchi, C., Lodola, F., Knaust, A.E., Hansen, A., Eschenhagen, T., Zaza, A.: Characterization of the PLN p.Arg14del Mutation in Human Induced Pluripotent Stem Cell-Derived Cardiomyocytes. Int J Mol Sci. 22, 13500 (2021). https://doi.org/10.3390/ijms222413500
12. Cuello, F., Knaust, A.E., Saleem, U., Loos, M., Raabe, J., Mosqueira, D., Laufer, S., Schweizer, M., Kraak, P., Flenner, F., Ulmer, B.M., Braren, I., Yin, X., Theofilatos, K., Ruiz-Orera, J., Patone, G., Klampe, B., Schulze, T., Piasecki, A., Pinto, Y., Vink, A., Hübner, N., Harding, S., Mayr, M., Denning, C., Eschenhagen, T., Hansen, A.: Impairment of the ER/mitochondria compartment in human cardiomyocytes with PLN p.Arg14del mutation. EMBO Mol Med. 13, (2021). https://doi.org/10.15252/emmm.202013074
13. Eijgenraam, T.R., Boukens, B.J., Boogerd, C.J., Schouten, E.M., van de Kolk, C.W.A., Stege, N.M., te Rijdt, W.P., Hoorntje, E.T., van der Zwaag, P.A., van Rooij, E., van Tintelen, J.P., van den Berg, M.P., van der Meer, P., van der Velden, J., Silljé,

H.H.W., de Boer, R.A.: The phospholamban p.(Arg14del) pathogenic variant leads to cardiomyopathy with heart failure and is unreponsive to standard heart failure therapy. Sci Rep. 10, (2020). https://doi.org/10.1038/s41598-020-66656-9

14. Lipskaia, L., Chemaly, E.R., Hadri, L., Lompre, A.-M., Hajjar, R.J.: Sarcoplasmic reticulum Ca $^{2+}$ ATPase as a therapeutic target for heart failure. Expert Opin Biol Ther. 10, 29–41 (2010). https://doi.org/10.1517/14712590903321462
15. Eisner, D.A., Caldwell, J.L., Kistamás, K., Trafford, A.W.: Calcium and Excitation-Contraction Coupling in the Heart. Circ Res. 121, 181–195 (2017). https://doi.org/10.1161/CIRCRESAHA.117.310230
16. Bers, D.M.: Calcium Cycling and Signaling in Cardiac Myocytes. Annu Rev Physiol. 70, 23–49 (2008). https://doi.org/10.1146/annurev.physiol.70.113006.100455
17. Fearnley, C.J., Llewelyn Roderick, H., Bootman, M.D.: Calcium signaling in cardiac myocytes. Cold Spring Harb Perspect Biol. 3, (2011). https://doi.org/10.1101/cshperspect.a004242
18. MacLennan, D.H., Kranias, E.G.: Phospholamban: A crucial regulator of cardiac contractility, (2003)
19. Bers, D.M.: Cardiac excitation–contraction coupling. Nature. 415, 198–205 (2002). https://doi.org/10.1038/415198a
20. Kranias, E.G., Hajjar, R.J.: Modulation of Cardiac Contractility by the Phopholamban/SERCA2a Regulatome. Circ Res. 110, 1646–1660 (2012). https://doi.org/10.1161/CIRCRESAHA.111.259754
21. Periasamy, M., Kalyanasundaram, A.: SERCA pump isoforms: Their role in calcium transport and disease. Muscle Nerve. 35, 430–442 (2007). https://doi.org/10.1002/mus.20745
22. Gustavsson, M., Verardi, R., Mullen, D.G., Mote, K.R., Traaseth, N.J., Gopinath, T., Veglia, G.: Allosteric regulation of SERCA by phosphorylationmediated conformational shift of phospholamban. Proc Natl Acad Sci U S A. 110, 17338–17343 (2013). https://doi.org/10.1073/pnas.1303006110
23. Brittsan, A.G., Kranias, E.G.: Phospholamban and Cardiac Contractile Function. J Mol Cell Cardiol. 32, 2131–2139 (2000). https://doi.org/10.1006/jmcc.2000.1270
24. Hof, I.E., van der Heijden, J.F., Kranias, E.G., Sanoudou, D., de Boer, R.A., van Tintelen, J.P., van der Zwaag, P.A., Doevendans, P.A.: Prevalence and cardiac

phenotype of patients with a phospholamban mutation. Netherlands Heart Journal. 27, 64–69 (2019). https://doi.org/10.1007/s12471-018-1211-4

25. Stege, N.M., Eijgenraam, T.R., Oliveira Nunes Teixeira, V., Feringa, A.M., Schouten, E.M., Kuster, D.W.D., van der Velden, J., Wolters, A.H.G., Giepmans, B.N.G., Makarewich, C.A., Bassel-Duby, R., Olson, E.N., de Boer, R.A., Silljé, H.H.W.: DWORF Extends Life Span in a PLN-R14del Cardiomyopathy Mouse Model by Reducing Abnormal Sarcoplasmic Reticulum Clusters. Circ Res. 133, 1006–1021 (2023). https://doi.org/10.1161/CIRCRESAHA.123.323304
26. Maniezzi, C., Eskandr, M., Florindi, C., Ferrandi, M., Barassi, P., Sacco, E., Pasquale, V., Maione, A.S., Pompilio, G., Teixeira, V.O.N., de Boer, R.A., Silljé, H.H.W., Lodola, F., Zaza, A.: Early consequences of the phospholamban mutation <scp>PLN-R14del</scp> $^{+/-}$ in a transgenic mouse model. Acta Physiologica. 240, (2024). https://doi.org/10.1111/apha.14082
27. Dorn, G.W., Vega, R.B., Kelly, D.P.: Mitochondrial biogenesis and dynamics in the developing and diseased heart. Genes Dev. 29, 1981–1991 (2015). https://doi.org/10.1101/gad.269894.115
28. Kwong, J.Q.: The mitochondrial calcium uniporter in the heart: energetics and beyond. J Physiol. 595, 3743–3751 (2017). https://doi.org/10.1113/JP273059
29. Piquereau, J., Caffin, F., Novotova, M., Lemaire, C., Veksler, V., Garnier, A., Ventura-Clapier, R., Joubert, F.: Mitochondrial dynamics in the adult cardiomyocytes: which roles for a highly specialized cell? Front Physiol. 4, (2013). https://doi.org/10.3389/fphys.2013.00102
30. Chaanine, A.H.: Metabolic Remodeling and Implicated Calcium and Signal Transduction Pathways in the Pathogenesis of Heart Failure. Int J Mol Sci. 22, 10579 (2021). https://doi.org/10.3390/ijms221910579
31. D’Souza, A.R., Minczuk, M.: Mitochondrial transcription and translation: overview. Essays Biochem. 62, 309–320 (2018). https://doi.org/10.1042/EBC20170102
32. Tarasov, A.I., Griffiths, E.J., Rutter, G.A.: Regulation of ATP production by mitochondrial Ca2+. Cell Calcium. 52, 28–35 (2012). https://doi.org/10.1016/j.ceca.2012.03.003
33. Taanman, J.-W.: The mitochondrial genome: structure, transcription, translation and replication. Biochimica et Biophysica Acta (BBA) - Bioenergetics. 1410, 103–123 (1999). https://doi.org/10.1016/S0005-2728(98)00161-3

34. Gincel, D., Zaid, H., Shoshan-Barmatz, V.: Calcium binding and translocation by the voltage-dependent anion channel : a possible regulatory mechanism in mitochondrial function. (2001)
35. Rosencrans, W.M., Rajendran, M., Bezrukov, S.M., Rostovtseva, T.K.: VDAC regulation of mitochondrial calcium flux: From channel biophysics to disease. Cell Calcium. 94, (2021). https://doi.org/10.1016/j.ceca.2021.102356
36. Chaanine, A.H.: Metabolic remodeling and implicated calcium and signal transduction pathways in the pathogenesis of heart failure, (2021)
37. Tarasov, A.I., Griffiths, E.J., Rutter, G.A.: Regulation of ATP production by mitochondrial Ca2+. Cell Calcium. 52, 28–35 (2012). https://doi.org/10.1016/j.ceca.2012.03.003
38. Kwong, J.Q.: The mitochondrial calcium uniporter in the heart: energetics and beyond, (2017)
39. Hopper, R.K., Carroll, S., Aponte, A.M., Johnson, D.T., French, S., Shen, R.F., Witzmann, F.A., Harris, R.A., Balaban, R.S.: Mitochondrial matrix phosphoproteome: Effect of extra mitochondrial calcium. Biochemistry. 45, 2524–2536 (2006). https://doi.org/10.1021/bi052475e
40. Ackers-Johnson, M., Li, P.Y., Holmes, A.P., O'Brien, S.M., Pavlovic, D., Foo, R.S.: A Simplified, Langendorff-Free Method for Concomitant Isolation of Viable Cardiac Myocytes and Nonmyocytes from the Adult Mouse Heart. Circ Res. 119, 909–920 (2016). https://doi.org/10.1161/CIRCRESAHA.116.309202.
41. Ferrandi, M., Barassi, P., Tadini-Buoninsegni, F., Bartolommei, G., Molinari, I., Tripodi, M.G., Reina, C., Moncelli, M.R., Bianchi, G., Ferrari, P.: Istaroxime stimulates <scp>SERCA2a</scp> and accelerates calcium cycling in heart failure by relieving phospholamban inhibition. Br J Pharmacol. 169, 1849–1861 (2013). https://doi.org/10.1111/bph.12278
42. Varro, A., Negretti, N., Hester, S.B., Eisner, D.A.: An estimate of the calcium content of the sarcoplasmic reticulum in rat ventricular myocytes. Pfl gers Archiv European Journal of Physiology. 423–423, 158–160 (1993). https://doi.org/10.1007/BF00374975
43. Teramoto, N., Tomoda, T., Yunoki, T., Ito, Y.: Different glibenclamide-sensitivity of ATP-sensitive K+ currents using different patch-clamp recording methods. Eur J Pharmacol. 531, 34–40 (2006). https://doi.org/10.1016/j.ejphar.2005.12.011

44. Alemanni, M., Rocchetti, M., Re, D., Zaza, A.: Role and mechanism of subcellular Ca2+ distribution in the action of two inotropic agents with different toxicity. J Mol Cell Cardiol. 50, 910–918 (2011). https://doi.org/10.1016/j.yjmcc.2011.02.008
45. Zucchi, R.: Modulation of sarcoplasmic reticulum function A new strategy in cardioprotection? Pharmacol Ther. 89, 47–65 (2001). https://doi.org/10.1016/S0163-7258(00)00103-0
46. Singh, R., Gupta, V., Kumar, A., Singh, K.: 2-Deoxy-D-Glucose: A Novel Pharmacological Agent for Killing Hypoxic Tumor Cells, Oxygen Dependence-Lowering in Covid-19, and Other Pharmacological Activities. Adv Pharmacol Pharm Sci. 2023, 1–15 (2023). https://doi.org/10.1155/2023/9993386
47. Perry, S.W., Norman, J.P., Barbieri, J., Brown, E.B., Gelbard, H.A.: Mitochondrial Membrane Potential Probes and the Proton Gradient: A Practical Usage Guide. Biotechniques. 50, 98–115 (2011). https://doi.org/10.2144/000113610
48. Mahaney, J.E., Albers, R.W., Waggoner, J.R., Kutchai, H.C., Froehlich, J.P.: Intermolecular Conformational Coupling and Free Energy Exchange Enhance the Catalytic Efficiency of Cardiac Muscle SERCA2a following the Relief of Phospholamban Inhibition. Biochemistry. 44, 7713–7724 (2005). https://doi.org/10.1021/bi048011i
49. Endoh, M.: Force-frequency relationship in intact mammalian ventricular myocardium: Physiological and pathophysiological relevance, (2004)
50. Kefaloyianni, E., Bao, L., Rindler, M.J., Hong, M., Patel, T., Taskin, E., Coetzee, W.A.: Measuring and evaluating the role of ATP-sensitive K+ channels in cardiac muscle. J Mol Cell Cardiol. 52, 596–607 (2012). https://doi.org/10.1016/j.yjmcc.2011.12.012
51. Cleary, S.R., Teng, A.C.T., Kongmeneck, A.D., Fang, X., Phillips, T.A., Cho, E.E., Kekenes-Huskey, P., Gramolini, A.O., Robia, S.L.: Dilated cardiomyopathy variant R14del increases phospholamban pentamer stability, blunting dynamic regulation of cardiac calcium handling, (2023)
52. Haghighi, K., Gardner, G., Vafiadaki, E., Kumar, M., Green, L.C., Ma, J., Crocker, J.S., Koch, S., Arvanitis, D.A., Bidwell, P., Rubinstein, J., van de Leur, R., Doevendans, P.A., Akar, F.G., Tranter, M., Wang, H.-S., Sadayappan, S., DeMazumder, D., Sanoudou, D., Hajjar, R.J., Stillitano, F., Kranias, E.G.: Impaired

Right Ventricular Calcium Cycling Is an Early Risk Factor in R14del-Phospholamban Arrhythmias. J Pers Med. 11, 502 (2021). https://doi.org/10.3390/jpm11060502

53. Dave, J., Raad, N., Mittal, N., Zhang, L., Fargnoli, A., Oh, J.G., Savoia, M.E., Hansen, J., Fava, M., Yin, X., Theofilatos, K., Ceholski, D., Kohlbrenner, E., Jeong, D., Wills, L., Nonnenmacher, M., Haghighi, K., Costa, K.D., Turnbull, I.C., Mayr, M., Cai, C.-L., Kranias, E.G., Akar, F.G., Hajjar, R.J., Stillitano, F.: Gene editing reverses arrhythmia susceptibility in humanized PLN-R14del mice: modelling a European cardiomyopathy with global impact. Cardiovasc Res. 118, 3140–3150 (2022). https://doi.org/10.1093/cvr/cvac021
54. Lehnart, S.E., Maier, L.S., Hasenfuss, G.: Abnormalities of calcium metabolism and myocardial contractility depression in the failing heart. Heart Fail Rev. 14, 213–224 (2009). https://doi.org/10.1007/s10741-009-9146-x
55. Slack, J.P., Grupp, I.L., Dash, R., Holder, D., Schmidt, A., Gerst, M.J., Tamura, T., Tilgmann, C., James, P.F., Johnson, R., Gerdes, A.M., Kranias, E.G.: The Enhanced Contractility of the Phospholamban-deficient Mouse Heart Persists with Aging. J Mol Cell Cardiol. 33, 1031–1040 (2001). https://doi.org/10.1006/jmcc.2001.1370
56. Jiang, Y., Li, X., Guo, T., Lu, W.-J., Ma, S., Chang, Y., Song, Y., Zhang, S., Bai, R., Wang, H., Qi, M., Jiang, H., Zhang, H., Lan, F.: Ranolazine rescues the heart failure phenotype of PLN-deficient human pluripotent stem cell-derived cardiomyocytes. Stem Cell Reports. 17, 804–819 (2022). https://doi.org/10.1016/j.stemcr.2022.02.016
57. Haghighi, K., Kolokathis, F., Pater, L., Lynch, R.A., Asahi, M., Gramolini, A.O., Fan, G.-C., Tsiapras, D., Hahn, H.S., Adamopoulos, S., Liggett, S.B., Dorn, G.W., MacLennan, D.H., Kremastinos, D.T., Kranias, E.G.: Human phospholamban null results in lethal dilated cardiomyopathy revealing a critical difference between mouse and human. Journal of Clinical Investigation. 111, 869–876 (2003). https://doi.org/10.1172/JCI17892
58. Shanmugam, M., Gao, S., Hong, C., Fefelova, N., Nowycky, M.C., Xie, L.-H., Periasamy, M., Babu, G.J.: Ablation of phospholamban and sarcolipin results in cardiac hypertrophy and decreased cardiac contractility. Cardiovasc Res. 89, 353–361 (2011). https://doi.org/10.1093/cvr/cvq294
59. Schmitt, J.P., Ahmad, F., Lorenz, K., Hein, L., Schulz, S., Asahi, M., MacLennan, D.H., Seidman, C.E., Seidman, J.G., Lohse, M.J.: Alterations of phospholamban function can exhibit cardiotoxic effects independent of excessive sarcoplasmic

reticulum Ca2+-ATPase inhibition. Circulation. 119, 436–444 (2009). https://doi.org/10.1161/CIRCULATIONAHA.108.783506

60. Sakata, S., Lebeche, D., Sakata, N., Sakata, Y., Chemaly, E.R., Liang, L.F., Tsuji, T., Takewa, Y., del Monte, F., Peluso, R., Zsebo, K., Jeong, D., Park, W.J., Kawase, Y., Hajjar, R.J.: Restoration of mechanical and energetic function in failing aortic-banded rat hearts by gene transfer of calcium cycling proteins. J Mol Cell Cardiol. 42, 852–861 (2007). https://doi.org/10.1016/j.yjmcc.2007.01.003.
61. Readnower, R.D., Brainard, R.E., Hill, B.G., Jones, S.P.: Standardized bioenergetic profiling of adult mouse cardiomyocytes. Physiol Genomics. 44, 1208–1213 (2012). https://doi.org/10.1152/physiolgenomics.00129.2012.-Mitochondria.
62. Senft, D., Ronai, Z.A.: UPR, autophagy, and mitochondria crosstalk underlies the ER stress response. Trends Biochem Sci. 40, 141–148 (2015). https://doi.org/10.1016/j.tibs.2015.01.002.
63. Rossi, D., Pierantozzi, E., Amadsun, D.O., Buonocore, S., Rubino, E.M., Sorrentino, V.: The Sarcoplasmic Reticulum of Skeletal Muscle Cells: A Labyrinth of Membrane Contact Sites. Biomolecules. 12, 488 (2022). https://doi.org/10.3390/biom12040488.
64. Carubelli, V., Zhang, Y., Metra, M., Lombardi, C., Felker, G.M., Filippatos, G., O’Connor, C.M., Teerlink, J.R., Simmons, P., Segal, R., Malfatto, G., La Rovere, M.T., Li, D., Han, X., Yuan, Z., Yao, Y., Li, B., Lau, L.F., Bianchi, G., Zhang, J.: Treatment with 24 hour istaroxime infusion in patients hospitalised for acute heart failure: a randomised, placebo-controlled trial. Eur J Heart Fail. 22, 1684–1693 (2020). https://doi.org/10.1002/ejhf.1743.
65. Stillitano, F., Turnbull, I.C., Karakikes, I., Nonnenmacher, M., Backeris, P., Hulot, J.-S., Kranias, E.G., Hajjar, R.J., Costa, K.D.: Genomic correction of familial cardiomyopathy in human engineered cardiac tissues. Eur Heart J. 37, 3282–3284 (2016). https://doi.org/10.1093/eurheartj/ehw307.

Chapter 3

Genetic variants risk assessment for Long QT Syndrome through machine learning and multielectrode array recordings.

Aleksandr Khudiakov PhD[1], Manuela Mura PhD[2], Federica Giannetti PhD[1], Vladislav Leonov PhD[1,3], Chiara Alberio[1], Marem Eskandra[4], Paul A Brink MD[5], Lia Crotti MD, PhD[1,6], Massimiliano, Gnecchi MD[2,7], Peter J Schwartz MD[1], Luca Sala PhD*[1,4]

1. Istituto Auxologico Italiano IRCCS, Center for Cardiac Arrhythmias of Genetic Origin and Laboratory of Cardiovascular Genetics, Milan, Italy
2. Translational Cardiology Unit, Fondazione IRCCS Policlinico San Matteo, Pavia, Italy.
3. Department of Surgery, Dentistry, Pediatrics and Gynecology, Cardiovascular Science, The University of Verona, Policlinico G.B. Rossi, Verona, Italy.
4. Department of Biotechnology and Biosciences, University of Milano - Bicocca, Italy
5. Department of Medicine, University of Stellenbosch, Tygerberg, South Africa.
6. Department of Medicine and Surgery, University of Milano-Bicocca, Milan, Italy
7. Department of Molecular Medicine, Unit of Cardiology, University of Pavia, Pavia, Italy

***Correspondence**

Luca Sala, PhD; Department of Biotechnology and Biosciences, University of Milano - Bicocca and Center for Cardiac Arrhythmias of Genetic Origin and Laboratory of Cardiovascular Genetics. Istituto Auxologico Italiano, IRCCS. Via Zucchi, 18 20095 Cusano Milanino (MI), Italy

[Under revision, medRxiv preprint doi: https://doi.org/10.1101/2025.03.25.25324187.]

3.1. Acronyms

ACMG: American College of Medical Genetics and Genomics

AP: Action Potential

APD: Action Potential Duration

APD90: Action Potential Duration at 90% repolarization

AUC: Area Under the Curve

cFPD: Corrected Field Potential Duration

DMSO: Dimethyl Sulfoxide

EGTA: Ethylene Glycol-bis(β-aminoethyl ether)-N,N,N′,N′-tetraacetic acid

FDA: Food and Drug Administration

FP: Field Potential

FPD: Field Potential Duration

HGMD: Human Gene Mutation Database

hiPSC: Human Induced Pluripotent Stem Cell

hiPSC-CM: Human Induced Pluripotent Stem Cell–Derived Cardiomyocyte

ICD: Implantable Cardioverter-Defibrillator

I_{CaL}: L-type Calcium Current

I_{Kr}: Rapid Delayed Rectifier Potassium Current

I_{Ks}: Slow Delayed Rectifier Potassium Current

I_{Na}: Sodium Current

JLNS: Jervell and Lange-Nielsen Syndrome

KCNH2: Potassium Voltage-Gated Channel Subfamily H Member 2 (gene encoding hERG)

KCNQ1: Potassium Voltage-Gated Channel Subfamily Q Member 1 (gene encoding Kv7.1)

LJP: Liquid Junction Potential

MEA: Multi-Electrode Array

ML: Machine Learning

MM: Maturation Medium

MICE: Multiple Ion Channel Effects

NOS1: Neuronal Nitric Oxide Synthase

NOS1AP: Nitric Oxide Synthase 1 Adaptor Protein

P/LP: Pathogenic / Likely Pathogenic

PK: Pharmacokinetic

PtPA: Peak-to-Peak Amplitude

RBins-: RPMI1640 medium with B27 supplement minus insulin

RR: Beat-to-Beat Interval

RT-PCR – Reverse Transcription Polymerase Chain Reaction

SCD: Sudden Cardiac Death

SERCA2a: Sarco/Endoplasmic Reticulum Ca^{2+}-ATPase 2a

SR: Sarcoplasmic Reticulum

TdP: Torsades de Pointes

VUS: Variant of Uncertain Significance

WT: Wild Type

3.2. Abstract

Background Long QT syndrome (LQTS) is a life-threatening genetic disorder characterized by prolonged QT intervals on electrocardiograms. Congenital forms are most frequently linked to pathogenic or likely pathogenic (P/LP) variants in the *KCNQ1* and *KCNH2* genes. Among these, certain variants confer a substantially higher incidence of cardiac events compared to others. Although current therapies have markedly reduced mortality, some patients remain unresponsive or intolerant, preserving their risk of severe arrhythmias, including sudden cardiac death. Current approaches for risk stratification remain limited, highlighting the critical need for more accurate identification and management of patients carrying high-risk genetic variants.

Objectives To explore the feasibility of a functional risk stratification approach for P/LP variants by applying machine learning based classification to electrophysiological data measured in human induced pluripotent stem cell-derived cardiomyocytes (hiPSC-CMs).

Methods Eleven patient-specific hiPSC lines carrying six P/LP variants in *KCNQ1* or *KCNH2* were differentiated to cardiomyocytes (hiPSC-CMs). Electrophysiological responses from multielectrode array recordings at baseline and after application of selective ion channel blockers or proarrhythmic compounds were used to train a machine learning model to classify variant-specific risk levels based on *in vitro* electrophysiological readouts.

Results Our findings revealed a correlation between variant risk level, hiPSC-CM electrophysiological profiles, and drug responses. The machine learning classifier, trained on multielectrode array recordings, achieved an 89% accuracy in the classification of P/LP genetic variants according to the associated risk levels.

Conclusions These findings support the feasibility of integrating hiPSC-CM electrophysiological data with machine learning to identify variant-specific arrhythmogenic risk signatures in LQTS. This work provides a proof of concept for functional risk stratification and sets the stage for validation in larger and more diverse variant cohorts.

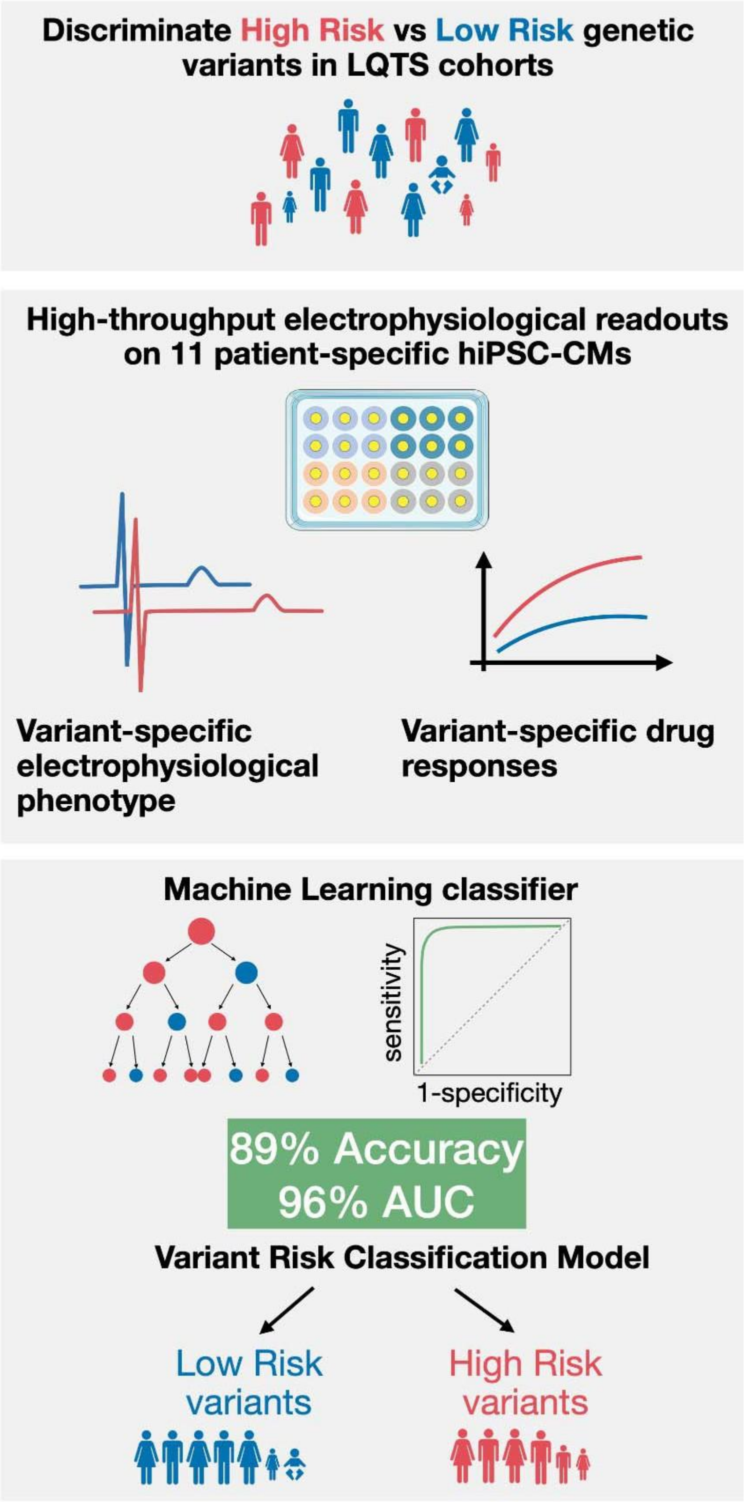
Discriminate High Risk vs Low Risk genetic variants in LQTS cohorts
High-throughput electrophysiological readouts on 11 patient-specific hiPSC-CMs
Variant-specific electrophysiological phenotype
Variant-specific drug responses
Machine Learning classifier
sensitivity
1-specificity
89% Accuracy
96% AUC
Variant Risk Classification Model
Low Risk variants
High Risk variants

3.3. Background

The long QT syndrome (LQTS) is a life-threatening genetic disorder characterized by a prolonged QT interval on the electrocardiogram, a predisposition to lethal arrhythmias particularly under stress, and an increased sensitivity to drugs affecting cardiac repolarization through block of the I_{Kr} potassium current [1–4]. Appropriate therapies based on beta-blockers [5], left cardiac sympathetic denervation [6, 7] and sodium channel blockers [8, 9] have effectively reduced the risk of potentially fatal ventricular arrhythmias and sudden cardiac death (SCD), limiting the use of an implantable cardioverter defibrillator only to selected patients [5, 10]. However, a major challenge for clinicians remains the accurate identification, management, and protection of patients at highest risk of SCD.

3.3.1. Genetic insights and limitations

Advancements in next-generation sequencing have enabled the identification of numerous variants in genes encoding cardiac ion channels, subunits, or associated proteins implicated in LQTS[11, 12]. While these insights have guided gene-specific patient management [8], current genetic interpretation guidelines [13] are often insufficient to identify patients at greatest risk, as many variants remain classified as variants of uncertain significance (VUS). Even variants classified as pathogenic or likely pathogenic (P/LP) according to the American College of Medical Genetics and Genomics (ACMG) guidelines may exhibit markedly different risks of life-threatening cardiac events, including SCD [14, 15], requiring profoundly different clinical management.

3.3.2. hiPSC-CM

Accurate clinical risk assessment for a variant requires data from many affected individuals and this is not feasible for most of the variants, limiting precision medicine and slows the development of variant-specific therapies [16, 17]. The classification of variant pathogenicity through *in vitro* or *in vivo* studies represents a promising approach to overcome this challenge [18, 19]. Studies using patient-specific cardiomyocytes derived from human induced pluripotent stem cells (hiPSC-CMs) have provided high-quality data on how variants affect action potentials, calcium transients or contractility. hiPSC-CM-based models have been particularly useful for disease modeling of congenital or acquired cardiac disorders such as LQTS [20–24], Jervell and Lange-

Nielsen syndrome (JLNS) [25], Timothy syndrome [26], cardiomyopathies [27–29], congenital heart defects [30], drug testing [31–33] and drug repurposing [34].

3.3.3. Objectives of the study

In the present study, we investigated a limited set of six well-characterized P/LP variants from the two most prevalent LQTS subtypes, LQT1 and LQT2, which together account for approximately 90% of cases. These variants were identified in individuals with clinically heterogeneous presentations, from normal to prolonged QT intervals and displaying low or high incidence of life-threatening cardiac events per variant (defined here as Low and High Risk P/LP variants).

Using patient-derived hiPSC-CMs and high-throughput multielectrode arrays (MEA), we aimed to:

i) determine whether hiPSC-CMs carrying P/LP variants with different clinical severities exhibit distinct drug responses in vitro;

ii) whether *in vitro* phenotypes match clinical records and may provide information relevant to variant-associated risk stratification;

iii) to explore the feasibility of applying machine learning to in vitro readouts for P/LP variant risk stratification.

3.4. Methods

3.4.1. Ethical statement

This study was conducted in accordance with the Declaration of Helsinki and the ethics committee of Istituto Auxologico Italiano IRCCS gave ethical approval for this work (Approval number: 2020_10_20_07). Appropriate informed consents were obtained from all donors.

3.4.2. Patient-specific hiPSC lines included in the study

A total of eleven hiPSC lines were used in this study. These lines were derived from LQT1, JLNS, and LQT2 patients carrying variants in the **KCNQ1** or **KCNH2** genes (see Table 1 for details). The line carrying the *KCNH2 p.A561V* variant was provided by Dr. Joseph C. Wu (Stanford Cardiovascular Institute). As a wild-type control (WT), we used the **WTC-11** line, generated from a healthy donor and obtained from the Coriell Institute for Medical Research (catalog no. GM25256), and used as a bona fide wild-type reference[35]. Detailed characterization of each hiPSC line, including genetic and functional properties, is provided in Table 2, Figure1 and Figure2.

3.4.3. Cardiac events frequency assessment

Clinical data on documented cardiac events (including syncope, sustained ventricular tachycardia, appropriate ICD shocks, sudden cardiac arrest, and sudden cardiac death), QTc values, and Schwartz scores (when available) were collected from our internal LQTS patient database, the Human Gene Mutation Database (HGMD) [36], and the Variant Browser database [37, 38]. The frequency of cardiac events was determined as the proportion of patients with a history of such events relative to the total number of patients carrying the corresponding variant.

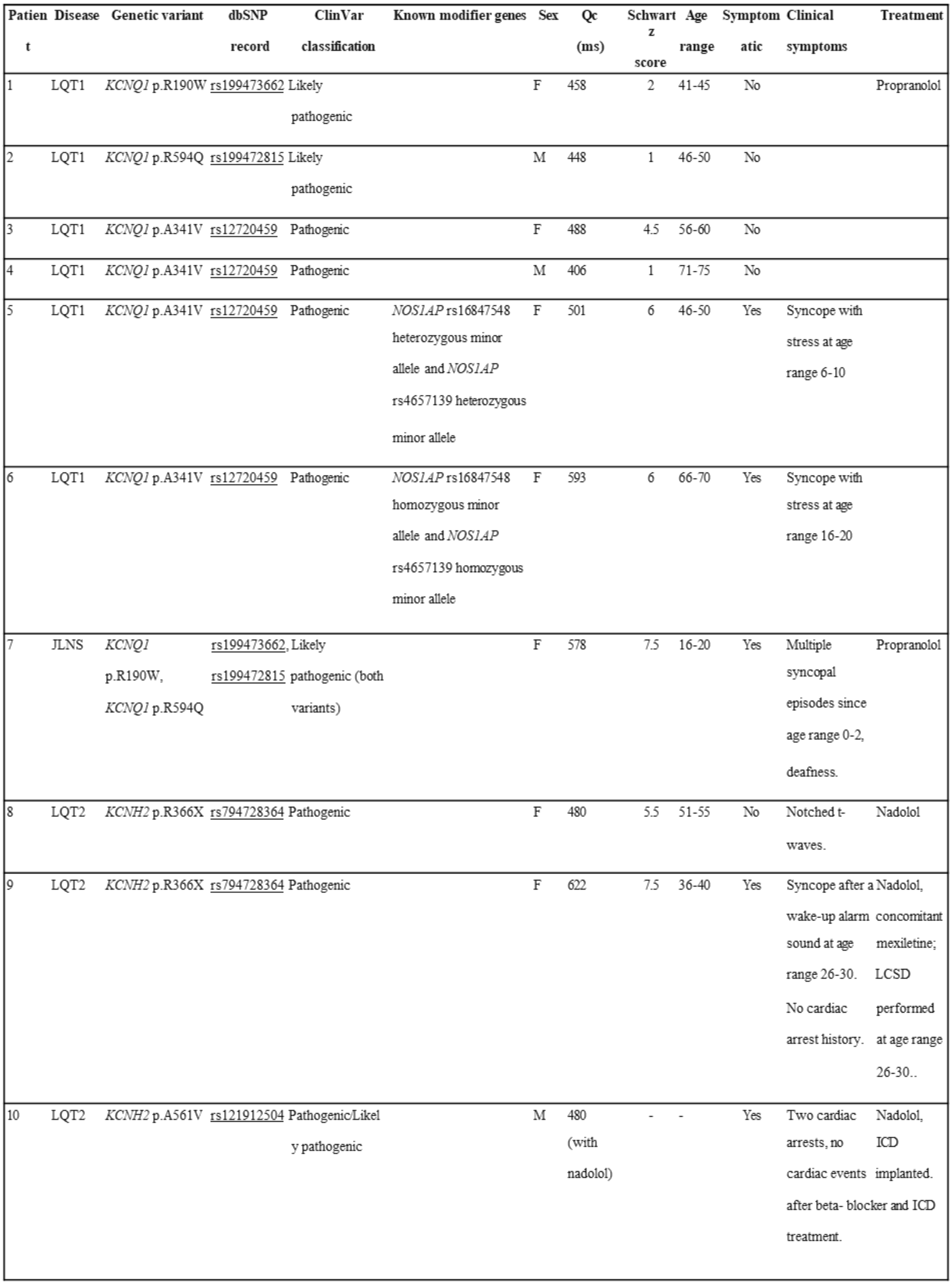

Patient	Disease	Genetic variant	dbSNP record	ClinVar classification	Known modifier genes	Sex	Qc (ms)	Schwartz score	Age range	Symptomatic	Clinical symptoms	Treatment
1	LQT1	*KCNQ1* p.R190W	rs199473662	Likely pathogenic		F	458	2	41-45	No		Propranolol
2	LQT1	*KCNQ1* p.R594Q	rs199472815	Likely pathogenic		M	448	1	46-50	No		
3	LQT1	*KCNQ1* p.A341V	rs12720459	Pathogenic		F	488	4.5	56-60	No		
4	LQT1	*KCNQ1* p.A341V	rs12720459	Pathogenic		M	406	1	71-75	No		
5	LQT1	*KCNQ1* p.A341V	rs12720459	Pathogenic	*NOS1AP* rs16847548 heterozygous minor allele and *NOS1AP* rs4657139 heterozygous minor allele	F	501	6	46-50	Yes	Syncope with stress at age range 6-10	
6	LQT1	*KCNQ1* p.A341V	rs12720459	Pathogenic	*NOS1AP* rs16847548 homozygous minor allele and *NOS1AP* rs4657139 homozygous minor allele	F	593	6	66-70	Yes	Syncope with stress at age range 16-20	
7	JLNS	*KCNQ1* p.R190W, *KCNQ1* p.R594Q	rs199473662, rs199472815	Likely pathogenic (both variants)		F	578	7.5	16-20	Yes	Multiple syncopal episodes since age range 0-2, deafness.	Propranolol
8	LQT2	*KCNH2* p.R366X	rs794728364	Pathogenic		F	480	5.5	51-55	No	Notched t-waves.	Nadolol
9	LQT2	*KCNH2* p.R366X	rs794728364	Pathogenic		F	622	7.5	36-40	Yes	Syncope after a wake-up alarm sound at age range 26-30. No cardiac arrest history.	Nadolol, concomitant mexiletine; LCSD performed at age range 26-30..
10	LQT2	*KCNH2* p.A561V	rs121912504	Pathogenic/Likely pathogenic		M	480 (with nadolol)	-	-	Yes	Two cardiac arrests, no cardiac events after beta- blocker and ICD treatment.	Nadolol, ICD implanted.

Table 1. Clinical characteristics of the patient cohort included in the study.

	Genetic variant	Known modifier gene	Disease	Line name	Line ID	Reference
1	Wild Type		Healthy	WTC-11		[39]
2	*KCNQ1* p.R190W		LQT1	29.7	PSMi005-A	[40]

3	*KCNQ1* p.R594Q		LQT1	28.44	PSMi004-A	[41]
4	*KCNQ1* p.A341V		LQT1	SA6.27	PSMi001-A	[42]
5	*KCNQ1* p.A341V		LQT1	SA15.14		Figure 1
6	*KCNQ*1 p.A341V	*NOS1AP* rs16847548 and rs4657139 heterozygous minor alleles	LQT1	SA14.19		Figure 1
7	*KCNQ1* p.A341V	*NOS1AP* rs16847548 and rs4657139 homozygous minor alleles	LQT1	SA13.5	PSMi007-A	[42, 43]
8	*KCNQ1* p.R190W & *KCNQ1* p.R594Q		JLNS	30.3	PSMi002-A	[44]
9	*KCNH2* p.R366X		LQT2	26.1		Figure 2
10	*KCNH2* p.R366X		LQT2	27.2		[34]
11	*KCNH2* p.A561V		LQT2	SCVI498c1		[45]

Table 2. List of hiPSC lines used in the study and their characterization status.

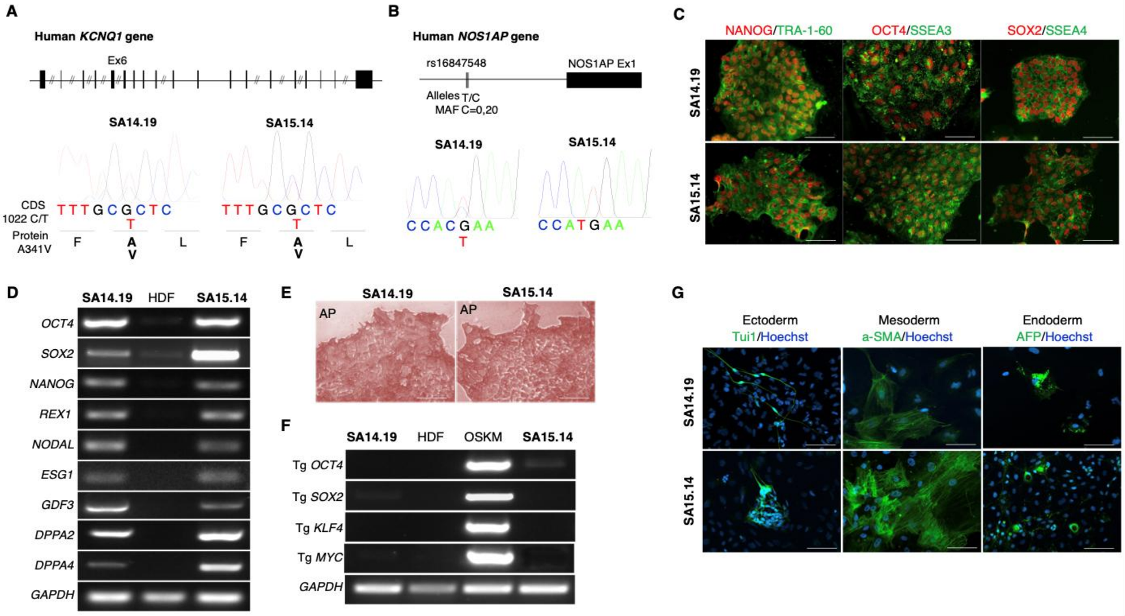

Figure 1. Characterization of SA14.19 and SA15.14 hiPSC lines.

A. Top: schematic representation of KCNQ1 gene (exons are vertical lines/boxes). Bottom: DNA sequencing results showing the mutation 1022 C/T in the KCNQ1 exon 6 (Ex6) in heterozygosis in the both SA14.19 and SA15.14 hiPSCs. B. Top: schematic representation of NOS1AP gene upstream region. MAF is the minor allele frequency in the SA founder population. Bottom: DNA sequencing results showing the rs16847548 minor allele in heterozygosis in SA14.19 but not in SA15.14 hiPSCs. C. Immunofluorescence stainings showing uniform expression of the indicated markers of pluripotency in the SA14.19 and SA15.14

hiPSCs. Nuclear transcription factors are in red, membrane antigens are in green. Scale bars 100 um. **D**. RT-PCR analysis showing induction of expression of the indicated markers of pluripotency in SA14.19 and SA15.14 hiPSCs compared with fibroblasts before reprogramming. **E**. Alkaline phosphatase colorimetric staining (AP). Scale bars 100 um. **F**. RT-PCR analysis showing no expression of the four viral transgenes (Tg) in naïve fibroblasts (HDF), expression of Tg OCT4, SOX2, KLF4 and cMYC five days after transduction (OSKM) and silencing of the four Tg in SA14.19 and SA15.14 at passages 12. **G**. Immunofluorescence staining for markers of the 3 germ layers in iPSC-derived EBs: neuronal class tubulin beta III (Tuj) for ectoderm, smooth muscle actin (SMA) for mesoderm, and alpha Fetoprotein (AFP) for endoderm. Scale bars 100 um.

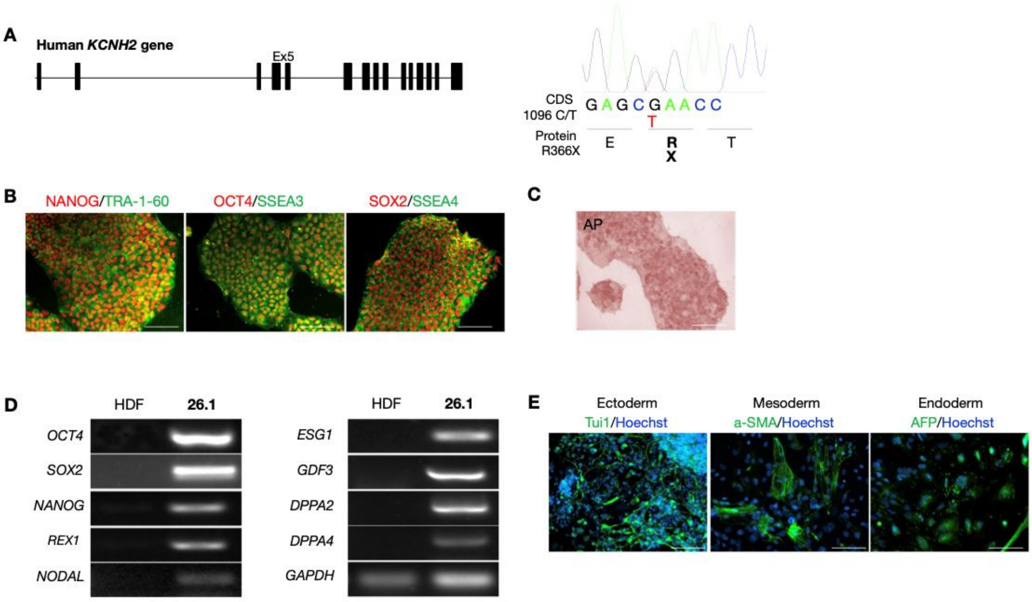

Figure 2. Characterization of 26.1 hiPSC line.

A. Left: schematic representation of KCNH2 gene (exons are vertical boxes). Right: DNA sequencing results showing the mutation 1096 C/T in the KCNH2 exon 5 (Ex5) in heterozygosis in 26.1 hiPSCs. **B**. Immunofluorescence stainings showing uniform expression of the indicated markers of pluripotency in the 26.1 hiPSCs. Nuclear transcription factors are in red, membrane antigens are in green. Scale bars 100 um. **C**. Alkaline phosphatase colorimetric staining (AP). Scale bars 100 um. **D**.RT-PCR analysis showing induction of expression of the indicated markers of pluripotency in 26.1 hiPSCs compared with parental fibroblasts. **E**. Immunofluorescence staining for markers of the three germ layers in iPSC-derived EBs: neuronal class tubulin beta III (Tuj) for ectoderm, smooth muscle actin (SMA) for mesoderm, and alpha Fetoprotein (AFP) for endoderm. Scale bars 100 um.

3.4.4. hiPSC culture and differentiation to hiPSC-CMs

hiPSCs were maintained on multiwell plates coated with recombinant human vitronectin (Gibco) in Essential 8 Flex medium (Gibco). For cardiac differentiation, hiPSCs were replated on Matrigel-coated plates (Corning). Differentiation into hiPSC-CMs was performed using a small-molecule–based protocol [46], followed by metabolic purification through glucose starvation [47] starting on day 7. Cells were cryopreserved in Bambanker (Nippon Genetics) between days 9 and 16. For subsequent experiments, hiPSC-CMs were thawed, replated at low density, and expanded as previously described [48]. A list of the main reagents is provided in Table 3. Data were collected from at least three independent differentiations of each hiPSC line for each experiment.

hiPSC cardiac differentiation

Cardiac differentiation was started 2-4 days after hiPSC plating, when hiPSCs reached 70-90% confluency. At this stage (Day 0), the culture medium was switched to RBins-medium, which consists of RPMI1640 supplemented with 1% of B27 supplement without insulin (Gibco), and 6 µM CHIR99021 (Selleckchem) was added to induce the differentiation. For the next two days, fresh RBins- medium was added (⅔ of the initial volume on day 1 and ⅓ on day 2). On day 3, the medium was switched to RBins- medium supplemented with 5 µM IWR1 (Merck). After two days of treatment with IWR1, the medium was replaced with RBK medium, consisting of RPMI1640 supplemented with 1% B27 Supplement (Gibco) and 1% Knock-Out Serum Replacement (Gibco). Starting from day 7 hiPSC-CMs were purified through glucose starvation [49] and cryopreserved in Bambanker (Nippon Genetics) at days 9-16. For the subsequent experiments hiPSC-CMs were thawed, replated at low density and expanded as previously reported [50]. Data were collected from at least three independent differentiations of each hiPSC line for each experiment.

Reagent	**Company**	**Product code**
B-27™ Supplement	Thermo Fisher Scientific [GIBCO]	17504044
B-27™ Supplement, minus insulin	Thermo Fisher Scientific [GIBCO]	A1895601
Bambanker	Nippon Genetics	BB03
CHIR-99021 HCl	Selleckchem	S2924
Chlorpromazine	SelleckChem	#S5749
Ciprofloxacin hydrochloride hydrate	SelleckChem	#S5208
Clarithromycin	SelleckChem	#S2555
Dofetilide	SelleckChem	#S1658
DPBS, no calcium, no magnesium	Thermo Fisher Scientific [GIBCO]	14190094
E4031 dihydrochloride	Tocris	#1808
EDTA (0.5 M), pH 8.0, RNase-free	Thermo Fisher Scientific [Invitrogen]	AM9262
Essential 8™ Flex Medium Kit	Thermo Fisher Scientific [GIBCO]	A2858501

Fibronectin bovine plasma	Merck [Sigma-Aldrich]	F1141
Haloperidol	SelleckChem	#S1920
HMR1556	Tocris	#5011
IWR-1	Merck [Sigma-Aldrich]	I0161
KOSR	Thermo Fisher Scientific [GIBCO]	10828028
Lactic acid	Merck	27714
Matrigel® Corning® hESC-Qualified Matrix, LDEV-free	Corning	354277
Moxifloxacin	SelleckChem	#S5535
Nifedipine	Merck	#N7634
RevitaCell™ Supplement	Thermo Fisher Scientific [GIBCO]	A2644501
RPMI 1640 Medium, no glucose	Thermo Fisher Scientific [GIBCO]	11879020
RPMI 1640 w/ L-Glutamine	Euroclone	ECB2000
Salbutamol	SelleckChem	#S2507
Tetrodotoxin citrate	Tocris	#1069
TrypLE™ Select Enzyme	Thermo Fisher Scientific [GIBCO]	A1217701
Vitronectin (VTN-N) Recombinant Human Protein, Truncated	Thermo Fisher Scientific [GIBCO]	A14700

Table 3. Data for each experiment were obtained from at least three independent differentiations of each hiPSC line**.**

3.4.5. Patch-clamp

For patch clamp experiments, metabolic maturation of hiPSC-CMs was performed as previously described [51]. Action potentials and I_{Ks} currents were recorded at 37 °C from isolated hiPSC-CMs plated on glass coverslips Action potentials were recorded in perforated patch mode under 1 Hz pacing.

Patch-clamp current-clamp and voltage-clamp recordings

Expanded hiPSC-CMs were dissociated with TrypLE Select Enzyme (10X) (Gibco) and plated in monolayers at a density $3 * 10^5/cm^2$ on 12-well plates coated with Matrigel (Corning) in RBK medium. The next day, RBK was replaced with a lipid-rich maturation medium (MM). Metabolic maturation was performed for two weeks and MM was refreshed twice a week. For action potential (AP) recordings, hiPSC-CMs were dissociated with TrypLE Select 10X (Gibco) and plated on Matrigel (Corning) coated glass coverslips as single cells with a density of $8.4 - 10.5 * 10^3/cm^2$.

Action potential recording

APs were recorded in perforated patch mode 3-10 days after hiPSC-CMs dissociation. The extracellular solution was based on modified Tyrode's solution and contained (mM): NaCl 154, KCl 5.4, $CaCl_2$ 1.8, HEPES-NaOH 5, D-Glucose 5.5. pH was set to 7.35 with NaOH. The intracellular solution contained (mM): K-Aspartate 125, KCl 20, NaCl 10,

Na_2-ATP 5, HEPES 10. pH was set to 7.3 with KOH. Amphotericin B 0.22 mM, dissolved in DMSO, was added to the intracellular solution to record APs.

APs were recorded with a Molecular Devices digidata 1440A and a Molecular Devices Axopatch 200B amplifier at physiological temperature (37 °C) and under 1 Hz pacing. Current pulses with duration of 2-3 ms and amplitudes of 0.5-1.5 nA were used to elicit APs. APs were digitized at 5 kHz and filtered at 2 kHz with a low-pass Bessel filter. Liquid junction potential was calculated according to the stationary Nernst-Planck equation using LJPcalc (Harden, SW and Brogioli, D (2020). LJPcalc [Online]. Available: https://swharden.com/software/LJPcalc, Accessed on 03/08/2021). The calculated LJP was 13.922 mV. The measured LJP was -11.2 ± 0.9 mV.

Slow delayed rectifier potassium current recording

The slow delayed rectifier potassium current (I_{Ks}) was recorded with the patch clamp technique in isolated hiPSC-CMs. Signals were digitized at 2 kHz and filtered at 1 kHz through a Molecular Device 1440A Digidata connected to a Molecular Devices 200B amplifier. Currents were recorded at physiological temperature (37 °C). The extracellular solution contained (mM): NaCl 154, KCl 5.4, CaCl2 1.8, HEPES-NaOH 5, D-Glucose 5.5; pH was set to 7.35 with NaOH. The intracellular solutions for I_{Ks} recordings contained (mM): K-Aspartate 110, KCl 23, $MgCl_2$ 3, EGTA-KOH 5, HEPES-KOH 5, Guanosine-5'-triphosphate disodium salt 0.4, Adenosine-5'-triphosphate disodium salt 5, Phosphatidylcholine sodium salt 5, and $CaCl_2$ 2. Currents were evoked from a holding potential of -40 mV, with depolarizing voltage steps of 4000 ms every 10 mV up to +60 mV, followed by 8000 ms at -40 mV. I_{Ks} was isolated as 1 µM HMR-1556 (Selleckchem) sensitive current, in the presence of 1 µM of the I_{Kr} blocker E4031 dihydrochloride (Selleckchem) and 1 µM of the L-type calcium channel blocker nifedipine (Merck). pClamp 10.4 was used to record the traces and Clampfit 10 was used for the analyses.

3.4.6. MultiElectrode Arrays

Multiwell MEAs (24 wells, MultiChannel Systems) were coated with 40 µg/mL bovine fibronectin (Merck) for 1h at 37 °C and processed as previously described described [52, 53]. Expanded hiPSC-CMs were dissociated with TrypLE Select Enzyme 10X (Gibco) and plated on the electrodes of Multiwell MEAs at a density of $5 * 10^4$ hiPSC-CMs per well in small drops. RBK medium supplemented with Revitacell (Gibco) was used for plating. The next day, and thereafter twice a week, half of the medium was refreshed with

RBK medium. After two weeks, baseline recordings were performed followed by acute drug treatment and cumulative concentration-response measurements.

3.4.7. Drug testing

The drug testing protocol included the following steps: 1) recording of baseline Field Potentials (FP), 2) addition of vehicle (RBK) medium to mimic temperature and mechanical impact of drug addiction 3) addition of cumulative doses of compounds. All the recordings simulated acute drug exposure and consisted in 1 minute of wash-in followed by two minutes of recording. The following drugs were tested: chlorpromazine hydrochloride (Selleckchem), ciprofloxacin hydrochloride hydrate (Selleckchem), clarithromycin (Selleckchem), dofetilide (Selleckchem), E4031 dihydrochloride (Selleckchem), haloperidol (Selleckchem), HMR-1556 (Selleckchem), moxifloxacin (Selleckchem), nifedipine (Merck), salbutamol sulfate (Selleckchem), tetrodotoxin citrate (Tocris).

Pro-arrhythmic compound selection

The selection of pro-arrhythmic compounds was performed using the CredibleMeds® QT prolonging drugs database 45 intersected with OpenFDA database (https://open.fda.gov/). Open FDA data were used to prioritize compounds based on their occurrence in the FDA Adverse Event Reporting System. The following query terms were utilized to extract the top 100 compounds from the OpenFDA database: "Cardiac failure", "Torsade de pointes", "Electrocardiogram QT prolonged", "Cardiac arrest", "Ventricular extrasystoles", "Ventricular arrhythmia". The common compounds between databases were 46 (Table 3). We excluded compounds that were unlikely to provide pro-arrhythmic effects in a pure culture of hiPSC-CMs (such as diuretics or drugs associated with chronic cardiotoxicity) as beyond the scope of this study. Seven drugs were then selected in the highest-risk category, i.e. those contraindicated in congenital LQTS and are known to pose a significant risk for developing drug-induced Torsades de Pointes (TdP). Detailed information on the compounds is provided in Table 3.

Compound	**Drug class**	**Therapeutic use**	**IC50 HERG**	**Cmax**	**Tested concentration range**	**Stock concentration**	**Vehicle**
Chlorpromazine	Antipsychotic, antiemetic	Schizophrenia, bipolar disorder, acute psychosis	21.6 µM [54]	0.0345 µM [31]	0.03 - 3 µM	100 mM	DMSO
Ciprofloxacin	Antibiotic	Bacterial infection	966 µM [55]	8.87 µM	3 - 30 µM	15 mM	DMSO

Clarithromycin	Antibiotic	Bacterial infection	45.7 µM [56]	1.206 µM [31]	1 - 10 µM	6 mM	DMSO
Dofetilide	Antiarrhythmic	Arrhythmia	0.007 µM [57]	0.0023 µM [31]	1 - 100 nM	50 mM	DMSO
E4031	Selective I_{Kr} blocker	-	0.0077 µM [58]	-	10 - 500 nM	10 mM	Water
Haloperidol	Antipsychotic	Schizophrenia, agitation	1 µM [59]	0.079 µM [60]	0.3 - 10 µM	150 mM	DMSO
HMR1556	Selective I_{Ks} blocker	-	-	-	0.3 - 10 µM	10 mM	DMSO
Moxifloxacin	Antibiotic	Bacterial infection	41.2 µM [61]	11.7 µM [62, 63]	1 - 100 µM	100 mM	DMSO
Nifedipine	Selective I_{CaL} blocker	Angina, high blood pressure	-	0.0077 µM [31]	0.03 - 2 µM	10 mM	Ethanol, 100%
Salbutamol (albuterol)	Bronchodilator	Asthma	-	0.059 µM [63]	0.003 - 0.3 µM	100 mM	Water
Tetrodotoxin	Selective I_{Na} blocker	-	-	-	0.1 - 30 µM	3.13 mM	Water

Table 3. Ion channel blockers and pro-arrhythmic compounds used in the study.

3.4.8. Field Potential analysis

MEA recordings were analyzed using Multiwell-Analyzer v2.0.6.0 (Multichannel Systems) and the following parameters were extracted: field potential duration (FPD), beat-to-beat interval (RR), peak-to-peak amplitude (PtPA), mean slope of depolarization (Mean slope), RR interval coefficient of variation (RRCV). The analysis of FPs was performed as previously described [52] and automated through custom R scripts (R v4.3.1). FPD was corrected for beating frequency (cFPD) using Bazett's formula.

Field Potential quality assessment

The quality of the FP was assessed with a scoring system as previously described [53] and then further stratified to four categories based on the beating patterns: normal beating (scores 3-5), irregular beating (score 2), arrhythmic beating (score 1), and quiescence (score 0). This was implemented with the rationale of separating drug effects on the quantitative properties of the FP (e.g. a FP prolongation) from the potential detrimental effects of the drug treatment on FP quality as no FPD was measured from recordings scored as 1 and 0.

3.4.9. Data Analysis and Statistics

RStudio (version 2023.09.1) and R (version 4.3.1) were used for data analysis. Multiple group comparisons were conducted using the Kruskal-Wallis test, followed by Dunn's test with Benjamini-Hochberg correction. Pairwise comparisons were performed using the Wilcoxon test. Categorical variable comparisons were assessed with Fisher's exact test. A statistical significance level of $p \leq 0.05$ was used for all tests. Figures denote significance as $*p \leq 0.05$, $**p \leq 0.01$, and $***p \leq 0.001$, while exact p-values are reported in text and tables. Numerical data are reported as mean ± standard error of the mean (SEM), and plots display mean ± SEM, combined with scattered individual data points when relevant. Categorical data are presented as bar plots.

3.5. Results

3.5.1. Patient cohort characteristics

The study included ten patients, whose clinical features are summarized in Table 1. The study cohort comprised a LQT1 family trio (Figure 3), which includes an asymptomatic mother carrying the KCNQ1 p.R190W variant, an asymptomatic father carrying the KCNQ1 p.R594Q variant. and their daughter affected by Jervell and Lange-Nielsen syndrome (JLNS) [64] carrying both variants in compound heterozygosity [65]. Four additional patients belonged to a large South African family carrying the KCNQ1 p.A341V variant associated with a very severe LQT1 phenotype [42, 66, 67]; two of these patients were asymptomatic while the other two were severely symptomatic, carrying polymorphisms in the modifier gene NOS1AP (one patient in heterozygous and one patient in homozygous state) associated with a prolonged QT interval and with an increased risk of life threatening events [68]. Among the LQT2 cases, two patients carried the KCNH2 p.R366X variant: one symptomatic and one asymptomatic. Both were treated with beta-blockers. The symptomatic patient also underwent left cardiac sympathetic denervation due to difficulties in optimizing betablocker therapy because of asthenia. No recurrence of symptoms was observed on therapy. A third symptomatic LQT2 patient, carrying the de novo KCNH2 p.A561V variant, experienced cardiac arrests and was treated with beta-blockers and an ICD implantation.

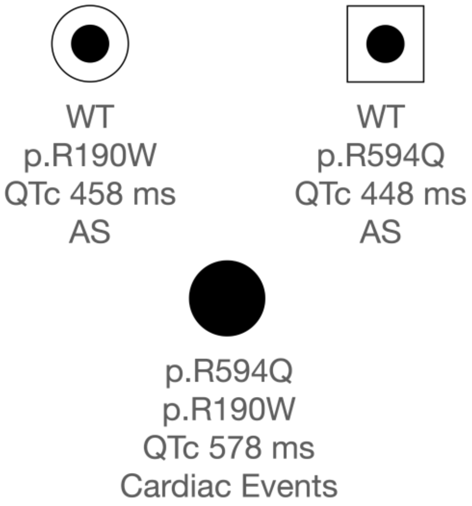

Figure 3. Trio carrying genetic variants KCNQ1 p.R190W and KCNQ1 p.R594Q.

3.5.2. Genetic variant risk level assignment

To establish a threshold for categorizing variants associated with different risks of cardiac events (Low Risk vs High Risk) we analyzed the frequency distribution of cardiac events across reported P/LP genetic variants in *KCNQ1* and *KCNH2* genes (the dataset included 1099 patients carrying 162 variants in *KCNQ1* and 623 patients carrying 175 variants in *KCNH2*) (Figure 4, A). In both genes, the distribution showed two distinct peaks: one at 0% (variants with no documented cardiac events) and another at ≥25% frequency (variants where at least 25% of carriers experienced cardiac events). Based on this analysis, a threshold of 25% was selected to differentiate these populations. Using this threshold, the variants in our study were categorized as follows: High Risk (*KCNQ1* p.R594Q and *KCNQ1* p.R190W & p.R594Q, *KCNQ1* p.A341V, and *KCNH2* p.A561V) and Low Risk (WT, *KCNQ1* p.R190W, and *KCNH2* p.R366X) (Figure 4, B).

Consistent with the incidence of cardiac events, carriers of the High Risk variants *KCNQ1 p.A341V* and *KCNH2 p.A561V* had significantly longer QTc values compared to carriers of the Low risk variants *KCNQ1* p.R190W and *KCNQ1* p.R366X respectively (Figure 4, C, Table 4). In addition, *KCNQ1 p.A341V* carriers had higher Schwartz scores than those with *KCNQ1 p.R190W KCNQ1 p.A341V* (Figure 4C, Table 4). Notably, the *KCNQ1* p.R190W & p.R594Q variant, observed in a single carrier, presented with deafness and exhibited markedly prolonged QTc (578 ms) and elevated Schwartz score (7.5), consistent with the severe JLNS phenotype.

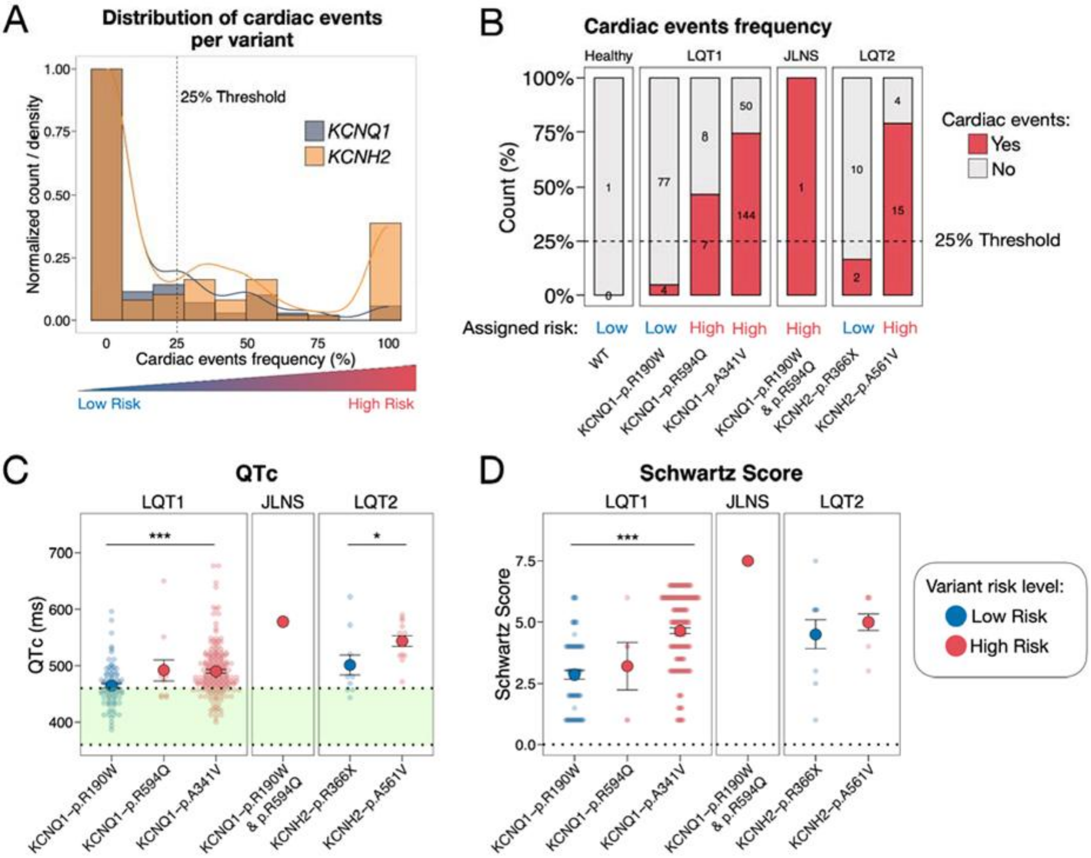

Figure 4. Clinical parameters and variant risk level assignment. A. Frequency of cardiac events across pathogenic/likely pathogenic genetic variants in KCNQ1 (blue) and KCNH2 (orange) genes. B. Percentage of patients with cardiac events for each variant, with assigned variant risk level indicated. C, D. Baseline QTc and Schwartz score values for each variant (N=1–183).

Variant	N	QTc (ms)	Schwartz Score
KCNQ1-p.R190W	102	464.7 ± 38	2.9 ± 1.5
KCNQ1-p.R594Q	16	491.9 ± 61.3	3.2 ± 2.2
KCNQ1-p.R190W & p.R594Q	1	578	7.5
KCNQ1-p.A341V	183	489.9 ± 45.8	4.7 ± 1.6
KCNH2-p.R366X	12	501.2 ± 56.9	4.5 ± 1.9
KCNH2-p.A561V	13	543.4 ± 34.6	5.0 ± 1.0

Table 4. Mean patients' QTc values and mean Schwartz scores for each genetic variant included in the study. Data is presented as mean ± standard deviation. N indicates the number of patients included in the analysis.

3.5.3. In vitro characterization of genetic variants selected for the study

Four of the six variants had previously been functionally characterized in the literature KCNQ1 p.R594Q, KCNQ1 p.A341V, KCNH2 p.R366X, and KCNH2 p.A561V, all resulting in loss of function, with KCNQ1 p.R594Q and KCNH2 p.A561V additionally exhibiting trafficking defects (Table 5). To complement these data, we provided a functional characterization of hiPSC-CMs derived from a family trio carrying KCNQ1 p.R190W, KCNQ1 p.R594Q, and the compound heterozygous KCNQ1 p.R190W & p.R594Q variants (Figure 3).

We observed the repolarization prolongation at single-cell level (APD90) and a reduced ability to follow high-frequency pacing in isolated hiPSC-CMs carrying KCNQ1 p.R190W, KCNQ1 p.R594Q, and KCNQ1 p.R190W & p.R594Q compared to WT (Figure 5 A, B; Figure 6, A, B). In addition, hiPSC-CM monolayers harboring KCNQ1 p.R594Q and KCNQ1 p.R190W & p.R594Q exhibited a significant prolongation of corrected FPD relative to WT (422.2 ± 126.7 ms and 424.9 ± 78.7 ms vs. 281.8 ± 77.4 ms, respectively; $p \leq 0.001$) (Figure 5C). Patch-clamp recordings of IKs revealed reduced end-step and tail current densities in hiPSC-CMs carrying KCNQ1 p.R190W, and an almost complete absence of IKs in those carrying KCNQ1 p.R594Q and KCNQ1 p.R190W & p.R594Q, consistent with the observed APD prolongation (Figure 5D–F).

Genetic variant	**Disease**	**dbSNP record**	**ClinVar classification**	**Functional characterization**	**Reference**
KCNQ1 p.R190W	LQT1	rs199473662	Likely pathogenic	This paper	
KCNQ1 p.R594Q	LQT1	rs199472815	Likely pathogenic	loss of function, trafficking defect	[27]
KCNQ1 p.A341V	LQT1	rs12720459	Pathogenic	loss of function	[28–30]
KCNQ1 p.R190W & *KCNQ1* p.R594Q	JLNS	rs199473662, rs199472815	-	This paper	
KCNH2 p.R366X	LQT2	rs794728364	Pathogenic	FPD prolongation (iPSC-CMs)	[8]
KCNH2 p.A561V	LQT2	rs121912504	Pathogenic/Likely pathogenic	loss of function, trafficking defect	[14, 31–34]

Table 5. Genetic variants selected for the study and their functional characterisation status.

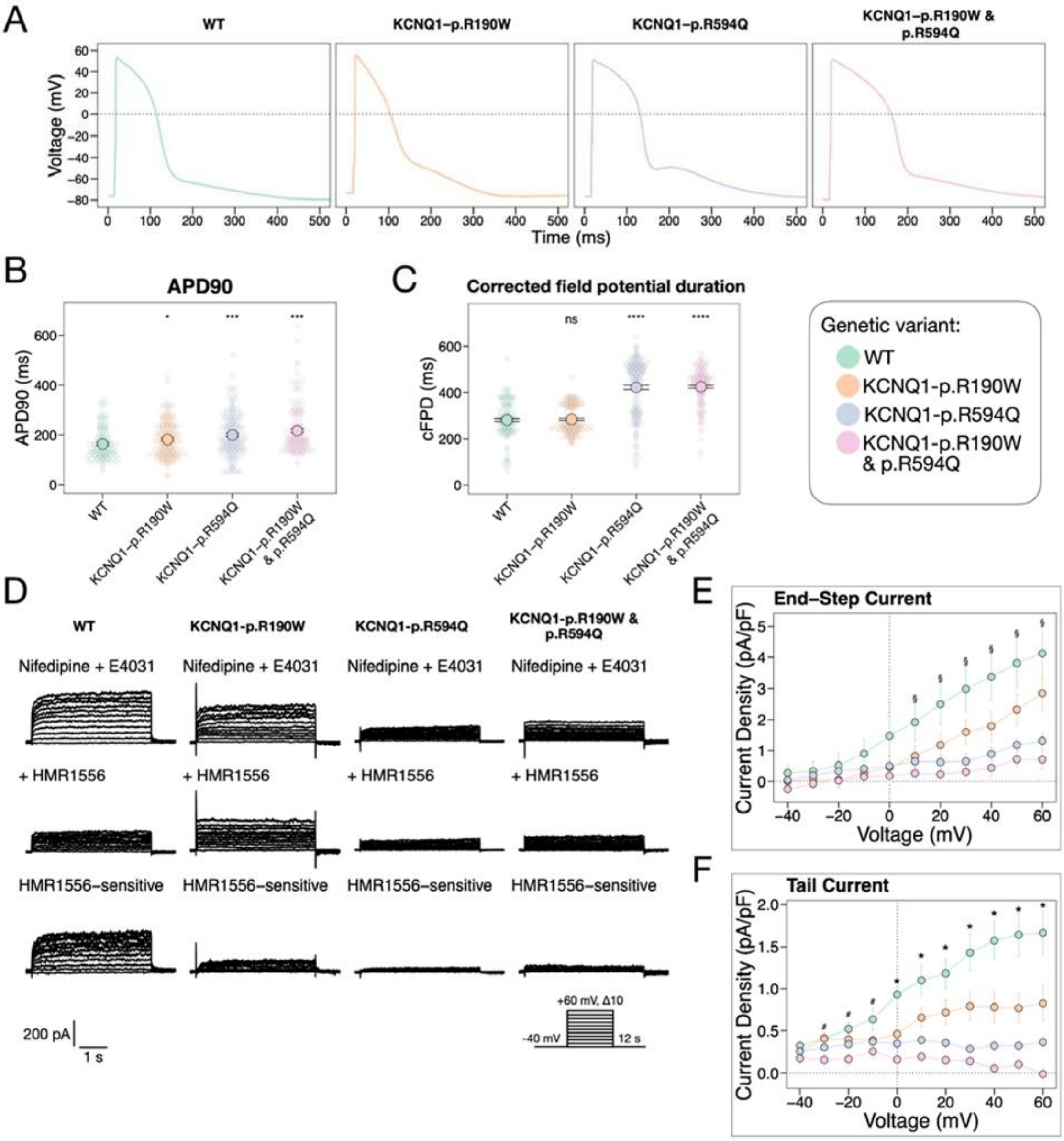

Figure 5. Characterization of hiPSC-CMs carrying genetic variants KCNQ1 p.R190W and KCNQ1 p.R594Q.

A. Representative action potential traces for each hiPSC-CM variant, elicited at 1 Hz stimulation. **B.** Action potential duration at 90% repolarization (APD90)**. C.** Corrected field potential duration (cFPD) measurements in hiPSC-CMs for each variant (N = 157–180). **D.** Representative IKs current traces (lower panel), obtained by subtracting HMR1556-insensitive current (middle panel) from the total inward potassium current recording (upper panel). **E, F** End- step and tail IKs current-voltage (I-V) relationships. * denotes $p < 0.05$ for all groups vs WT, # for WT vs KCNQ1 p.R190W & p.R594Q, § for WT vs KCNQ1 p.R594Q and vs KCNQ1 p.R190W & p.R594Q.

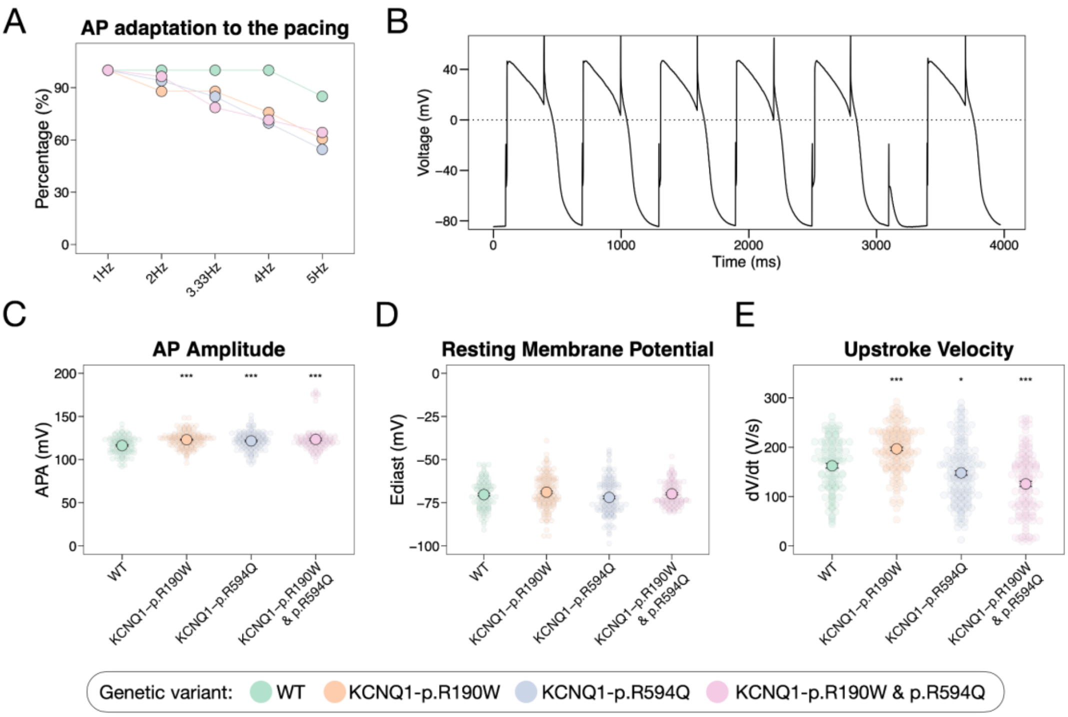

Figure 6. Characterization of hiPSC-CMs derived from family trio carrying genetic variants KCNQ1 p.R190W and KCNQ1 p.R594Q

Color defines hiPSC-CMs carrying different genetic variants - green: wild type (WT), orange: KCNQ1 p.R190W, blue: KCNQ1 p.R594Q, and pink: KCNQ1 p.R190W & p.R594Q. A. Percentage of hiPSC-CMs adapted to the increasing frequency pacing rate. B. Example of AP recording from hiPSC-CM carrying KCNQ1 p.R190W & p.R594Q genetic variants not able to follow the 3 Hz pacing. C. hiPSC-CM action potential amplitude (APA). D. hiPSC-CM resting membrane potential. E. hiPSC-CM upstroke velocity.

3.5.4. Baseline electrophysiology of hiPSC-CM cohort

Baseline MEA recordings recapitulated the variant-associated risk stratification. High Risk hiPSC-CMs showed prolonged FPD, corrected FPD (cFPD), and RR interval duration (Figure 7, A-D; Table 6) in comparison to wild type hiPSC-CMs from the Low Risk group. The propensity for irregular beating patterns at baseline was significantly higher in the High Risk group (20.2% of wells in High Risk group vs 8.7% in Low Risk group, $p \leq 0.001$) (Figure 7, E).

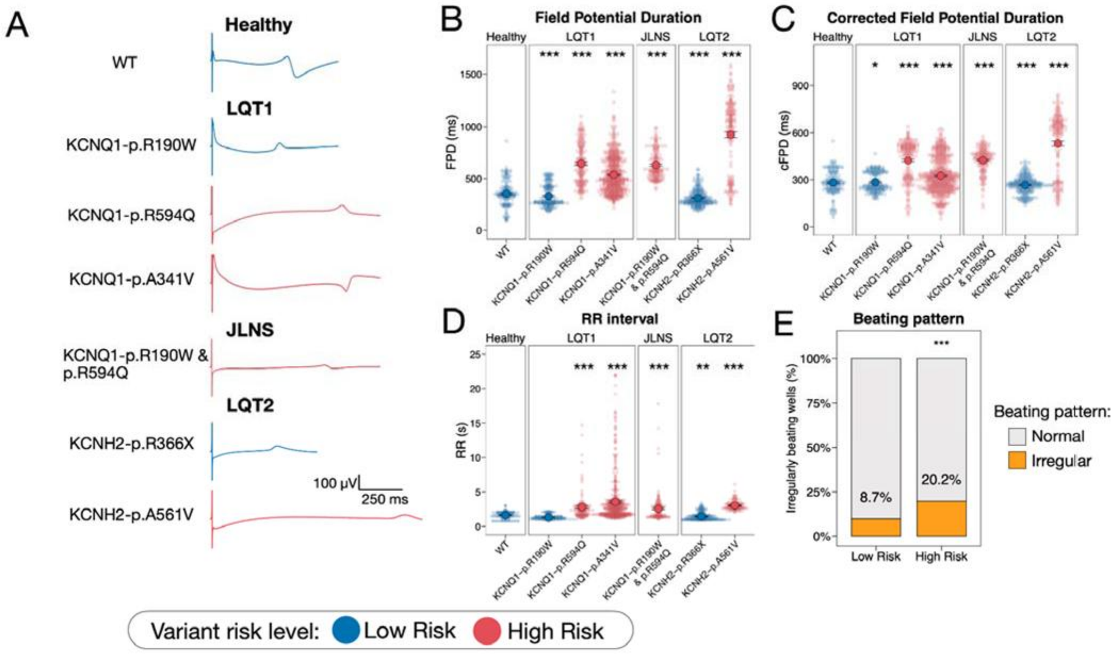

Figure 7. Baseline electrophysiology of hiPSC-CMs carrying High Risk and Low Risk genetic variants. **A.** Representative field potentials obtained for each variant. B-D. Baseline field potential duration (FPD), corrected FPD (cFPD), and beat-to-beat interval (RR) measurements of hiPSC- CMs for each variant; asterisks indicate statistical significance with the WT group. N = 154-547. E. Incidence of regular (gray) or irregular (yellow) beating patterns for hiPSC-CMs carrying Low Risk and High Risk variants (N = 589-1038).

Variant	**N**	**FPD, ms**	**cFPD, ms**	**RR, s**
WT	154	356 ± 120.3	281.8 ± 77.4	1.63 ± 0.49
KCNQ1-p.R190W	180	331.3 ± 104.9, $p = 0.07$	284.6 ± 60.6, $p = 0.69$	1.33 ± 0.34, $p \leq 0.001$
KCNQ1-p.R594Q	173	643.7 ± 190.2, $p \leq 0.001$	422.2 ± 126.7, $p \leq 0.001$	2.82 ± 2.6, $p \leq 0.001$
KCNQ1-p.A341V	547	536.9 ± 173.2, $p \leq 0.001$	325.1 ± 109.2, $p \leq 0.001$	3.57 ± 3.71, $p \leq 0.001$
KCNQ1-p.R190W & p.R594Q	157	629.8 ± 133, $p \leq 0.001$	424.9 ± 78.7, $p \leq 0.001$	2.56 ± 2.05, $p \leq 0.001$
KCNH2-p.R366X	255	311.4 ± 74.3, $p \leq 0.001$	265.9 ± 53.4, $p = 0.06$	1.45 ± 0.56, $p \leq 0.001$
KCNH2-p.A561V	161	923.1 ± 355.4, $p \leq 0.001$	531.1 ± 197.3, $p \leq 0.001$	3.04 ± 0.61, $p \leq 0.001$

Table 6. Baseline electrophysiological parameters obtained from MEA recording for each variant

3.5.5. HiPSC-CMs from High Risk and Low Risk groups demonstrate distinct drug responses to ion channel blockers

To further discriminate hiPSC-CMs carrying variants with different risk levels we obtained concentration-response curves for 11 selected drugs (Figure 8, 9; Table 7). Selective ion channel blockers E4031 (I_{Kr}, Kv11.1), HMR-1556 (I_{Ks}, Kv7.1), nifedipine (I_{CaL}, CaV 1.2), and tetrodotoxin (I_{Na}, Nav 1.5) were used to assess ion channel specific drug responses as previously proposed by multiple ion channel effects (MICE) approach for drug testing assays [69]. Since I_{Ks} blockers were previously reported to be more effective with reduced cardiac repolarization reserve caused by *KCNH2* genetic variants or I_{Kr} pharmacological block [70], we also tested the effect of HMR1556 on hiPSC-CMs pre-treated with 20 nM I_{Kr} blocker E4031.

Among pure ion channel blockers, we observed a differential response to the I_{Kr} blocker E4031 and to I_{Ks} blocker HMR1556 after E4031 pretreatment between hiPSC-CMs carrying High Risk and Low Risk variants. Specifically, hiPSC-CMs with High Risk variants showed a greater concentration-dependent prolongation of cFPD following treatment with E4031 (up to 350.0 ± 183.2% vs Vehicle for High Risk and up to 218.2 ± 69.9% vs Vehicle for Low Risk, $p \leq 0.001$). Furthermore, E4031 increased the RR interval duration in hiPSC-CMs carrying High Risk variants more than in those carrying Low Risk variants (Figure 8, A). The High Risk group also demonstrated a higher incidence of beating abnormalities at high concentrations of E4031 (Figure 8A). HMR1556 treatment alone resulted in a small cFPD prolongation that was similar between the High Risk and Low Risk groups (Figure 8B). In contrast the combination of E4031 pre-treatment followed by HMR1556 concentration-response led to a significant cFPD prolongation (up to 188.4 ± 40.6% vs. Vehicle for High Risk and up to 169.2 ± 26.4% vs. Vehicle for Low Risk, $p = 0.004$) (Figure 8C). Treatment with the I_{CaL} blocker nifedipine led to a cFPD and RR interval decrease (Figure 8D). High concentrations of the I_{Na} blocker tetrodotoxin (10 µM and 30 µM) led to a decrease in peak-to-peak amplitude and prolongation of the RR interval, along with an increased incidence of beating abnormalities (Figure 8E). The High-Risk group exhibited significantly more beating abnormalities at 10 µM of tetrodotoxin compared to the Low Risk group (73.6% vs. 46.9%, respectively; $p = 0.003$).

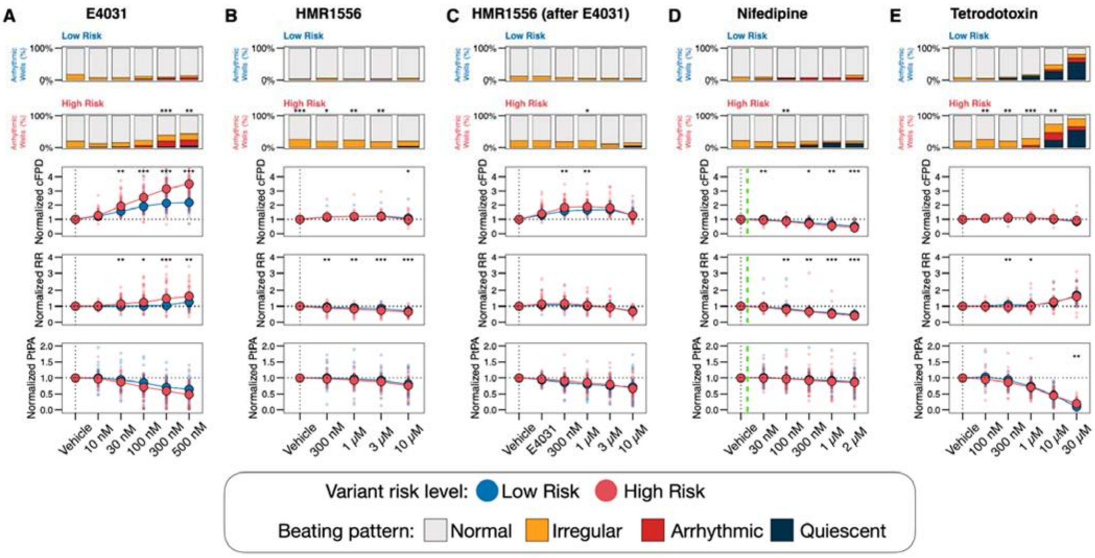

Figure 8: HiPSC-CMs from Low Risk and High-Risk groups exhibit differential responses to ion channel blockers. A-E: Concentration-dependent response curves to ion channel blockers E4031, HMR1556, HMR1556 following E4031 pre-treatment, nifedipine, and tetrodotoxin. Responses are shown for normalized corrected field potential duration (normalized cFPD), normalized RR interval (normalized RR), and normalized peak-to-peak amplitude (normalized PtPA). Bar plots illustrate the distribution of beating pattern abnormalities. Green dashed lines indicate reported Cmax values for each drug. Asterisks indicate statistical significance of comparisons between the High Risk and Low Risk groups. N = 19-80 per group per drug concentration.

Variant Risk Level	Drug	Dose	N	Normalized FPD (% of Vehicle)	Normalized cFPD (% of Vehicle)	Normalized RR (% of Vehicle)	Normalized PtPA (% of Vehicle)
Low Risk	Chlorpromazine	30 nM	32	108.7±7, p = 0.01	113.7 ± 16.2, p = 0.58	93.7 ± 13.8, p = 0.94	99.6 ± 15.5, p = 0.27
Low Risk	Chlorpromazine	100 nM	32	113.2±10.5, p = 0.01	122.9 ± 24.5, p = 0.78	88.6 ± 15.8, p = 0.26	98.2 ± 20.6, p = 0.17
Low Risk	Chlorpromazine	300 nM	32	116.4±12.2, p ≤ 0.001	129.6 ± 27.4, p = 0.06	84.5 ± 15.2, p = 0.1	97.8 ± 23.9, p = 0.68
Low Risk	Chlorpromazine	1 µM	32	118.5±13.2, p ≤ 0.001	134.6 ± 28.5, p = 0.005	80.9 ± 13.7, p = 0.01	92.7 ± 37.2, p = 0.52
Low Risk	Chlorpromazine	3 µM	32	117±18.6, p ≤ 0.001	138.1 ± 35.7, p ≤ 0.001	75.8 ± 14.7, p = 0.08	67.5 ± 34.5, p = 0.15
High Risk	Chlorpromazine	30 nM	67	105.8± 4.3, p = 0.01	108.9 ± 7.8, p = 0.58	95.4 ± 12, p = 0.94	101.5 ± 16.1, p = 0.27
High Risk	Chlorpromazine	100 nM	67	106.8 ±6.3, p = 0.01	114.9 ± 9.9, p = 0.78	87.9 ± 13.3, p = 0.26	101.7 ± 20.7, p = 0.17
High Risk	Chlorpromazine	300 nM	67	105.6 ± 8.6, p ≤ 0.001	117.7 ± 12.6, p = 0.06	82.7 ± 18.6, p = 0.1	97.1 ± 24, p = 0.68
High Risk	Chlorpromazine	3 µM	67	93.7 ± 17.6, p ≤ 0.001	112.9 ± 23, p ≤ 0.001	72.2 ± 27, p = 0.08	74.2 ± 29.1, p = 0.15
Low Risk	Ciprofloxacin	30 µM	56	95.3 ± 9.3, p ≤ 0.001	104.7 ± 9.4, p = 0.92	83.2 ± 8.9, p ≤ 0.001	106.8 ± 46.3, p = 0.68
High Risk	Ciprofloxacin	3 µM	104	106.6 ± 5.5, p = 0.59	110.1 ± 9.5, p = 0.01	95.3 ± 14.2, p = 0.003	98.2 ± 16.3, p = 0.14

High Risk	Ciprofloxacin	10 µM	104	108.8 ± 7.9, p = 0.28	113.5 ± 13.3, p = 0.54	94.3 ± 16.7, p = 0.14	98.1 ± 22.9, p = 0.28
High Risk	Ciprofloxacin	30 µM	104	90.2 ± 10.5, p ≤ 0.001	107.1 ± 16.7, p = 0.92	73.2 ± 14.5, p ≤ 0.001	103.3 ± 27.7, p = 0.68
Low Risk	Clarithromycin	1 µM	57	108.6 ± 4.7, p = 0.09	109.8 ± 6, p = 0.79	98.3 ± 8.7, p = 0.27	100.3 ± 14.3, p = 0.17
Low Risk	Clarithromycin	3 µM	57	113 ± 10, p = 0.09	120.1 ± 9.6, p = 0.99	89 ± 10.5, p = 0.27	96.8 ± 16.3, p = 0.02
Low Risk	Clarithromycin	10 µM	57	64.6 ± 27.4, p = 0.54	89.5 ± 28.2, p = 0.12	55.1 ± 22.8, p = 0.03	43.5 ± 44.8, p = 0.74
High Risk	Clarithromycin	1 µM	111	106.6 ± 6.3, p = 0.09	109.4 ± 7.3, p = 0.79	95.9 ± 12.8, p = 0.27	96.8 ± 9.3, p = 0.17
High Risk	Clarithromycin	3 µM	111	110.3 ± 11.4, p = 0.09	120.6 ± 15.8, p = 0.99	86.3 ± 19.4, p = 0.27	90.3 ± 14.6, p = 0.02
High Risk	Clarithromycin	10 µM	111	74.8 ± 79.5, p = 0.54	93.2 ± 78.8, p = 0.12	88.3 ± 136.7, p = 0.03	41.8 ± 36.1, p = 0.74
Low Risk	Dofetilide	1 nM	64	109.7 ± 3.2, p = 0.22	108.4 ± 4.1, p = 0.002	102.8 ± 7.1, p = 0.02	98.4 ± 12.1, p = 0.49
Low Risk	Dofetilide	3 nM	64	125.2 ± 8.3, p = 0.002	124.4 ± 8.8, p ≤ 0.001	101.8 ± 9.4, p = 0.04	95.9 ± 18, p = 0.97
Low Risk	Dofetilide	10 nM	64	158.9 ± 23.8, p ≤ 0.001	153.8 ± 20.8, p ≤ 0.001	107.5 ± 17.3, p = 0.73	88.4 ± 23.8, p = 0.09
Low Risk	Dofetilide	30 nM	64	201.3 ± 54.8, p ≤ 0.001	188.4 ± 38, p ≤ 0.001	114.6 ± 26.2, p = 0.24	81.5 ± 23, p = 0.005
Low Risk	Dofetilide	100 nM	64	224.3 ± 94.8, p ≤ 0.001	208.2 ± 61.4, p ≤ 0.001	134.9 ± 71.9, p = 0.4	65 ± 27.4, p = 0.03
High Risk	Dofetilide	1 nM	121	111.1 ± 7, p = 0.22	111.9 ± 9.9, p = 0.002	100.2 ± 16.3, p = 0.02	99.7 ± 8.8, p = 0.49
High Risk	Dofetilide	3 nM	121	133.2 ± 19.3, p = 0.002	135.4 ± 17.5, p ≤ 0.001	98.1 ± 18.3, p = 0.04	95.5 ± 15.6, p = 0.97
High Risk	Dofetilide	10 nM	121	202.4 ± 55.8, p ≤ 0.001	192.1 ± 45.3, p ≤ 0.001	128.2 ± 193.3, p = 0.73	84.3 ± 21.5, p = 0.09
High Risk	Dofetilide	30 nM	121	298.9 ± 114.8, p ≤ 0.001	269.6 ± 101.7, p ≤ 0.001	132.4 ± 80.5, p = 0.24	68.5 ± 30.6, p = 0.005
High Risk	Dofetilide	100 nM	121	374.1 ± 153.7, p ≤ 0.001	317.5 ± 128.5, p ≤ 0.001	156.4 ± 142.2, p = 0.4	54.6 ± 32.4, p = 0.03
Low Risk	E4031	10 nM	48	121.8 ± 16.6, p = 0.75	122.1 ± 14.8, p = 0.96	99.8 ± 10.4, p = 0.6	100.1 ± 24.1, p = 0.21
Low Risk	E4031	30 nM	48	156.7 ± 27.3, p ≤ 0.001	157.3 ± 26.8, p = 0.003	100.3 ± 15.2, p = 0.009	93.9 ± 32.7, p = 0.27
Low Risk	E4031	100 nM	48	192.8 ± 49.5, p ≤ 0.001	191.3 ± 47.9, p ≤ 0.001	102.3 ± 15.9, p = 0.01	85 ± 41.7, p = 0.07
Low Risk	E4031	300 nM	48	219 ± 66.2, p ≤ 0.001	213.7 ± 58.9, p ≤ 0.001	105.6 ± 21.8, p ≤ 0.001	70.8 ± 49.1, p = 0.25
Low Risk	E4031	500 nM	48	226.2 ± 70.7, p ≤ 0.001	218.2 ± 69.9, p ≤ 0.001	126 ± 143.4, p = 0.003	64.4 ± 51.7, p = 0.08
High Risk	E4031	10 nM	77	128.3 ± 35, p = 0.75	126.8 ± 28.4, p = 0.96	101.8 ± 13.8, p = 0.6	97 ± 12.6, p = 0.21
High Risk	E4031	30 nM	77	204 ± 80.4, p ≤ 0.001	192.5 ± 78.7, p = 0.003	114.2 ± 28.1, p = 0.009	87.5 ± 16.3, p = 0.27
High Risk	E4031	100 nM	77	290.4 ± 186.5, p ≤ 0.001	253.8 ± 129.3, p ≤ 0.001	124.4 ± 46.6, p = 0.01	71.1 ± 27.4, p = 0.07
High Risk	E4031	300 nM	77	374.1 ± 215.6, p ≤ 0.001	314 ± 166.4, p ≤ 0.001	148 ± 73, p ≤ 0.001	59.4 ± 25, p = 0.25
High Risk	E4031	500 nM	73	413.6 ± 245.1, p ≤ 0.001	350 ± 183.2, p ≤ 0.001	162.6 ± 166.1, p = 0.003	48.3 ± 29.8, p = 0.08
Low Risk	Haloperidol	300 nM	57	139.4 ± 32.3, p ≤ 0.001	129.8 ± 27.1, p ≤ 0.001	115.6 ± 18.9, p = 0.06	93.4 ± 21.9, p = 0.21
Low Risk	Haloperidol	1 µM	57	204.7 ± 76.2, p ≤ 0.001	178.2 ± 50.6, p ≤ 0.001	132.4 ± 43.4, p = 0.007	69 ± 30, p = 0.72
Low Risk	Haloperidol	3 µM	57	200.1 ± 64, p ≤ 0.001	177.8 ± 40.1, p ≤ 0.001	126.7 ± 42.7, p = 0.05	49.5 ± 31.7, p = 0.86
Low Risk	Haloperidol	10 µM	57	163.8 ± 48.1, p = 0.003	150.5 ± 31.8, p ≤ 0.001	124.7 ± 62.1, p = 0.63	41.1 ± 29.8, p = 0.06

High Risk	Haloperidol	300 nM	118	203.4 ± 143.1, p ≤ 0.001	180.1 ± 109, p ≤ 0.001	123.5 ± 33.3, p = 0.06	91.8 ± 16.1, p = 0.21
High Risk	Haloperidol	1 µM	118	306.9 ± 180.3, p ≤ 0.001	253.1 ± 134, p ≤ 0.001	149.2 ± 65.7, p = 0.007	71.9 ± 26.1, p = 0.72
High Risk	Haloperidol	3 µM	118	287.2 ± 148.6, p ≤ 0.001	251 ± 125.2, p ≤ 0.001	139.8 ± 59.9, p = 0.05	47.4 ± 28.1, p = 0.86
High Risk	Haloperidol	10 µM	118	236.9 ± 169.1, p = 0.003	212.9 ± 126, p ≤ 0.001	144.6 ± 128.6, p = 0.63	32.4 ± 26.3, p = 0.06
Low Risk	HMR1556	300 nM	43	111.4 ± 5.8, p = 0.006	115 ± 14.1, p = 0.43	95.4 ± 10.8, p = 0.002	100.1 ± 24.5, p = 0.21
Low Risk	HMR1556	1 µM	43	112.9 ± 7.3, p ≤ 0.001	120.2 ± 15.5, p = 0.65	89.8 ± 10.7, p = 0.005	96.8 ± 26.9, p = 0.15
Low Risk	HMR1556	3 µM	43	112.9 ± 9.5, p ≤ 0.001	123.3 ± 18.6, p = 0.05	85.6 ± 12, p ≤ 0.001	92.3 ± 25.2, p = 0.17
Low Risk	HMR1556	10 µM	43	89.4 ± 19.7, p ≤ 0.001	107.3 ± 27.3, p = 0.04	70.8 ± 12.9, p ≤ 0.001	80.8 ± 43.9, p = 0.87
High Risk	HMR1556	300 nM	75	107.8 ± 7.6, p = 0.006	116.9 ± 17.5, p = 0.43	88.5 ± 18.6, p = 0.002	96.9 ± 11.8, p = 0.21
High Risk	HMR1556	1 µM	75	106.2 ± 8.1, p ≤ 0.001	120.1 ± 21.5, p = 0.65	82.1 ± 17.7, p = 0.005	92.7 ± 15.7, p = 0.15
High Risk	HMR1556	3 µM	75	99.4 ± 9.6, p ≤ 0.001	120 ± 25.1, p = 0.05	73.2 ± 18.9, p ≤ 0.001	88.1 ± 16.2, p = 0.17
High Risk	HMR1556	10 µM	72	74 ± 18.7, p ≤ 0.001	97.5 ± 26.2, p = 0.04	63.8 ± 46.5, p ≤ 0.001	75.9 ± 21.5, p = 0.87
Low Risk	HMR1556 (after E4031)	E4031 20 nM	46	135.3 ± 21.7, p = 0.84	131 ± 21.3, p = 0.83	108.3 ± 18.6, p = 0.91	94.1 ± 10.8, p = 0.07
Low Risk	HMR1556 (after E4031)	300 nM	46	163.1 ± 25.9, p ≤ 0.001	159 ± 23.2, p = 0.001	106.1 ± 15.6, p = 0.08	85.8 ± 18, p = 0.28
Low Risk	HMR1556 (after E4031)	1 µM	46	167.7 ± 29.2, p = 0.003	167.4 ± 26.5, p = 0.004	101.1 ± 15.1, p = 0.9	80 ± 21.1, p = 0.32
Low Risk	HMR1556 (after E4031)	3 µM	46	163.7 ± 26.3, p = 0.37	169.2 ± 26.4, p = 0.25	94.4 ± 12.8, p = 0.08	75.7 ± 21.3, p = 0.39
Low Risk	HMR1556 (after E4031)	10 µM	46	107.1 ± 21.4, p = 0.2	128.6 ± 26.6, p = 0.8	70.3 ± 11.2, p = 0.06	71.9 ± 34.3, p = 0.39
High Risk	HMR1556 (after E4031)	E4031 20 nM	73	151.1 ± 61.1, p = 0.84	140.2 ± 41, p = 0.83	114.5 ± 31.2, p = 0.91	96.7 ± 10.5, p = 0.07
High Risk	HMR1556 (after E4031)	300 nM	73	196.5 ± 53.4, p ≤ 0.001	183.2 ± 42.6, p = 0.001	116.4 ± 30.1, p = 0.08	90.8 ± 17.6, p = 0.28
High Risk	HMR1556 (after E4031)	1 µM	73	190.6 ± 43.8, p = 0.003	188.4 ± 40.6, p = 0.004	105.2 ± 28.7, p = 0.9	85.2 ± 18.4, p = 0.32
High Risk	HMR1556 (after E4031)	3 µM	73	169.5 ± 34.4, p = 0.37	180.2 ± 42.7, p = 0.25	92.8 ± 26.7, p = 0.08	79.6 ± 20.8, p = 0.39
High Risk	HMR1556 (after E4031)	10 µM	73	102.6 ± 29.4, p = 0.2	128.1 ± 35.9, p = 0.8	66.3 ± 18.4, p = 0.06	67.3 ± 22.1, p = 0.39
Low Risk	Moxifloxacin	1 µM	44	106.2 ± 4.8, p = 0.07	108.2 ± 7.9, p = 0.78	97.6 ± 11.8, p = 0.53	96.6 ± 18.7, p = 0.5
Low Risk	Moxifloxacin	3 µM	44	109.5 ± 8.3, p = 0.03	114.5 ± 15, p = 0.71	93.3 ± 12.8, p = 0.1	94.6 ± 16.5, p = 0.4
Low Risk	Moxifloxacin	10 µM	44	114 ± 10.4, p = 0.007	122 ± 22.4, p = 0.98	90.1 ± 13.1, p = 0.03	92.8 ± 16, p = 0.61
Low Risk	Moxifloxacin	30 µM	44	122.7 ± 12.5, p = 0.02	132 ± 27.2, p = 0.99	89.7 ± 13.7, p = 0.006	90.3 ± 14.8, p = 0.39
Low Risk	Moxifloxacin	100 µM	43	260.7 ± 72.3, p = 0.005	236.6 ± 73.8, p = 0.04	137.9 ± 60.2, p ≤ 0.001	24.2 ± 36.1, p = 0.05
High Risk	Moxifloxacin	1 µM	68	104.8 ± 4.9, p = 0.07	108.2 ± 9.2, p = 0.78	96 ± 18.6, p = 0.53	99 ± 8.9, p = 0.5
High Risk	Moxifloxacin	3 µM	68	106.5 ± 7.8, p = 0.03	114.8 ± 13.8, p = 0.71	88.7 ± 16.6, p = 0.1	98.1 ± 9, p = 0.4
High Risk	Moxifloxacin	10 µM	68	108.8 ± 11.1, p = 0.007	123.4 ± 26.5, p = 0.98	82.7 ± 19.3, p = 0.03	93.4 ± 10.4, p = 0.61
High Risk	Moxifloxacin	30 µM	68	116.6 ± 18, p = 0.02	134.3 ± 32.8, p = 0.99	80.5 ± 20, p = 0.006	88.1 ± 21.5, p = 0.39
High Risk	Moxifloxacin	100 µM	68	480.7 ± 277.4, p = 0.005	357.1 ± 199.6, p = 0.04	331.4 ± 452.4, p ≤ 0.001	21.8 ± 14.9, p = 0.05

Low Risk	Nifedipine	30 nM	49	97.3 ± 7.6, p = 0.02	99.8 ± 8.6, p = 0.006	95.8 ± 13.6, p = 0.29	101.5 ± 16.1, p = 0.62
Low Risk	Nifedipine	100 nM	49	81.7 ± 15.9, p = 0.07	89.6 ± 14.8, p = 0.17	86.7 ± 28.4, p = 0.008	97.8 ± 22.1, p = 1
Low Risk	Nifedipine	300 nM	49	64.7 ± 19.1, p = 0.01	77.2 ± 18.4, p = 0.02	68.9 ± 11.4, p = 0.01	94.5 ± 23.2, p = 0.73
Low Risk	Nifedipine	1 µM	49	50.5 ± 21, p = 0.003	64.8 ± 21.5, p = 0.007	58.3 ± 12.1, p ≤ 0.001	91.5 ± 23, p = 0.77
Low Risk	Nifedipine	2 µM	49	35.6 ± 16.1, p ≤ 0.001	50.9 ± 18.4, p ≤ 0.001	47.1 ± 11.4, p ≤ 0.001	87.6 ± 29, p = 0.81
High Risk	Nifedipine	30 nM	80	91.5 ± 17.1, p = 0.02	94.1 ± 13.8, p = 0.006	94.8 ± 23.7, p = 0.29	99.5 ± 16.9, p = 0.62
High Risk	Nifedipine	100 nM	80	75.2 ± 17.3, p = 0.07	85.4 ± 17.6, p = 0.17	78.5 ± 22.5, p = 0.008	97 ± 20.7, p = 1
High Risk	Nifedipine	300 nM	80	55.5 ± 19.4, p = 0.01	68.7 ± 20.5, p = 0.02	65.9 ± 30.9, p = 0.01	92.3 ± 22.6, p = 0.73
High Risk	Nifedipine	1 µM	80	39.4 ± 17.9, p = 0.003	54.1 ± 19.1, p = 0.007	52 ± 22.9, p ≤ 0.001	89 ± 24.8, p = 0.77
High Risk	Nifedipine	2 µM	76	26.2 ± 13.7, p ≤ 0.001	41.1 ± 19.2, p ≤ 0.001	39.2 ± 8, p ≤ 0.001	86 ± 24.9, p = 0.81
Low Risk	Salbutamol	3 nM	41	104.3 ± 4.9, p ≤ 0.001	107.6 ± 7.8, p = 0.7	94.4 ± 7.7, p ≤ 0.001	98.8 ± 14.5, p = 1
Low Risk	Salbutamol	10 nM	41	98.7 ± 9.6, p ≤ 0.001	108 ± 14.3, p = 0.73	84.6 ± 9, p ≤ 0.001	101.2 ± 16.7, p = 0.74
Low Risk	Salbutamol	30 nM	41	86.5 ± 11.5, p ≤ 0.001	101.9 ± 16.5, p = 0.62	73.3 ± 10, p ≤ 0.001	102.4 ± 22.3, p = 0.2
Low Risk	Salbutamol	100 nM	41	72.5 ± 10.4, p = 0.001	90.4 ± 14.1, p = 0.44	65.3 ± 9.4, p ≤ 0.001	102.7 ± 30.1, p = 0.33
Low Risk	Salbutamol	300 nM	41	68.7 ± 7.9, p ≤ 0.001	87.1 ± 13.1, p = 0.97	67.2 ± 40.6, p ≤ 0.001	99.6 ± 26.3, p = 0.21
High Risk	Salbutamol	3 nM	72	99.5 ± 8.9, p ≤ 0.001	109.2 ± 14.7, p = 0.7	85.4 ± 14.9, p ≤ 0.001	100.7 ± 14.3, p = 1
High Risk	Salbutamol	10 nM	72	91.6 ± 11.2, p ≤ 0.001	110.9 ± 21.5, p = 0.73	71.9 ± 16.5, p ≤ 0.001	103.1 ± 17.4, p = 0.74
High Risk	Salbutamol	30 nM	72	76.2 ± 16, p ≤ 0.001	102.7 ± 24.4, p = 0.62	57.6 ± 14.7, p ≤ 0.001	98.2 ± 20.5, p = 0.2
High Risk	Salbutamol	100 nM	72	62.9 ± 15.7, p = 0.001	92.6 ± 24.3, p = 0.44	48.3 ± 13.3, p ≤ 0.001	97.6 ± 26, p = 0.33
High Risk	Salbutamol	300 nM	72	56.5 ± 13.5, p ≤ 0.001	87.8 ± 20.9, p = 0.97	43.5 ± 12, p ≤ 0.001	94.4 ± 26.1, p = 0.21
Low Risk	Tetrodotoxin	100 nM	49	107.1 ± 4.9, p = 0.02	106.4 ± 5, p = 0.48	101.6 ± 7.4, p = 0.27	103.1 ± 41.9, p = 0.08
Low Risk	Tetrodotoxin	300 nM	49	110.3 ± 6.8, p = 0.05	108.7 ± 11.2, p = 0.44	108.6 ± 52.8, p = 0.002	93.6 ± 38, p = 0.2
Low Risk	Tetrodotoxin	1 µM	49	111.4 ± 7.6, p = 0.15	109.3 ± 8, p = 0.77	104.6 ± 13.5, p = 0.05	74.4 ± 30.6, p = 0.88
Low Risk	Tetrodotoxin	10 µM	49	109.7 ± 9.3, p = 0.84	101.2 ± 10.7, p = 0.59	121.2 ± 31.4, p = 0.3	45.9 ± 22.3, p = 0.98
Low Risk	Tetrodotoxin	30 µM	49	102 ± 7.8, p = 0.04	84.8 ± 10.3, p = 0.55	168.9 ± 87.5, p = 0.71	9.5 ± 8.8, p = 0.003
High Risk	Tetrodotoxin	100 nM	72	105 ± 4, p = 0.02	106.4 ± 7.8, p = 0.48	98.6 ± 13.9, p = 0.27	95.5 ± 18.3, p = 0.08
High Risk	Tetrodotoxin	300 nM	72	107.5 ± 7, p = 0.05	111.1 ± 10.9, p = 0.44	95.3 ± 16.4, p = 0.002	86.4 ± 19.8, p = 0.2
High Risk	Tetrodotoxin	1 µM	72	108.1 ± 8.5, p = 0.15	109.6 ± 13.2, p = 0.77	101.6 ± 28.8, p = 0.05	70.6 ± 20.3, p = 0.88
High Risk	Tetrodotoxin	10 µM	72	108.7 ± 9.3, p = 0.84	103.6 ± 18.6, p = 0.59	127.9 ± 92.6, p = 0.3	44.5 ± 19, p = 0.98
High Risk	Tetrodotoxin	30 µM	69	108.7 ± 12.2, p = 0.04	92 ± 27.1, p = 0.55	160.4 ± 60.5, p = 0.71	19.2 ± 13.5, p = 0.003

Table 7. Differential response of Low Risk and High Risk hiPSC-CMs to ion channel blockers and proarrhythmic drugs.

3.5.6. HiPSC-CMs carrying High Risk and Low Risk P/LP variants demonstrate distinct drug responses to proarrhythmic drugs

These included the β2-adrenergic receptor agonist albuterol (salbutamol); the antibiotics clarithromycin, ciprofloxacin, and moxifloxacin; the antipsychotic agents chlorpromazine and haloperidol; and the antiarrhythmic drug dofetilide. Among these, dofetilide, haloperidol, and salbutamol elicited distinct concentration–response relationships between the High Risk and Low Risk groups (Figure 9). Specifically, responses to the antibiotics clarithromycin and ciprofloxacin were similar between the two groups (Figure 9 A, C). At its highest tested concentration (10 μM), clarithromycin induced arrhythmias and led to cessation of beating (Figure 9A). Another antibiotic, moxifloxacin, demonstrated a similar effect, with notable toxicity at a concentration of 100 μM, expressed by cFPD and RR increases, a drop in peak-to-peak amplitude, arrhythmias, and cessation of beating similar for both groups (Figure 9F). Treatment of hiPSC-CMs with the antipsychotic drug chlorpromazine resulted in moderate cFPD prolongation that was similar between the two groups (Figure 9B). hiPSC-CMs carrying High Risk variants showed a concentration-dependent increase in cFPD following treatment with the dofetilide (up to 317.5 ± 128.5% vs. Vehicle for High Risk and up to 208.2 ± 61.4% vs. Vehicle for Low Risk, $p \leq 0.001$) (Figure 9D) and haloperidol (up to 253.1 ± 134.0% vs. Vehicle for High Risk and up to 178.2 ± 50.6% vs. Vehicle for Low Risk, $p \leq 0.001$) (Figure 9E). Salbutamol decreased the RR interval of hiPSC-CMs carrying High Risk variants to a greater extent compared to those carrying Low Risk variants (Figure 9G).

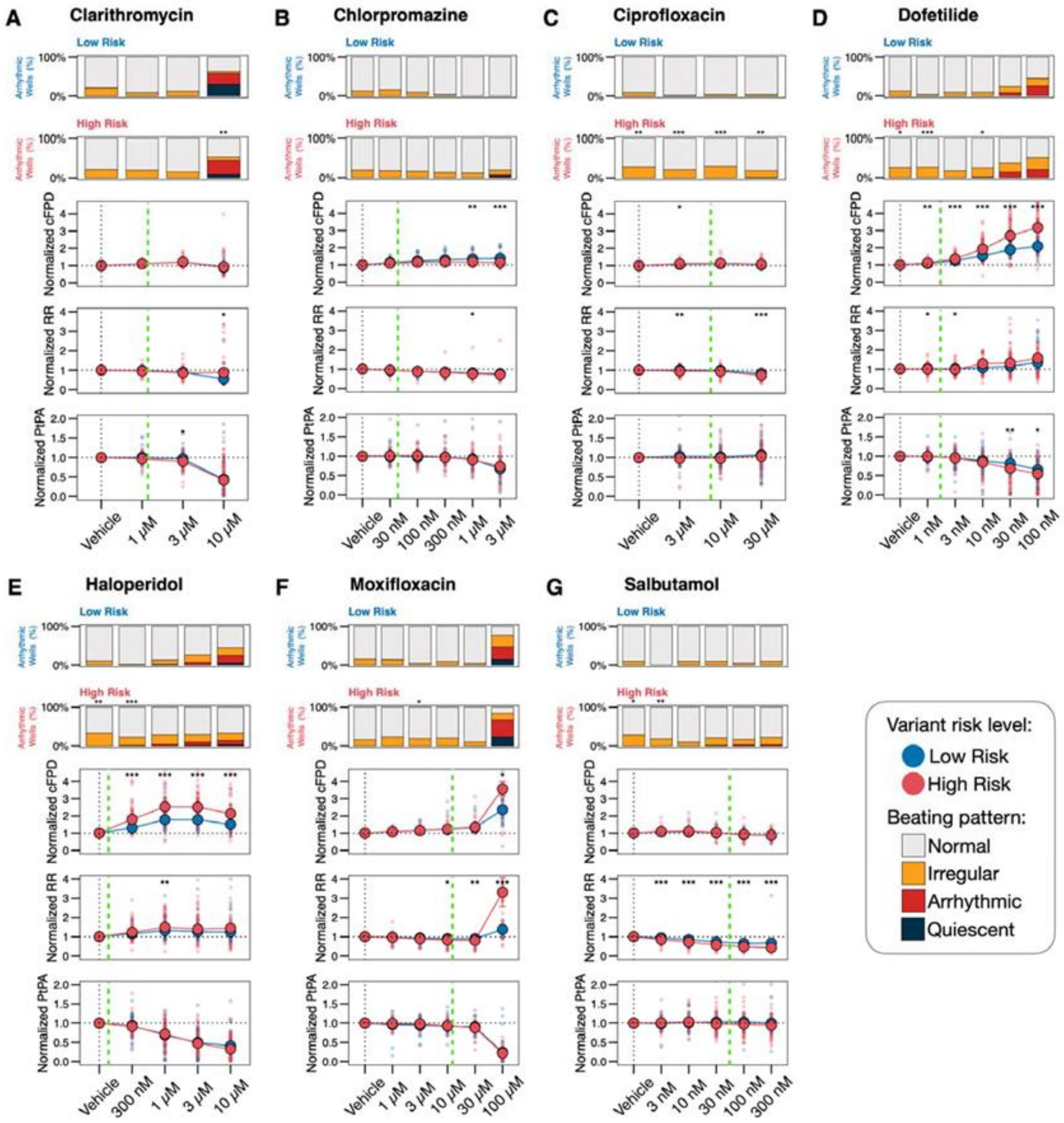

Figure 9. HiPSC-CMs from Low Risk and High Risk groups exhibit differential responses to proarrhythmic drugs. A-G: Concentration-dependent response curves for proarrhythmic drugs clarithromycin, chlorpromazine, ciprofloxacin, dofetilide, haloperidol, moxifloxacin, and salbutamol. Responses are presented for normalized corrected field potential duration (normalized cFPD), normalized RR interval (normalized RR), and normalized peak-to-peak amplitude (normalized PtPA). Bar plots illustrate the distribution of beating pattern abnormalities. Green dashed lines indicate reported Cmax values for each drug. Asterisks indicate statistical significance of comparisons between the High Risk and Low Risk groups. N = 26-121 per group per drug concentration.

3.5.7. Gene-specific drug response differences between in hiPSC-CMs carrying High Risk and Low Risk P/LP variants

To evaluate gene-specific drug responses, we compared the concentration-response curves between High and Low Risk P/LP variants, separating hiPSC-CMs with KCNQ1 variants (LQT1, JLNS) from those with KCNH2 variants (LQT2). We analyzed responses to I_{Kr} -blocking drugs - dofetilide, E4031, and haloperidol - which demonstrated the strongest discrimination between High Risk and Low Risk P/LP variants. Gene-specific features emerged in drug responses between hiPSC-CMs with High and Low Risk P/LP variants. High Risk hiPSC-CMs carrying KCNQ1 variants showed significant FPD prolongation upon drug treatment (Figure 10 A, C), while, in contrast, High Risk KCNH2 variant carriers demonstrated cFPD prolongation similar to the Low Risk KCNH2 group but exhibited a marked decrease in peak-to-peak amplitude and an increased incidence of abnormal beating patterns (Figure 10 D, F).

3.5.8. Machine learning model classifies P/LP variant risk from hiPSC-CM multielectrode array data

We curated a MEA dataset from eleven patient-specific hiPSC lines carrying seven variants, exposed to a panel of 11 drugs. The complete dataset comprises 10 410 data points and it was used to train a machine learning for classifying P/LP variant risk, in a proof-of-concept setting, based on in vitro drug responses in patient-specific hiPSC-CMs. To reduce prediction bias, we deliberately included all drug responses, even those from drugs that did not show apparent discrimination between High Risk and Low Risk variants according to concentration-response curves. The random forest model achieved a classification accuracy of 89% within the analyzed dataset and a high discriminative performance, with an area under the receiver operating characteristic (ROC) curve (AUC) of 96% (Figure 11, A). The model also showed the ability to distinguish between LQTS subtypes within the analyzed dataset, achieving a classification accuracy of 79% and an AUC of 94% (Figure11,B).

3.5.9. Machine learning validation supported model performance for predicting individual variant risk

To further explore the model's generalization performance and its ability to predict risk levels for novel variants, we performed leave-one-out cross-validation by sequentially excluding each variant from the training dataset and estimating its risk as if it were a novel variant. The model classified 6 out of 7 variants in agreement with the predefined risk categories, with one exception (*KCNH2* p.R366X), achieving an overall prediction accuracy of 72.6% (Figure 11, C).

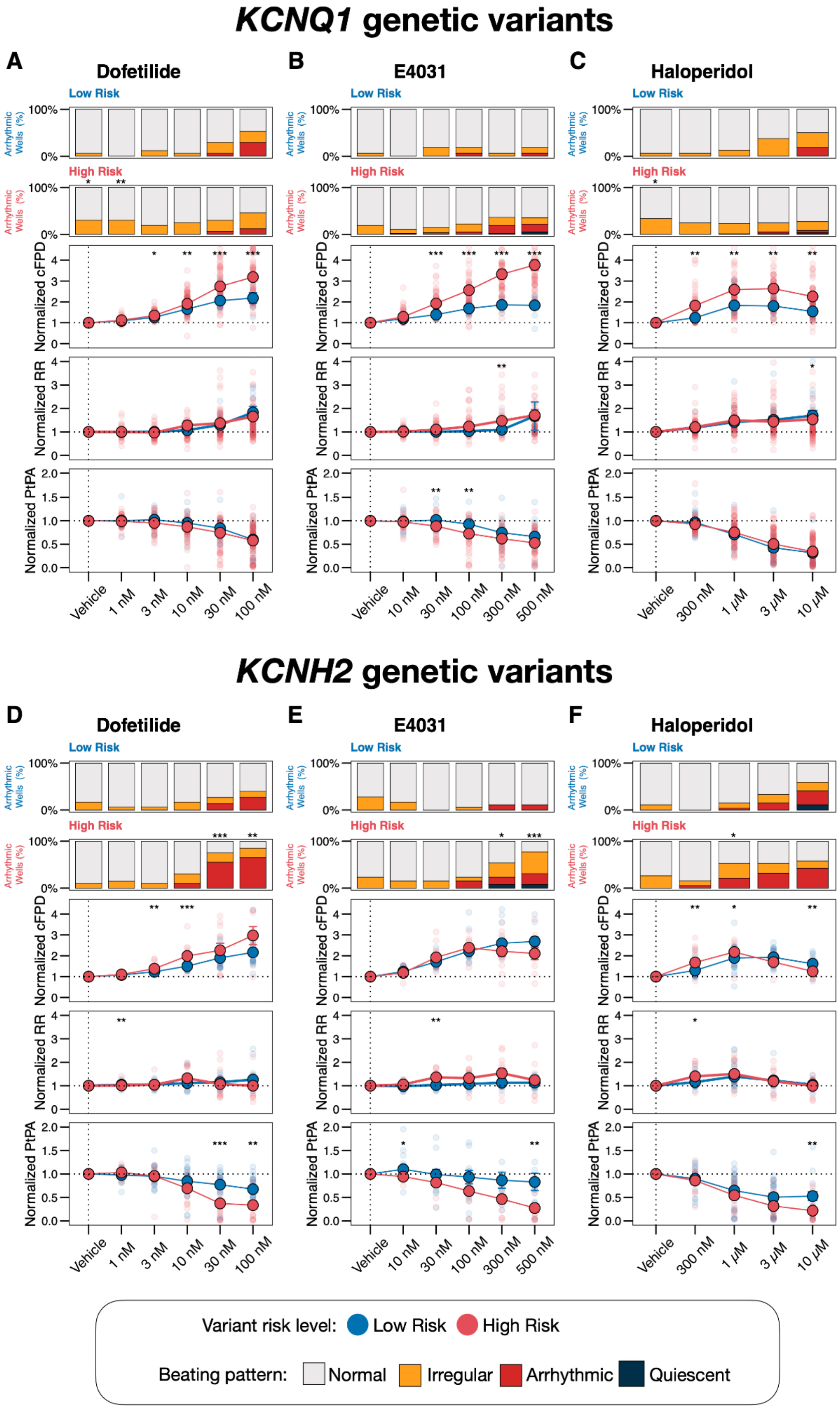
KCNQ1 genetic variants
A
Dofetilide
B
E4031
C
Haloperidol
Low Risk
High Risk
Arrhythmic Wells (%)
100%
0%
Normalized cFPD
Normalized RR
Normalized PtPA
Vehicle
1 nM
3 nM
10 nM
30 nM
100 nM
300 nM
500 nM
1 μM
3 μM
10 μM
KCNH2 genetic variants
D
Dofetilide
E
E4031
F
Haloperidol
Variant risk level: ● Low Risk ● High Risk
Beating pattern: ☐ Normal 🟧 Irregular 🟥 Arrhythmic ■ Quiescent

Figure 10. HiPSC-CMs carrying High Risk and Low Risk variants demonstrate gene-specific drug responses. A-F. Concentration-dependent response curves for dofetilide, E4031, and haloperidol on normalized corrected field potential duration (normalized cFPD), normalized RR interval (normalized RR), and normalized peak-to-peak amplitude (normalized PtPA). Bar plots illustrate the distribution of beating pattern abnormalities. Asterisks indicate statistical significance of comparisons between High Risk and Low Risk groups. N = 8-101 per group per drug concentration.

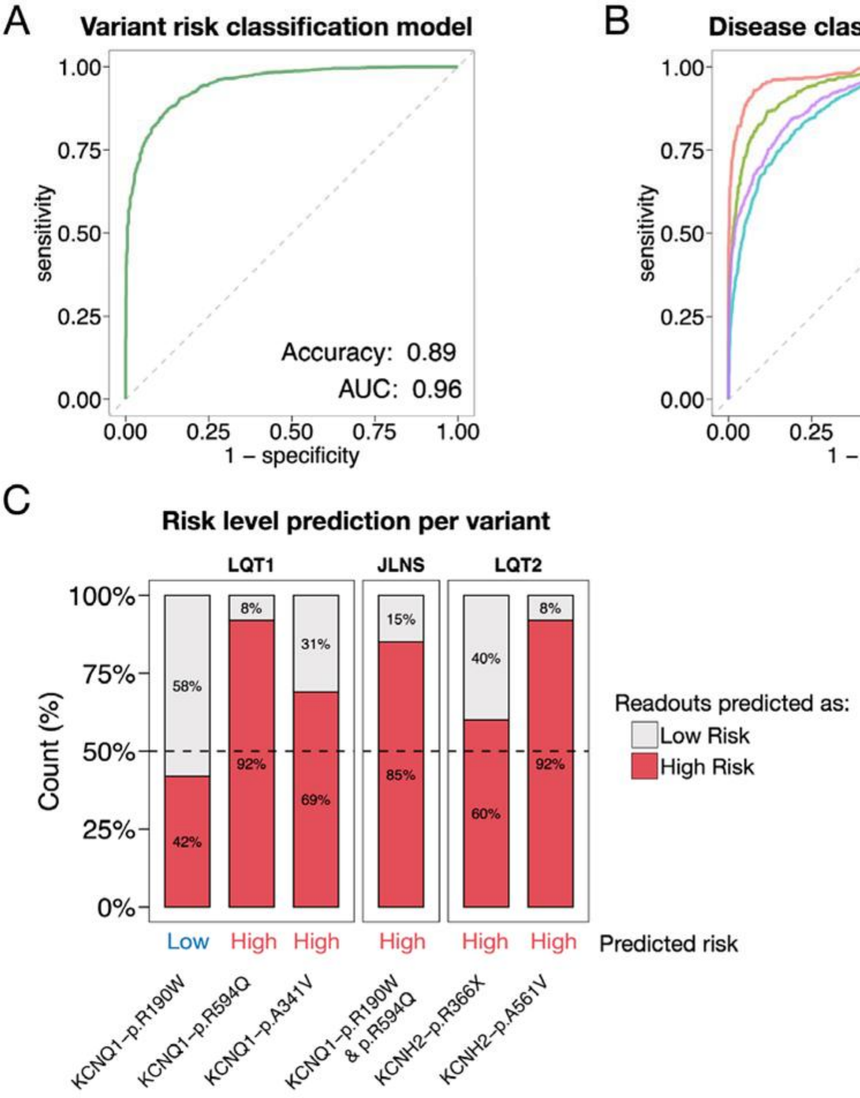

Figure 11. Variant risk levels and disease type prediction using MEA measurements and machine learning model. A. Receiver Operating Characteristic (ROC) curve illustrating the performance of a classification model for variant risk prediction. B. ROC curves representing the model's performance in predicting disease type. C. Model validation for single-variant risk level predictions. The proportion of readouts predicted as High Risk (red) and Low Risk (gray) is shown for each variant. The 50% threshold line delineates variants classified as High Risk (above) from those classified as Low Risk (below).

3.6. Discussion

Risk stratification for LQTS patients remains a significant clinical challenge, particularly for carriers of ultra-rare P/LP variants or for those identified in a single proband. These limitations impact our ability to identify patients who are at low or high risk of developing cardiac events that could potentially lead to SCD. Here, we developed and evaluated a proof-of-concept machine learning pipeline to explore whether in vitro electrophysiological readouts from patient-specific hiPSC-CMs can support P/LP variant risk classification. Our findings support prior evidence demonstrating that hiPSC-CMs can effectively recapitulate the clinical phenotype of LQTS [20–23]. This was particularly evident in hiPSC-CMs carrying severe genetic variants, such as compound heterozygous *KCNQ1* p.R190W & p.R594Q, *KCNQ1* p.A341V, and *KCNH2* p.A561V, where a clear prolongation of the repolarization duration was observed.

We further strengthened the dataset beyond baseline measurements by challenging each variant with ion channel blockers and pro-arrhythmic compounds, thus creating variant-specific drug response profiles not immediately obtainable in clinical practice. This is supported by previous research demonstrating excellent capacity of hiPSC-CMs to discriminate between high/low responders to an acute sotalol administration [71] or to tyrosine kinase inhibitors [72, 73]. To overcome the high baseline variability typical of hiPSC-CM measurements, often observed in cohort studies, we used relative readouts obtained from normalized drug responses to improve discrimination between disease phenotypes. Indeed, High Risk variants could be distinguished from their exacerbated response to certain pro-arrhythmic drug treatments, leading to more severe changes in FPD, cFPD, and RR intervals or to a higher occurrence of beating pattern abnormalities. The panel of pure ion channel blockers targeting four key ion channels responsible for action potential regulation revealed that pharmacological I_{Kr} blockade alone already provides effective variant risk discrimination. Conversely, treatment of hiPSC-CMs with the I_{Ks} blocker HMR1556 caused only minimal FPD prolongation [74, 75]. Reducing the repolarization reserve by pre-treating hiPSC-CMs with I_{Kr} blocker E4031 [70, 76] increased the sensitivity to HMR1556 and discriminated between High Risk and Low Risk groups. As expected, the I_{CaL} blocker nifedipine and the I_{Na} blocker tetrodotoxin were not effective in distinguishing High Risk from Low Risk groups within our LQT1 and LQT2 cohort, which is expected since no pathogenic variants were identified in genes encoding for calcium and sodium channel subunits. These blockers could be useful for identifying Ca^{2+} or Na^{+} handling abnormalities in other LQTS subtypes beyond LQT1 and LQT2, e.g. LQT3 or CALM-LQTS [77, 78].

Among the pro-arrhythmic drugs selected based on analyses of the OpenFDA and Credible Meds databases, acute treatment of hiPSC-CMs with the potent I_{Kr} blocker dofetilide and the antipsychotic drug haloperidol demonstrated clear concentration-dependent cFPD prolongation, consistently distinguishing between the High Risk and Low Risk groups. Acute treatment with salbutamol, a β2-adrenergic agonist commonly used as a bronchodilator and typically precluded to LQTS patients [79], differentially increased the spontaneous beating frequency in hiPSC-CMs; this allowed the discrimination of High Risk variants, which revealed a higher sensitivity, from Low Risk variants and could be influenced by a difference in beating frequencies at baseline between these two groups. No arrhythmic events were observed, supporting previous studies on commercially available hiPSC-CMs [80]. Treatment of hiPSC-CMs with ciprofloxacin, clarithromycin, and moxifloxacin within therapeutic concentration ranges resulted in moderate FPD prolongation as similarly emerged in commercially available wild-type hiPSC-CMs [31, 80]

There is limited information available on gene-specific drug responses in LQT1 and LQT2 both *in vivo* and *in vitro* [81–83]. In our study, three drugs with increased potency to block hERG (E4031, dofetilide, and haloperidol) well discriminated diseased hiPSC-CMs carrying High Risk variants in either *KCNQ1* or *KCNH2* genes. This observation aligns with findings from adult transgenic rabbit models, where LQT2 rabbits exhibited greater susceptibility to drug-induced TdP than LQT1 rabbits after administration of the anesthetic propofol, with a known hERG channel blocking effect [82]. These results are consistent with the concept of a severely compromised repolarization reserve in LQT2 cardiomyocytes, which renders them more vulnerable to proarrhythmic triggers [76].

Variant risk prediction based on multiparametric readouts is a novel and rapidly developing field. A recent study combined clinical data, trafficking assays and automated patch clamp data from heterologous expression systems, to score the risk of *KCNH2* variants associated with LQT2 [84]. The use of hiPSC-CMs provides enhanced precision by addressing the limitations of heterologous systems that lack cardiac-specific context. Based on our observations, hiPSC-CM drug responses allow discrimination between High Risk and Low Risk P/LP variants within the experimental setting of this study. We developed the ML model trained on *in vitro* hiPSC-CM electrophysiological readouts to retrospectively assess variant risk categories, a methodology that, to our knowledge, has not been previously applied to LQTS. While we deliberately chose known P/LP genetic variants with a loss-of-function mechanism for our study, the model may, in principle, be extended beyond retrospective analyses to support the functional assessment of ultra-rare variants and VUS. Importantly, the ML model trained for disease discrimination achieved a classification accuracy of 79% for LQTS subtype. This performance indicates that disease-specific electrophysiological features are distinct from variant classification features, providing evidence to expand the model incorporating other LQTS subtypes.

The application of the model to predict the risk level of single variants on which it was not originally trained provides an additional level of validation, supporting the potential applicability of our approach for assessing novel, previously unreported variants within the experimental framework of the study. The observed discrepancy in predicting the risk level for the *KCNH2* p.R366X variant underscores the impact of patient-specific drug responses. Although assigned as Low Risk due to a low cardiac event frequency (16.7%), two hiPSC-CM lines from different LQT2 patients exhibited divergent drug response patterns. One line, derived from a patient with no cardiac events, aligned with Low Risk variants, whereas the other, from a patient with documented cardiac events, markedly prolonged QTc (622 ms), and LSCD performed, with those of High Risk. This highlights the importance of separating the genetic background from the primary disease-causing variant, particularly for P/LP variants that fall within the intermediate range of the risk level distribution. Indeed, in the case of High Risk *KCNQ1 p.A341V* variant, despite differences in genetic background (such as NOS1AP genetic variants) the primary variant itself is so severe that the probability of misclassification is lower. Overall, these findings emphasize the necessity of integrating data from multiple sources for accurate variant risk classification, including multicentral *in vitro* data, clinical cohort records, structural variant pathogenicity predictions, and Bayesian penetrance estimates [37].

In conclusion, we developed a machine learning–based framework that integrates electrophysiological recordings from patient-specific hiPSC-CMs to support the functional stratification of P/LP variant risk in LQTS. This approach represents a preliminary contribution to the stratification of LQTS variant risk, complementing available clinical data and offering potential added value particularly for variants characterized by limited clinical information.

3.7. Study limitations

First, experiments were performed on hiPSC-CMs which, despite significant progress in maturation techniques, still exhibit an immature phenotype compared to adult cardiomyocytes [85, 86]. This immaturity could partially explain blunted or exacerbated drug responses for specific compounds.

Second, we focused on six LQTS-causing P/LP variants. While this demonstrates proof of concept for retrospective variant risk stratification, further investigations are necessary to extend this approach to a broader range of variants or LQTS subtypes.

Third, this study is limited by the relatively small and unbalanced dataset used to train and validate the machine learning classifier, particularly with respect to low-risk variants. Nevertheless, the observed classification performance supports the feasibility of the proposed approach and its interpretation as a functional proof of concept. Moreover, while the current model simplifies clinical risk into a binary classification, future developments could incorporate multiple risk categories to better capture intermediate disease phenotypes based on both qualitative and quantitative cardiac event profiles associated with each variant.

Funding Sources

This project has received funding from the Horizon Europe EU (HORIZON-MSCA-2022-PF-01 PREPARE No. 101105561 to AK), Horizon 2020 (H2020-MSCA-IF-2017 No. 795209 to LS), Fondazione CARIPLO grant No. 2019-1691 to LS, Leducq Foundation grant 18CVD05 to PJS. Italian Ministry of University and Research within Mission 4, “Education and Research”, Component 2, “From Research to Business”, Investment 1.2, “Funding projects presented by young researchers” of the National Recovery and Resilience Plan. Project No. 2022-NAZ-0485 (H45E22001210006) to LS.

3.8. *References*

1. Schwartz, P.J., Periti, M., Malliani, A.: The long Q-T syndrome. Am Heart J. 89, 378–390 (1975). https://doi.org/10.1016/0002-8703(75)90089-7.
2. Schwartz, P.J., Priori, S.G., Spazzolini, C., Moss, A.J., Vincent, G.M., Napolitano, C., Denjoy, I., Guicheney, P., Breithardt, G., Keating, M.T., Towbin, J.A., Beggs, A.H., Brink, P., Wilde, A.A.M., Toivonen, L., Zareba, W., Robinson, J.L., Timothy, K.W., Corfield, V., Wattanasirichaigoon, D., Corbett, C., Haverkamp, W., Schulze-Bahr, E., Lehmann, M.H., Schwartz, K., Coumel, P., Bloise, R.: Genotype-Phenotype Correlation in the Long-QT Syndrome. Circulation. 103, 89–95 (2001). https://doi.org/10.1161/01.CIR.103.1.89.
3. Behr, E.R., Roden, D.: Drug-induced arrhythmia: pharmacogenomic prescribing? Eur Heart J. 34, 89–95 (2013). https://doi.org/10.1093/eurheartj/ehs351.
4. Weeke, P.E., Kellemann, J.S., Jespersen, C.B., Theilade, J., Kanters, J.K., Hansen, M.S., Christiansen, M., Marstrand, P., Gislason, G.H., Torp-Pedersen, C., Bundgaard, H., Jensen, H.K., Tfelt-Hansen, J.: Long-term proarrhythmic pharmacotherapy among patients with congenital long QT syndrome and risk of arrhythmia and mortality. Eur Heart J. 40, 3110–3117 (2019). https://doi.org/10.1093/eurheartj/ehz228.
5. Zeppenfeld, K., Tfelt-Hansen, J., de Riva, M., Winkel, B.G., Behr, E.R., Blom, N.A., Charron, P., Corrado, D., Dagres, N., de Chillou, C., Eckardt, L., Friede, T., Haugaa, K.H., Hocini, M., Lambiase, P.D., Marijon, E., Merino, J.L., Peichl, P., Priori, S.G., Reichlin, T., Schulz-Menger, J., Sticherling, C., Tzeis, S., Verstrael, A., Volterrani, M., Cikes, M., Kirchhof, P., Abdelhamid, M., Aboyans, V., Arbelo, E., Arribas, F., Asteggiano, R., Basso, C., Bauer, A., Bertaglia, E., Biering-Sørensen, T., Blomström-Lundqvist, C., Borger, M.A., Čelutkienė, J., Cosyns, B., Falk, V., Fauchier, L., Gorenek, B., Halvorsen, S., Hatala, R., Heidbuchel, H., Kaab, S., Konradi, A., Koskinas, K.C., Kotecha, D., Landmesser, U., Lewis, B.S., Linhart, A., Løchen, M.L., Lund, L.H., Metzner, A., Mindham, R., Nielsen, J.C., Norekvål, T.M., Patten, M., Prescott, E., Rakisheva, A., Remme, C.A., Roca-Luque, I., Sarkozy, A., Scherr, D., Sitges, M., Touyz, R.M., Van Mieghem, N., Velagic, V., Viskin, S., Volders, P.G.A., Kichou, B., Martirosyan, M., Scherr, D., Aliyev, F., Willems, R., Naser, N., Shalganov, T., Milicic, D., Christophides, T.,

Kautzner, J., Hansen, J., Allam, L., Kampus, P., Junttila, J., Leclercq, C., Etsadashvili, K., Steven, D., Gatzoulis, K., Gellér, L., Arnar, D.O., Galvin, J., Haim, M., Pappone, C., Elezi, S., Kerimkulova, A., Kalejs, O., Rabah, A., Puodziukynas, A., Dimmer, C., Sammut, M.A., David, L., Boskovic, A., Moustaghfir, A., Maass, A.H., Poposka, L., Mjolstad, O.C., Mitkowski, P., Parreira, L., Cozma, D., Golukhova, E., Bini, R., Stojkovic, S., Hlivak, P., Pernat, A., Castellano, N.P., Platonov, P.G., Duru, F., Saadi, A.R. Al, Ouali, S., Demircan, S., Sychov, O., Slade, A.: 2022 ESC Guidelines for the management of patients with ventricular arrhythmias and the prevention of sudden cardiac death. Eur Heart J. 43, 3997–4126 (2022). https://doi.org/10.1093/eurheartj/ehac262.

6. Schwartz, P.J.: Cardiac sympathetic denervation to prevent life-threatening arrhythmias. Nat Rev Cardiol. 11, 346–353 (2014). https://doi.org/10.1038/nrcardio.2014.19.
7. Dusi, V., Pugliese, L., De Ferrari, G.M., Odero, A., Crotti, L., Dagradi, F., Castelletti, S., Vicentini, A., Rordorf, R., Li, C., Shkolnikova, M., Spazzolini, C., Schwartz, P.J.: Left Cardiac Sympathetic Denervation for Long QT Syndrome. JACC Clin Electrophysiol. 8, 281–294 (2022). https://doi.org/10.1016/j.jacep.2021.09.002.
8. Schwartz, P.J., Priori, S.G., Locati, E.H., Napolitano, C., Cantù, F., Towbin, J.A., Keating, M.T., Hammoude, H., Brown, A.M., Chen, L.-S.K., Colatsky, T.J.: Long QT Syndrome Patients With Mutations of the SCN5A and HERG Genes Have Differential Responses to Na + Channel Blockade and to Increases in Heart Rate. Circulation. 92, 3381–3386 (1995). https://doi.org/10.1161/01.CIR.92.12.3381.
9. Crotti, L., Neves, R., Dagradi, F., Musu, G., Giannetti, F., Bos, J.M., Barbieri, M., Cerea, P., Giovenzana, F.L.F., Torchio, M., Mura, M., Gnecchi, M., Conte, G., Auricchio, A., Sala, L., Odening, K.E., Ackerman, M.J., Schwartz, P.J.: Therapeutic Efficacy of Mexiletine for Long QT Syndrome Type 2: Evidence From Human Induced Pluripotent Stem Cell–Derived Cardiomyocytes, Transgenic Rabbits, and Patients. Circulation. 150, 531–543 (2024). https://doi.org/10.1161/CIRCULATIONAHA.124.068959.
10. Schwartz, P.J., Ackerman, M.J.: The long QT syndrome: a transatlantic clinical approach to diagnosis and therapy. Eur Heart J. 34, 3109–3116 (2013). https://doi.org/10.1093/eurheartj/eht089.

11. Schwartz, P.J., Ackerman, M.J., George, A.L., Wilde, A.A.M.: Impact of Genetics on the Clinical Management of Channelopathies. J Am Coll Cardiol. 62, 169–180 (2013). https://doi.org/10.1016/j.jacc.2013.04.044.

12. Giudicessi, J.R., Wilde, A.A.M., Ackerman, M.J.: The genetic architecture of long QT syndrome: A critical reappraisal. Trends Cardiovasc Med. 28, 453–464 (2018). https://doi.org/10.1016/j.tcm.2018.03.003.

13. Richards, S., Aziz, N., Bale, S., Bick, D., Das, S., Gastier-Foster, J., Grody, W.W., Hegde, M., Lyon, E., Spector, E., Voelkerding, K., Rehm, H.L.: Standards and guidelines for the interpretation of sequence variants: a joint consensus recommendation of the American College of Medical Genetics and Genomics and the Association for Molecular Pathology. Genetics in Medicine. 17, 405–424 (2015). https://doi.org/10.1038/gim.2015.30.

14. Aziz, P.F., Wieand, T.S., Ganley, J., Henderson, J., Patel, A.R., Iyer, V.R., Vogel, R.L., McBride, M., Vetter, V.L., Shah, M.J.: Genotype- and Mutation Site–Specific QT Adaptation During Exercise, Recovery, and Postural Changes in Children With Long-QT Syndrome. Circ Arrhythm Electrophysiol. 4, 867–873 (2011). https://doi.org/10.1161/CIRCEP.111.963330.

15. Schwartz, P.J., Moreno, C., Kotta, M.-C., Pedrazzini, M., Crotti, L., Dagradi, F., Castelletti, S., Haugaa, K.H., Denjoy, I., Shkolnikova, M.A., Brink, P.A., Heradien, M.J., Seyen, S.R.M., Spätjens, R.L.H.M.G., Spazzolini, C., Volders, P.G.A.: Mutation location and I Ks regulation in the arrhythmic risk of long QT syndrome type 1: the importance of the KCNQ1 S6 region. Eur Heart J. 42, 4743–4755 (2021). https://doi.org/10.1093/eurheartj/ehab582.

16. Ackerman, M.J.: Genetic purgatory and the cardiac channelopathies: Exposing the variants of uncertain/unknown significance issue. Heart Rhythm. 12, 2325–2331 (2015). https://doi.org/10.1016/j.hrthm.2015.07.002.

17. Gnecchi, M., Sala, L., Schwartz, P.J.: Precision Medicine and cardiac channelopathies: when dreams meet reality. Eur Heart J. 42, 1661–1675 (2021). https://doi.org/10.1093/eurheartj/ehab007.

18. Brnich, S.E., Abou Tayoun, A.N., Couch, F.J., Cutting, G.R., Greenblatt, M.S., Heinen, C.D., Kanavy, D.M., Luo, X., McNulty, S.M., Starita, L.M., Tavtigian, S. V., Wright, M.W., Harrison, S.M., Biesecker, L.G., Berg, J.S.: Recommendations for application of the functional evidence PS3/BS3 criterion using the

ACMG/AMP sequence variant interpretation framework. Genome Med. 12, 3 (2020). https://doi.org/10.1186/s13073-019-0690-2.

19. Lichou, F., Trynka, G.: Functional studies of GWAS variants are gaining momentum. Nat Commun. 11, 6283 (2020). https://doi.org/10.1038/s41467-020-20188-y.

20. Moretti, A., Bellin, M., Welling, A., Jung, C.B., Lam, J.T., Bott-Flügel, L., Dorn, T., Goedel, A., Höhnke, C., Hofmann, F., Seyfarth, M., Sinnecker, D., Schömig, A., Laugwitz, K.-L.: Patient-Specific Induced Pluripotent Stem-Cell Models for Long-QT Syndrome. New England Journal of Medicine. 363, 1397–1409 (2010). https://doi.org/10.1056/NEJMoa0908679.

21. Itzhaki, I., Maizels, L., Huber, I., Zwi-Dantsis, L., Caspi, O., Winterstern, A., Feldman, O., Gepstein, A., Arbel, G., Hammerman, H., Boulos, M., Gepstein, L.: Modelling the long QT syndrome with induced pluripotent stem cells. Nature. 471, 225–229 (2011). https://doi.org/10.1038/nature09747.

22. Rocchetti, M., Sala, L., Dreizehnter, L., Crotti, L., Sinnecker, D., Mura, M., Pane, L.S., Altomare, C., Torre, E., Mostacciuolo, G., Severi, S., Porta, A., De Ferrari, G.M., George, A.L., Schwartz, P.J., Gnecchi, M., Moretti, A., Zaza, A.: Elucidating arrhythmogenic mechanisms of long-QT syndrome CALM1-F142L mutation in patient-specific induced pluripotent stem cell-derived cardiomyocytes. Cardiovasc Res. 113, 531–541 (2017). https://doi.org/10.1093/cvr/cvx006.

23. Garg, P., Garg, V., Shrestha, R., Sanguinetti, M.C., Kamp, T.J., Wu, J.C.: Human Induced Pluripotent Stem Cell–Derived Cardiomyocytes as Models for Cardiac Channelopathies. Circ Res. 123, 224–243 (2018). https://doi.org/10.1161/CIRCRESAHA.118.311209.

24. Lee, Y.-K., Sala, L., Mura, M., Rocchetti, M., Pedrazzini, M., Ran, X., Mak, T.S.H., Crotti, L., Sham, P.C., Torre, E., Zaza, A., Schwartz, P.J., Tse, H.-F., Gnecchi, M.: MTMR4 SNVs modulate ion channel degradation and clinical severity in congenital long QT syndrome: insights in the mechanism of action of protective modifier genes. Cardiovasc Res. 117, 767–779 (2021). https://doi.org/10.1093/cvr/cvaa019.

25. Zhang, M., D'Aniello, C., Verkerk, A.O., Wrobel, E., Frank, S., Ward-van Oostwaard, D., Piccini, I., Freund, C., Rao, J., Seebohm, G., Atsma, D.E., Schulze-Bahr, E., Mummery, C.L., Greber, B., Bellin, M.: Recessive cardiac phenotypes in

induced pluripotent stem cell models of Jervell and Lange-Nielsen syndrome: Disease mechanisms and pharmacological rescue. Proceedings of the National Academy of Sciences. 111, (2014). https://doi.org/10.1073/pnas.1419553111.

26. Yazawa, M., Hsueh, B., Jia, X., Pasca, A.M., Bernstein, J.A., Hallmayer, J., Dolmetsch, R.E.: Using induced pluripotent stem cells to investigate cardiac phenotypes in Timothy syndrome. Nature. 471, 230–234 (2011). https://doi.org/10.1038/nature09855.

27. Lan, F., Lee, A.S., Liang, P., Sanchez-Freire, V., Nguyen, P.K., Wang, L., Han, L., Yen, M., Wang, Y., Sun, N., Abilez, O.J., Hu, S., Ebert, A.D., Navarrete, E.G., Simmons, C.S., Wheeler, M., Pruitt, B., Lewis, R., Yamaguchi, Y., Ashley, E.A., Bers, D.M., Robbins, R.C., Longaker, M.T., Wu, J.C.: Abnormal Calcium Handling Properties Underlie Familial Hypertrophic Cardiomyopathy Pathology in Patient-Specific Induced Pluripotent Stem Cells. Cell Stem Cell. 12, 101–113 (2013). https://doi.org/10.1016/j.stem.2012.10.010.

28. Ma, D., Wei, H., Lu, J., Ho, S., Zhang, G., Sun, X., Oh, Y., Tan, S.H., Ng, M.L., Shim, W., Wong, P., Liew, R.: Generation of patient-specific induced pluripotent stem cell-derived cardiomyocytes as a cellular model of arrhythmogenic right ventricular cardiomyopathy. Eur Heart J. 34, 1122–1133 (2013). https://doi.org/10.1093/eurheartj/ehs226.

29. Sun, N., Yazawa, M., Liu, J., Han, L., Sanchez-Freire, V., Abilez, O.J., Navarrete, E.G., Hu, S., Wang, L., Lee, A., Pavlovic, A., Lin, S., Chen, R., Hajjar, R.J., Snyder, M.P., Dolmetsch, R.E., Butte, M.J., Ashley, E.A., Longaker, M.T., Robbins, R.C., Wu, J.C.: Patient-Specific Induced Pluripotent Stem Cells as a Model for Familial Dilated Cardiomyopathy. Sci Transl Med. 4, (2012). https://doi.org/10.1126/scitranslmed.3003552.

30. Miao, Y., Tian, L., Martin, M., Paige, S.L., Galdos, F.X., Li, J., Klein, A., Zhang, H., Ma, N., Wei, Y., Stewart, M., Lee, S., Moonen, J.-R., Zhang, B., Grossfeld, P., Mital, S., Chitayat, D., Wu, J.C., Rabinovitch, M., Nelson, T.J., Nie, S., Wu, S.M., Gu, M.: Intrinsic Endocardial Defects Contribute to Hypoplastic Left Heart Syndrome. Cell Stem Cell. 27, 574-589.e8 (2020). https://doi.org/10.1016/j.stem.2020.07.015.

31. Blinova, K., Dang, Q., Millard, D., Smith, G., Pierson, J., Guo, L., Brock, M., Lu, H.R., Kraushaar, U., Zeng, H., Shi, H., Zhang, X., Sawada, K., Osada, T., Kanda,

Y., Sekino, Y., Pang, L., Feaster, T.K., Kettenhofen, R., Stockbridge, N., Strauss, D.G., Gintant, G.: International Multisite Study of Human-Induced Pluripotent Stem Cell-Derived Cardiomyocytes for Drug Proarrhythmic Potential Assessment. Cell Rep. 24, 3582–3592 (2018). https://doi.org/10.1016/j.celrep.2018.08.079.

32. Sala, L., Bellin, M., Mummery, C.L.: Integrating cardiomyocytes from human pluripotent stem cells in safety pharmacology: has the time come? Br J Pharmacol. 174, 3749–3765 (2017). https://doi.org/10.1111/bph.13577.
33. Paik, D.T., Chandy, M., Wu, J.C.: Patient and Disease–Specific Induced Pluripotent Stem Cells for Discovery of Personalized Cardiovascular Drugs and Therapeutics. Pharmacol Rev. 72, 320–342 (2020). https://doi.org/10.1124/pr.116.013003.
34. Mehta, A., Ramachandra, C.J.A., Singh, P., Chitre, A., Lua, C.H., Mura, M., Crotti, L., Wong, P., Schwartz, P.J., Gnecchi, M., Shim, W.: Identification of a targeted and testable antiarrhythmic therapy for long-QT syndrome type 2 using a patient-specific cellular model. Eur Heart J. 39, 1446–1455 (2018). https://doi.org/10.1093/eurheartj/ehx394.
35. Roberts, B., Haupt, A., Tucker, A., Grancharova, T., Arakaki, J., Fuqua, M.A., Nelson, A., Hookway, C., Ludmann, S.A., Mueller, I.A., Yang, R., Horwitz, R., Rafelski, S.M., Gunawardane, R.N.: Systematic gene tagging using CRISPR/Cas9 in human stem cells to illuminate cell organization. Mol Biol Cell. 28, 2854–2874 (2017). https://doi.org/10.1091/mbc.e17-03-0209.
36. Stenson, P.D., Ball, E. V., Mort, M., Phillips, A.D., Shiel, J.A., Thomas, N.S.T., Abeysinghe, S., Krawczak, M., Cooper, D.N.: Human Gene Mutation Database (HGMD ®): 2003 update. Hum Mutat. 21, 577–581 (2003). https://doi.org/10.1002/humu.10212.
37. O'Neill, M.J., Sala, L., Denjoy, I., Wada, Y., Kozek, K., Crotti, L., Dagradi, F., Kotta, M.-C., Spazzolini, C., Leenhardt, A., Salem, J.-E., Kashiwa, A., Ohno, S., Tao, R., Roden, D.M., Horie, M., Extramiana, F., Schwartz, P.J., Kroncke, B.M.: Continuous Bayesian variant interpretation accounts for incomplete penetrance among Mendelian cardiac channelopathies. Genetics in Medicine. 25, 100355 (2023). https://doi.org/10.1016/j.gim.2022.12.002.
38. Kozek, K., Wada, Y., Sala, L., Denjoy, I., Egly, C., O'Neill, M.J., Aiba, T., Shimizu, W., Makita, N., Ishikawa, T., Crotti, L., Spazzolini, C., Kotta, M.-C., Dagradi, F.,

Castelletti, S., Pedrazzini, M., Gnecchi, M., Leenhardt, A., Salem, J.-E., Ohno, S., Zuo, Y., Glazer, A.M., Mosley, J.D., Roden, D.M., Knollmann, B.C., Blume, J.D., Extramiana, F., Schwartz, P.J., Horie, M., Kroncke, B.M.: Estimating the Posttest Probability of Long QT Syndrome Diagnosis for Rare KCNH2 Variants. Circ Genom Precis Med. 14, (2021). https://doi.org/10.1161/CIRCGEN.120.003289.

39. Pantazis, C.B., Yang, A., Lara, E., McDonough, J.A., Blauwendraat, C., Peng, L., Oguro, H., Kanaujiya, J., Zou, J., Sebesta, D., Pratt, G., Cross, E., Blockwick, J., Buxton, P., Kinner-Bibeau, L., Medura, C., Tompkins, C., Hughes, S., Santiana, M., Faghri, F., Nalls, M.A., Vitale, D., Ballard, S., Qi, Y.A., Ramos, D.M., Anderson, K.M., Stadler, J., Narayan, P., Papademetriou, J., Reilly, L., Nelson, M.P., Aggarwal, S., Rosen, L.U., Kirwan, P., Pisupati, V., Coon, S.L., Scholz, S.W., Priebe, T., Öttl, M., Dong, J., Meijer, M., Janssen, L.J.M., Lourenco, V.S., van der Kant, R., Crusius, D., Paquet, D., Raulin, A.-C., Bu, G., Held, A., Wainger, B.J., Gabriele, R.M.C., Casey, J.M., Wray, S., Abu-Bonsrah, D., Parish, C.L., Beccari, M.S., Cleveland, D.W., Li, E., Rose, I.V.L., Kampmann, M., Calatayud Aristoy, C., Verstreken, P., Heinrich, L., Chen, M.Y., Schüle, B., Dou, D., Holzbaur, E.L.F., Zanellati, M.C., Basundra, R., Deshmukh, M., Cohen, S., Khanna, R., Raman, M., Nevin, Z.S., Matia, M., Van Lent, J., Timmerman, V., Conklin, B.R., Johnson Chase, K., Zhang, K., Funes, S., Bosco, D.A., Erlebach, L., Welzer, M., Kronenberg-Versteeg, D., Lyu, G., Arenas, E., Coccia, E., Sarrafha, L., Ahfeldt, T., Marioni, J.C., Skarnes, W.C., Cookson, M.R., Ward, M.E., Merkle, F.T.: A reference human induced pluripotent stem cell line for large-scale collaborative studies. Cell Stem Cell. 29, 1685-1702.e22 (2022). https://doi.org/10.1016/j.stem.2022.11.004.

40. Mura, M., Lee, Y.-K., Pisano, F., Ginevrino, M., Boni, M., Calabrò, F., Crotti, L., Valente, E.M., Schwartz, P.J., Tse, H.-F., Gnecchi, M.: Generation of the human induced pluripotent stem cell (hiPSC) line PSMi004-A from a carrier of the KCNQ1-R594Q mutation. Stem Cell Res. 37, 101431 (2019). https://doi.org/10.1016/j.scr.2019.101431.

41. Mura, M., Lee, Y.-K., Pisano, F., Ginevrino, M., Boni, M., Calabrò, F., Crotti, L., Valente, E.M., Schwartz, P.J., Tse, H.-F., Gnecchi, M.: Generation of the human induced pluripotent stem cell (hiPSC) line PSMi004-A from a carrier of the

KCNQ1-R594Q mutation. Stem Cell Res. 37, 101431 (2019). https://doi.org/10.1016/j.scr.2019.101431.

42. Ronchi, C., Bernardi, J., Mura, M., Stefanello, M., Badone, B., Rocchetti, M., Crotti, L., Brink, P., Schwartz, P.J., Gnecchi, M., Zaza, A.: NOS1AP polymorphisms reduce NOS1 activity and interact with prolonged repolarization in arrhythmogenesis. Cardiovasc Res. 117, 472–483 (2021). https://doi.org/10.1093/cvr/cvaa036.
43. Mura, M., Pisano, F., Stefanello, M., Ginevrino, M., Boni, M., Calabrò, F., Crotti, L., Valente, E.M., Schwartz, P.J., Brink, P.A., Gnecchi, M.: Generation of two human induced pluripotent stem cell (hiPSC) lines from a long QT syndrome South African founder population. Stem Cell Res. 39, 101510 (2019). https://doi.org/10.1016/j.scr.2019.101510.
44. Mura, M., Lee, Y.-K., Pisano, F., Ginevrino, M., Boni, M., Calabrò, F., Crotti, L., Valente, E.M., Schwartz, P.J., Tse, H.-F., Gnecchi, M.: Generation of the human induced pluripotent stem cell (hiPSC) line PSMi004-A from a carrier of the KCNQ1-R594Q mutation. Stem Cell Res. 37, 101431 (2019). https://doi.org/10.1016/j.scr.2019.101431.
45. Mehta, A., Sequiera, G.L., Ramachandra, C.J.A., Sudibyo, Y., Chung, Y., Sheng, J., Wong, K.Y., Tan, T.H., Wong, P., Liew, R., Shim, W.: Re-trafficking of hERG reverses long QT syndrome 2 phenotype in human iPS-derived cardiomyocytes. Cardiovasc Res. 102, 497–506 (2014). https://doi.org/10.1093/cvr/cvu060.
46. Lian, X., Hsiao, C., Wilson, G., Zhu, K., Hazeltine, L.B., Azarin, S.M., Raval, K.K., Zhang, J., Kamp, T.J., Palecek, S.P.: Robust cardiomyocyte differentiation from human pluripotent stem cells via temporal modulation of canonical Wnt signaling. Proceedings of the National Academy of Sciences. 109, (2012). https://doi.org/10.1073/pnas.1200250109.
47. Tohyama, S., Hattori, F., Sano, M., Hishiki, T., Nagahata, Y., Matsuura, T., Hashimoto, H., Suzuki, T., Yamashita, H., Satoh, Y., Egashira, T., Seki, T., Muraoka, N., Yamakawa, H., Ohgino, Y., Tanaka, T., Yoichi, M., Yuasa, S., Murata, M., Suematsu, M., Fukuda, K.: Distinct Metabolic Flow Enables Large-Scale Purification of Mouse and Human Pluripotent Stem Cell-Derived Cardiomyocytes. Cell Stem Cell. 12, 127–137 (2013). https://doi.org/10.1016/j.stem.2012.09.013.

48. Buikema, J.W., Lee, S., Goodyer, W.R., Maas, R.G., Chirikian, O., Li, G., Miao, Y., Paige, S.L., Lee, D., Wu, H., Paik, D.T., Rhee, S., Tian, L., Galdos, F.X., Puluca, N., Beyersdorf, B., Hu, J., Beck, A., Venkamatran, S., Swami, S., Wijnker, P., Schuldt, M., Dorsch, L.M., van Mil, A., Red-Horse, K., Wu, J.Y., Geisen, C., Hesse, M., Serpooshan, V., Jovinge, S., Fleischmann, B.K., Doevendans, P.A., van der Velden, J., Garcia, K.C., Wu, J.C., Sluijter, J.P.G., Wu, S.M.: Wnt Activation and Reduced Cell-Cell Contact Synergistically Induce Massive Expansion of Functional Human iPSC-Derived Cardiomyocytes. Cell Stem Cell. 27, 50-63.e5 (2020). https://doi.org/10.1016/j.stem.2020.06.001.

49. Tohyama, S., Hattori, F., Sano, M., Hishiki, T., Nagahata, Y., Matsuura, T., Hashimoto, H., Suzuki, T., Yamashita, H., Satoh, Y., Egashira, T., Seki, T., Muraoka, N., Yamakawa, H., Ohgino, Y., Tanaka, T., Yoichi, M., Yuasa, S., Murata, M., Suematsu, M., Fukuda, K.: Distinct Metabolic Flow Enables Large-Scale Purification of Mouse and Human Pluripotent Stem Cell-Derived Cardiomyocytes. Cell Stem Cell. 12, 127–137 (2013). https://doi.org/10.1016/j.stem.2012.09.013.

50. Buikema, J.W., Lee, S., Goodyer, W.R., Maas, R.G., Chirikian, O., Li, G., Miao, Y., Paige, S.L., Lee, D., Wu, H., Paik, D.T., Rhee, S., Tian, L., Galdos, F.X., Puluca, N., Beyersdorf, B., Hu, J., Beck, A., Venkamatran, S., Swami, S., Wijnker, P., Schuldt, M., Dorsch, L.M., van Mil, A., Red-Horse, K., Wu, J.Y., Geisen, C., Hesse, M., Serpooshan, V., Jovinge, S., Fleischmann, B.K., Doevendans, P.A., van der Velden, J., Garcia, K.C., Wu, J.C., Sluijter, J.P.G., Wu, S.M.: Wnt Activation and Reduced Cell-Cell Contact Synergistically Induce Massive Expansion of Functional Human iPSC-Derived Cardiomyocytes. Cell Stem Cell. 27, 50-63.e5 (2020). https://doi.org/10.1016/j.stem.2020.06.001.

51. Feyen, D.A.M., McKeithan, W.L., Bruyneel, A.A.N., Spiering, S., Hörmann, L., Ulmer, B., Zhang, H., Briganti, F., Schweizer, M., Hegyi, B., Liao, Z., Pölönen, R.-P., Ginsburg, K.S., Lam, C.K., Serrano, R., Wahlquist, C., Kreymerman, A., Vu, M., Amatya, P.L., Behrens, C.S., Ranjbarvaziri, S., Maas, R.G.C., Greenhaw, M., Bernstein, D., Wu, J.C., Bers, D.M., Eschenhagen, T., Metallo, C.M., Mercola, M.: Metabolic Maturation Media Improve Physiological Function of Human iPSC-Derived Cardiomyocytes. Cell Rep. 32, 107925 (2020). https://doi.org/10.1016/j.celrep.2020.107925.

52. Sala, L., Ward-van Oostwaard, D., Tertoolen, L.G.J., Mummery, C.L., Bellin, M.: Electrophysiological Analysis of human Pluripotent Stem Cell-derived Cardiomyocytes (hPSC-CMs) Using Multi-electrode Arrays (MEAs). Journal of Visualized Experiments. (2017). https://doi.org/10.3791/55587.
53. Sala, L., Leonov, V., Mura, M., Giannetti, F., Khudiakov, A., Moretti, A., Crotti, L., Gnecchi, M., Schwartz, P.J.: Use of hiPSC-Derived Cardiomyocytes to Rule Out Proarrhythmic Effects of Drugs: The Case of Hydroxychloroquine in COVID-19. Front Physiol. 12, (2022). https://doi.org/10.3389/fphys.2021.730127.
54. Thomas, D., Wu, K., Kathöfer, S., Katus, H.A., Schoels, W., Kiehn, J., Karle, C.A.: The antipsychotic drug chlorpromazine inhibits HERG potassium channels. Br J Pharmacol. 139, 567–574 (2003). https://doi.org/10.1038/sj.bjp.0705283.
55. Kang, J., Wang, L., Chen, X.-L., Triggle, D.J., Rampe, D.: Interactions of a Series of Fluoroquinolone Antibacterial Drugs with the Human Cardiac K + Channel HERG. Mol Pharmacol. 59, 122–126 (2001). https://doi.org/10.1124/mol.59.1.122.
56. Stanat, S.J.C., Carlton, C.G., Crumb, W.J., Agrawal, K.C., Clarkson, C.W.: Characterization of the inhibitory effects of erythromycin and clarithromycin on the HERG potassium channel. Mol Cell Biochem. 254, 1–7 (2003). https://doi.org/10.1023/A:1027309703313.
57. Orvos, P., Kohajda, Z., Szlovák, J., Gazdag, P., Árpádffy-Lovas, T., Tóth, D., Geramipour, A., Tálosi, L., Jost, N., Varró, A., Virág, L.: Evaluation of Possible Proarrhythmic Potency: Comparison of the Effect of Dofetilide, Cisapride, Sotalol, Terfenadine, and Verapamil on hERG and Native I Kr Currents and on Cardiac Action Potential. Toxicological Sciences. 168, 365–380 (2019). https://doi.org/10.1093/toxsci/kfy299.
58. Zhou, Z., Gong, Q., Ye, B., Fan, Z., Makielski, J.C., Robertson, G.A., January, C.T.: Properties of HERG Channels Stably Expressed in HEK 293 Cells Studied at Physiological Temperature. Biophys J. 74, 230–241 (1998). https://doi.org/10.1016/S0006-3495(98)77782-3.
59. Suessbrich, H., Schönherr, R., Heinemann, S.H., Attali, B., Lang, F., Busch, A.E.: The inhibitory effect of the antipsychotic drug haloperidol on HERG potassium channels expressed in Xenopus oocytes. Br J Pharmacol. 120, 968–974 (1997). https://doi.org/10.1038/sj.bjp.0700989.

60. Uematsu, T., Matsuno, H., Sato, H., Hirayama, H., Hasegawa, K., Nakashima, M.: Steady-State Pharmacokinetics of Haloperidol and Reduced Haloperidol in Schizophrenic Patients: Analysis of Factors Determining their Concentrations in Hair. J Pharm Sci. 81, 1008–1011 (1992). https://doi.org/10.1002/jps.2600811010.
61. Bischoff, U., Schmidt, C., Netzer, R., Pongs, O.: Effects of fluoroquinolones on HERG currents. Eur J Pharmacol. 406, 341–343 (2000). https://doi.org/10.1016/S0014-2999(00)00693-2.
62. Stass, H., Dalhoff, A., Kubitza, D., Schühly, U.: Pharmacokinetics, Safety, and Tolerability of Ascending Single Doses of Moxifloxacin, a New 8-Methoxy Quinolone, Administered to Healthy Subjects. Antimicrob Agents Chemother. 42, 2060–2065 (1998). https://doi.org/10.1128/AAC.42.8.2060.
63. Kruizinga, M.D., Birkhoff, W.A.J., van Esdonk, M.J., Klarenbeek, N.B., Cholewinski, T., Nelemans, T., Dröge, M.J., Cohen, A.F., Zuiker, R.G.J.A.: Pharmacokinetics of intravenous and inhaled salbutamol and tobramycin: An exploratory study to investigate the potential of exhaled breath condensate as a matrix for pharmacokinetic analysis. Br J Clin Pharmacol. 86, 175–181 (2020). https://doi.org/10.1111/bcp.14156.
64. Schwartz, P.J., Spazzolini, C., Crotti, L., Bathen, J., Amlie, J.P., Timothy, K., Shkolnikova, M., Berul, C.I., Bitner-Glindzicz, M., Toivonen, L., Horie, M., Schulze-Bahr, E., Denjoy, I.: The Jervell and Lange-Nielsen Syndrome. Circulation. 113, 783–790 (2006). https://doi.org/10.1161/CIRCULATIONAHA.105.592899.
65. Mura, M., Lee, Y.-K., Pisano, F., Ginevrino, M., Boni, M., Calabrò, F., Crotti, L., Valente, E.M., Schwartz, P.J., Tse, H.-F., Gnecchi, M.: Generation of the human induced pluripotent stem cell (hiPSC) line PSMi004-A from a carrier of the KCNQ1-R594Q mutation. Stem Cell Res. 37, 101431 (2019). https://doi.org/10.1016/j.scr.2019.101431.
66. Brink, P.A., Crotti, L., Corfield, V., Goosen, A., Durrheim, G., Hedley, P., Heradien, M., Geldenhuys, G., Vanoli, E., Bacchini, S., Spazzolini, C., Lundquist, A.L., Roden, D.M., George, A.L., Schwartz, P.J.: Phenotypic Variability and Unusual Clinical Severity of Congenital Long-QT Syndrome in a Founder Population. Circulation. 112, 2602–2610 (2005). https://doi.org/10.1161/CIRCULATIONAHA.105.572453.

67. Crotti, L., Spazzolini, C., Schwartz, P.J., Shimizu, W., Denjoy, I., Schulze-Bahr, E., Zaklyazminskaya, E. V., Swan, H., Ackerman, M.J., Moss, A.J., Wilde, A.A.M., Horie, M., Brink, P.A., Insolia, R., De Ferrari, G.M., Crimi, G.: The Common Long-QT Syndrome Mutation KCNQ1/A341V Causes Unusually Severe Clinical Manifestations in Patients With Different Ethnic Backgrounds. Circulation. 116, 2366–2375 (2007). https://doi.org/10.1161/CIRCULATIONAHA.107.726950.
68. Crotti, L., Monti, M.C., Insolia, R., Peljto, A., Goosen, A., Brink, P.A., Greenberg, D.A., Schwartz, P.J., George, A.L.: NOS1AP Is a Genetic Modifier of the Long-QT Syndrome. Circulation. 120, 1657–1663 (2009). https://doi.org/10.1161/CIRCULATIONAHA.109.879643.
69. Kramer, J., Obejero-Paz, C.A., Myatt, G., Kuryshev, Y.A., Bruening-Wright, A., Verducci, J.S., Brown, A.M.: MICE Models: Superior to the HERG Model in Predicting Torsade de Pointes. Sci Rep. 3, 2100 (2013). https://doi.org/10.1038/srep02100.
70. Braam, S.R., Tertoolen, L., Casini, S., Matsa, E., Lu, H.R., Teisman, A., Passier, R., Denning, C., Gallacher, D.J., Towart, R., Mummery, C.L.: Repolarization reserve determines drug responses in human pluripotent stem cell derived cardiomyocytes. Stem Cell Res. 10, 48–56 (2013). https://doi.org/10.1016/j.scr.2012.08.007.
71. Stillitano, F., Hansen, J., Kong, C.-W., Karakikes, I., Funck-Brentano, C., Geng, L., Scott, S., Reynier, S., Wu, M., Valogne, Y., Desseaux, C., Salem, J.-E., Jeziorowska, D., Zahr, N., Li, R., Iyengar, R., Hajjar, R.J., Hulot, J.-S.: Modeling susceptibility to drug-induced long QT with a panel of subject-specific induced pluripotent stem cells. Elife. 6, (2017). https://doi.org/10.7554/eLife.19406.
72. Golforoush, P., Schneider, M.D.: Intensive care for human hearts in pluripotent stem cell models. NPJ Regen Med. 5, 4 (2020). https://doi.org/10.1038/s41536-020-0090-7.
73. Shead, K.D., Huethorst, E., Burton, F., Lang, N.N., Myles, R.C., Smith, G.L.: Human Induced Pluripotent Stem Cell-Derived Cardiomyocytes for Preclinical Cardiotoxicity Screening in Cardio-Oncology. JACC CardioOncol. 6, 678–683 (2024). https://doi.org/10.1016/j.jaccao.2024.07.012.
74. Wada, Y., Wang, L., Hall, L.D., Yang, T., Short, L.L., Solus, J.F., Glazer, A.M., Roden, D.M.: The electrophysiologic effects of KCNQ1 extend beyond expression

of I Ks: evidence from genetic and pharmacologic block. Cardiovasc Res. 120, 735–744 (2024). https://doi.org/10.1093/cvr/cvae042.

75. Zeng, H., Wang, J., Clouse, H., Lagrutta, A., Sannajust, F.: Human-induced pluripotent stem cell-derived cardiomyocytes have limited I Ks for repolarization reserve as revealed by specific KCNQ1/KCNE1 blocker. JRSM Cardiovasc Dis. 8, (2019). https://doi.org/10.1177/2048004019854919.

76. Varró, A., Baczkó, I.: Cardiac ventricular repolarization reserve: a principle for understanding drug-related proarrhythmic risk. Br J Pharmacol. 164, 14–36 (2011). https://doi.org/10.1111/j.1476-5381.2011.01367.x.

77. Sala, L., Gnecchi, M., Schwartz, P.J.: Long QT Syndrome Modelling with Cardiomyocytes Derived from Human-induced Pluripotent Stem Cells. Arrhythm Electrophysiol Rev. 8, 105–110 (2019). https://doi.org/10.15420/aer.2019.1.1.

78. Itzhaki, I., Maizels, L., Huber, I., Zwi-Dantsis, L., Caspi, O., Winterstern, A., Feldman, O., Gepstein, A., Arbel, G., Hammerman, H., Boulos, M., Gepstein, L.: Modelling the long QT syndrome with induced pluripotent stem cells. Nature. 471, 225–229 (2011). https://doi.org/10.1038/nature09747.

79. Zreik, J., LaPage, M.J., Zreik, H.: Congenital Long QT Syndrome Unmasked by Albuterol in an Adolescent with Asthma. J Emerg Med. 67, e446–e450 (2024). https://doi.org/10.1016/j.jemermed.2024.05.011.

80. Kopljar, I., Lu, H.R., Van Ammel, K., Otava, M., Tekle, F., Teisman, A., Gallacher, D.J.: Development of a Human iPSC Cardiomyocyte-Based Scoring System for Cardiac Hazard Identification in Early Drug Safety De-risking. Stem Cell Reports. 11, 1365–1377 (2018). https://doi.org/10.1016/j.stemcr.2018.11.007.

81. Noda, T.: Gene-specific response of dynamic ventricular repolarization to sympathetic stimulation in LQT1, LQT2 and LQT3 forms of congenital long QT syndrome. Eur Heart J. 23, 975–983 (2002). https://doi.org/10.1053/euhj.2001.3079.

82. Odening, K.E., Hyder, O., Chaves, L., Schofield, L., Brunner, M., Kirk, M., Zehender, M., Peng, X., Koren, G.: Pharmacogenomics of anesthetic drugs in transgenic LQT1 and LQT2 rabbits reveal genotype-specific differential effects on cardiac repolarization. American Journal of Physiology-Heart and Circulatory Physiology. 295, H2264–H2272 (2008). https://doi.org/10.1152/ajpheart.00680.2008.

83. Yoshinaga, D., Baba, S., Makiyama, T., Shibata, H., Hirata, T., Akagi, K., Matsuda, K., Kohjitani, H., Wuriyanghai, Y., Umeda, K., Yamamoto, Y., Conklin, B.R., Horie, M., Takita, J., Heike, T.: Phenotype-Based High-Throughput Classification of Long QT Syndrome Subtypes Using Human Induced Pluripotent Stem Cells. Stem Cell Reports. 13, 394–404 (2019). https://doi.org/10.1016/j.stemcr.2019.06.007.

84. Ma, J.G., O'Neill, M.J., Richardson, E., Thomson, K.L., Ingles, J., Muhammad, A., Solus, J.F., Davogustto, G., Anderson, K.C., Shoemaker, M.B., Stergachis, A.B., Floyd, B.J., Dunn, K., Parikh, V.N., Chubb, H., Perrin, M.J., Roden, D.M., Vandenberg, J.I., Ng, C.-A., Glazer, A.M.: Multisite Validation of a Functional Assay to Adjudicate SCN5A Brugada Syndrome–Associated Variants. Circ Genom Precis Med. 17, (2024). https://doi.org/10.1161/CIRCGEN.124.004569.

85. Karbassi, E., Fenix, A., Marchiano, S., Muraoka, N., Nakamura, K., Yang, X., Murry, C.E.: Cardiomyocyte maturation: advances in knowledge and implications for regenerative medicine. Nat Rev Cardiol. 17, 341–359 (2020). https://doi.org/10.1038/s41569-019-0331-x.

86. Veerman, C.C., Kosmidis, G., Mummery, C.L., Casini, S., Verkerk, A.O., Bellin, M.: Immaturity of Human Stem-Cell-Derived Cardiomyocytes in Culture: Fatal Flaw or Soluble Problem? Stem Cells Dev. 24, 1035–1052 (2015). https://doi.org/10.1089/scd.2014.0533.

Chapter 4

Summary and Conclusions

Inherited arrhythmogenic heart diseases (AHDs) constitute a heterogeneous group of conditions unified by their potential to precipitate malignant ventricular arrhythmias and sudden cardiac death (SCD). Traditionally, they have been divided into arrhythmogenic cardiomyopathies (ACM), in which progressive structural remodeling provides the arrhythmic substrate, and channelopathies, where electrical dysfunction emerges in the context of an otherwise structurally normal heart. Increasing evidence, however, demonstrates substantial overlap at the genetic and pathophysiological levels, challenging this rigid dichotomy and supporting the view of AHDs as a continuum in which structural and electrical abnormalities coexist and interact [1,2]. Within this framework, the present thesis focused on two paradigmatic conditions that exemplify opposite ends of the spectrum, cardiomyopathy associated with the *PLN-R14del* mutation and congenital LQTS, with the aim of dissecting early molecular mechanisms in the first case and of refining the current understanding risk stratification strategies in the second.

The experimental work on *PLN-R14del* cardiomyopathy has provided novel insights that reframe the understanding of this disease. Early studies had suggested that the mutation acted as a “super-inhibitor” of SERCA2a, producing excessive restraint of SR Ca^{2+} uptake [3]. However, our results, obtained from a transgenic mouse model at a presymptomatic stage, indicate a different scenario. Mutant cardiomyocytes displayed hyperdynamic Ca^{2+} cycling, with accelerated decay kinetics and reduced diastolic Ca^{2+} levels, consistent with a loss of PLN inhibitory function. These findings are supported by the complete insensitivity of mutant cells to PST-3093, a selective PLN antagonist, and by concordant observations in human hiPSC-derived cardiomyocytes carrying the same mutation [4,5]. Thus, rather than acting as a super-inhibitor, *PLN-R14del* appears to abolish the physiological restraint exerted by PLN on SERCA2a, shifting Ca^{2+} handling toward an unbalanced state of excessive SR uptake.

Parallel to these alterations in Ca^{2+} homeostasis, mutant cardiomyocytes exhibited a profound downregulation of energy metabolism, with reductions in oxidative phosphorylation and glycolysis. Interestingly, mitochondrial potential and reactive oxygen species remained normal, indicating that overt damage was not yet present. Instead, energy charge was maintained at rest, but when cells were subjected to pacing, they failed to sustain ATP production, revealing a stress-dependent incompetence. This maladaptive interplay between hyperdynamic Ca^{2+} uptake and insufficient energetic reserve may be silent under baseline conditions but becomes destabilizing when workload increases. Over time, such an imbalance could trigger maladaptive remodeling, progressive contractile dysfunction, and the fibrofatty replacement typical of clinical ACM.

These findings have important therapeutic implications. If *PLN-R14del* truly caused SERCA2a super-inhibition, as originally proposed, then pharmacological SERCA2a activators would represent rational therapy. Instead, both our results and independent studies demonstrate that these drugs lose efficacy in the mutant background [4,5]. This evidence suggests that treatment strategies should move away from indiscriminate SERCA2a activation and toward approaches that address mutant protein toxicity, ER stress, and impaired ER–mitochondria crosstalk [6]. Moreover, the recognition that early disease stages are dominated by hyperdynamic Ca^{2+} handling and metabolic dysfunction, whereas later stages are characterized by SR depression typical of remodeling, underscores the importance of timing in therapy design. Interventions aimed at correcting early molecular defects may offer the best chance of altering disease progression before irreversible structural damage ensues.

The second focus of the thesis was Long QT Syndrome, a prototypical channelopathy in which the risk of SCD varies greatly among carriers of pathogenic or likely pathogenic variants.

Although therapies based on beta-blockers [7], left cardiac sympathetic denervation [8,9], and sodium channel blockers [10,11] have effectively reduced the risk of potentially fatal ventricular arrhythmias and sudden cardiac death (SCD), clinical risk stratification remains limited. QTc prolongation is neither specific nor sufficient, and even within the same family, carriers of an identical mutation may present dramatically different phenotypes due to incomplete penetrance and variable expressivity, largely modulated by genetic modifiers such as *NOS1AP* [12,13]. This variability hampers the identification of those individuals who are truly at high risk and therefore most likely to benefit from invasive interventions.

To address this challenge, we developed an integrated methodological approach combining hiPSC-derived cardiomyocytes with multielectrode array (MEA) recordings and machine learning. hiPSC-CMs from patients carrying different variants reproduced the expected phenotypes: high-risk variants such as *KCNQ1 p.A341V* and *KCNH2 p.A561V* displayed pronounced prolongation of repolarization and greater arrhythmic instability, while low-risk variants showed more stable electrophysiological profiles.

Importantly, drug-response profiles provided an additional discriminative dimension: pharmacological I_{Kr} blockade was particularly effective in separating high- from low-risk variants, reflecting differences in repolarization reserve. By training Machine Learning classifiers on multiparametric readouts, we achieved ~90% accuracy in distinguishing between high- and low-risk groups, and importantly, the model showed potential generalizability to ultra-rare variants and VUS where clinical annotation was limited [14]. These results show that patient-derived functional genomics, coupled with computational analysis, can contribute to the refinement of clinical risk assessment and support precision medicine approaches in LQTS.

By elucidating early pathogenic events in *PLN-R14del* cardiomyopathy and by implementing a predictive framework for variant-specific risk stratification in LQTS, this thesis contributes both mechanistic and translational advances. It demonstrates that stage-appropriate experimental models can reveal unexpected drivers of pathology, while patient-derived cellular systems, when integrated with computational analysis, can transform genetic data into functionally informed risk predictions with potential clinical relevance. The broader implication is that inherited arrhythmogenic disorders should be approached with an integrated strategy, in which mechanistic dissection informs therapeutic targets and predictive modeling guides individualized management. Ultimately, the combination of molecular insights, functional genomics, and computational analysis represents a path forward toward the precision prevention of arrhythmic sudden death.

4.1. References

1. Silvia G Priori, Carol Ann Remme, Inherited conditions of arrhythmia: translating disease mechanisms to patient management, *Cardiovascular Research*, Volume 116, Issue 9, 15 July 2020, Pages 1539–1541, https://doi.org/10.1093/cvr/cvaa150
2. Silvia G. Priori, Inherited Arrhythmogenic Diseases: The Complexity Beyond Monogenic Disorders, *Circulation Research,* Volume 94, Number 2, https://doi.org/10.1161/01.RES.0000115750.12807.7E
3. Haghighi, K., Kolokathis, F., Gramolini, A.O., Waggoner, J.R., Pater, L., Lynch, R.A., Fan, G.-C., Tsiapras, D., Parekh, R.R., Dorn Ii, G.W., Maclennan, D.H., Kremastinos, D.T., Kranias, E.G.: A mutation in the human phospholamban gene, deleting arginine 14, results in lethal, hereditary cardiomyopathy. (2006).
4. Maniezzi C, Eskandr M, Florindi C, Ferrandi M, Barassi P, Sacco E, Pasquale V, Maione AS, Pompilio G, Teixeira VON, de Boer RA, Sillje HHW, Lodola F and Zaza A. Early consequences of the phospholamban mutation PLN-R14del(+/-) in a transgenic mouse model. Acta Physiol (Oxf). 2024;240:e14082.
5. Badone, B., Ronchi, C., Lodola, F., Knaust, A.E., Hansen, A., Eschenhagen, T., Zaza, A.: Characterization of the PLN p.Arg14del Mutation in Human Induced Pluripotent Stem Cell-Derived Cardiomyocytes. Int J Mol Sci. 22, 13500 (2021). https://doi.org/10.3390/ijms222413500.
6. Cuello F, Knaust AE, Saleem U, Loos M, Raabe J,. Impairment of the ER/mitochondria compartment in human cardiomyocytes with PLN p.Arg14del mutation. EMBO Mol Med. 2021;13:e13074. https://doi.org/10.15252/emmm.202013074
7. Zeppenfeld, K., Tfelt-Hansen, J., de Riva, M., Winkel, B.G., Behr, E.R., Blom, N.A., Charron, P., Corrado, D., Dagres, N., de Chillou, C., Eckardt, L., Friede, T., Haugaa, K.H., Hocini, M., Lambiase, P.D., Marijon, E., Merino, J.L., Peichl, P., Priori, S.G., Reichlin, T., Schulz-Menger, J., Sticherling, C., Tzeis, S., Verstrael, A., Volterrani, M., Cikes, M., Kirchhof, P., Abdelhamid, M., Aboyans, V., Arbelo, E., Arribas, F., Asteggiano, R., Basso, C., Bauer, A., Bertaglia, E., Biering-Sørensen, T., Blomström-Lundqvist, C., Borger, M.A., Čelutkienė, J., Cosyns, B., Falk, V., Fauchier, L., Gorenek, B., Halvorsen, S., Hatala, R., Heidbuchel, H., Kaab, S., Konradi, A.,

Koskinas, K.C., Kotecha, D., Landmesser, U., Lewis, B.S., Linhart, A., Løchen, M.L., Lund, L.H., Metzner, A., Mindham, R., Nielsen, J.C., Norekvål, T.M., Patten, M., Prescott, E., Rakisheva, A., Remme, C.A., Roca-Luque, I., Sarkozy, A., Scherr, D., Sitges, M., Touyz, R.M., Van Mieghem, N., Velagic, V., Viskin, S., Volders, P.G.A., Kichou, B., Martirosyan, M., Scherr, D., Aliyev, F., Willems, R., Naser, N., Shalganov, T., Milicic, D., Christophides, T., Kautzner, J., Hansen, J., Allam, L., Kampus, P., Junttila, J., Leclercq, C., Etsadashvili, K., Steven, D., Gatzoulis, K., Gellér, L., Arnar, D.O., Galvin, J., Haim, M., Pappone, C., Elezi, S., Kerimkulova, A., Kalejs, O., Rabah, A., Puodziukynas, A., Dimmer, C., Sammut, M.A., David, L., Boskovic, A., Moustaghfir, A., Maass, A.H., Poposka, L., Mjolstad, O.C., Mitkowski, P., Parreira, L., Cozma, D., Golukhova, E., Bini, R., Stojkovic, S., Hlivak, P., Pernat, A., Castellano, N.P., Platonov, P.G., Duru, F., Saadi, A.R. Al, Ouali, S., Demircan, S., Sychov, O., Slade, A.: 2022 ESC Guidelines for the management of patients with ventricular arrhythmias and the prevention of sudden cardiac death. Eur Heart J. 43, 3997–4126 (2022). https://doi.org/10.1093/eurheartj/ehac262

8. Schwartz, P.J.: Cardiac sympathetic denervation to prevent life-threatening arrhythmias. Nat Rev Cardiol. 11, 346–353 (2014). https://doi.org/10.1038/nrcardio.2014.19.
9. Dusi, V., Pugliese, L., De Ferrari, G.M., Odero, A., Crotti, L., Dagradi, F., Castelletti, S., Vicentini, A., Rordorf, R., Li, C., Shkolnikova, M., Spazzolini, C., Schwartz, P.J.: Left Cardiac Sympathetic Denervation for Long QT Syndrome. JACC Clin Electrophysiol. 8, 281–294 (2022). https://doi.org/10.1016/j.jacep.2021.09.002.
10. Schwartz, P.J., Priori, S.G., Locati, E.H., Napolitano, C., Cantù, F., Towbin, J.A., Keating, M.T., Hammoude, H., Brown, A.M., Chen, L.-S.K., Colatsky, T.J.: Long QT Syndrome Patients With Mutations of the *SCN5A* and *HERG* Genes Have Differential Responses to Na + Channel Blockade and to Increases in Heart Rate. Circulation. 92, 3381–3386 (1995). https://doi.org/10.1161/01.CIR.92.12.3381.
11. Crotti, L., Neves, R., Dagradi, F., Musu, G., Giannetti, F., Bos, J.M., Barbieri, M., Cerea, P., Giovenzana, F.L.F., Torchio, M., Mura, M., Gnecchi, M., Conte, G., Auricchio, A., Sala, L., Odening, K.E., Ackerman, M.J., Schwartz, P.J.: Therapeutic Efficacy of Mexiletine for Long QT Syndrome Type 2: Evidence From Human Induced Pluripotent Stem Cell–Derived Cardiomyocytes, Transgenic Rabbits, and

Patients. Circulation. 150, 531–543 (2024). https://doi.org/10.1161/CIRCULATIONAHA.124.068959.

12. Ronchi, C., Bernardi, J., Mura, M., Stefanello, M., Badone, B., Rocchetti, M., Crotti, L., Brink, P., Schwartz, P.J., Gnecchi, M., Zaza, A.: NOS1AP polymorphisms reduce NOS1 activity and interact with prolonged repolarization in arrhythmogenesis. Cardiovasc Res. 117, 472–483 (2021). https://doi.org/10.1093/cvr/cvaa036.
13. Crotti, L., Monti, M.C., Insolia, R., Peljto, A., Goosen, A., Brink, P.A., Greenberg, D.A., Schwartz, P.J., George, A.L.: *NOS1AP* Is a Genetic Modifier of the Long-QT Syndrome. Circulation. 120, 1657–1663 (2009). https://doi.org/10.1161/CIRCULATIONAHA.109.879643
14. Schwartz, P.J., Moreno, C., Kotta, M.-C., Pedrazzini, M., Crotti, L., Dagradi, F., Castelletti, S., Haugaa, K.H., Denjoy, I., Shkolnikova, M.A., Brink, P.A., Heradien, M.J., Seyen, S.R.M., Spätjens, R.L.H.M.G., Spazzolini, C., Volders, P.G.A.: Mutation location and *I* Ks regulation in the arrhythmic risk of long QT syndrome type 1: the importance of the KCNQ1 S6 region. Eur Heart J. 42, 4743–4755 (2021). https://doi.org/10.1093/eurheartj/ehab582

Chapter 5

Papers

1. Maniezzi C, **Eskandr M**, Florindi C, Ferrandi M, Barassi P, Sacco E, Pasquale V, Maione AS, Pompilio G, Teixeira VON, de Boer RA, Sillje HHW, Lodola F and Zaza A. Early consequences of the phospholamban mutation PLN-R14del(+/-) in a transgenic mouse model. Acta Physiol (Oxf). 2024;240:e14082.2.

2. Khudiakov A, Mura M, Giannetti F, Leonov V, Alberio C, **Eskandr M**, et al. Genetic variants risk assessment for Long QT Syndrome through machine learning and multielectrode array recordings. medRxiv. 2025. https://doi.org/10.1101/2025.03.25.25324187

Received: 7 July 2023 | Revised: 11 December 2023 | Accepted: 1 January 2024

DOI: 10.1111/apha.14082

ACTA PHYSIOLOGICA

RESEARCH PAPER

Early consequences of the phospholamban mutation PLN-R14del$^{+/-}$ in a transgenic mouse model

Claudia Maniezzi[1] | **Marem Eskandr**[1] | **Chiara Florindi**[1] | **Mara Ferrandi**[2] | **Paolo Barassi**[2] | **Elena Sacco**[1] | **Valentina Pasquale**[1] | **Angela S. Maione**[3] | **Giulio Pompilio**[3,4] | **Vivian Oliveira Nunes Teixeira**[5] | **Rudolf A. de Boer**[6] | **Herman H. W. Silljé**[5] | **Francesco Lodola**[1] | **Antonio Zaza**[1]

[1]Department of Biotechnology and Bioscience, University of Milano-Bicocca, Milan, Italy

[2]Windtree Therapeutics Inc., Warrington, Pennsylvania, USA

[3]Unit of Vascular Biology and Regenerative Medicine, Centro Cardiologico Monzino IRCCS, Milan, Italy

[4]Department of Biomedical, Surgical and Dentist Sciences, University of Milano, Milan, Italy

[5]Department of Cardiology, University Medical Center Groningen, University of Groningen, Groningen, Netherlands

[6]Department of Cardiology, Erasmus University Medical Center, University of Rotterdam, Rotterdam, Netherlands

Correspondence

Francesco Lodola and Antonio Zaza, Department of Biotechnology and Bioscience, University of Milano-Bicocca, P.za della Scienza 2, Milan 20126, Italy.
Email: francesco.lodola@unimib.it and antonio.zaza@unimib.it

Funding information

Generation of the PLN-R14del murine model was supported by grants from the Netherlands Heart Foundation (CVON PREDICT2, Grant/award: 2018-30; CVON DOUBLE DOSE, Grant/award; 2020B005 and CarMa, Grant/award:01-003-2022-0358).

Abstract

Aims: The heterozygous phospholamban (PLN) mutation R14del (PLN R14del$^{+/-}$) is associated with a severe arrhythmogenic cardiomyopathy (ACM) developing in the adult. "Superinhibition" of SERCA2a by PLN R14del is widely assumed to underlie the pathogenesis, but alternative mechanisms such abnormal energy metabolism have also been reported. This work aims to (1) to evaluate Ca^{2+} dynamics and energy metabolism in a transgenic (TG) mouse model of the mutation prior to cardiomyopathy development; (2) to test whether they are causally connected.

Methods: Ca^{2+} dynamics, energy metabolism parameters, reporters of mitochondrial integrity, energy, and redox homeostasis were measured in ventricular myocytes of 8–12 weeks-old, phenotypically silent, TG mice. Mutation effects were compared to pharmacological PLN antagonism and analyzed during modulation of sarcoplasmic reticulum (SR) and cytosolic Ca^{2+} compartments. Transcripts and proteins of relevant signaling pathways were evaluated.

Results: The mutation was characterized by hyperdynamic Ca^{2+} handling, compatible with a loss of SERCA2a inhibition by PLN. All components of energy metabolism were depressed; myocyte energy charge was preserved under quiescence but reduced during stimulation. Cytosolic Ca^{2+} buffering or SERCA2a blockade reduced O_2 consumption with larger effect in the mutant. Signaling changes suggest cellular adaptation to perturbed Ca^{2+} dynamics and response to stress.

Conclusions: (1) PLN R14del$^{+/-}$ loses its ability to inhibit SERCA2a, which argues against SERCA2a superinhibition as a pathogenetic mechanism; (2) depressed energy metabolism, its enhanced dependency on Ca^{2+} and activation of signaling responses point to an early involvement of metabolic stress in the pathogenesis of this ACM model.

KEYWORDS

arrhythmogenic cardiomyopathy, energy metabolism, phospholamban, PLN R14del$^{+/-}$, PLN-SERCA2a interaction

Francesco Lodola and Antonio Zaza equally contributed to this work.

1 | INTRODUCTION

Phospholamban (PLN) is a small protein which restrains SERCA2a operation, thus limiting Ca^{2+} uptake by the sarcoplasmic reticulum (SR) under resting conditions. Receptor triggered phosphorylation (e.g., by PKA) positively regulates SERCA2a by relieving inhibition by PLN.

The heterozygous deletion of arginine 14 in PLN (PLN R14del$^{+/-}$) is associated with a form of arrhythmogenic dilated cardiomyopathy (ACM), characterized by PLN aggregate formation, myocardial fibrosis, and heart failure, with typical onset at middle age.[1] PLN R14del$^{+/-}$ is among the prevailing cardiomyopathy-related mutations, particularly in the Netherlands[2] and currently lacks a specific treatment. More than a decade ago, the pioneering work of Haghighi et al.[3] ascribed PLN R14del$^{+/-}$ phenotype to a "superinhibitory" effect on SERCA2a detected, in a heterologous expression system, as a decrease in sensitivity of pump function to Ca^{2+}. Several subsequent studies, inspired by this interpretation, provided more or less indirect support[4–6] but also conflicting results.[7–9] At any rate, even among the supporting studies, the mechanisms proposed to account for the superinhibitory effect were inconsistent and remain debated.

The "superinhibition" theory motivated us to test reversal of PLN R14del$^{+/-}$ phenotype by a recently developed compound (PST-3093) that selectively stimulates SERCA2a by antagonizing its interaction with PLN.[10] Unexpectedly, human iPS cardiomyocytes (hiPS-CMs), derived from a heterozygous human mutation carrier, displayed a hyperdynamic Ca^{2+} handling instead, a phenotype that is obviously incompatible with SERCA2a "superinhibition". Notably, PST-3093 mimicked the effect of the mutation when applied to the WT hiPS-CMs, but was ineffective in mutant ones.[11] Studies on contracting engineered tissues (EHT), obtained from the same hiPS-CMs, detected a major decrease in force development and energy metabolism derangements, but no clear abnormalities in intracellular Ca^{2+} dynamics.[12] Nonetheless, being such studies based on immature cells from a single mutation carrier, caution is warranted in generalization of these results, particularly in light of the wide acceptance of the superinhibition hypothesis.

We have developed and characterized a PLN R14del$^{+/-}$ transgenic (TG) mouse model which closely recapitulates the human ACM phenotype, including lack of cardiac abnormalities at young age.[13] The present work characterizes cardiomyocytes (CMs) obtained from this disease model in terms of mutation effect on intracellular Ca^{2+} dynamics and energy metabolism. This with the aim of testing the "superinhibition" theory in native mature CMs and compare them to hiPS-CMs for metabolic derangements, thus providing cross-validation of experimental models of the disease.

Evaluation of primary pathogenetic mechanisms in mutations leading to contractile deficit is complicated by overlap with the etiology-unspecific maladaptive process induced by the deficit itself, in which SERCA2a loss of function dominates.[14] To minimize this potential confounder, we selected an animal age at which cardiac contraction is still normal in the PLN R14del$^{+/-}$ TG mice.[13]

2 | RESULTS

2.1 | SERCA2a ATPase activity

SERCA2a ATPase activity correlates with Ca^{2+} transport rate,[15] its measurement in myocardial homogenates provides direct information on the transporter function in a simplified (cell-free) system. Ca^{2+}-sensitivity of SERCA2a activity is mostly determined by SERCA2a-PLN interaction and is therefore suitable to detect its abnormalities.[15] In myocardial homogenate preparations, the Ca^{2+} dissociation constant [Kd_{Ca}] of SERCA2a ATPase activity was 21% lower (unpaired Student's *t*-test, $p = 0.0005$) in Mut; the maximum velocity of SERCA2a ATPase activity was similar between Mut and WT preparations. Mut SERCA2a ATPase activity exceeded WT one above 300 nM Ca^{2+} (Figure 1).

This observation suggests reduced inhibition of SERCA2a by PLN in Mut preparations.

2.2 | Intracellular Ca^{2+} dynamics

Next, we evaluated SERCA2a function in the context of an intact myocyte. To improve mechanistic interpretation of the mutation effect, studies with an agent known to increase SERCA2a function by preventing its interaction with PLN[10] were included. SERCA2a function may have different impact on intracellular Ca^{2+} dynamics at different heart rates; therefore, the rate-dependency of changes in Ca^{2+} dynamics was also evaluated in a separate set of CMs field-stimulated at four rates between 1 and 2 Hz. Since these experiments aim to compare the rate-dependency of effect, statistical significance refers to the Treatment × Rate interaction.

2.2.1 | Effect of the mutation

Steady-state stimulation (1 Hz)

Mut effect on intracellular Ca^{2+} dynamics was assessed in intact WT and Mut CMs during steady-state field-stimulation at 1 Hz (Figure 2). Ca^{2+} transient (CaT) parameters were measured as described in Section 5. In Mut CMs τ_{decay} (Figure 2E) was shorter by 43% (Mann–Whitney *U*-test, $p < 0.0001$ vs. WT), diastolic Ca^{2+} (CaD, Figure 2F) was 5% lower

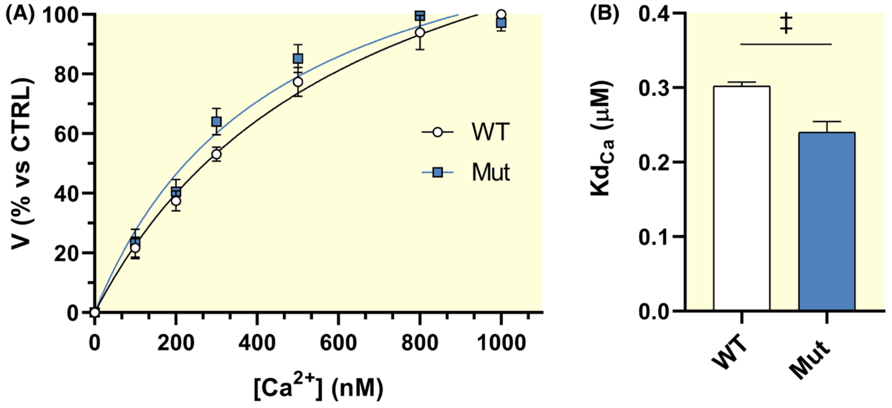

FIGURE 1 Ca^{2+}-dependent activation of SERCA2a ATPase in ventricular homogenates. (A) SERCA2a (CPA-sensitive) ATPase activity as function of medium Ca^{2+} concentration; solid lines obtained by fitting with Hill functions. (B) Ca^{2+} dissociation constant (Kd_{Ca}, lower values reflect increased affinity) estimated from the fitting (WT: 0.30 ± 0.01, $n = 10$; Mut: 0.24 ± 0.01, $n = 8$). WT: $N = 2$ preparations (4–5 technical replicates each); Mut: $N = 2$ preparations (4 technical replicates each). Data are expressed as mean ± SEM. Unpaired Student's *t*-test.

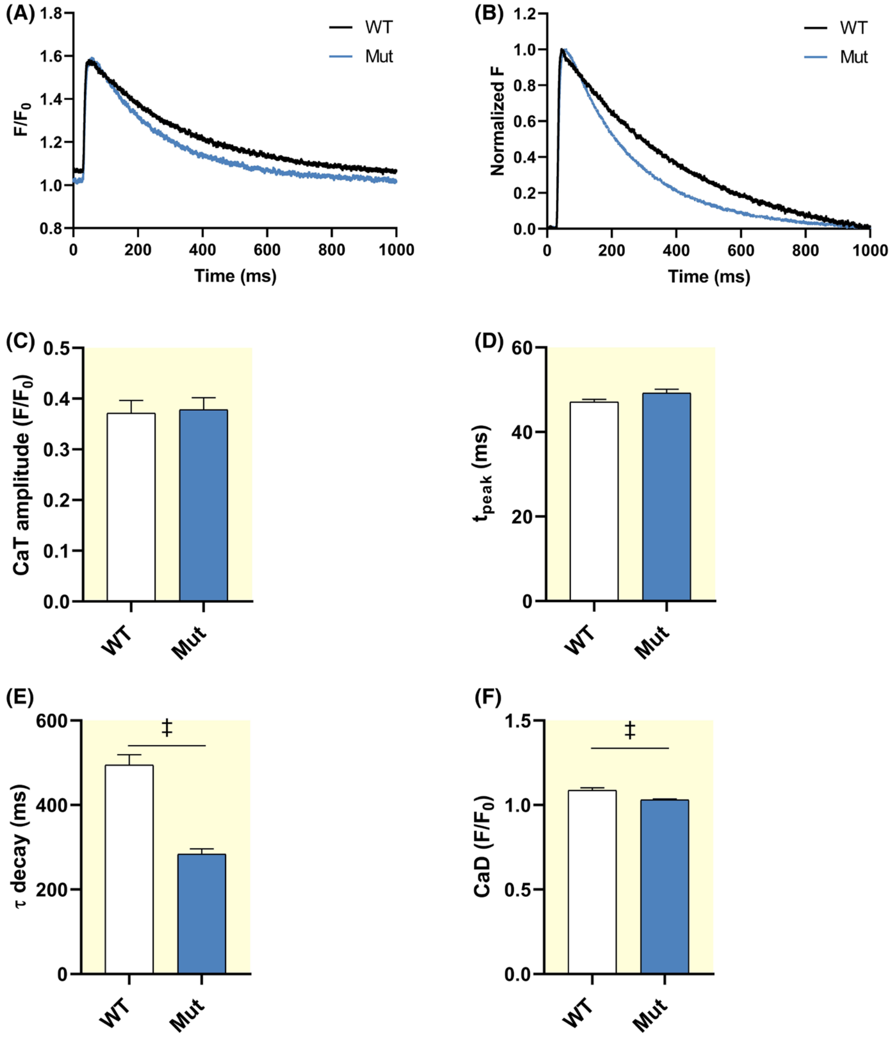

FIGURE 2 Parameters of calcium transients. (A) Representative Ca^{2+} transients (CaT). (B) CaT normalized to peak amplitude to illustrate changes in kinetics. (C) CaT amplitude (WT: 0.37 ± 0.03, $n = 32$; Mut: 0.38 ± 0.02, $n = 27$). (D) CaT time to peak, t_{peak} (WT: 47.1 ± 0.56, $n = 30$; Mut: 49.2 ± 0.94 $n = 27$). (E) Ca^{2+} transient decay kinetics, τ_{decay} (WT: 495 ± 24.1, $n = 32$; Mut 284 ± 12.2, $n = 27$). (F) Diastolic Ca^{2+}, CaD (WT: 1.09 ± 0.02, $n = 31$; Mut: 1.03 ± 0.01, $n = 27$). WT: $N = 4$; Mut: $N = 4$. Data expressed as mean ± SEM; *p* by Mann–Whitney *U*-test.

(Mann–Whitney *U*-test, $p = 0.0002$ vs. WT) and remarkably less variable. CaT amplitude (Figure 2C) and rise-time (t_{peak}, Figure 2D) were comparable between the two genotypes.

Rate-dependency

The following CaT parameters showed significant rate-dependency in WT CMs (Figure S1): t_{peak} (inverse,

$p < 0.0001$), τ_{decay} (inverse, $p < 0.0001$), CaD (direct, $p < 0.0001$).

As compared to WT, in Mut CMs: τ_{decay} had a shallower rate-dependency (Figure S1C, Mixed-effects model, Treatment × Rate, $p = 0.0015$ vs. WT) due to preferential shortening at slow rates. As expected from faster SR Ca^{2+} uptake, CaD accumulation was less pronounced in Mut CMs (Figure S1D, Mixed-effects model, Treatment × Rate, $p = 0.0114$ vs. WT).

For the remaining parameters, rate dependency was similar between the two genotypes.

SR reloading rate and steady-state SR Ca^{2+} content

SR Ca^{2+} uptake function was assessed in V-clamped CMs by the "SR reloading" protocol and by measuring caffeine-releasable SR Ca^{2+} content (CaSR) (Figure 3A, see Section 5). The difference between Mut and WT CMs in the behavior of CaT parameters during SR reloading (from step 1 to 15) is reported below (Figure 3).

CaT amplitude progressively increased during SR reloading, as expected (Figure 3C). The rate of such increment, as well as the final amplitude value, were larger for Mut CMs (Mixed-effects model, Treatment × Step, $p < 0.0001$ vs. WT). The same pattern was observed after CaT normalization for Ca^{2+} influx through I_{CaL} (Figure 3F, CICR gain); however, because of the larger variance in Mut data, for this parameter statistical significance was not achieved.

The τ_{decay} progressively decreased during SR reloading (Figure 3D). In Mut CMs it started off from considerably lower values, but its progressive decline over the protocol was shallower (Mixed-effects model, Treatment × Step, $p < 0.0001$ vs. WT). CaD started off from a lower value in Mut CMs (unpaired Student's *t*-test, $p = 0.0085$), but the difference decreased thereafter (Figure 3E, Mixed-effects model, Treatment × Step, $p = 0.0061$ vs. WT).

Under the conditions of this experiment, SR Ca^{2+} content (CaSR) was considerably larger in Mut CMs (Figure 3H, unpaired Student's *t*-test, $p = 0.0003$ vs. WT); fractional release was similar between Mut and WT CMs (Figure 3I).

To summarize, as compared to WT ones, Mut CMs were characterized by "hyperdynamic" Ca^{2+} handling, compatible with loss of SERCA2a inhibition (as opposed to enhanced inhibition). This pattern was consistent between CaT parameters of intact CMs during field-stimulation and evaluation of SR reloading under V-clamp.

NCX "conductance" and equilibrium

NCX functional parameters were measured during the caffeine pulse, that is under conditions short-circuiting SR transports (Figure S2).

In Mut CMs NCX "conductance" was significantly decreased (Figure S2B, Mann–Whitney *U*-test, $p = 0.02$ vs. WT); Ca^{2+} concentration at the (extrapolated) 0 I_{NCX} value (transport equilibrium point) was not significantly changed (Figure S2C).

2.2.2 | Effect of PLN antagonism (PST-3093) in MUT versus WT CMs

Steady state stimulation (1 Hz)

The effect of PLN antagonism by PST-3093 on intracellular Ca^{2+} dynamics was assessed in intact WT and Mut CMs during steady-state field-stimulation at 1 Hz. CaT parameters were measured as described in the Section 5.

In WT CMs, PST-3093 reduced τ_{decay} by 24% (Figure S3E, One-way ANOVA, post-hoc $p = 0.0209$ vs. Control); the remaining parameters were unaffected (Figure S3).

In Mut CMs, PST-3093 failed to affect the CaT parameters significantly (Figure S3), notably including τ_{decay} (Figure S3E).

Rate dependency

For both WT and Mut CMs, CaT parameters showing significant rate dependency (direct or inverse) under control conditions were: t_{peak} (inverse, $p < 0.0001$), τ_{decay} (inverse, $p < 0.0001$) and CaD (direct, $p < 0.0001$) (Figures S4 and S5).

In Mut CMs, PST-3093 enhanced rate-dependent accumulation of CaD (Figure S5D, Mixed-effects model, Treatment × Rate, $p = 0.004$ vs. Control). Rate dependency of all the remaining parameters was not significantly affected by PST-3093 in both genotypes (Figures S4 and S5).

To summarize, in WT CMs PST-3093 had, as postulated, effects compatible with SERCA2a activation (hyperdynamic Ca^{2+} handling), although quantitatively smaller than those exerted by the mutation. On the

FIGURE 3 SR Ca^{2+} uptake and content. (A) Experimental protocol. (B) Representative Ca^{2+} transients (CaT, upper panels) and voltage-dependent calcium currents (I_{CaL}) (lower panels) recorded during SR reloading after caffeine-induced depletion. WT (black) and Mut (green) traces are superimposed for comparison. (C–F) Mean values of CaT parameters measured during each voltage step (1–15) of the loading train. WT: $n = 9$, $N = 7$; Mut: $n = 11$, $N = 6$; p by Mixed-effects ANOVA for loading rate. (G) Representative traces of Ca^{2+} transients (upper panels) and membrane currents, I_m (lower panels) recorded during caffeine-induced SR release. (H) SR Ca^{2+} content (CaSR) estimated from the integral of I_m (representative of I_{NCX}) (WT: 0.89 ± 0.11, $n = 9$; Mut: 1.91 ± 0.19, $n = 11$). (I) Fractional SR Ca^{2+} release (WT: 0.83 ± 0.04, $n = 9$; Mut: 0.91 ± 0.06, $n = 11$). WT: $N = 7$; Mut: $N = 6$. Data expressed as mean ± SEM; p by unpaired Student's *t*-test.

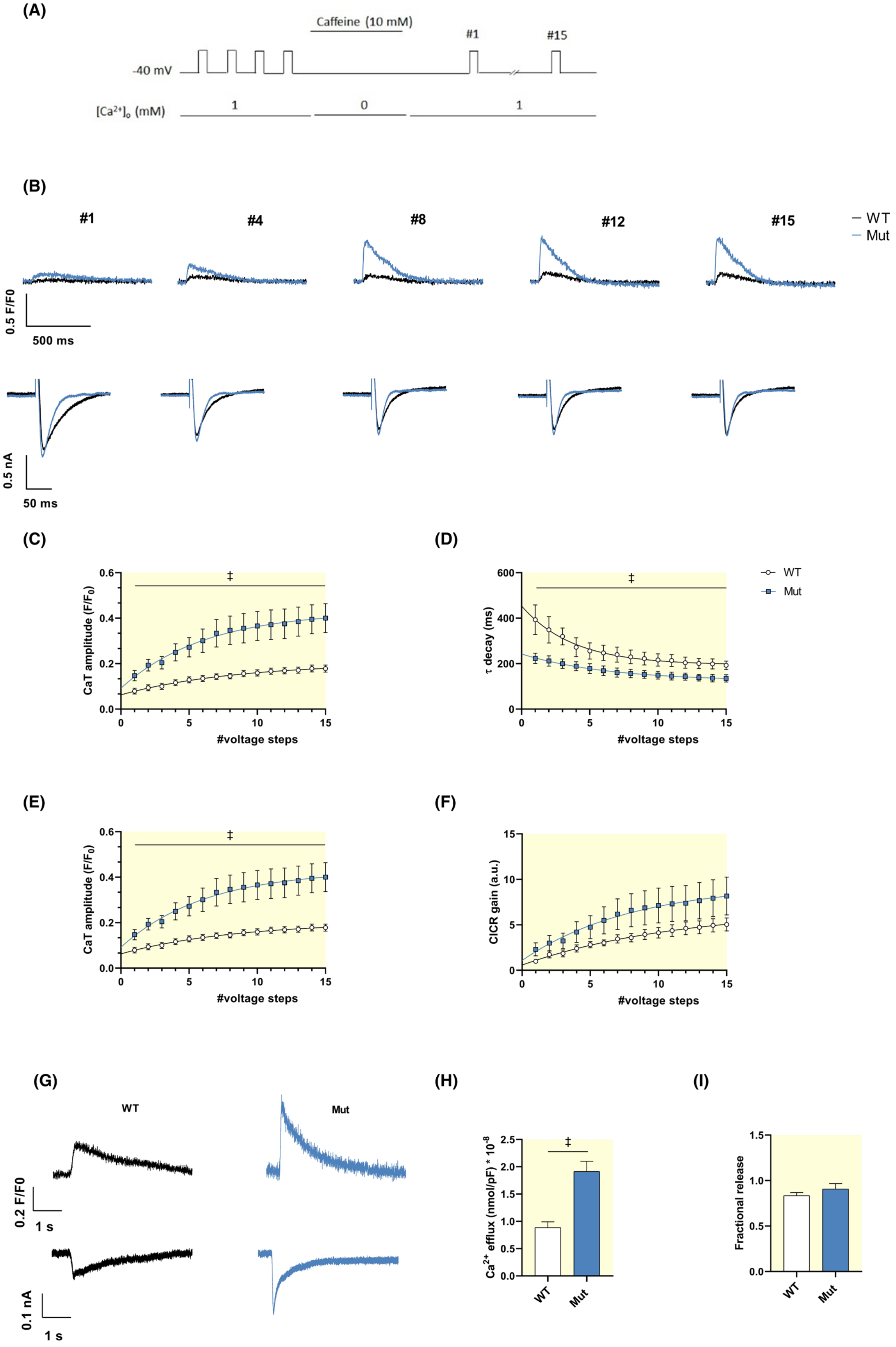
(A)
Caffeine (10 mM)
#1
#15
-40 mV
[Ca2+]o (mM)
1
0
1
(B)
#1
#4
#8
#12
#15
WT
Mut
0.5 F/F0
500 ms
0.5 nA
50 ms
(C)
CaT amplitude (F/F0)
#voltage steps
‡
(D)
τ decay (ms)
#voltage steps
‡
WT
Mut
(E)
CaT amplitude (F/F0)
#voltage steps
‡
(F)
CICR gain (a.u.)
#voltage steps
(G)
WT
Mut
0.2 F/F0
1 s
0.1 nA
1 s
(H)
Ca2+ efflux (nmol/pF) * 10-8
‡
WT
Mut
(I)
Fractional release
WT
Mut

other hand, PST-3093 effects were nil, or even opposite, in Mut CMs.

2.3 | Energy metabolism

Derangement of mitochondrial function is a common feature of the (secondary) "remodeling" process and is related to mishandling of intracellular Ca^{2+} and it ultimately contributes to the development of heart failure. The aim of this set of experiments was to test whether the energy metabolism was altered in Mut CMs at a stage preceding overt contractile failure, thus possibly acting as a primary pathogenetic factor instead. Notably, because of technical constraints, metabolic measurements were performed in unstimulated (quiescent) CMs.

2.3.1 | Oxygen consumption rate

O_2 consumption rate (OCR) was compared between quiescent WT and Mut CMs within the same multiwell plate (Figure 4). OCR values were normalized for the number of cells in each well. Mitochondrial respiration profile, from which the respiration parameters were derived, was obtained by modulating specific functions with pharmacological agents, as described in the Section 5. The pattern observed in Mut CMs is reported below as relative to that of WT ones.

Overall, OCR was significantly depressed in Mut CMs (Figure 4A); the observation was reproduced with remarkable consistency across all the preparations tested. The largest difference was found in maximal OCR (Figure 4C, −36%; Mann–Whitney *U*-test, $p < 0.0001$); nonetheless, basal OCR (Figure 4B, −39%; unpaired Student's *t*-test, $p = 0.0006$) and spare respiratory capacity (Figure 4D, −35%; Mann–Whitney *U*-test, $p < 0.0001$) were also reduced. Notably, significantly lower values were also found for the non-mitochondrial component of OCR (Figure 4E, −38%; unpaired Student's *t*-test, $p = 0.0003$).

Modulation of OCR by cytosolic Ca^{2+}, and by the SR compartment specifically, was evaluated in a subset of samples. To this end, cytosolic Ca^{2+} was chelated by BAPTA-AM (BAPTA) (Figure 5A,B,C,E) and SERCA2a was inhibited by thapsigargin (THAPSI) incubation, thus functionally removing the SR contribution (Figure 5A,B,D,F). Both interventions depressed basal OCR, though, THAPSI effect did not differ significantly between WT and Mut CMs (Figure 5 middle panels). Maximal OCR was instead unaffected by THAPSI in WT CMs, but significantly depressed in Mut ones (Figure 5 bottom panels). There was no obvious difference between BAPTA and THAPSI effects on OCR. The drugs vehicle (DMSO) unexpectedly increased OCR in Mut myocytes only. Nonetheless, the same DMSO concentration was present across the experimental groups; therefore, this effect does not impact on the evaluation of BAPTA and THAPSI effect.

2.3.2 | Glycolysis

Anaerobic glycolytic metabolism was evaluated, in the same plates subjected to OCR measurements, as proton efflux rate (PER) (Figure 6). PER values were normalized for the number of cells in the wells of the Seahorse plate. PER was measured under basal conditions, after inhibiting mitochondrial respiration (by Rotenone/Antimycin A) to assess compensatory glycolysis, and after blocking glycolysis by 2-deoxy-D-glucose (2DG) to assess non-glycolytic acidification.

Anaerobic glycolysis was depressed in Mut CMs as compared to WT ones (Figure 6A). While basal glycolysis showed only a trend to reduction (Figure 6B, −23%; unpaired *t*-test, $p = 0.0882$), compensatory glycolysis (Figure 6C, −47%; unpaired Student's *t*-test, $p = 0.0005$) and glycolytic reserve (Figure 6D, −58%; unpaired Student's *t*-test, $p = 0.0015$) were severely depressed. Non-glycolytic acidification was slightly (−23%), but still significantly, reduced (Figure 6E, Mann–Whitney *U*-test, $p = 0.0089$).

2.3.3 | Cell energy charge

To assess whether the reduction in energy metabolism of Mut CMs leads to energy starvation, we measured the current carried by the glibenclamide-sensitive K^+ channel (I_{KATP}), whose conductance is sensitive to the ADP/ATP ratio.[16] This surrogate measurement (validation reported in Figure S6B) was adopted because, in preliminary experiments, we found bulk fluorescence ATP assays to be confounded by unusually large number of dead CMs in the preparations (see Figure S6A). To avoid intracellular dialysis by the pipette content, measurements were performed with the perforated-patch technique. I_{KATP} was recorded at −120 mV, membrane potential at which K^+ currents are expectedly inward (i.e., a positive current shift reflects a decrease in I_{KATP}). I_{KATP} was normalized to membrane capacitance to obtain current density.

Under quiescence, no significant difference in mean I_{KATP} density was observed between WT and Mut CMs; nonetheless, very large I_{KATP} values were occasionally recorded in Mut CMs (Figure 7A,B). Immediately after stimulation, mean I_{KATP} density was approximately 3-fold larger in Mut CMs than in WT ones (Figure 7C,D).

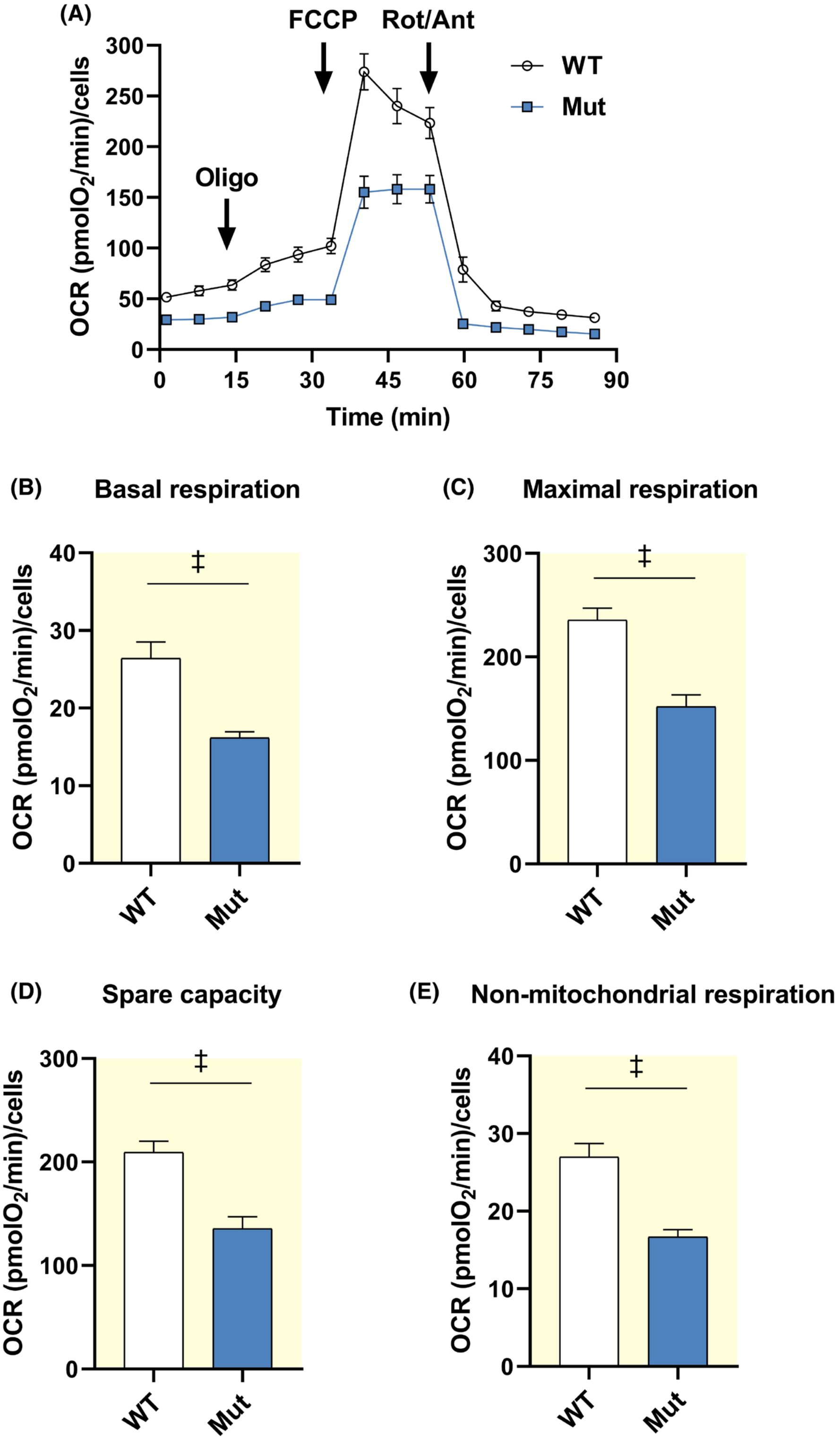

FIGURE 4 Parameters of mitochondrial respiration. (A) Oxygen consumption rate (OCR) profiles of WT and Mut CMs subjected to sequential injections of 1.5 μM Oligo, 0.5 μM FCCP and 3 μM Rot/Ant A (XF Mito Stress Test protocol). (B) Basal OCR (WT: 26.40 ± 2.13, $n = 31$; Mut: 16.20 ± 0.76, $n = 19$). (C) Maximal OCR (WT: 235 ± 11.46, $n = 31$; Mut: 151 ± 11.54, $n = 19$). (D) Spare respiratory capacity (209 ± 10.76, $n = 31$; Mut: 129 ± 12.6, $n = 17$). (E) Non-mitochondrial OCR (WT: 26.97 ± 1.74, $n = 31$; Mut: 16.68 ± 0.94 $n = 19$). WT: $N = 3$; Mut: $N = 3$. Data are expressed as mean ± SEM; p by unpaired Student's t-test and Mann–Whitney U-test.

2.3.4 | Intracellular ROS and mitochondrial membrane potential (Ψ_m)

Intracellular radical oxygen species (ROS) content was estimated in quiescent CMs by measuring 2′7′-dichlorofluorescin diacetate (DCFDA) fluorescence; confocal images were automatically analyzed to quantify the signal from individual vital cells. In Mut CMs, DCFDA signal was marginally, but significantly, lower than in WT CMs (Figure S7A, −5%; unpaired Student's t-test, $p = 0.0115$ vs. WT), to indicate a slight reduction in ROS content.

Mitochondrial membrane potential (Ψ_m) was evaluated by the fluorescent probe tetramethylrhodamine, ethyl ester (TMRE). TMRE signal was similar between Mut and WT CMs (Figure S7B). In the same CMs of both groups,

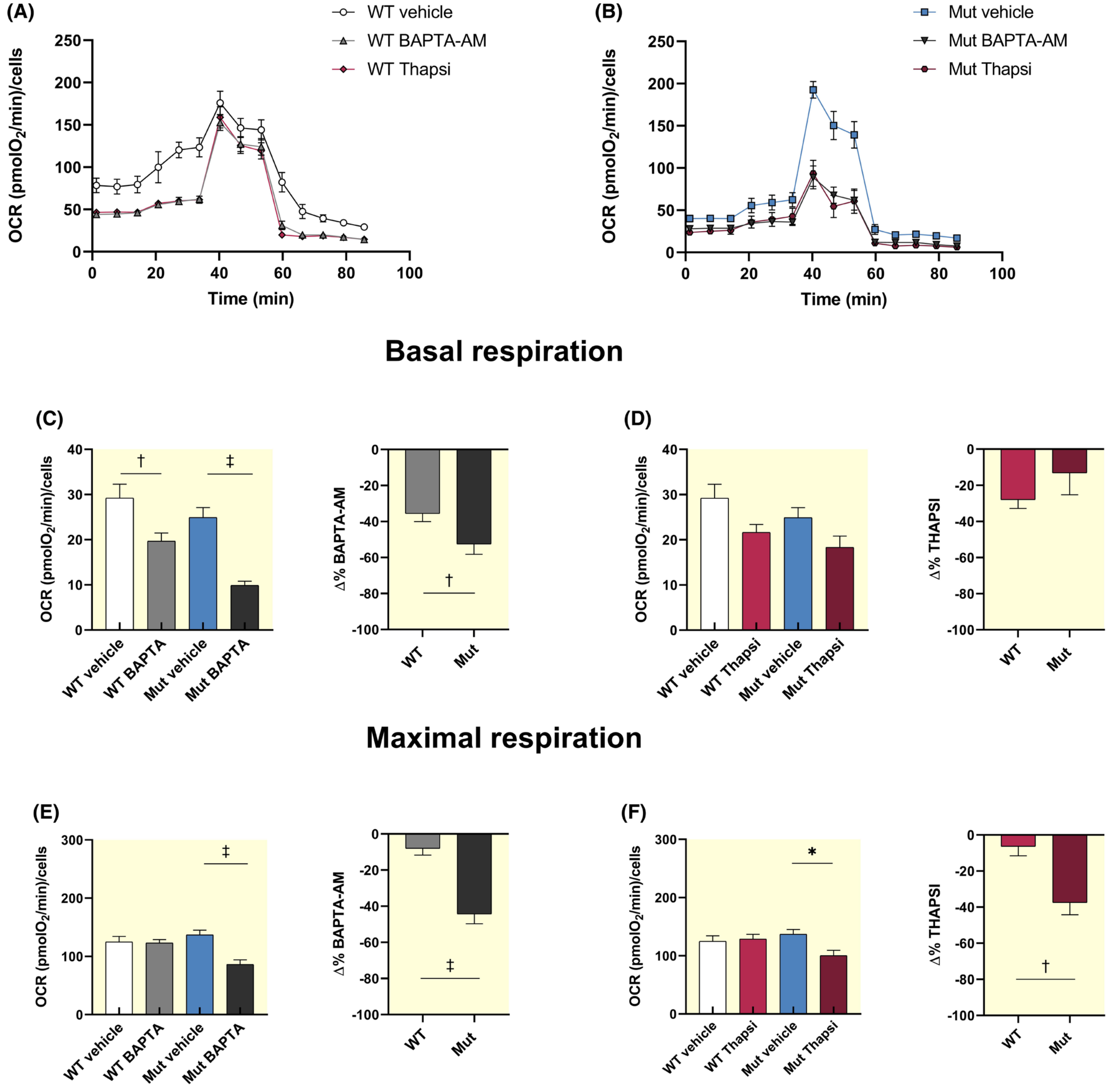

FIGURE 5 Effect of BAPTA-AM and Thapsigargin on oxygen consumption rate (OCR). (A, B) OCR profiles of WT and Mut CMs (protocol as in Figure 4) treated with BAPTA-AM (BAPTA, 5 μM) or thapsigargin (THAPSI, 5 μM). (C, D) Treatment Effect on basal OCR (WT vehicle: 29.22 ± 3.04, *n* = 19 wells; WT BAPTA: 19.69 ± 1.79, *n* = 35 wells; Mut vehicle: 24.92 ± 2.20, *n* = 15 wells; Mut BAPTA: 9.89 ± 0.93, *n* = 26 wells); (WT vehicle: 29.22 ± 3.04, *n* = 19 wells; WT THAPSI: 21.67 ± 1.71, *n* = 30 wells; Mut vehicle: 24.92 ± 2.20, *n* = 15 wells; Mut THAPSI: 18.32 ± 2.51, *n* = 24 wells). (E, F) Treatment effect on maximal OCR (WT vehicle: 125 ± 9.42, *n* = 18 wells; WT BAPTA: 123 ± 5.61, *n* = 35 wells; Mut vehicle: 137 ± 8.00, *n* = 15 wells; Mut BAPTA: 86.43 ± 7.63, *n* = 27 wells); (WT vehicle: 125 ± 9.42, *n* = 18 wells; WT THAPSI: 129 ± 7.97, *n* = 31 wells; Mut vehicle: 137 ± 8.00, *n* = 15 wells; Mut THAPSI: 100 ± 9.08, *n* = 24 wells). WT: *N* = 3; Mut: *N* = 3. Data are expressed as mean ± SEM. One-way ANOVA and Kruskal–Wallis test for % data.

short-circuit of mitochondrial membrane by FCCP significantly increased TMRE signal, thus confirming responsiveness of the probe to Ψ_m changes (Figure S7B-inset).

To summarize, despite the absence of overt mitochondrial damage (normal ROS content and membrane polarization), both the oxidative and anaerobic components of energy metabolism were depressed in Mut CMs. While OCR was clearly sensitive to interventions affecting cytosolic Ca^{2+}, only the response of maximal OCR differed between WT and Mut CMs. A defect in cell energy charge of Mut CMs, undetectable under quiescence, was clearly uncovered by stimulation.

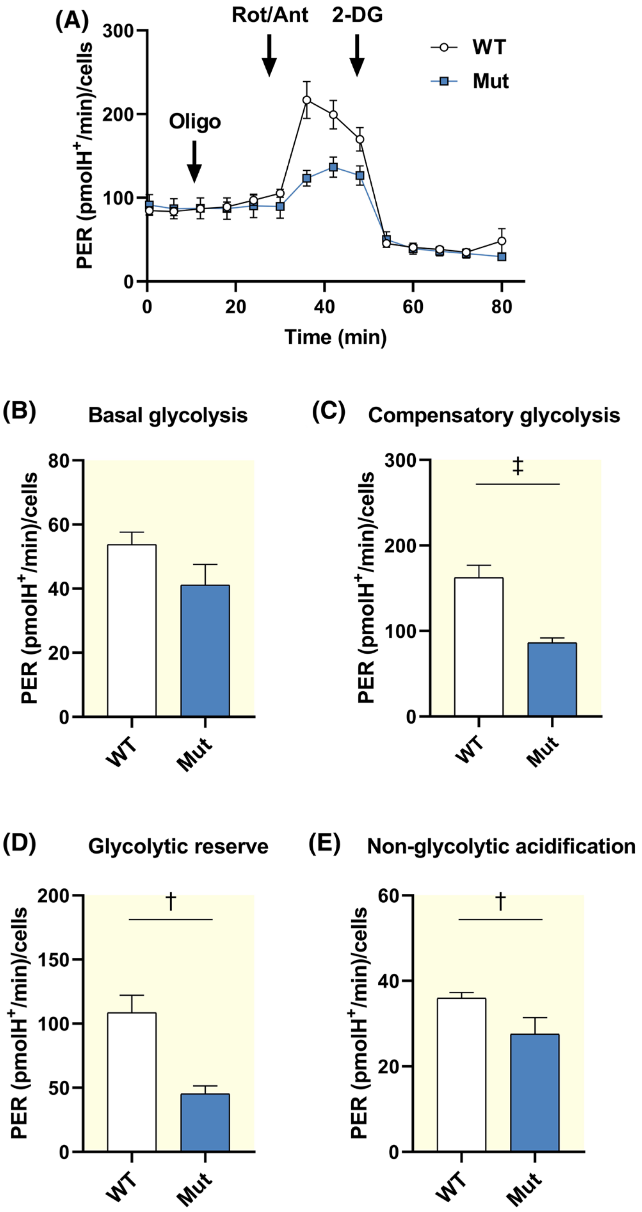

FIGURE 6 Parameters of anaerobic glycolysis. (A) Proton efflux rate (PER) profile of WT and Mut CMs subjected to sequential injections of 1.5 μM Oligo, 3 μM Rot/Ant and 50 mM 2-DG. (B) Basal glycolysis (WT: 53.77 ± 3.84, $n = 13$; Mut: 41.15 ± 6.42, $n = 9$). (C) Compensatory glycolysis (WT: 162 ± 14.52, $n = 13$; Mut: 86.34 ± 5.48, $n = 9$). (D) Glycolytic reserve (WT: 109 ± 13.58, $n = 13$; Mut: 45.19 ± 6.23, $n = 9$). (E) Non-glycolytic acidification (WT: 36 ± 1.29, $n = 13$; Mut: 27.56 ± 3.84, $n = 9$). WT: $N = 3$; Mut: $N = 3$. Data expressed as mean ± SEM; p by unpaired Student's t-test or Mann–Whitney U-test.

2.4 | Transcript and protein analysis

The functional derangements reported above may suggest profound changes in Mut CMs biology, may they depend on altered Ca^{2+} handling, or on direct toxicity of mutated PLN. In a broad, but focused, attempt to identify specific processes involved in the overall cell response to the mutation, we analyzed transcriptional expression of elements clustering in the following functional groups: (1) remodeling of mitochondria (Mitophagy) and their SR contact sites (MERCS); (2) antioxidant response (DETOX); (3) response to energy starvation (AMPK); (4) response to ER stress (UPR); (5) CaMKII signaling (Figure S8). Western blots were obtained for pErk/Erk (Figure 8A), Bax (Figure 8B), IP_3R, pAMPK/AMPK (Figure 8C), pCaMKII/CaMKII (Figure 8D) and SERCA2 (Figure 8E).

The transcription of genes involved in UPR and mitophagy were unchanged (Figure S8). Nonetheless, a trend to activation of signals involved in the response to ER-stress (pErk/Erk and Bax) was observed at the protein level (Figure 8A,B).

Genes encoding a couple of AMPK isoforms were upregulated by 1.5–2 fold (Figure S8); however, the pAMPK/AMPK protein ratio showed, if anything, a trend to decrease, thus arguing against activation of energy starvation signaling, at least under quiescence (Figure 8C).

Genes encoding IP_3R were unchanged (Figure S8); nonetheless, IP_3R protein level was significantly increased (Figure 8C), perhaps as a compensation to increased OCR dependency on Ca^{2+} (see Figure 5).[12]

Genes encoding CaMKII were unchanged; moreover, at protein level, the pCaMKII/CaMKII ratio was not increased (Figure 8D). Thus, CaMKII signaling may not be activated at this disease stage.

Albeit failing to achieve statistical significance, SERCA2 expression showed a trend to increase in Mut myocardium (Figure 8E).

To summarize, transcript and protein analysis mainly led to negative conclusions regarding activation of energy starvation, CaMKII signaling or ROS detoxification. The few positive results hint to activation of ER-stress response and perturbed functional interaction between SR and mitochondria.

3 | DISCUSSION

The main findings of this study are as follows. As compared to WT ones, Mut hearts were characterized by (1) a lower Kd_{Ca} (higher Ca^{2+} affinity) of SERCA2a ATPase activity (Figure 1B); (2) intracellular Ca^{2+} dynamics compatible with enhanced SR Ca^{2+} uptake (Figure 2); (3) insensitivity of Ca^{2+} dynamics to PLN antagonism by PST-3093 (Figures S3–S5); (4) lower NCX conductance (Figure S2). All these findings point to diminished SERCA2a inhibition by Mut PLN, resulting in increased Ca^{2+} cycling by the pump. These changes in intracellular Ca^{2+} handling were accompanied by an overall depression of energy metabolism, consisting in a parallel reduction of OCR and anaerobic glycolysis (Figures 4

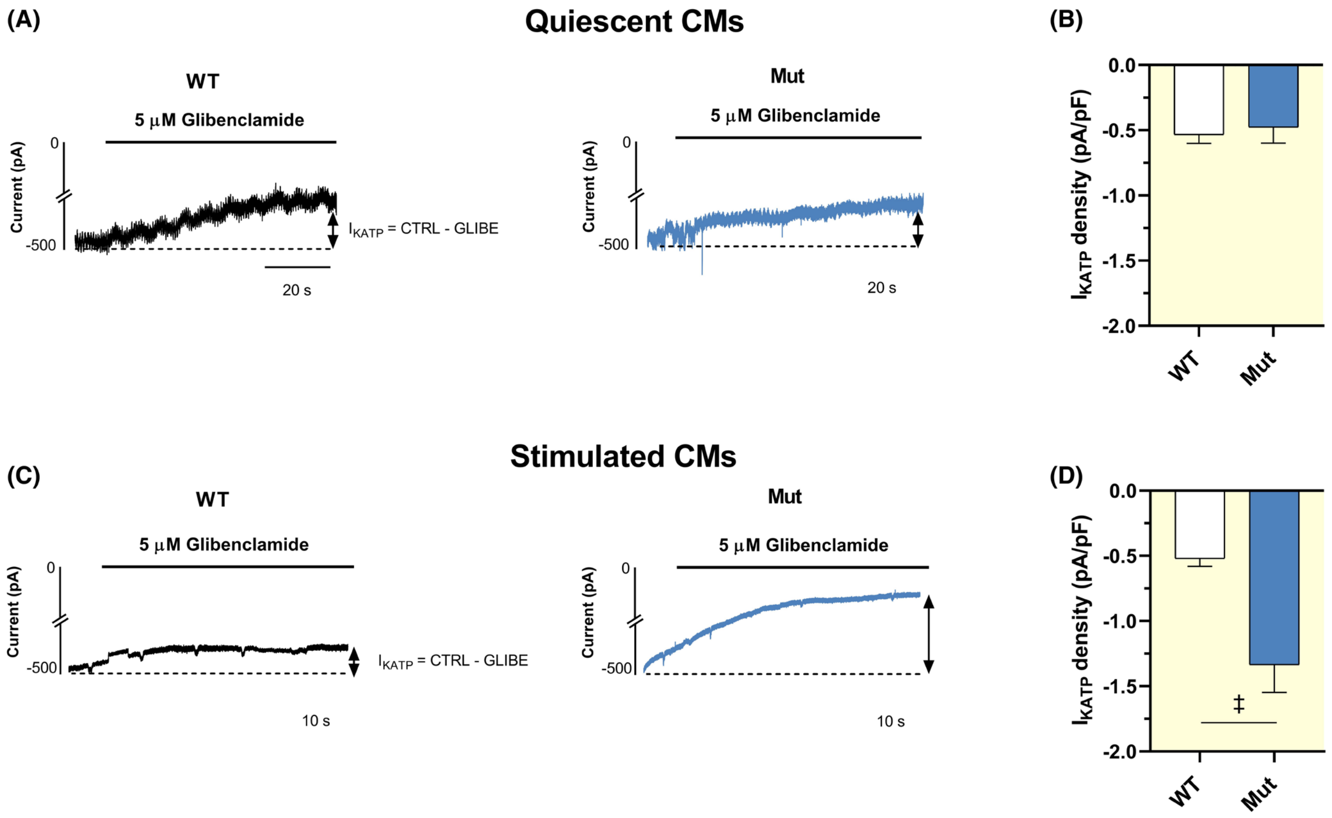

FIGURE 7 Energy charge in quiescent and paced CMs. Energy charge was estimated from the conductance of ATP-sensitive K^+ current (I_{KATP}), which is proportional to the ADP/ATP ratio. (A) Representative current traces recorded in quiescent CMs (holding potential −120 mV), in control conditions and during perfusion with 5 µM glibenclamide; I_{KATP} was calculated as the current difference (control − glibe) normalized to membrane capacitance to obtain current density. (B) Statistics of I_{KATP} density in quiescent CMs (WT: −0.53 ± 0.07, $n = 9$; Mut: −0.47 ± 0.12, $n = 8$). WT: $N = 7$; Mut: $N = 6$. (C) Representative current traces recorded after pacing (2 Hz) in control conditions and during perfusion with 5 µM glibenclamide. (D) Statistics of I_{KATP} density after pacing (WT: −0.52 ± 0.06, $n = 12$; Mut: −1.34 ± 0.21, $n = 10$). WT: $N = 3$; Mut: $N = 4$. Data expressed as mean ± SEM; p by unpaired Student's t-test.

and 6). Despite the apparent oxidative impairment, ROS content and mitochondrial membrane polarization were remarkably normal in Mut CMs (Figure S7). The Ca^{2+}-dependency of maximal OCR was increased in Mut CMs (Figure 5). Under quiescence, cell energy charge and energy starvation signaling (pAMPK/AMPK) were unperturbed (Figure 8); nonetheless, the pacing-induced reduction of cell energy charge was larger in Mut CMs (Figure 7).

3.1 | Intracellular Ca^{2+} dynamics

The mutation-associated changes in the parameters describing intracellular Ca^{2+} dynamics of intact CMs confirm the hyperdynamic state we observed in hiPS-CMs of a patient carrying the PLN-R14del mutation,[11] thus allowing generalization of that observation. The view that hyperdynamic Ca^{2+} handling reflects enhanced SERCA2a activity is reinforced by (1) increased Ca^{2+} sensitivity (lower Kd_{Ca}) of SERCA2a ATPase activity in myocardial homogenates; (2) similarity with the effect of PST-3093, a SERCA2a stimulator. The latter is known to increase SERCA2a activity by weakening its interaction with PLN,[10] thus suggesting reduced affinity for SERCA2a as a mechanism of PLN R14del behavior. In the PLN R14del heterozygous state, PST-3093 should have retained part of its stimulatory effect by displacing residual WT PLN. However, both in the PLN-R14del mouse (present study) and in heterozygous PLN R14del$^{+/-}$ patient-derived hiPS-CMs,[11] PST-3093 lost its SERCA2a stimulating effect completely (Figures S3–S5). This may suggest negative dominance of the mutation, one putative mechanism being enhanced PLN trapping in the non-inhibitory pentameric form.[17]

The hyperdynamic Ca^{2+} handling observed in the present study contrasts with the depressed Ca^{2+} handling reported in a heterozygous PLN R14del mouse based on knock-in of human PLN genes.[18,19] The development of cardiac abnormalities has a rather different time-course in the two models: whereas in the former signs of depressed contractility appear at 18–20 months of age,[13] clear-cut

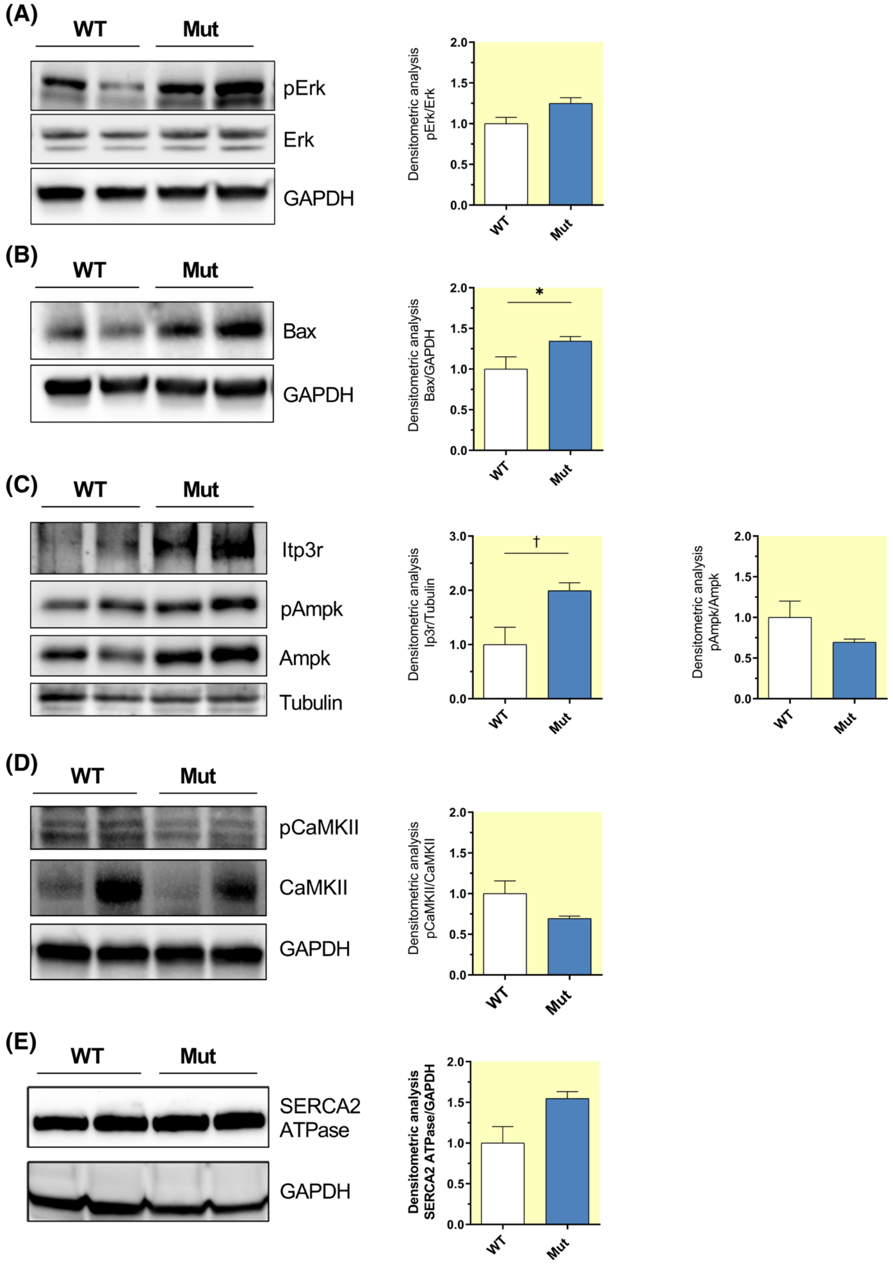

FIGURE 8 Protein analysis in myocardial homogenates. *Left panels*: representative Western Blots of proteins extracted from RV samples of WT and Mut mice (GAPDH or Tubulin included as housekeeping for normalization); *Right panels*: blot quantification by densitometric analysis normalized to housekeeping. (A) Erk and pErk (WT: 1.0000 ± 0.0777, $N=4$; Mut: 1.2493 ± 0.0691, $N=4$). (B) Bax (WT: 1.0000 ± 0.1506, $N=5$; Mut: 1.3475 ± 0.0529, $N=8$). (C) Ip3r (WT: 1.0000 ± 0.3180, $N=5$; Mut: 1.9938 ± 0.1457; $N=8$), total Ampk and pAmpk; densitometry shows pAmpk/total Ampk (WT: 1.0000 ± 0.2013, $N=5$; Mut: 0.6950 ± 0.0396, $N=8$). (D) CaMKII and pCaMKII; densitometry shows the pCaMKII/total CaMKII ratio (WT: 1.0000 ± 0.1566, $N=4$; Mut: 0.6936 ± 0.0309, $N=4$). (E) SERCA2 (WT: 1.0000 ± 0.2026, $N=3$; Mut: 1.5468 ± 0.0861, $N=3$). Data expressed as mean ± SEM; p by unpaired Student's t-test.

chamber dilatation and electrical remodeling were already present at 3 months in the latter.[18,19] The age at which myocyte studies were carried out is roughly similar in the two studies (2–3 months), that is in a markedly different relationship with the development of a failing phenotype. As depression of SR function is a landmark of the remodeled myocardium[20] this might explain the different Ca^{2+} handling phenotypes observed in the two models.

SERCA2a functional downregulation is a common consequence of maladaptive remodeling and plays an undisputable role in evolution of contractile dysfunction and arrhythmogenesis in heart failure. By analogy, enhanced SERCA2a inhibition would easily explain the PLN R14del$^{+/-}$ ACM phenotype, as previously claimed.[3] The present results suggest instead that PLN R14del$^{+/-}$ loses the ability to inhibit SERCA2a; the resulting "hyperdynamic" Ca^{2+} handling might look less plausible as a cause of reduced contractility. PLN knockout, and the resulting "hyperdynamic state" of Ca^{2+} handling, may be well tolerated in TG mice;[21] nonetheless, it may lead to overt cardiomyopathy over longer time spans in hiPS-CMs.[22] In the latter case, cellular derangements were supported by I_{NaL} enhancement,[22] but it was unclear whether this represented a primary mutation effect. The present results show that ROS and CaMKII signaling (well-known I_{NaL} enhancers) was unperturbed at the pre-symptomatic stage of the mutation, thus suggesting that hyperdynamic Ca^{2+} handling per se may be inadequate to enhance I_{NaL}. The view that PLN loss of function may be harmful on the long run is also supported by its association with ACM in human mutations,[23] by the observation that PLN-sarcolipin double knock-out triggers hypertrophic remodeling[24] and by the significant derangements occurring 2 months after PLN knock-out in hiPS-CMs.[22] Altogether, these findings indicate that constitutively unrestrained SERCA2a function may, in the long term, have a negative impact on myocyte biology. Notably, clinical ACM is indeed of late onset in PLN R14del$^{+/-}$ carriers.[1]

The discussion thus far assumes that PLN R14del detrimental effects depend on the impact of SERCA2a dysregulation on intracellular Ca^{2+} dynamics; however, this is not necessarily the case. For instance, in the case of the PLN R9C mutation, late ACM developed independently of the sign of changes in SERCA2a function.[25] Thus, mechanisms linked to the PLN mutation, but perhaps independent of Ca^{2+} dynamics, may derange myocyte biology. Unfortunately, this considerably broadens the array of mechanisms to be considered and, eventually, to be targeted with therapy (other than mutation reversal). Hence, we undertook a preliminary analysis of additional cell dysfunctions, potentially involved in the ACM of the PLN R14del$^{+/-}$ TG mouse. Although admittedly far from exhaustive, this analysis may provide relevant clues.

3.2 | Energy metabolism

Recent work on contracting hiPS-CMs organoids (EHTs) from a PLN R14del$^{+/-}$ carrier[12] detected abnormalities of the ER/mitochondrial compartment, reduced mitochondria number and function. Contraction force was halved in this preparation, despite a nearly normal SR function. Hence, we tested whether PLN R14del$^{+/-}$ TG affects energy metabolism in the mouse model, notably prior to the development of contractile dysfunction (i.e., as a primary abnormality). At least when quiescent (as dictated by the experimental setup), PLN R14del$^{+/-}$ CMs showed a substantial downregulation of energy metabolism, including its oxidative and anaerobic components (Figures 4 and 6).

Compatibility of overall depression of energy metabolism with grossly normal cardiac function in-vivo[13] is more surprising. Either function is maintained despite energy starvation, or ATP demand is reduced (at least at rest) in PLN R14del$^{+/-}$ CMs. To discriminate between these possibilities, we measured the I_{KATP} conductance (Figure 7), a surrogate of the ADP/ATP ratio, and activation of AMPK a major "energy starvation" signal (Figure 8). Albeit some heterogeneity was observed in I_{KATP} density, neither of the two measurements points to a mismatch between ATP production and demand under resting conditions. Why should PLN R14del$^{+/-}$ CMs consume significantly less ATP than WT ones? Under quiescence the Na^+/K^+ pump dominates as energy consumer.[26] Sarcolemmal Ca^{2+} extrusion, by the energetically coupled NCX-Na^+/K^+ pump complex, costs twice as much ATP as Ca^{2+} recycling to the SR by SERCA2.[27] Therefore, lowering of SERCA2a Kd_{Ca}, as in PLN R14del$^{+/-}$ CMs, might theoretically alleviate the load on the Na^+/K^+ pump and be energy saving. The reduction in NCX "conductance" (Figure S2), possibly an adaptation to SERCA2a dominance, would contribute to limit energy consumption. Coexistence of the energetic defect with normal ROS levels and mitochondrial membrane polarization (Figure S7) suggests that, at this stage, the former may reflect mitochondrial dysregulation, as opposed to overt damage. Increased OCR dependency on intracellular Ca^{2+} (Figure 5) might underlie such dysregulation (see below). On the other hand, pacing unveiled energetic incompetence in Mut CMs. This suggests that hyperdynamic Ca^{2+} handling may be inadequate to compensate for the metabolic defect when contraction dominates ATP consumption, thus perturbing the subtle balance preserving energy charge at rest.

3.3 | Coupling between Ca^{2+} dynamics and energy metabolism

Mitochondrial Ca^{2+} plays a pivotal role in the regulation of mitochondrial respiration and ATP synthesis. To test the involvement of altered Ca^{2+} dynamics in the reduction of (resting) OCR, the latter was measured in the presence of cytosolic Ca^{2+} chelation (BAPTA), or "functional deletion" of the SR store (THAPSI). Both interventions decreased OCR (Figure 5), thus confirming the role of Ca^{2+}, and the SR contribution, in its regulation. Interestingly, maximal-, but not basal-OCR, was differentially regulated in Mut versus WT CMs. This can be tentatively interpreted by considering that, whereas basal OCR responds to multiple Ca^{2+}-sensitive factors (including extra-mitochondrial ones), maximal OCR should depend exclusively on the intrinsic electron transport (ET) rate. ET rate is expectedly sensitive to matrix Ca^{2+}, required to support the production of reduced substrates fuelling the ET reactions. This considered, the stronger sensitivity of maximal-OCR to BAPTA and THAPSI peculiar of Mut CMs may reflect increased Ca^{2+} requirements of the reactions fuelling ET, or of ET reactions themselves. While this might be seen as adaptive to hyperdynamic Ca^{2+} handling, energetic incompetence of Mut CMs after pacing indicates a genuine defect in energy production.

The link between Ca^{2+} handling and energy metabolism abnormalities is still elusive. The metabolic response to PLN knock-out in hiPS-CMs is a transient increase in OCR, followed by mitochondrial damage only at a later stage.[22] This argues against hyperdynamic Ca^{2+} handling as a primary cause of mitochondrial dysfunction. Notably, while both PLN R14del$^{+/-}$ and PLN knock out induce a hyperdynamic state, in the latter PLN protein is missing. This may point to an additional pathogenetic mechanism in ACM caused by PLN R14del$^{+/-}$ but perhaps independent from changes in SERCA2a function.

3.4 | Transcript and protein analysis

Cell damage might be caused, independent of SERCA2a dysregulation, by direct toxicity of the mutant protein (ER-stress) and the resulting activation of the "unfolded protein response" (UPR).[28] ER-stress activation and reduced mitochondria abundance were indeed the main derangement detected in PLN R14del$^{+/-}$.[12] In the present study, transcript and protein analysis (Figure 8; Figure S8) mainly yielded negative results, which may nonetheless be informative. Failure to detect activation of energy starvation signaling under rest is in line with unchanged cell energy charge (normal resting I_{KATP} density, Figure 7). Lack of activation of ROS scavenging genes, along with normal ROS content and mitochondrial membrane potential, stand for the absence of major mitochondrial damage under quiescence. Similarly, lack of CaMKII activation argues against early involvement of Ca^{2+} decompartmentalization in disease pathogenesis.

4 | LIMITATIONS

Because of technical constraints, energy production and signaling were assessed in quiescent CMs. SERCA2a might be marginally activated in such condition and the presence of just a trend of OCR decrease in response to THAPSI (Figure 5D) supports this view. The cell metabolic state would be obviously different in contracting myocytes. This demands attention in referring each finding to the state (resting or contracting) under which measurements were carried out (clearly specified throughout the manuscript) and some speculation is necessarily involved in translating the study outcome to the contracting heart.

With the aim of disclosing initiating mechanisms, the present study evaluates mutation's effects before the development of overt cardiac abnormalities. As commonly occurs in cardiac remodeling, additional mechanisms may contribute to myocardial dysfunction at later stages.

The choice of sex uniformity to minimize variability fails to consider potentials sex differences in determining the extent of mutation manifestations.

Due to limited availability of material, SERCA ATPase activity (Figure 1) was measured from 2 hearts per experimental group. However, multiple technical replicates were obtained from each heart; furthermore, the result of this measurement is only part of the evidence leading to the conclusion that the mutation enhances SERCA2a function.

5 | MATERIALS AND METHODS

The methods are described here to the extent of allowing interpretation of results. A detailed description is given in the Data S1.

5.1 | Experimental model

The studies were performed on tissues from PLN R14del$^{+/-}$ (Mut) mice aged 8 to 12 weeks and their WT littermates (controls). In this age range, the animals are healthy; overt physical or echocardiographic signs of chamber remodeling or contractile dysfunction arise in this model at 18 months of age.[13] This is crucial to the interpretation of the observed changes as directly resulting from the mutation, rather than secondary to unspecific myocardial remodeling.

Myocytes were enzymatically dissociated with a manual perfusion method[29] which does not discriminate between right and left ventricles and studied within 24 h.

All experiments involving animals confirmed to the guidelines for Animal Care endorsed by the Milano-Bicocca and to the Directive 2010/63/EU of the European Parliament on the protection of animals used for scientific purposes.

5.2 | Measurements and techniques

- CPA-sensitive (SERCA2a) ATPase activity was measured in myocardial homogenates at multiple Ca^{2+} concentrations; data points were fitted to a sigmoidal (Hill) function, from which the maximum velocity (V_{max}) and Ca^{2+} affinity [Kd_{Ca}] parameters were estimated.
- Electrophysiological experiments were carried out by whole-cell patch clamp on isolated ventricular cardiomyocytes (CMs) in the ruptured- or perforated-patch configuration, as specified in the relevant Section 2.
- Cytosolic Ca^{2+} was optically measured from isolated CMs by using Fluo 4-AM as the Ca^{2+}-sensitive probe; fluorescence (F) was normalized to the value measured after prolonged quiescence (F0). Ca^{2+} measurements were carried out in field-stimulated CMs, or V-clamped CMs, as specified in the relevant Section 2.
- OCR and PER were measured under basal and metabolically stressed conditions in quiescent CMs seeded

in multiwell plates using the Seahorse technology (Agilent Extracellular Flux Analyzer XFe96) in order to determine mitochondrial respiratory and glycolytic bioenergetics. All measurements were normalized to the (automatically counted) number of viable CMs in the measuring well. All the experimental conditions were represented in each plate to allow comparisons within the same experiment; the position of each condition in the plate was swapped between experiments to prevent technical bias. The preparations were exposed to reagents to obtain specific OCR and PER parameters, as described in the Section 5.3.

- ROS content of CMs was measured after incubation with the fluorescent probe DCFDA. *Automated* (unbiased) confocal *single-cell* fluorescence measurement was performed by Operetta CLS™ (Operetta– Perkin Elmer) at 40× magnification.
- Mitochondrial membrane potential (Ψ_m) was measured from CMs using TMRE as probe. Stained CMs were seeded at the concentration 2.5×10^3 per well. TMRE fluorescence was analyzed by confocal imaging at 63× magnification (Operetta CLS™). At the concentration used in the present study, TMRE works in "quenching mode," that is emission increases as Ψ_m depolarizes.[30] At any rate, TMRE fluorescence signal was calibrated in each measurement by short-circuiting mitochondrial electron transport with FCCP.
- qRT-PCR was performed on mRNA extracted from myocardial samples and quantified by a NanoDrop spectrophotometer. qRT-PCR was performed with the primers reported in Table S1. All reactions were performed in a 384-well format. The relative quantities of specific mRNAs were obtained by the delta–delta Ct method with normalization to the housekeeping transcript glyceraldehyde 3-phosphate dehydrogenase (GAPDH).
- Western Blot Analysis was performed on RV samples. Total protein extracts were subjected to SDS-PAGE and transferred onto a nitrocellulose membrane, blocked for 1 h at room temperature and incubated overnight at 4°C with the appropriate primary antibodies (reported in Table S2). Peroxidase-conjugated secondary antibodies were then applied for 1 h and the peroxidase signal visualized using a chemiluminescent substrate. Blot images were acquired and blot densitometric analysis was performed by ImageJ software. Protein signals were normalized to that of the housekeeping proteins GAPDH or Tubulin.

5.3 | Experimental protocols

Significant parameters were extracted from the above measurements by applying suitable experimental protocols.

- Ca^{2+} transients (CaT) were evaluated in intact CMs., field-stimulated at 1 Hz. Ca^{2+} transient amplitude (CaT amplitude), Ca^{2+} transient decay kinetics (τ_{decay}), Ca^{2+} transient rise-time (t_{peak}) and diastolic Ca^{2+} (CaD) were measured. Rate-dependency of CaT properties was tested by stepwise increments in pacing rate (to 1, 1.3, 1.7, and 2 Hz).
- SR Ca^{2+} content was estimated in V-clamped CMs as the integral of the I_m (mostly representing I_{NCX}) elicited by a caffeine (10 mM) pulse, applied after a loading train of V steps (−40 to 0 mV at 1 Hz).[31] To avoid extracellular Ca^{2+} influx, caffeine was dissolved in Ca^{2+}-free solution (containing 1 mM EGTA CsOH).
- The "gain" of Ca^{2+}-induced Ca^{2+} release (CICR) was measured in V-clamped CMs as the Ca^{2+} release/influx ratio, as previously described.[32]
- The fraction of SR Ca^{2+} content released by membrane excitation (fractional release) was calculated as the ratio between the amplitudes of V- and caffeine-triggered CaT.
- Information on NCX function was obtained by linear fitting of the trailing branch of the $I_{NCX}/[Ca^{2+}]$ loops, recorded during caffeine-induced transients. The slope coefficient and the 0 I_{NCX} intercept were used as surrogate of NCX "conductance" and cytosolic $[Ca^{2+}]$ at electrochemical equilibrium, respectively.
- The Ca^{2+} uptake function of the SR was evaluated through a "SR reloading" protocol, applied under V-clamp; CaT and I_{CaL} were simultaneously recorded.[33] The SR was initially emptied by a caffeine pulse and progressively reloaded by a train (0.25 Hz) of 200 ms V steps from −40 to 0 mV. The following parameters were analyzed from each step of the protocol: (i) CaT amplitude, (ii) CICR gain, (iii) τ_{decay}, (iv) CaD. The rate of increment of the former two parameters during the loading protocol reports the rate of SR refilling. The time constant of CaT decay (τ_{decay}) reports the rate of cytosolic Ca^{2+} clearance (the faster Ca^{2+} removal, the smaller τ_{decay}) within each step, i.e., at varying SR filling levels. CaD course reports the rate of cytosolic Ca^{2+} accumulation.
- OCR and PER were monitored during sequential exposure of preparations to Oligomycin A (ATP synthase inhibitor), FCCP (in OCR only, short-circuits the electron transfer chain, ETC), Rotenone/Antimycin (block ETC complexes I and III) or 2-deoxy-D-glucose (2DG in PER only, inhibits glycolysis). Functional parameters were derived as follows:
  - OCR parameters: (i) mitochondrial basal respiration = OCR before Oligomycin − OCR after Rotenone/Antimycin; (ii) mitochondrial maximal respiration = OCR after FCCP − OCR after Rotenone/Antimycin; (iii) spare respiratory

capacity = mitochondrial maximal respiration – mitochondrial basal respiration; (iv) non-mitochondrial respiration = OCR after Rotenone/Antimycin.

  - PER parameters: (i) basal glycolysis = PER before Oligomycin – PER after 2DG; (ii) compensatory glycolysis = PER after Rotenone/Antimycin − PER after 2DG; (iii) glycolytic reserve = compensatory glycolysis – basal glycolysis; (iv) non-glycolytic acidification = PER after 2DG.

- I_{KATP} was used as surrogate reporter of the ADP/ATP ratio (see validation in Figure S6B). I_{KATP} was measured as glibenclamide-sensitive current while holding membrane potential at −120 mV (i.e., negative to K^+ equilibrium potential) in the perforated-patch configuration. Measurements were performed in unstimulated myocytes (quiescence) and immediately after a train of pacing of pulses at 2 Hz.

5.4 | Statistical analysis

Statistical analysis was carried out with GraphPad Prism 8. Normality of distribution was assessed using D'Agostino-Pearson's normality test. Comparison of sample means was carried out with parametric or non-parametric tests, according to the data type (continuous or categorical) and distribution normality. Parametric or non-parametric ANOVA (with the respective post-hoc corrections) were used for multiple comparisons of continuous or categorical data respectively. In the case of repeated measurements (e.g., rate-dependency and SR loading protocols) a mixed-effects ANOVA model containing "Treatment" (WT vs. Mut, PST-3093 vs. Control) and "Variable" (rate or step #) factors was used. Significance of "Treatment × Variable interaction" (i.e., difference between Treatments in their response to the Variable) was first tested; in its absence, significance of difference between Treatments at all Variable values was tested. In figures, data are presented as mean ± SEM. Whenever the threshold for statistical significance was achieved, the following symbols were used: $^*p < 0.05$, † $p < 0.01$, ‡ $p < 0.001$. Throughout the text, the actual p-value for the comparison was reported as an index of robustness. For each experiment, the number of preparations or cells (n) and the number of animals from which they were obtained (N) are indicated in the respective figure legend.

6 | CONCLUSIONS

The present results extend our previous observation in patient-derived hiPS-CMs[11] to indicate that PLN R14del$^{+/-}$ may upregulate SERCA2a activity, thus inducing hyperdynamic Ca^{2+} handling, in native mature CMs of the TG mouse. The mutation also results in a substantial downregulation of energetic metabolism at rest, not associated with signs of overt mitochondrial damage, but leading to energetic incompetence during pacing. Downregulation of energy production in resting mutant CMs might be seen as the "physiological" response to reduced ATP demand, expected from switch to SERCA2a dominance in Ca^{2+} handling. Nonetheless, increased OCR dependency on Ca^{2+} and pacing-induced energetic incompetence point to genuine mitochondrial dysfunction in Mut CMs.

While hyperdynamic Ca^{2+} handling is unlikely the primary cause of the metabolic defect at this disease stage, previous work suggests that toxicity of the mutant protein may be involved. Indeed, pronounced ER stress has been reported in PLN R14del$^{+/-}$ hiPS-CMs[12] and, despite the early disease stage, the present findings include activation of some signals related to unfolded protein response (UPR). Once initiated, UPR could be responsible for a host of cellular abnormalities, including major mitochondrial remodeling and SR damage.[28] Since many of these processes are Ca^{2+}-dependent, the view that ACM pathogenesis might be independent of hyperdynamic Ca^{2+} handling may not conflict with the observation that strong Ca^{2+} buffering may prevent phenotype development.[12]

Last but not least, the cellular mutation phenotype of the TG mouse described in the present study is mostly consistent with that of patient-derived hiPS-CMs,[11,12] thus providing cross-validation of these experimental models.

7 | THERAPEUTIC IMPLICATIONS

The initial hypothesis of SERCA2a superinhibition by PLN R14del$^{+/-}$ pointed to the therapeutic potential of PLN-displacing SERCA2a activators, now available as drugs.[10,33,34] The loss of SERCA2a function detected in the zebrafish TG model of the mutation, was indeed reversed by one of these compounds (istaroxime).[5] However, consistent with a loss of SERCA2a inhibition by PLN R14del$^{+/-}$, the prototypical selective SERCA2a activator PST-3093, was totally ineffective in patient-derived hiPS-CMs[11] and TG mouse CMs (present results). This, and the likely involvement of pathogenetic mechanisms beyond SERCA2a dysregulation, may suggest to invest on mutation reversal,[35] or at least on improvement of mutant protein processing (e.g. by "chaperone" molecules), or reducing the impact of pathogenic PLN protein[13,36] as the most logical mechanism-based therapeutic approaches. Speaking of more generic approaches, countering the enhancement of sustained Na^+ current (a common response to cell stress) has proven effective in preventing the consequences of chronic upregulation of Ca^{2+} cycling in hiPS-CMs.[22]

AUTHOR CONTRIBUTIONS

Francesco Lodola: Conceptualization; project administration; supervision; writing – original draft. **Claudia Maniezzi:** Data curation; formal analysis; investigation; writing – original draft. **Marem Eskandr:** Data curation; formal analysis; investigation. **Chiara Florindi:** Data curation; formal analysis; investigation. **Mara Ferrandi:** Investigation; methodology. **Paolo Barassi:** Investigation; methodology. **Elena Sacco:** Data curation; formal analysis; supervision. **Valentina Pasquale:** Formal analysis; investigation. **Angela S. Maione:** Data curation; investigation; formal analysis. **Giulio Pompilio:** Supervision; resources. **Vivian Oliveira Nunes Teixeira:** Methodology. **Rudolf A. de Boer:** Funding acquisition. **Herman H. W. Silljé:** Funding acquisition; methodology. **Antonio Zaza:** Writing – original draft; conceptualization; funding acquisition; resources; supervision; validation; writing – review and editing.

ACKNOWLEDGMENTS

The authors are grateful to Prof. Giuseppe Bianchi (Windtree Therapeutics) for supplying PST3093 and to Beatrice Ferè, and Daniele Martone for optimizing the Langendorff-Free isolation methodology.

FUNDING INFORMATION

This work was funded by grants from CVie Therapeutics Limited for the development of PLN antagonists (to AZ) and from the European Union-Italian Ministry of University and Research – grant PNRR – M4C2-I1.3 Project PE_00000019 “HEAL ITALIA” (to BtBs Department). The Operetta and Seahorse platforms were acquired through the MUR-Competitive Grant for Excellent Departments (2018–2022) to University Milano-Bicocca. Generation of the PLN-R14del murine model was supported by grants from the Netherlands Heart Foundation (CVON PREDICT2, grant 2018-30; and CVON DOUBLE DOSE, grant 2020B005; CarMa 01-003-2022-0358), by a grant from the leDucq Foundation (Cure PhosphoLambaN induced Cardiomyopathy [Cure-PLaN]), by a grant from the European Research Council (ERC CoG 818715, SECRETE-HF) and grants from the Netherlands Heart Institute (NLHI) and the PLN heart Foundation.

CONFLICT OF INTEREST STATEMENT

AZ recipient of research funding by CVie Therapeutics Limited (Taipei, Taiwan), WindTree Therapeutics (Warrington, USA) for research on PLN antagonists. The UMCG which employed/employs several of the authors received research grants and/or fees from AstraZeneca, Abbott, Boehringer Ingelheim, Cardior Pharmaceuticals GmbH, Ionis Pharmaceuticals, Inc., Novo Nordisk, and Roche. Dr. de Boer has had speaker engagements with Abbott, AstraZeneca, Bayer, Bristol Myers Squibb, Novartis, and Roche. The views and opinions expressed in this manuscript are those of the authors only and do not necessarily reflect those of the European Union or the European Commission. Neither the European Union nor the European Commission can be held responsible for them.

DATA AVAILABILITY STATEMENT

The authors confirm that the data supporting the findings of this study are available within the article and/or its supplementary materials. The data that support the findings of this study are available from the corresponding author upon request.

ORCID

Elena Sacco https://orcid.org/0000-0002-3190-7671
Francesco Lodola https://orcid.org/0000-0002-3506-5619

REFERENCES

1. van der Zwaag PA, van Rijsingen IAW, Asimaki A, et al. Phospholamban R14del mutation in patients diagnosed with dilated cardiomyopathy or arrhythmogenic right ventricular cardiomyopathy: evidence supporting the concept of arrhythmogenic cardiomyopathy. *Eur J Heart Fail*. 2012;14(11):1199-1207.
2. van der Zwaag PA, van Rijsingen IAW, de Ruiter R, et al. Recurrent and founder mutations in The Netherlands—Phospholamban p.Arg14del mutation causes arrhythmogenic cardiomyopathy. *Neth Heart J*. 2013;21(6):286-293.
3. Haghighi K, Kolokathis F, Gramolini AO, et al. A mutation in the human phospholamban gene, deleting arginine 14, results in lethal, hereditary cardiomyopathy. *Proc Natl Acad Sci*. 2006;103(5):1388-1393.
4. Stroik DR, Ceholski DK, Bidwell PA, et al. Viral expression of a SERCA2a-activating PLB mutant improves calcium cycling and synchronicity in dilated cardiomyopathic hiPSC-CMs. *J Mol Cell Cardiol*. 2020;138:59-65.
5. Kamel SM, van Opbergen CJM, Koopman CD, et al. Istaroxime treatment ameliorates calcium dysregulation in a zebrafish model of phospholamban R14del cardiomyopathy. *Nat Commun*. 2021;12(1):7151.
6. Vafiadaki E, Haghighi K, Arvanitis DA, Kranias EG, Sanoudou D. Aberrant PLN-R14del protein interactions intensify SERCA2a inhibition, driving impaired Ca2+ handling and arrhythmogenesis. *Int J Mol Sci*. 2022;23(13):6947.
7. Ceholski DK, Trieber CA, Young HS. Hydrophobic imbalance in the cytoplasmic domain of Phospholamban is a determinant for lethal dilated cardiomyopathy. *J Biol Chem*. 2012;287(20):16521-16529.
8. Hughes E, Middleton DA. Comparison of the structure and function of Phospholamban and the Arginine-14 deficient

mutant associated with dilated cardiomyopathy. *PloS One*. 2014;9(9):e106746.
9. Vostrikov VV, Soller KJ, Ha KN, Gopinath T, Veglia G. Effects of naturally occurring arginine 14 deletion on phospholamban conformational dynamics and membrane interactions. *Biochim Biophys Acta*. 2015;1848(1):315-322.
10. Arici M, Ferrandi M, Barassi P, et al. Istaroxime metabolite PST3093 selectively stimulates SERCA2a and reverses disease-induced changes in cardiac function. *J Pharmacol Exp Ther*. 2023;384(1):231-244.
11. Badone B, Ronchi C, Lodola F, et al. Characterization of the PLN p.Arg14del mutation in human induced pluripotent stem cell-derived cardiomyocytes. *Int J Mol Sci*. 2021;22:13500.
12. Cuello F, Knaust AE, Saleem U, et al. Impairment of the ER/mitochondria compartment in human cardiomyocytes with PLN p.Arg14del mutation. *EMBO mol Med*. 2021;13:e13074. doi:10.15252/emmm.202013074
13. Eijgenraam TR, Boukens BJ, Boogerd CJ, et al. The phospholamban p.(Arg14del) pathogenic variant leads to cardiomyopathy with heart failure and is unreponsive to standard heart failure therapy. *Sci Rep*. 2020;10(1):9819.
14. Lipskaia L, Chemaly ER, Hadri L, Lompre A-M, Hajjar RJ. Sarcoplasmic reticulum Ca^{2+} ATPase as a therapeutic target for heart failure. *Expert Opin Biol Ther*. 2010;10(1):29-41.
15. Mahaney JE, Albers RW, Waggoner JR, Kutchai HC, Froehlich JP. Intermolecular conformational coupling and free energy exchange enhance the catalytic efficiency of cardiac muscle SERCA2a following the relief of Phospholamban inhibition. *Biochemistry*. 2005;44(21):7713-7724.
16. Kefaloyianni E, Bao L, Rindler MJ, et al. Measuring and evaluating the role of ATP-sensitive K+ channels in cardiac muscle. *J Mol Cell Cardiol*. 2012;52(3):596-607.
17. Cleary SR, Teng ACT, Phillips TA, et al. A dilated cardiomyopathy mutation of phospholamban, R14del, increases phospholamban pentamer stability. *Biophys J*. 2023;122(3):527a.
18. Haghighi K, Gardner G, Vafiadaki E, et al. Impaired right ventricular calcium cycling is an early risk factor in R14del-Phospholamban arrhythmias. *J Pers Med*. 2021;11(6):502.
19. Dave J, Raad N, Mittal N, et al. Gene editing reverses arrhythmia susceptibility in humanized PLN-R14del mice: modelling a European cardiomyopathy with global impact. *Cardiovasc Res*. 2022;118:3140-3150.
20. Lehnart SE, Maier LS, Hasenfuss G. Abnormalities of calcium metabolism and myocardial contractility depression in the failing heart. *Heart Fail Rev*. 2009;14(4):213-224.
21. Slack JP, Grupp IL, Dash R, et al. The enhanced contractility of the Phospholamban-deficient mouse heart persists with aging. *J Mol Cell Cardiol*. 2001;33(5):1031-1040.
22. Jiang Y, Li X, Guo T, et al. Ranolazine rescues the heart failure phenotype of PLN-deficient human pluripotent stem cell-derived cardiomyocytes. *Stem Cell Reports*. 2022;17(4):804-819.
23. Haghighi K, Kolokathis F, Pater L, et al. Human phospholamban null results in lethal dilated cardiomyopathy revealing a critical difference between mouse and human. *J Clin Invest*. 2003;111(6):869-876.
24. Shanmugam M, Gao S, Hong C, et al. Ablation of phospholamban and sarcolipin results in cardiac hypertrophy and decreased cardiac contractility. *Cardiovasc Res*. 2011;89(2):353-361.
25. Schmitt JP, Ahmad F, Lorenz K, et al. Alterations of Phospholamban function can exhibit cardiotoxic effects independent of excessive sarcoplasmic reticulum Ca $^{2+}$-ATPase inhibition. *Circulation*. 2009;119(3):436-444.
26. Readnower RD, Brainard RE, Hill BG, Jones SP. Standardized bioenergetic profiling of adult mouse cardiomyocytes. *Physiol Genomics*. 2012;44(24):1208-1213.
27. Sakata S, Lebeche D, Sakata N, et al. Restoration of mechanical and energetic function in failing aortic-banded rat hearts by gene transfer of calcium cycling proteins. *J Mol Cell Cardiol*. 2007;42(4):852-861.
28. Senft D, Ronai ZA. UPR, autophagy, and mitochondria crosstalk underlies the ER stress response. *Trends Biochem Sci*. 2015;40(3):141-148.
29. Ackers-Johnson M, Li PY, Holmes AP, O'Brien SM, Pavlovic D, Foo RS. A simplified, Langendorff-free method for concomitant isolation of viable cardiac myocytes and nonmyocytes from the adult mouse heart. *Circ Res*. 2016;119(8):909-920.
30. Perry SW, Norman JP, Barbieri J, Brown EB, Gelbard HA. Mitochondrial membrane potential probes and the proton gradient: a practical usage guide. *Biotechniques*. 2011;50(2):98-115.
31. Varro A, Negretti N, Hester SB, Eisner DA. An estimate of the calcium content of the sarcoplasmic reticulum in rat ventricular myocytes. *Pflugers Arch*. 1993;423(1–2):158-160.
32. Alemanni M, Rocchetti M, Re D, Zaza A. Role and mechanism of subcellular Ca^{2+} distribution in the action of two inotropic agents with different toxicity. *J Mol Cell Cardiol*. 2011;50(5):910-918.
33. Rocchetti M, Besana A, Mostacciuolo G, et al. Modulation of sarcoplasmic reticulum function by Na+/K+pump inhibitors with different toxicity: digoxin and PST2744 [(E,Z)-3-((2-aminoethoxy)imino)androstane-6,17-dione hydrochloride]. *J Pharmacol Exp Ther*. 2005;313(1):207-215.
34. Carubelli V, Zhang Y, Metra M, et al. Treatment with 24 hour istaroxime infusion in patients hospitalised for acute heart failure: a randomised, placebo-controlled trial. *Eur J Heart Fail*. 2020;22(9):1684-1693.
35. Stillitano F, Turnbull IC, Karakikes I, et al. Genomic correction of familial cardiomyopathy in human engineered cardiac tissues. *Eur Heart J*. 2016;37(43):3282-3284.
36. Stege NM, Eijgenraam TR, Oliveira Nunes Teixeira V, et al. DWORF extends life span in a PLN-R14del cardiomyopathy mouse model by reducing abnormal sarcoplasmic reticulum clusters. *Circ Res*. 2023;133:1006-1021.

SUPPORTING INFORMATION

Additional supporting information can be found online in the Supporting Information section at the end of this article.

How to cite this article: Maniezzi C, Eskandr M, Florindi C, et al. Early consequences of the phospholamban mutation PLN-R14del$^{+/-}$ in a transgenic mouse model. *Acta Physiol*. 2024;240:e14082. doi:10.1111/apha.14082

Genetic variants risk assessment for Long QT Syndrome through machine learning and multielectrode array recordings

Aleksandr Khudiakov PhD[a], Manuela Mura PhD[b], Federica Giannetti PhD[a], Vladislav Leonov PhD[a,c], Chiara Alberio[a], Marem Eskandr[a,d], Paul A Brink MD[e], Lia Crotti MD, PhD[a,f], Massimiliano Gnecchi MD[b,h], Peter J Schwartz MD[a], Luca Sala PhD*[a,d]

[a] *Istituto Auxologico Italiano IRCCS, Center for Cardiac Arrhythmias of Genetic Origin and Laboratory of Cardiovascular Genetics, Milan, Italy*

[b] *Translational Cardiology Unit, Fondazione IRCCS Policlinico San Matteo, Pavia, Italy.*

[c] *Department of Surgery, Dentistry, Pediatrics and Gynecology, Cardiovascular Science, The University of Verona, Policlinico G.B. Rossi, Verona, Italy*

[d] *Department of Biotechnology and Biosciences, University of Milano - Bicocca, Italy*

[e] *Department of Medicine, University of Stellenbosch, Tygerberg, South Africa.*

[f] *Department of Medicine and Surgery, University of Milano-Bicocca, Milan, Italy*

[g] *Department of Molecular Medicine, Unit of Cardiology, University of Pavia, Pavia, Italy*

*** Correspondence to:**

Luca Sala, PhD; Department of Biotechnology and Biosciences, University of Milano - Bicocca and Center for Cardiac Arrhythmias of Genetic Origin and Laboratory of Cardiovascular Genetics. Istituto Auxologico Italiano, IRCCS. Via Zucchi, 18 20095 Cusano Milanino (MI), Italy

Clinical Perspectives

Clinical Aspects:

Understanding which patients may be at risk of cardiac events or sudden cardiac death is crucial to implement appropriate preventive measures. This study leverages patient-specific *in vitro* models and machine learning to improve the risk stratification of pathogenic/likely pathogenic variants associated with LQTS, better supporting clinical decisions related to risk assessment and management of LQTS patients. This scalable approach can be implemented across multiple centres, enhancing the risk stratification of LQTS variants beyond what is currently possible when clinical data are limited.

Translational Outlook:

Machine learning-based variant risk stratification is a novel approach for integrating hiPSC-CM-derived electrophysiological data into clinical workflows. While this study demonstrates the feasibility of our approach, further research is required to validate these findings across larger and more diverse patient cohorts. Additionally, efforts to standardize the pipeline and adapt it for multicentric implementation are necessary.

Graphical Abstract

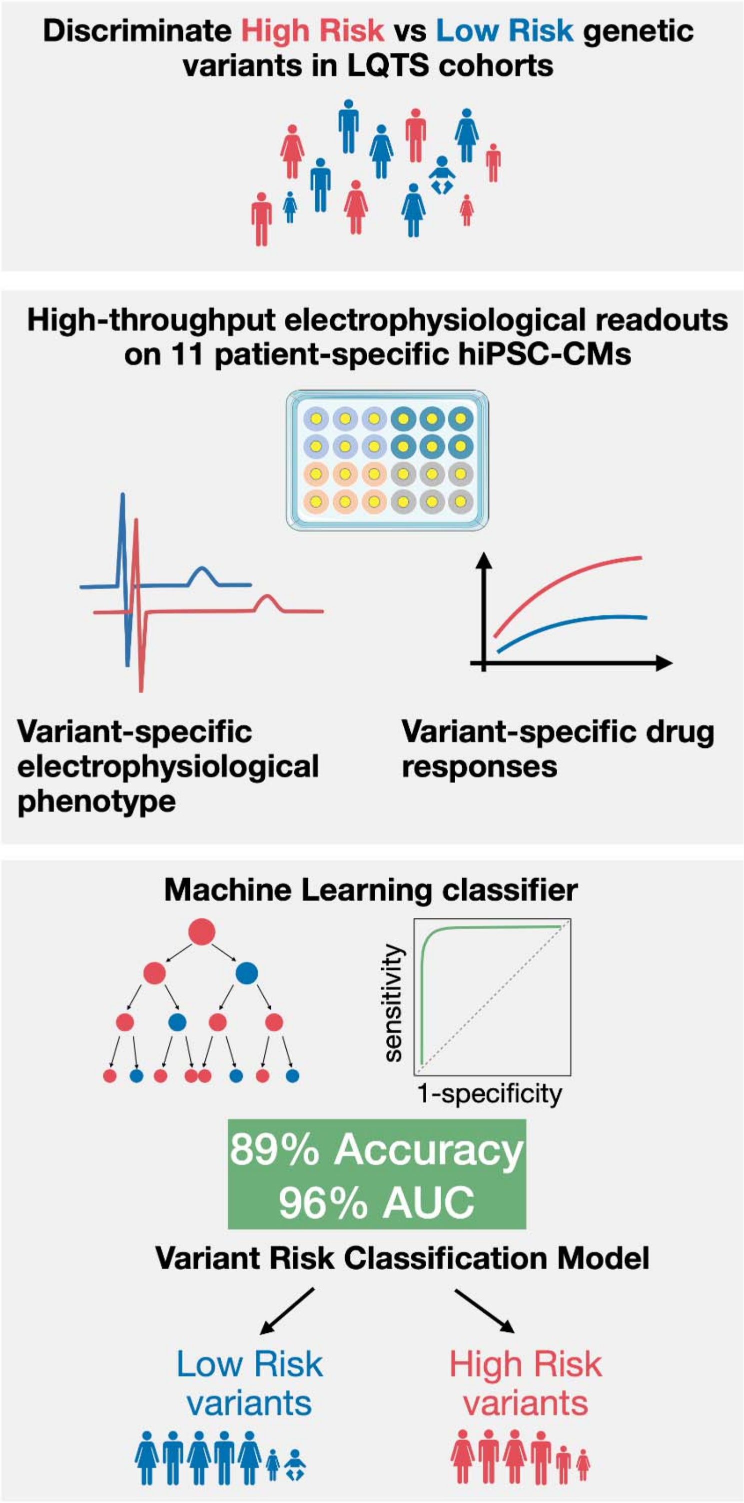

Abstract

Background

Long QT syndrome (LQTS) is a life-threatening genetic disorder characterized by prolonged QT intervals on electrocardiograms. Congenital forms are mostly associated with variants in the *KCNQ1* and *KCNH2* genes. Among pathogenic or likely pathogenic (P/LP) variants, some are associated with a significantly higher incidence of cardiac events compared to others. While therapies have significantly reduced mortality, some patients are unresponsive or intolerant to therapy, perpetuating their arrhythmic risk, including sudden cardiac death. Current approaches for risk stratification are insufficient, highlighting the critical need for more accurate identification and management of patients carrying high risk genetic variants.

Objectives

To develop a refined risk stratification model for P/LP variants by applying machine learning classification to electrophysiological data measured in human induced pluripotent stem cell-derived cardiomyocytes (hiPSC-CMs).

Methods

Eleven patient-specific hiPSC lines carrying six P/LP variants in *KCNQ1* or *KCNH2* were differentiated to cardiomyocytes (hiPSC-CMs). Electrophysiological responses from multielectrode array recordings at baseline and after application of selective ion channel blockers or pro-arrhythmic compounds were used to train a machine learning model to classify variant-specific risk levels based on *in vitro* electrophysiological readouts.

Results

Our findings revealed a correlation between variant risk level, hiPSC-CM electrophysiological profiles, and drug responses. The machine learning classifier, trained on multielectrode array recordings, achieved 89% accuracy in classification of P/LP genetic variants according to the associated risk levels.

Conclusions

This study demonstrates that integrating hiPSC-CM electrophysiological profiling with machine learning provides a robust method to improve variant-specific risk stratification for LQTS patients.

Keywords

Precision medicine, genetic variants, risk assessment, machine learning, long QT syndrome, hiPSC-derived cardiomyocytes, multielectrode arrays, proarrhythmic drugs, safety pharmacology.

Highlights

- Discriminating LQTS patients at high or low risk for sudden death is a clinical challenge.
- Improved stratification of pathogenic/likely pathogenic variants is achievable through machine learning classification on in vitro electrophysiological data.
- Integration of the clinical workflow with data from patient-specific in vitro models will enhance risk stratification.

Abbreviations and acronyms:

APD = Action Potential Duration

FPD = Field Potential Duration

iPSC-CMs = Cardiomyocytes derived from human induced pluripotent stem cells

JLNS = Jervell and Lange-Nielsen Syndrome

LQTS = Long QT Syndrome

MEA = Multielectrode Arrays

ML = Machine Learning

P/LP = Pathogenic/Likely Pathogenic

TdP = Torsades de Pointes

QTc = QT interval corrected for heart rate

WT = Wild type

Introduction

The long QT syndrome (LQTS) is a life-threatening disease of genetic origin characterized by a prolonged QT interval on the electrocardiogram, by propensity to lethal arrhythmias especially under stress, and by an increased sensitivity to drugs affecting cardiac repolarization through block of the I_{Kr} potassium current [1–4]. Appropriate therapies based on beta-blockers [5], left cardiac sympathetic denervation [6,7] and sodium channel blockers [8,9] have effectively reduced the risk for patients to develop potentially-lethal ventricular arrhythmias or sudden cardiac death (SCD), limiting the use of an implantable cardioverter defibrillator only to selected patients [5,10]; one of the main challenges for clinicians dealing with LQTS is the identification, clinical management and protection of patients who are more at risk of developing SCD.

Advancements in next-generation sequencing have led to the discovery of numerous variants in genes encoding cardiac ion channels, subunits, or associated proteins implicated in LQTS [11,12]. While these insights have guided gene-specific patient management [8], current genetic interpretation guidelines [13] often do not help identify patients at higher risk, with a large number of variants classified as variants of uncertain significance (VUS). Even variants classified as pathogenic or likely pathogenic (P/LP) according to the American College of Medical Genetics and Genomics (ACMG) guidelines may exhibit divergent risks of life-threatening cardiac events, including SCD [14,15], requiring profoundly different clinical management.

Accurate clinical risk assessment for a variant requires data from many affected individuals and this is not feasible for most of the variants, limiting precision medicine and hampering the development of variant-specific therapies [16,17]. The classification of variant pathogenicity through *in vitro* or *in vivo* studies offers a promising solution to address this limitation [18,19]. Functional studies using patient-specific cardiomyocytes derived from human induced pluripotent stem cells (hiPSC-CMs) further refined this, providing high-quality functional data on the effect of the variants on action potentials, calcium transients or contractility. hiPSC-CM-based models have been particularly useful for disease modeling of congenital or acquired cardiac disorders such as LQTS [20–24], Jervell and Lange-Nielsen syndrome (JLNS) [25], Timothy syndrome [26], cardiomyopathies [27–29], congenital heart defects [30], drug testing [31–33] and drug repurposing [34]. In the present study, using hiPSC-CMs from eleven patients, we focused on six well-characterized P/LP variants from the two most prevalent LQTS subtypes, LQT1 and LQT2, which together account for 90% of cases. These variants were identified in individuals with clinically heterogeneous presentations, from normal to prolonged QT intervals and displaying low or high incidence of life-threatening cardiac events per variant (defined here as Low and High Risk P/LP variants).

Using patient-derived hiPSC-CMs and high-throughput multielectrode arrays (MEA), we investigated i) whether hiPSC-CMs carrying P/LP variants with differing clinical severities exhibit distinct drug responses *in vitro*; ii) whether *in vitro* phenotypes match clinical records and could be used for a more accurate variant-associated risk stratification; iii) whether accurate P/LP variant risk stratification can be automated through machine learning on *in vitro* readouts.

Methods

Ethical statement

This study was conducted in accordance with the Declaration of Helsinki and the ethics committee of Istituto Auxologico Italiano IRCCS gave ethical approval for this work (Approval number: 2020_10_20_07). Appropriate informed consents were obtained from all donors.

Patient-specific hiPSC lines included in the study

A total of eleven hiPSC lines were utilized in this study. HiPSC lines were derived from LQT1, JLNS, and LQT2 patients carrying the variants in *KCNQ1* or *KCNH2* gene (See Table 1 for detailed information). The line carrying the *KCNH2* p.A561V variant was provided by Joseph C. Wu, MD, PhD, at the Stanford Cardiovascular Institute. As a wild-type control (WT), the WTC-11 line, generated from a healthy subject, was obtained from the Coriell Institute for Medical Research (catalog No. GM25256) and used as a bona fide wild-type reference [35]. Detailed characterization of each hiPSC line, including genetic and functional properties, is provided in Supplemental Table 1 and Supplemental Figure 1 and Supplemental Figure 2.

Cardiac events frequency assessment

Clinical data on documented cardiac events (syncope, sustained ventricular tachycardia, appropriate ICD shock, sudden cardiac arrest, sudden cardiac death), QTc values and Schwartz scores (when reported) were extracted from our internal database of LQTS patients, The Human Gene Mutation Database (HGMD)[36] and Variant Browser database [37,38] . The frequency of cardiac events was calculated as the proportion of patients with a history of such events relative to the total number of patients carrying the specific variant.

hiPSC culture and differentiation to hiPSC-CMs

HiPSCs were cultured on multiwell plates coated with recombinant human vitronectin (Gibco) in Essential 8 Flex medium kit (Gibco). HiPSCs were plated on Matrigel (Corning) coated plates for cardiac differentiation. hiPSCs were differentiated to hiPSC-CMs following a small-molecule based protocol [39], purified through glucose starvation [40], starting from day 7, and cryopreserved in Bambanker (Nippon Genetics) at days 9-16. For the subsequent experiments hiPSC-CMs were thawed, replated at low density and expanded as previously reported [41]. A list of main reagents used in the study is reported in Supplemental Table 2. Data were collected from at least three independent differentiations of each hiPSC line for each experiment.

Patch-clamp

For patch clamp experiments, metabolic maturation of hiPSC-CMs was performed as previously described [42]. Action potentials and I_{Ks} currents were recorded at 37 °C from isolated hiPSC-CMs plated on glass coverslips as described in detail in the Supplemental Methods section. Action potentials were recorded in perforated patch mode under 1 Hz pacing.

MultiElectrode Arrays

HiPSC-CMs were plated on 24-well multiwell MEAs (MultiChannel Systems) coated with bovine fibronectin (Merck) as previously described [43,44]. The recordings were performed on spontaneously beating hiPSC-CMs at 37°C. The detailed description of drug treatments and analysis of the recordings is present in the Supplemental Methods section.

Pro-arrhythmic compound selection

The selection of pro-arrhythmic compounds was performed using the CredibleMeds® QT prolonging drugs database [45] intersected with OpenFDA database (https://open.fda.gov/). OpenFDA data were used to prioritize compounds based on their occurrence in the FDA Adverse Event Reporting System. The following query terms were utilized to extract the top 100 compounds from the OpenFDA database: "*Cardiac failure*", "*Torsade de pointes*", "*Electrocardiogram QT prolonged*", "*Cardiac arrest*", "*Ventricular extrasystoles*", "*Ventricular arrhythmia*". The common compounds between databases were 46 (Supplemental Table 3). We excluded compounds that were unlikely to provide pro-arrhythmic effects in a pure culture of hiPSC-CMs (such as diuretics or drugs associated with chronic cardiotoxicity) as beyond the scope of this study. Seven drugs were then selected in the highest-risk category, i.e. those contraindicated in congenital LQTS and are known to pose a significant risk for developing drug-induced Torsades de Pointes (TdP). Detailed information on the compounds is provided in Supplemental Table 4.

Data Analysis and Statistics

RStudio (version 2023.09.1) and R (version 4.3.1) were used for data analysis. Multiple group comparisons were conducted using the Kruskal-Wallis test, followed by Dunn's test with Benjamini-Hochberg correction. Pairwise comparisons were performed using the Wilcoxon test. Categorical variable comparisons were assessed with Fisher's exact test. A statistical significance level of $p \leq 0.05$ was used for all tests. Figures denote significance as $*p \leq 0.05$, $**p \leq 0.01$, and

***$p \leq 0.001$, while exact p-values are reported in text and tables. Numerical data are reported as mean ± standard error of the mean (SEM), and plots display mean ± SEM, combined with scattered individual data points when relevant. Categorical data are presented as bar plots.

Machine learning model for variant risk prediction

A random forest dichotomous classification model was implemented using the comprehensive *tidymodels* framework [46]. The dataset was stochastically divided into training and validation subsets with a ratio of 70:30, ensuring that drug readouts were evenly distributed between the two datasets. A v-fold (v = 10) cross validation was performed to evaluate the model performance. To further evaluate the classification performance of the model for each genetic variant, a leave-one-out cross validation was performed by recursively removing the data for each variant. The accuracy of variant prediction was calculated as the percentage of correctly predicted readouts (rows) on the total number of readouts of the dataset. Overall score of variant prediction was calculated as a sum of accuracies of each variant risk classification per number of variants. The datasets, models and R code used for the analyses are available in the lab's GitHub repository: https://github.com/invitroheart.

Results

Patient cohort characteristics

The study included ten patients, with their clinical information summarized in Table 1. The study cohort comprised a LQT1 family trio (Supplemental Figure 3), which includes an asymptomatic mother carrying the *KCNQ1* p.R190W variant, an asymptomatic father carrying the *KCNQ1* p.R594Q variant, and their daughter affected by Jervell and Lange-Nielsen syndrome[47] (JLNS) carrying both variants in compound heterozygosity [48]. Four patients from a large South African family carrying the *KCNQ1* p.A341V variant associated with a very severe LQT1 phenotype [49–51];

two of these patients were asymptomatic while the other two were severely symptomatic, carrying polymorphisms in the modifier gene *NOS1AP* (one patient in heterozygous and one patient in homozygous state) associated with a prolonged QT interval and with an increased risk of life-threatening events [52]. Among the LQT2 cases, two patients carried the *KCNH2* p.R366X variant: one symptomatic and one asymptomatic. Both were treated with beta-blockers. The symptomatic patient also underwent left cardiac sympathetic denervation due to difficulties in optimizing beta-blocker therapy because of asthenia. No recurrence of symptoms was observed on therapy. A third symptomatic LQT2 patient, carrying the de novo *KCNH2* p.A561V variant, experienced cardiac arrests and was treated with beta-blockers and an ICD implantation.

Genetic variant risk level assignment

To define the threshold for categorizing variants associated with different risks of cardiac events (Low Risk vs High Risk) we analyzed the frequency distribution of cardiac events across reported P/LP genetic variants in *KCNQ1* and *KCNH2* genes (1099 patients carrying 162 variants in *KCNQ1* and 623 patients carrying 175 variants in *KCNH2*) (Figure 1, A). For both genes, two distinct peaks in the distribution were identified: one at 0% frequency (variants with no reported cardiac events) and another at ≥25% frequency (variants where at least 25% of carriers experienced cardiac events). Based on this analysis, a threshold of 25% was selected to differentiate these populations. Using this threshold, the variants in our study were categorized as follows: High Risk (*KCNQ1* p.R594Q and *KCNQ1* p.R190W & p.R594Q, *KCNQ1* p.A341V, and *KCNH2* p.A561V) and Low Risk (WT, *KCNQ1* p.R190W, and *KCNH2* p.R366X) (Figure 1, B).

Consistent with the incidence of cardiac events, carriers of High Risk variants *KCNQ1* p.A341V and *KCNH2* p.A561V had significantly longer QTc values compared to carriers of the Low Risk variants *KCNQ1* p.R190W and *KCNQ1* p.R366X respectively (Figure 1, C, Supplemental Table 5). In addition, the Schwartz scores of *KCNQ1* p.A341V carriers were higher than those of *KCNQ1* p.R190W (Figure 1, C, Supplemental Table 5). Notably, the *KCNQ1* p.R190W & p.R594Q variant, observed in a single carrier, presented with deafness and exhibited markedly prolonged QTc (578 ms) and elevated Schwartz score (7.5), consistent with the severe JLNS phenotype.

In vitro characterisation of genetic variants selected for the study

Four out of six variants had functional characterization from literature: *KCNQ1* p.R594Q, *KCNQ1* p.A341V, *KCNH2* p.R366X, *KCNH2* p.A561V leading to loss-of-function, with *KCNQ1* p.R594Q and *KCNH2* p.A561V being also trafficking-deficient (Supplemental Table 6). We complemented the characterization providing data for the hiPSC-CMs derived from a family trio (*KCNQ1* p.R190W, *KCNQ1* p.R594Q, and *KCNQ1* p.R190W & p.R594Q) (Figure 2).

We observed the repolarization prolongation at single-cell level (APD90) and a reduced ability to follow high-frequency pacing in isolated hiPSC-CMs carrying *KCNQ1* p.R190W, *KCNQ1* p.R594Q, and *KCNQ1* p.R190W & p.R594Q compared to WT (Figure 2, A, B; Supplemental Figure 4, A, B). HiPSC-CM monolayers carrying *KCNQ1* p.R594Q and *KCNQ1* p.R190W & p.R594Q demonstrated also corrected FPD prolongation in comparison to WT (422.2 ± 126.7 ms and 424.9 ± 78.7 ms vs 281.8 ± 77.4 ms respectively, $p \leq 0.001$) (Figure 2, C). Measurement of I_{Ks} with patch clamp demonstrated decreased end-step and tail current densities in hiPSC-CMs carrying *KCNQ1* p.R190W, compared to WT, and almost absent I_{Ks} in hiPSC-CMs carrying *KCNQ1* p.R594Q and *KCNQ1* p.R190W & p.R594Q, in line with their APD prolongation (Figure 2, D-F).

Baseline electrophysiology of hiPSC-CM cohort

Baseline hiPSC-CM electrophysiology assessed with MEA measurements accurately reflected the risk level assigned to each variant. Specifically, hiPSC-CMs from the High Risk group exhibited increased baseline FPD, corrected FPD (cFPD), and RR interval duration (Figure 3, A-D; Table 2) in comparison to wild type hiPSC-CMs from the Low Risk group. The propensity for irregular beating patterns at baseline was significantly higher in the High Risk group (20.2% of wells in High Risk group vs 8.7% in Low Risk group, $p \leq 0.001$) (Figure 3, E).

HiPSC-CMs from High Risk and Low Risk groups demonstrate distinct drug responses to ion channel blockers

To further discriminate hiPSC-CMs carrying variants with different risk levels we obtained concentration-response curves for 11 selected drugs (Figure 4, 5; Supplemental Figures 5-16; Supplemental Table 7). Selective ion channel blockers E4031 (I_{Kr}, Kv11.1), HMR-1556 (I_{Ks}, Kv7.1), nifedipine (I_{CaL}, CaV 1.2), and tetrodotoxin (I_{Na}, Nav 1.5) were used to assess ion channel-specific drug responses as previously proposed by multiple ion channel effects (MICE) approach for drug testing assays [53]. Since I_{Ks} blockers were previously reported to be more effective with reduced cardiac repolarization reserve caused by *KCNH2* genetic variants or I_{Kr} pharmacological block [54], we also tested the effect of HMR1556 on hiPSC-CMs pre-treated with 20 nM I_{Kr} blocker E4031.

Among pure ion channel blockers, we observed a differential response to the I_{Kr} blocker E4031 and to I_{Ks} blocker HMR1556 after E4031 pretreatment between hiPSC-CMs carrying High Risk and Low Risk variants. Specifically, hiPSC-CMs with High Risk variants showed a greater concentration-dependent prolongation of cFPD following treatment with E4031 (up to 350.0 ± 183.2% vs Vehicle for High Risk and up to 218.2 ± 69.9% vs Vehicle for Low Risk, $p \leq 0.001$). Furthermore, E4031 increased the RR interval duration in hiPSC-CMs carrying High Risk variants more than in those carrying Low Risk variants (Figure 4, A). The High Risk group also demonstrated a higher incidence of beating abnormalities at high concentrations of E4031 (Figure 4, A). HMR1556 treatment alone resulted in a small cFPD prolongation that was similar between the High Risk and Low Risk groups (Figure 4, B). In contrast the combination of E4031 pre-treatment followed by HMR1556 concentration-response led to a significant cFPD prolongation (up to 188.4 ± 40.6% vs. Vehicle for High Risk and up to 169.2 ± 26.4% vs. Vehicle for Low Risk, $p = 0.004$) (Figure 4, C). Treatment with the I_{CaL} blocker nifedipine led to a cFPD and RR interval decrease (Figure 4, D). High concentrations of the I_{Na} blocker tetrodotoxin (10 µM and 30 µM) led to a decrease in peak-to-peak amplitude and prolongation of the RR interval, along with an increased incidence of beating abnormalities (Figure 4, E). The High Risk group exhibited significantly more beating abnormalities at 10 µM of tetrodotoxin compared to the Low Risk group (73.6% vs. 46.9%, respectively; $p = 0.003$).

HiPSC-CMs carrying High Risk and Low Risk P/LP variants demonstrate distinct drug responses to proarrhythmic drugs

In addition to pure ion channel blockers seven proarrhythmic compounds were selected using the OpenFDA and CredibleMeds databases, as described in the Methods: β2-adrenergic receptor agonist albuterol (salbutamol); the antibiotics clarithromycin, ciprofloxacin, and moxifloxacin; the antipsychotic drugs chlorpromazine and haloperidol; the antiarrhythmic drug dofetilide. Among these compounds dofetilide, haloperidol, and the β2-adrenergic receptor agonist salbutamol demonstrated differential concentration-response curves between High Risk and Low Risk groups (Figure 5). Specifically, responses to the antibiotics clarithromycin and ciprofloxacin were similar between the two groups (Figure 5 A, C). The highest concentration of clarithromycin tested (10 µM) led to arrhythmias and cessation of beating (Figure 5 A). Another antibiotic, moxifloxacin, demonstrated a similar effect, with notable toxicity at a concentration of 100 µM, expressed by cFPD and RR increases, a drop in peak-to-peak amplitude, arrhythmias, and cessation of beating similar for both groups (Figure 5, F). Treatment of hiPSC-CMs with the antipsychotic drug chlorpromazine resulted in moderate cFPD prolongation that was similar between the two groups (Figure 5, B). hiPSC-CMs carrying High Risk variants showed a concentration-dependent increase in cFPD following treatment with the dofetilide (up to 317.5 ± 128.5% vs. Vehicle for High Risk and up to 208.2 ± 61.4% vs. Vehicle for Low Risk, $p \leq 0.001$) (Figure 5, D) and haloperidol (up to 253.1 ± 134.0% vs. Vehicle for High Risk and up to 178.2 ± 50.6% vs. Vehicle for Low Risk, $p \leq 0.001$) (Figure 5, E). Salbutamol decreased the RR interval of hiPSC-CMs carrying High Risk variants to a greater extent compared to those carrying Low Risk variants (Figure 5, G).

Gene-specific drug response differences between in hiPSC-CMs carrying High Risk and Low Risk P/LP variants

To evaluate gene-specific drug responses, we compared the concentration-response curves between High and Low Risk P/LP variants, separating hiPSC-CMs with *KCNQ1* variants (LQT1, JLNS) from those with *KCNH2* variants (LQT2). We analyzed responses to I_{Kr}-blocking drugs - dofetilide, E4031, and haloperidol - which demonstrated the strongest discrimination between High Risk and Low Risk P/LP variants.

Gene-specific features emerged in drug responses between hiPSC-CMs with High and Low Risk P/LP variants. High Risk hiPSC-CMs carrying *KCNQ1* variants showed significant FPD prolongation upon drug treatment (Figure 6A–C; Supplemental Table 8), while, in contrast, High Risk *KCNH2* variant carriers demonstrated cFPD prolongation similar to the Low Risk *KCNH2* group, but exhibited a marked decrease in peak-to-peak amplitude and an increased incidence of abnormal beating patterns (Figure 6D–F; Supplemental Table 9).

Machine learning model stratifies P/LP variant risk from hiPSC-CM multielectrode array data

We curated a MEA dataset from eleven patient-specific hiPSC lines carrying seven variants, exposed to a panel of 11 drugs. The complete dataset comprises 10,410 data points and it was used to train a machine learning classifier for stratifying P/LP variant risk based on in vitro drug responses in patient-specific hiPSC-CMs. To ensure robust and unbiased predictions, we deliberately included all drug-responses, even those from drugs that did not show apparent discrimination between High Risk and Low Risk variants according to concentration-response curves. The random forest model demonstrated robust classification performance with 89% accuracy and excellent discriminative ability, with an area under the receiver operating characteristic (ROC) curve (AUC) of 96% (Figure 7, A). The model also demonstrated a strong discriminative ability for LQTS subtype, achieving 79% classification accuracy and an AUC of 94% (Figure 7, B).

Machine learning validation confirmed model accuracy for predicting individual variant risk

To further evaluate the model's generalization performance and its ability to predict risk levels for novel variants, we performed leave-one-out cross-validation by sequentially excluding each variant from the training dataset and predicting its risk level as if it were a novel variant. The model correctly classified 6 out of 7 variants into their appropriate risk categories, with one exception (*KCNH2* p.R366X), achieving an overall prediction accuracy of 72.6% (Figure 7, C, Table 3).

Discussion

Risk stratification for LQTS patients remains a significant clinical challenge, particularly for carriers of ultra-rare P/LP variants or for those identified in a single proband. These shortcomings impact our ability to identify patients who are at low or high risk of developing cardiac events that could potentially lead to SCD. Here, we developed a machine learning pipeline to classify P/LP variant risk based on *in vitro* electrophysiological readouts from patient-specific hiPSC-CM lines carrying genetic variants associated with varying frequencies of cardiac events (Low Risk or High Risk).

Our findings support prior evidence demonstrating that hiPSC-CMs can effectively recapitulate the clinical phenotype of LQTS [20–24]. This was particularly evident in hiPSC-CMs carrying severe genetic variants, such as compound heterozygous *KCNQ1* p.R190W & p.R594Q, *KCNQ1* p.A341V, and *KCNH2* p.A561V, where a clear prolongation in the repolarization duration was clearly observed *in vitro*.

We further strengthened the dataset beyond baseline measurements by challenging each variant with ion channel blockers and pro-arrhythmic compounds, thus creating variant-specific drug response profiles not immediately obtainable in clinical practice. This is supported by previous research demonstrating excellent capacity of hiPSC-CMs to discriminate high/low responders to an acute sotalol administration [55] or to tyrosine kinase inhibitors [56,57]. To overcome the high baseline variability typical of hiPSC-CM measurements, often observed in cohort studies, we used relative readouts obtained from normalized drug responses to provide a more accurate discrimination between disease phenotypes. Indeed, High Risk variants were clearly discriminated from their exacerbated response to certain pro-arrhythmic drug treatments, leading to more severe changes in FPD, cFPD, and RR intervals or to a higher occurrence of beating pattern abnormalities.

The panel of pure ion channel blockers targeting four key ion channels responsible for action potential regulation revealed that pharmacological I_{Kr} blockade alone already provides effective variant risk discrimination. Conversely, treatment of hiPSC-CMs with the I_{Ks} blocker HMR1556 caused only minimal FPD prolongation [58,59]. Reducing the repolarization reserve by pre-treating hiPSC-CMs with I_{Kr} blocker E4031 [54,60] increased the sensitivity to HMR1556 and discriminated between High Risk and Low Risk groups. As expected, the I_{CaL} blocker nifedipine and the I_{Na} blocker tetrodotoxin were not effective in distinguishing High Risk from Low Risk groups within our LQT1 and LQT2 cohort, which is expected since no pathogenic variants were identified in genes encoding for calcium and sodium channel subunits. These blockers could be useful for identifying Ca^{2+} or Na^{+} handling abnormalities to other LQTS subtypes beyond LQT1 and LQT2, e.g. LQT3 or CALM-LQTS [22,61].

Among the pro-arrhythmic drugs selected based on analyses of the OpenFDA and CredibleMeds databases, acute treatment of hiPSC-CMs with the potent I_{Kr} blocker dofetilide and the antipsychotic drug haloperidol demonstrated clear concentration-dependent cFPD prolongation, consistently distinguishing between the High Risk and Low Risk groups. Acute treatment with salbutamol, a β_2-adrenergic agonist commonly used as a bronchodilator and typically precluded to LQTS patients [62], differentially increased the spontaneous beating frequency in hiPSC-CMs; this allowed the discrimination of High Risk variants, which revealed a higher sensitivity, from Low Risk variants and could be influenced by a difference in beating frequencies at baseline between these two groups. No arrhythmic events were observed supporting previous studies on commercially available hiPSC-CMs [63]. Treatment of hiPSC-CMs with ciprofloxacin, clarithromycin, and moxifloxacin within therapeutic concentration ranges resulted in moderate FPD prolongation as similarly emerged in commercially available wild-type hiPSC-CMs [31,64].

There is limited information available on gene-specific drug responses in LQT1 and LQT2 both *in vivo* and *in vitro* [65–67]. In our study, three drugs with increased potency to block hERG (E4031, dofetilide, and haloperidol) well discriminated diseased hiPSC-CMs carrying High Risk variants in either *KCNQ1* or *KCNH2* genes. This observation aligns with findings from adult transgenic rabbit models, where LQT2 rabbits exhibited greater susceptibility to drug-induced TdP than LQT1 rabbits after administration of the anesthetic propofol, with a known hERG channel blocking effect [66]. These results are consistent with the concept of a severely compromised repolarization reserve in LQT2 cardiomyocytes, which renders them more vulnerable to proarrhythmic triggers [60].

Variant risk prediction based on multiparametric readouts is a novel and rapidly developing field. A recent study combined clinical data, trafficking assays and automated patch clamp data from heterologous expression systems, to score the risk of *KCNH2* variants associated with LQT2 [68]. The use of hiPSC-CMs provides enhanced precision by addressing the limitations of heterologous systems that lack cardiac-specific context. Having demonstrated that hiPSC-CM drug responses effectively discriminate between High Risk and Low Risk P/LP variants, we developed the ML model trained on *in vitro* hiPSC-CM electrophysiological readouts able to predict retrospectively severity of variants with high precision - a methodology that, to our knowledge, has not been previously applied to LQTS. While we deliberately chose well-known P/LP genetic variants with a loss-of-function mechanism for our study, the model's versatility extends beyond retrospective analyses to the classification of ultra-rare variants and VUS. Importantly, the ML model trained for disease discrimination predicted each disease subtype with a 79% accuracy. This robust performance indicates that disease-specific electrophysiological features are distinct from variant risk classification features, providing solid evidence to expand the model incorporating other LQTS subtypes.

Successful application of the model to predict the risk level of single variants on which it was not originally trained represents a high-level validation, further demonstrating applicability of our approach for assessing novel, previously unreported variants. The observed discrepancy in predicting the risk level for the *KCNH2* p.R366X variant underscores the impact of patient-specific drug responses. Although assigned as Low Risk due to a low cardiac event frequency (16.7%), two hiPSC-CM lines from different LQT2 patients exhibited divergent drug response patterns. One line, derived from a patient with no cardiac events, aligned with Low Risk variants, whereas the other, from a patient with documented cardiac events, markedly prolonged QTc (622 ms), and LSCD performed, with those of High Risk. This highlights the importance of separating the genetic background from the primary disease-causing variant, particularly for P/LP variants that fall within the intermediate range of the risk level distribution. Indeed, in the case of High Risk *KCNQ1* p.A341V variant, despite differences in genetic background (such as *NOS1AP* genetic variants) the primary variant itself is so severe that the probability of misclassification is lower. These findings emphasize the necessity of integrating data from multiple sources for accurate variant risk classification, including multicentral *in vitro* data, clinical cohort records, structural variant pathogenicity predictions, and Bayesian penetrance estimates [37].

In conclusion, we established a robust method for stratifying P/LP variant risk by integrating ML classification to electrophysiological recordings in patient-specific hiPSC-CMs. This approach enhances the risk stratification of LQTS variants beyond what is currently possible from clinical data alone, providing value for variants with limited clinical information.

Study limitations

First, experiments were performed on hiPSC-CMs which, despite significant progress in maturation techniques, still exhibit an immature phenotype compared to adult cardiomyocytes [69,70]. This immaturity could partially explain blunted or exacerbated drug responses for specific compounds.

Secondly, we focused on six LQTS-causing LP/P variants. While this demonstrates proof of principle for retrospective variant risk stratification, further investigations are necessary to extend this approach to a broader range of variants or LQTS subtypes.

Third, while our model simplifies clinical risk into a binary classification, further evolutions of this approach could consider incorporating multiple classification states to accommodate intermediate disease phenotypes based on both qualitative and quantitative cardiac events associated with each variant.

Funding Sources

This project has received funding from the Horizon Europe EU (HORIZON-MSCA-2022-PF-01 PREPARE No. 101105561 to AK), Horizon 2020 (H2020-MSCA-IF-2017 No. 795209 to LS), Fondazione CARIPLO grant No. 2019-1691 to LS, Leducq Foundation grant 18CVD05 to PJS. Italian Ministry of University and Research within Mission 4, “Education and Research”, Component 2, “From Research to Business”, Investment 1.2, “Funding projects presented by young researchers” of the National Recovery and Resilience Plan. Project No. 2022-NAZ-0485 (H45E22001210006) to LS.

References

1. Schwartz PJ, Periti M, Malliani A. The long Q-T syndrome. *Am Heart J*. 1975;89:378–390.

2. Schwartz PJ, Priori SG, Spazzolini C, et al. Genotype-Phenotype Correlation in the Long-QT Syndrome. *Circulation*. 2001;103:89–95.

3. Behr ER, Roden D. Drug-induced arrhythmia: pharmacogenomic prescribing? *Eur Heart J*. 2013;34:89–95.

4. Weeke PE, Kellemann JS, Jespersen CB, et al. Long-term proarrhythmic pharmacotherapy among patients with congenital long QT syndrome and risk of arrhythmia and mortality. *Eur Heart J*. 2019;40:3110–3117.

5. Zeppenfeld K, Tfelt-Hansen J, De Riva M, et al. 2022 ESC Guidelines for the management of patients with ventricular arrhythmias and the prevention of sudden cardiac death. *Eur Heart J*. 2022;43:3997–4126.

6. Schwartz PJ. Cardiac sympathetic denervation to prevent life-threatening arrhythmias. *Nat Rev Cardiol*. 2014;11:346–353.

7. Dusi V, Pugliese L, De Ferrari GM, et al. Left Cardiac Sympathetic Denervation for Long QT Syndrome. *JACC Clin Electrophysiol*. 2022;8:281–294.

8. Schwartz PJ, Priori SG, Locati EH, et al. Long QT Syndrome Patients With Mutations of the *SCN5A* and *HERG* Genes Have Differential Responses to Na^+ Channel Blockade and to Increases in Heart Rate: Implications for Gene-Specific Therapy. *Circulation*. 1995;92:3381–3386.

9. Crotti L, Neves R, Dagradi F, et al. Therapeutic Efficacy of Mexiletine for Long QT Syndrome Type 2: Evidence From Human Induced Pluripotent Stem Cell–Derived Cardiomyocytes, Transgenic Rabbits, and Patients. *Circulation*. 2024;150:531–543.

10. Schwartz PJ, Ackerman MJ. The long QT syndrome: A transatlantic clinical approach to diagnosis and therapy. *Eur Heart J*. 2013;34:3109–3116.

11. Schwartz PJ, Ackerman MJ, George AL, Wilde AAM. Impact of Genetics on the Clinical Management of Channelopathies. *J Am Coll Cardiol*. 2013;62:169–180.

12. Giudicessi JR, Wilde AAM, Ackerman MJ. The genetic architecture of long QT syndrome: A critical reappraisal. *Trends Cardiovasc Med*. 2018;28:453–464.

13. Richards S, Aziz N, Bale S, et al. Standards and guidelines for the interpretation of sequence variants: A joint consensus recommendation of the American College of Medical Genetics and Genomics and the Association for Molecular Pathology. *Genet Med*. 2015;17:405–424.

14. Aziz PF, Wieand TS, Ganley J, et al. Genotype- and Mutation Site–Specific QT Adaptation During Exercise, Recovery, and Postural Changes in Children With Long-QT Syndrome. *Circ Arrhythm Electrophysiol*. 2011;4:867–873.

15. Schwartz PJ, Moreno C, Kotta M-C, et al. Mutation location and *I* Ks regulation in the arrhythmic risk of long QT syndrome type 1: the importance of the KCNQ1 S6 region. *Eur Heart J*. 2021;42:4743–4755.

16. Ackerman MJ. Genetic purgatory and the cardiac channelopathies: Exposing the variants of uncertain/unknown significance issue. *Heart Rhythm*. 2015;12:2325–2331.

17. Gnecchi M, Sala L, Schwartz PJ. Precision Medicine and cardiac channelopathies: when dreams meet reality. *Eur Heart J*. 2021;42:1661–1675.

18. Brnich SE, Abou Tayoun AN, Couch FJ, et al. Recommendations for application of the functional evidence PS3/BS3 criterion using the ACMG/AMP sequence variant interpretation framework. *Genome Med*. 2020;12:3.

19. Lichou F, Trynka G. Functional studies of GWAS variants are gaining momentum. *Nat Commun*. 2020;11:6283.

20. Moretti A, Bellin M, Welling A, et al. Patient-Specific Induced Pluripotent Stem-Cell Models for Long-QT Syndrome. *N Engl J Med*. 2010;363:1397–1409.

21. Itzhaki I, Maizels L, Huber I, et al. Modelling the long QT syndrome with induced pluripotent stem cells. *Nature*. 2011;471:225–229.

22. Rocchetti M, Sala L, Dreizehnter L, et al. Elucidating arrhythmogenic mechanisms of long-QT syndrome CALM1-F142L mutation in patient-specific induced pluripotent stem cell-derived cardiomyocytes. *Cardiovasc Res*. 2017;113:531–541.

23. Garg P, Garg V, Shrestha R, Sanguinetti MC, Kamp TJ, Wu JC. Human Induced Pluripotent Stem Cell–Derived Cardiomyocytes as Models for Cardiac Channelopathies. *Circ Res*. 2018;123:224–243.

24. Lee Y-K, Sala L, Mura M, et al. *MTMR4* SNVs modulate ion channel degradation and clinical severity in congenital long QT syndrome: insights in the mechanism of action of protective modifier genes. *Cardiovasc Res*. 2021;117:767–779.

25. Zhang M, D'Aniello C, Verkerk AO, et al. Recessive cardiac phenotypes in induced pluripotent stem cell models of Jervell and Lange-Nielsen syndrome: Disease mechanisms and pharmacological rescue. *Proc Natl Acad Sci*. 2014;111.

26. Yazawa M, Hsueh B, Jia X, et al. Using induced pluripotent stem cells to investigate cardiac phenotypes in Timothy syndrome. *Nature*. 2011;471:230–234.

27. Lan F, Lee AS, Liang P, et al. Abnormal Calcium Handling Properties Underlie Familial Hypertrophic Cardiomyopathy Pathology in Patient-Specific Induced Pluripotent Stem Cells. *Cell*

Stem Cell. 2013;12:101–113.

28. Ma D, Wei H, Lu J, et al. Generation of patient-specific induced pluripotent stem cell-derived cardiomyocytes as a cellular model of arrhythmogenic right ventricular cardiomyopathy. *Eur Heart J*. 2013;34:1122–1133.

29. Sun N, Yazawa M, Liu J, et al. Patient-Specific Induced Pluripotent Stem Cells as a Model for Familial Dilated Cardiomyopathy. *Sci Transl Med*. 2012;4.

30. Miao Y, Tian L, Martin M, et al. Intrinsic Endocardial Defects Contribute to Hypoplastic Left Heart Syndrome. *Cell Stem Cell*. 2020;27:574-589.e8.

31. Blinova K, Dang Q, Millard D, et al. International Multisite Study of Human-Induced Pluripotent Stem Cell-Derived Cardiomyocytes for Drug Proarrhythmic Potential Assessment. *Cell Rep*. 2018;24:3582–3592.

32. Sala L, Bellin M, Mummery CL. Integrating cardiomyocytes from human pluripotent stem cells in safety pharmacology: has the time come? *Br J Pharmacol*. 2017;174:3749–3765.

33. Paik DT, Chandy M, Wu JC. Patient and Disease–Specific Induced Pluripotent Stem Cells for Discovery of Personalized Cardiovascular Drugs and Therapeutics Ohlstein EH, editor. *Pharmacol Rev*. 2020;72:320–342.

34. Mehta A, Ramachandra CJA, Singh P, et al. Identification of a targeted and testable antiarrhythmic therapy for long-QT syndrome type 2 using a patient-specific cellular model. *Eur Heart J*. 2018;39:1446–1455.

35. Roberts B, Haupt A, Tucker A, et al. Systematic gene tagging using CRISPR/Cas9 in human stem cells to illuminate cell organization Drubin DG, editor. *Mol Biol Cell*. 2017;28:2854–2874.

36. Stenson PD, Ball EV, Mort M, et al. Human Gene Mutation Database (HGMD®): 2003 update:

HGMD 2003 UPDATE. *Hum Mutat*. 2003;21:577–581.

37. O'Neill MJ, Sala L, Denjoy I, et al. Continuous Bayesian variant interpretation accounts for incomplete penetrance among Mendelian cardiac channelopathies. *Genet Med*. 2023;25:100355.

38. Kozek K, Wada Y, Sala L, et al. Estimating the Posttest Probability of Long QT Syndrome Diagnosis for Rare *KCNH2* Variants. *Circ Genomic Precis Med*. 2021;14:e003289.

39. Lian X, Hsiao C, Wilson G, et al. Robust cardiomyocyte differentiation from human pluripotent stem cells via temporal modulation of canonical Wnt signaling. *Proc Natl Acad Sci U S A*. 2012;109:E1848-57.

40. Tohyama S, Hattori F, Sano M, et al. Distinct Metabolic Flow Enables Large-Scale Purification of Mouse and Human Pluripotent Stem Cell-Derived Cardiomyocytes. *Cell Stem Cell*. 2013;12:127–137.

41. Buikema JW, Lee S, Goodyer WR, et al. Wnt Activation and Reduced Cell-Cell Contact Synergistically Induce Massive Expansion of Functional Human iPSC-Derived Cardiomyocytes. *Cell Stem Cell*. 2020;27:50-63.e5.

42. Feyen DAM, McKeithan WL, Bruyneel AAN, et al. Metabolic Maturation Media Improve Physiological Function of Human iPSC-Derived Cardiomyocytes. *Cell Rep*. 2020;32:107925.

43. Sala L, Ward-van Oostwaard D, Tertoolen LGJ, Mummery CL, Bellin M. Electrophysiological Analysis of human Pluripotent Stem Cell-derived Cardiomyocytes (hPSC-CMs) Using Multi-electrode Arrays (MEAs). *J Vis Exp*. 2017:55587.

44. Sala L, Leonov V, Mura M, et al. Use of hiPSC-Derived Cardiomyocytes to Rule Out Proarrhythmic Effects of Drugs: The Case of Hydroxychloroquine in COVID-19. *Front Physiol*. 2022;12:730127.

45. Woosley RL, Heise CW, Gallo T, Romero KA, Woosley RD, Lambson J. www.CredibleMeds.org, QTdrugs List

46. Kuhn M, Wickham H. *Tidymodels: a collection of packages for modeling and machine learning using tidyverse principles*. 2020.

47. Schwartz PJ, Spazzolini C, Crotti L, et al. The Jervell and Lange-Nielsen Syndrome: Natural History, Molecular Basis, and Clinical Outcome. *Circulation*. 2006;113:783–790.

48. Mura M, Lee Y, Ginevrino M, et al. Generation of the human induced pluripotent stem cell (hiPSC) line PSMi002-A from a patient affected by the Jervell and Lange-Nielsen syndrome and carrier of two compound heterozygous mutations on the KCNQ1 gene. *Stem Cell Res*. 2018;29:157–161.

49. Brink PA, Crotti L, Corfield V, et al. Phenotypic Variability and Unusual Clinical Severity of Congenital Long-QT Syndrome in a Founder Population. *Circulation*. 2005;112:2602–2610.

50. Crotti L, Spazzolini C, Schwartz PJ, et al. The Common Long-QT Syndrome Mutation KCNQ1/A341V Causes Unusually Severe Clinical Manifestations in Patients With Different Ethnic Backgrounds: Toward a Mutation-Specific Risk Stratification. *Circulation*. 2007;116:2366–2375.

51. Ronchi C, Bernardi J, Mura M, et al. NOS1AP polymorphisms reduce NOS1 activity and interact with prolonged repolarization in arrhythmogenesis. *Cardiovasc Res*. 2021;117:472–483.

52. Crotti L, Monti MC, Insolia R, et al. *NOS1AP* Is a Genetic Modifier of the Long-QT Syndrome. *Circulation*. 2009;120:1657–1663.

53. Kramer J, Obejero-Paz CA, Myatt G, et al. MICE Models: Superior to the HERG Model in Predicting Torsade de Pointes. *Sci Rep*. 2013;3:2100.

54. Braam SR, Tertoolen L, Casini S, et al. Repolarization reserve determines drug responses in

human pluripotent stem cell derived cardiomyocytes. *Stem Cell Res*. 2013;10:48–56.

55. Stillitano F, Hansen J, Kong C-W, et al. Modeling susceptibility to drug-induced long QT with a panel of subject-specific induced pluripotent stem cells. *eLife*. 2017;6:e19406.

56. Golforoush P, Schneider MD. Intensive care for human hearts in pluripotent stem cell models. *Npj Regen Med*. 2020;5:4.

57. Shead KD, Huethorst E, Burton F, Lang NN, Myles RC, Smith GL. Human Induced Pluripotent Stem Cell-Derived Cardiomyocytes for Preclinical Cardiotoxicity Screening in Cardio-Oncology. *JACC CardioOncology*. 2024:S2666087324002710.

58. Wada Y, Wang L, Hall LD, et al. The electrophysiologic effects of *KCNQ1* extend beyond expression of *I* Ks: evidence from genetic and pharmacologic block. *Cardiovasc Res*. 2024;120:735–744.

59. Zeng H, Wang J, Clouse H, Lagrutta A, Sannajust F. Human-induced pluripotent stem cell-derived cardiomyocytes have limited I_{Ks} for repolarization reserve as revealed by specific KCNQ1/KCNE1 blocker. *JRSM Cardiovasc Dis*. 2019;8:204800401985491.

60. Varró A, Baczkó I. Cardiac ventricular repolarization reserve: a principle for understanding drug-related proarrhythmic risk: Repolarization reserve and proarrhythmia. *Br J Pharmacol*. 2011;164:14–36.

61. Ma D, Wei H, Zhao Y, et al. Modeling type 3 long QT syndrome with cardiomyocytes derived from patient-specific induced pluripotent stem cells. *Int J Cardiol*. 2013;168:5277–5286.

62. Zreik J, LaPage MJ, Zreik H. Congenital Long QT Syndrome Unmasked by Albuterol in an Adolescent with Asthma. *J Emerg Med*. 2024;67:e446–e450.

63. Kopljar I, Lu HR, Van Ammel K, et al. Development of a Human iPSC Cardiomyocyte-Based

Scoring System for Cardiac Hazard Identification in Early Drug Safety De-risking. *Stem Cell Rep*. 2018;11:1365–1377.

64. Ando H, Yoshinaga T, Yamamoto W, et al. A new paradigm for drug-induced torsadogenic risk assessment using human iPS cell-derived cardiomyocytes. *J Pharmacol Toxicol Methods*. 2017;84:111–127.

65. Noda T. Gene-specific response of dynamic ventricular repolarization to sympathetic stimulation in LQT1, LQT2 and LQT3 forms of congenital long QT syndrome. *Eur Heart J*. 2002;23:975–983.

66. Odening KE, Hyder O, Chaves L, et al. Pharmacogenomics of anesthetic drugs in transgenic LQT1 and LQT2 rabbits reveal genotype-specific differential effects on cardiac repolarization. *Am J Physiol-Heart Circ Physiol*. 2008;295:H2264–H2272.

67. Yoshinaga D, Baba S, Makiyama T, et al. Phenotype-Based High-Throughput Classification of Long QT Syndrome Subtypes Using Human Induced Pluripotent Stem Cells. *Stem Cell Rep*. 2019;13:394–404.

68. O'Neill MJ, Ng C-A, Aizawa T, et al. Assays of Variant Effect and Automated Patch Clamping Improve *KCNH2* -LQTS Variant Classification and Cardiac Event Risk Stratification. *Circulation*. 2024:CIRCULATIONAHA.124.069828.

69. Karbassi E, Fenix A, Marchiano S, et al. Cardiomyocyte maturation: advances in knowledge and implications for regenerative medicine. *Nat Rev Cardiol*. 2020;17:341–359.

70. Veerman CC, Kosmidis G, Mummery CL, Casini S, Verkerk AO, Bellin M. Immaturity of Human Stem-Cell-Derived Cardiomyocytes in Culture: Fatal Flaw or Soluble Problem? *Stem Cells Dev*. 2015;24:1035–1052.

Figure titles and legends

Figure 1. Clinical parameters and variant risk level assignment. A. Frequency of cardiac events across pathogenic/likely pathogenic genetic variants in *KCNQ1* (blue) and *KCNH2* (orange) genes. B. Percentage of patients with cardiac events for each variant, with assigned variant risk level indicated. C, D. Baseline QTc and Schwartz score values for each variant (N = 1–183).

Figure 2. Characterization of hiPSC-CMs carrying genetic variants *KCNQ1* p.R190W and *KCNQ1* p.R594Q. A. Representative action potential traces for each hiPSC-CM variant, elicited at 1 Hz stimulation. B. Action potential duration at 90% repolarization (APD90). C. Corrected field potential duration (cFPD) measurements in hiPSC-CMs for each variant (N = 157–180). D. Representative I_{Ks} current traces (lower panel), obtained by subtracting HMR1556-insensitive current (middle panel) from the total inward potassium current recording (upper panel). E, F End-step and tail I_{Ks} current-voltage (I-V) relationships. * denotes $p < 0.05$ for all groups vs WT, # for WT vs *KCNQ1* p.R190W & p.R594Q, § for WT vs KCNQ1 p.R594Q and vs KCNQ1 p.R190W & p.R594Q.

Figure 3. Baseline electrophysiology of hiPSC-CMs carrying High Risk and Low Risk genetic variants. A. Representative field potentials obtained for each variant. B-D. Baseline field potential duration (FPD), corrected FPD (cFPD), and beat-to-beat interval (RR) measurements of hiPSC-CMs for each variant; asterisks indicate statistical significance with the WT group. N = 154-547. E. Incidence of regular (gray) or irregular (yellow) beating patterns for hiPSC-CMs carrying Low Risk and High Risk variants (N = 589-1038).

Figure 4: HiPSC-CMs from Low Risk and High Risk groups exhibit differential responses to ion channel blockers. A-E: Concentration-dependent response curves to ion channel blockers E4031, HMR1556, HMR1556 following E4031 pre-treatment, nifedipine, and tetrodotoxin. Responses are shown for normalized corrected field potential duration (normalized cFPD),

normalized RR interval (normalized RR), and normalized peak-to-peak amplitude (normalized PtPA). Bar plots illustrate the distribution of beating pattern abnormalities. Green dashed lines indicate reported Cmax values for each drug. Asterisks indicate statistical significance of comparisons between the High Risk and Low Risk groups. N = 19-80 per group per drug concentration.

Figure 5. HiPSC-CMs from Low Risk and High Risk groups exhibit differential responses to proarrhythmic drugs. A-G: Concentration-dependent response curves for proarrhythmic drugs clarithromycin, chlorpromazine, ciprofloxacin, dofetilide, haloperidol, moxifloxacin, and salbutamol. Responses are presented for normalized corrected field potential duration (normalized cFPD), normalized RR interval (normalized RR), and normalized peak-to-peak amplitude (normalized PtPA). Bar plots illustrate the distribution of beating pattern abnormalities. Green dashed lines indicate reported Cmax values for each drug. Asterisks indicate statistical significance of comparisons between the High Risk and Low Risk groups. N = 26-121 per group per drug concentration.

Figure 6. HiPSC-CMs carrying High Risk and Low Risk variants demonstrate gene-specific drug responses. A-F. Concentration-dependent response curves for dofetilide, E4031, and haloperidol on normalized corrected field potential duration (normalized cFPD), normalized RR interval (normalized RR), and normalized peak-to-peak amplitude (normalized PtPA). Bar plots illustrate the distribution of beating pattern abnormalities. Asterisks indicate statistical significance of comparisons between High Risk and Low Risk groups. N = 8-101 per group per drug concentration.

Figure 7. Variant risk levels and disease type prediction using MEA measurements and machine learning model. A. Receiver Operating Characteristic (ROC) curve illustrating the

performance of a classification model for variant risk prediction. B. ROC curves representing the model's performance in predicting disease type. C. Model validation for single-variant risk level predictions. The proportion of readouts predicted as High Risk (red) and Low Risk (gray) is shown for each variant. The 50% threshold line delineates variants classified as High Risk (above) from those classified as Low Risk (below).

Tables

Table 1. Clinical characteristics of the patient cohort included in the study.

Patient	Disease	Genetic variant	dbSNP record	ClinVar classification	Known modifier genes	Sex	Qc (ms)	Schwartz score	Age range	Symptomatic	Clinical symptoms	Treatment
1	LQT1	*KCNQ1* p.R190W	rs199473662	Likely pathogenic		F	458	2	41-45	No		Propranolol
2	LQT1	*KCNQ1* p.R594Q	rs199472815	Likely pathogenic		M	448	1	46-50	No		
3	LQT1	*KCNQ1* p.A341V	rs12720459	Pathogenic		F	488	4.5	56-60	No		
4	LQT1	*KCNQ1* p.A341V	rs12720459	Pathogenic		M	406	1	71-75	No		
5	LQT1	*KCNQ1* p.A341V	rs12720459	Pathogenic	*NOS1AP* rs16847548 heterozygous minor allele and *NOS1AP* rs4657139 heterozygous minor allele	F	501	6	46-50	Yes	Syncope with stress at age range 6-10	
6	LQT1	*KCNQ1* p.A341V	rs12720459	Pathogenic	*NOS1AP* rs16847548 homozygous minor allele and *NOS1AP* rs4657139 homozygous minor allele	F	593	6	66-70	Yes	Syncope with stress at age range 16-20	
7	JLNS	*KCNQ1* p.R190W, *KCNQ1* p.R594Q	rs199473662, rs199472815	Likely pathogenic (both variants)		F	578	7.5	16-20	Yes	Multiple syncopal episodes since age range 0-2, deafness.	Propranolol
8	LQT2	*KCNH2* p.R366X	rs794728364	Pathogenic		F	480	5.5	51-55	No	Notched t-waves.	Nadolol
9	LQT2	*KCNH2* p.R366X	rs794728364	Pathogenic		F	622	7.5	36-40	Yes	Syncope after a wake-up alarm sound at age range 26-30. No cardiac arrest history.	Nadolol, concomitant mexiletine; LCSD performed at age range 26-30..
10	LQT2	*KCNH2* p.A561V	rs121912504	Pathogenic/Likely pathogenic		M	480 (with nadolol)	-	-	Yes	Two cardiac arrests, no cardiac events after beta-blocker and	Nadolol, ICD implanted.

	ICD treatment.

Table 2. Baseline electrophysiological parameters obtained from MEA recording for each variant

Variant	**N**	**FPD, ms**	**cFPD, ms**	**RR, s**
WT	154	356 ± 120.3	281.8 ± 77.4	1.63 ± 0.49
KCNQ1-p.R190W	180	331.3 ± 104.9, $p = 0.07$	284.6 ± 60.6, $p = 0.69$	1.33 ± 0.34, $p \leq 0.001$
KCNQ1-p.R594Q	173	643.7 ± 190.2, $p \leq 0.001$	422.2 ± 126.7, $p \leq 0.001$	2.82 ± 2.6, $p \leq 0.001$
KCNQ1-p.A341V	547	536.9 ± 173.2, $p \leq 0.001$	325.1 ± 109.2, $p \leq 0.001$	3.57 ± 3.71, $p \leq 0.001$
KCNQ1-p.R190W & p.R594Q	157	629.8 ± 133, $p \leq 0.001$	424.9 ± 78.7, $p \leq 0.001$	2.56 ± 2.05, $p \leq 0.001$
KCNH2-p.R366X	255	311.4 ± 74.3, $p \leq 0.001$	265.9 ± 53.4, $p = 0.06$	1.45 ± 0.56, $p \leq 0.001$
KCNH2-p.A561V	161	923.1 ± 355.4, $p \leq 0.001$	531.1 ± 197.3, $p \leq 0.001$	3.04 ± 0.61, $p \leq 0.001$

Table 3. LQTS variant risk level prediction accuracy for each genetic variant included in the study.

Variant	**Disease**	**Variant risk level**	**Predicted variant risk level**	**Accuracy**
KCNQ1-p.R190W	LQT1	Low Risk	Low Risk	0.58
KCNQ1-p.R594Q	LQT1	High Risk	High Risk	0.92
KCNQ1-p.A341V	LQT1	High Risk	High Risk	0.69
KCNQ1-p.R190W & p.R594Q	JLNS	High Risk	High Risk	0.85
KCNH2-p.R366X	LQT2	Low Risk	High Risk	0.4
KCNH2-p.A561V	LQT2	High Risk	High Risk	0.92
Overall accuracy of variant prediction 0.73				

Accuracy above 0.5 indicates correct variant risk level prediction.

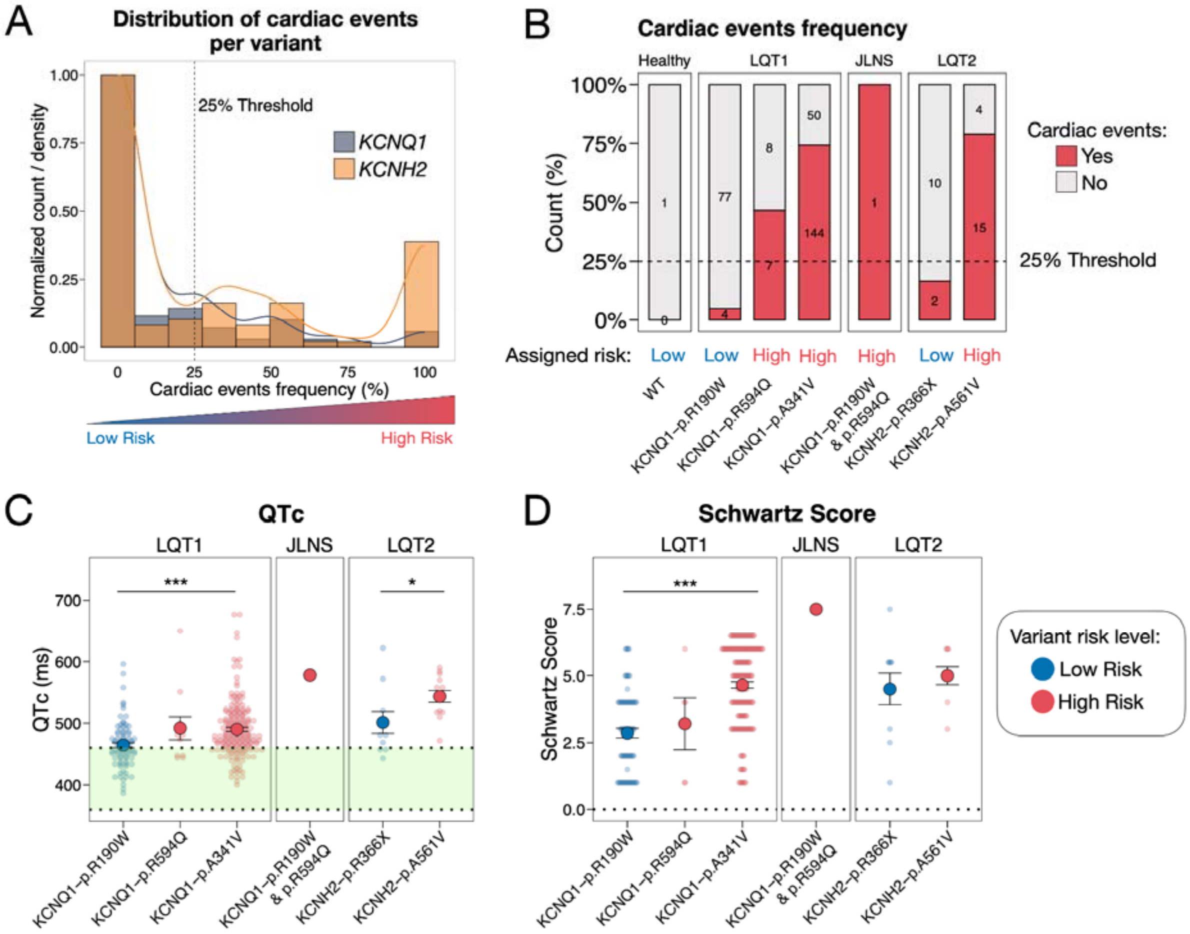
A
Distribution of cardiac events per variant
25% Threshold
KCNQ1
KCNH2
Normalized count / density
1.00
0.75
0.50
0.25
0.00
0
25
50
75
100
Cardiac events frequency (%)
Low Risk
High Risk
B
Cardiac events frequency
Healthy
LQT1
JLNS
LQT2
100%
75%
50%
25%
0%
Count (%)
1
0
77
4
8
7
50
144
1
10
2
4
15
Cardiac events:
Yes
No
25% Threshold
Assigned risk:
Low
Low
High
High
High
Low
High
WT
KCNQ1–p.R190W
KCNQ1–p.R594Q
KCNQ1–p.A341V
KCNQ1–p.R190W & p.R594Q
KCNH2–p.R366X
KCNH2–p.A561V
C
QTc
LQT1
JLNS
LQT2
***
*
700
600
500
400
QTc (ms)
KCNQ1–p.R190W
KCNQ1–p.R594Q
KCNQ1–p.A341V
KCNQ1–p.R190W & p.R594Q
KCNH2–p.R366X
KCNH2–p.A561V
D
Schwartz Score
LQT1
JLNS
LQT2
***
7.5
5.0
2.5
0.0
Schwartz Score
KCNQ1–p.R190W
KCNQ1–p.R594Q
KCNQ1–p.A341V
KCNQ1–p.R190W & p.R594Q
KCNH2–p.R366X
KCNH2–p.A561V
Variant risk level:
Low Risk
High Risk

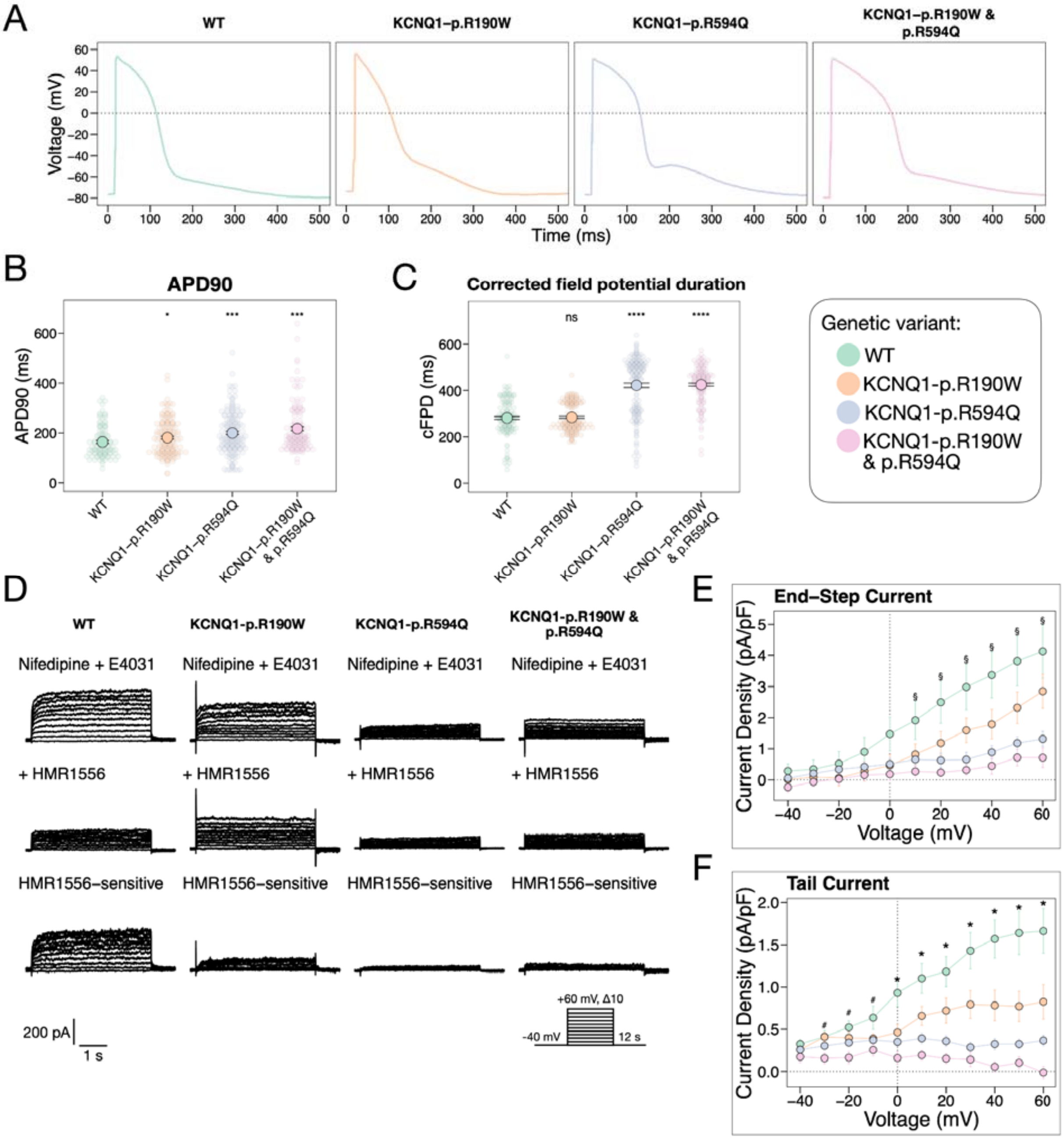
A
WT
KCNQ1−p.R190W
KCNQ1−p.R594Q
KCNQ1−p.R190W & p.R594Q
Voltage (mV)
60
40
20
0
−20
−40
−60
−80
0
100
200
300
400
500
Time (ms)
B
APD90
APD90 (ms)
600
400
200
0
*
***
***
WT
KCNQ1−p.R190W
KCNQ1−p.R594Q
KCNQ1−p.R190W & p.R594Q
C
Corrected field potential duration
cFPD (ms)
600
400
200
0
ns
****
****
WT
KCNQ1−p.R190W
KCNQ1−p.R594Q
KCNQ1−p.R190W & p.R594Q
Genetic variant:
WT
KCNQ1−p.R190W
KCNQ1−p.R594Q
KCNQ1−p.R190W & p.R594Q
D
WT
KCNQ1−p.R190W
KCNQ1−p.R594Q
KCNQ1−p.R190W & p.R594Q
Nifedipine + E4031
+ HMR1556
HMR1556−sensitive
200 pA
1 s
+60 mV, Δ10
−40 mV
12 s
E
End−Step Current
Current Density (pA/pF)
5
4
3
2
1
0
§
−40
−20
0
20
40
60
Voltage (mV)
F
Tail Current
Current Density (pA/pF)
2.0
1.5
1.0
0.5
0.0
#
*
−40
−20
0
20
40
60
Voltage (mV)

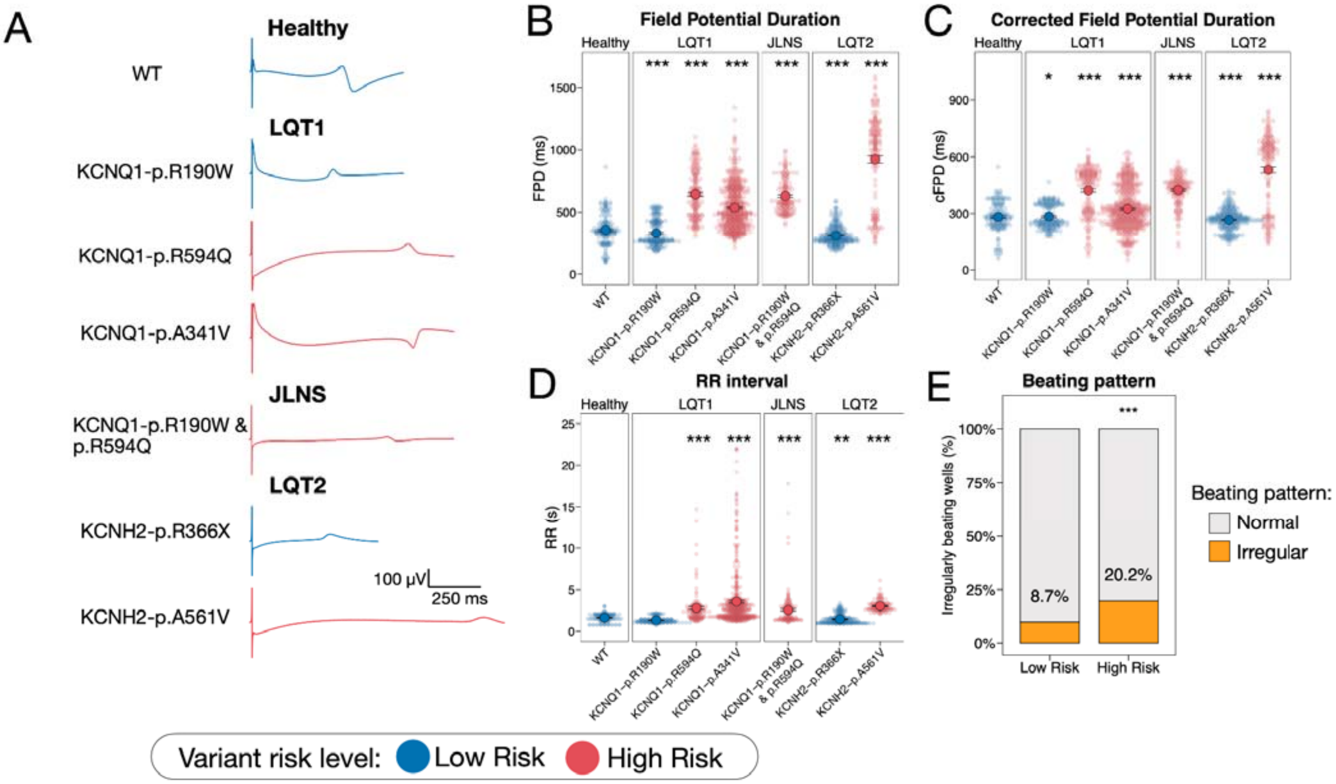
A
Healthy
WT
LQT1
KCNQ1-p.R190W
KCNQ1-p.R594Q
KCNQ1-p.A341V
JLNS
KCNQ1-p.R190W & p.R594Q
LQT2
KCNH2-p.R366X
KCNH2-p.A561V
100 µV
250 ms
B
Field Potential Duration
Healthy
LQT1
JLNS
LQT2
FPD (ms)
0
500
1000
1500
*** *** *** *** *** ***
WT
KCNQ1-p.R190W
KCNQ1-p.R594Q
KCNQ1-p.A341V
KCNQ1-p.R190W & p.R594Q
KCNH2-p.R366X
KCNH2-p.A561V
C
Corrected Field Potential Duration
Healthy
LQT1
JLNS
LQT2
cFPD (ms)
0
300
600
900
* *** *** *** *** ***
WT
KCNQ1-p.R190W
KCNQ1-p.R594Q
KCNQ1-p.A341V
KCNQ1-p.R190W & p.R594Q
KCNH2-p.R366X
KCNH2-p.A561V
D
RR interval
Healthy
LQT1
JLNS
LQT2
RR (s)
0
5
10
15
20
25
*** *** *** ** ***
WT
KCNQ1-p.R190W
KCNQ1-p.R594Q
KCNQ1-p.A341V
KCNQ1-p.R190W & p.R594Q
KCNH2-p.R366X
KCNH2-p.A561V
E
Beating pattern
Irregularly beating wells (%)
0%
25%
50%
75%
100%
***
8.7%
20.2%
Low Risk
High Risk
Beating pattern:
Normal
Irregular
Variant risk level:
Low Risk
High Risk

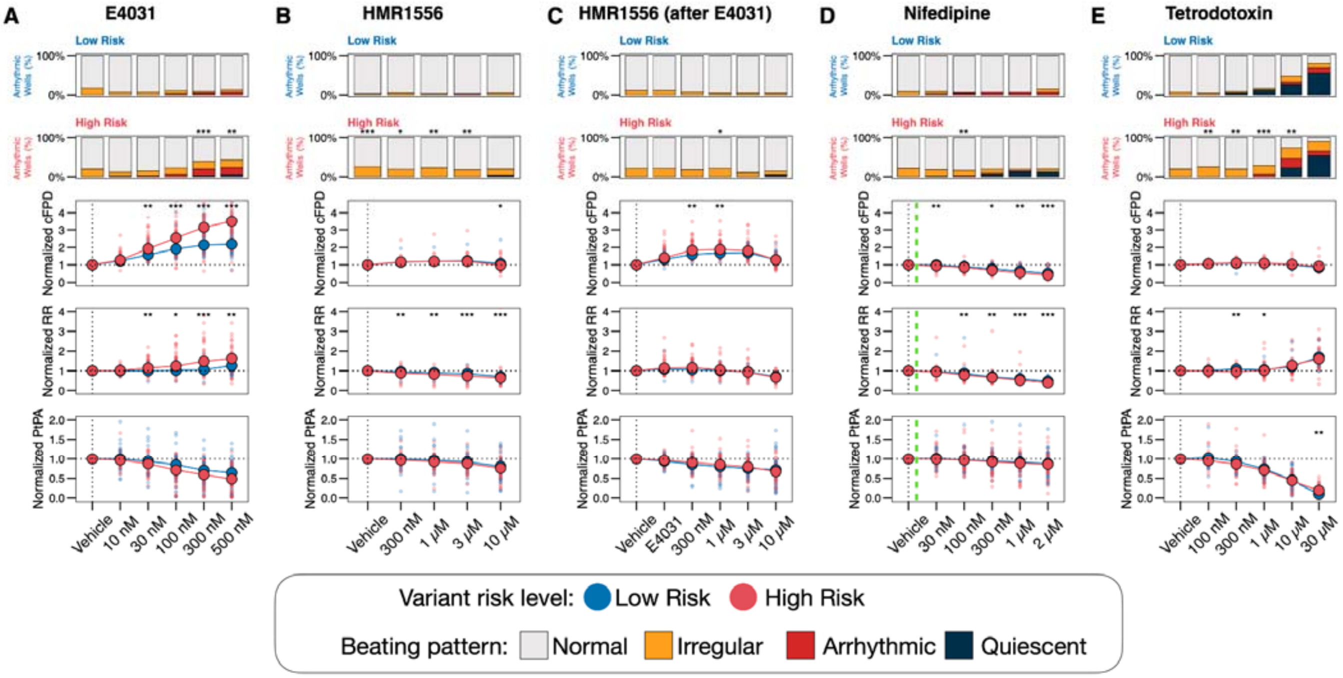
A
E4031
B
HMR1556
C
HMR1556 (after E4031)
D
Nifedipine
E
Tetrodotoxin
Low Risk
High Risk
Arrhythmic Wells (%)
100%
0%
Normalized cFPD
Normalized RR
Normalized PtPA
Vehicle
10 nM
30 nM
100 nM
300 nM
500 nM
1 μM
3 μM
10 μM
E4031
2 μM
30 μM
Variant risk level: ● Low Risk ● High Risk
Beating pattern: ☐ Normal 🟧 Irregular 🟥 Arrhythmic ■ Quiescent

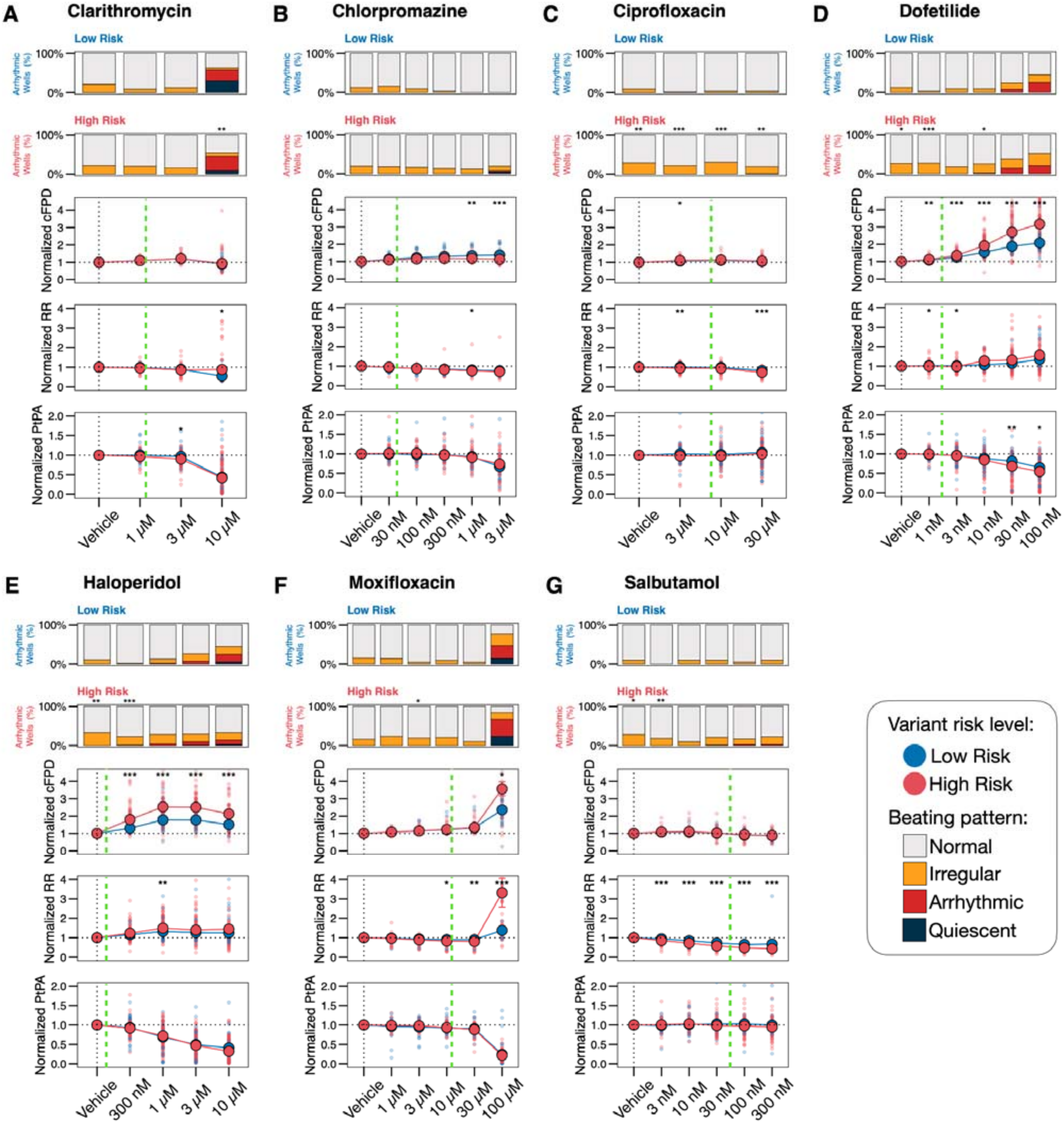
A Clarithromycin
B Chlorpromazine
C Ciprofloxacin
D Dofetilide
E Haloperidol
F Moxifloxacin
G Salbutamol
Low Risk
High Risk
Arrhythmic Wells (%)
100%
0%
Normalized cFPD
Normalized RR
Normalized PtPA
Vehicle
1 μM
3 μM
10 μM
30 nM
100 nM
300 nM
30 μM
1 nM
3 nM
10 nM
100 μM
Variant risk level:
● Low Risk
● High Risk
Beating pattern:
Normal
Irregular
Arrhythmic
Quiescent

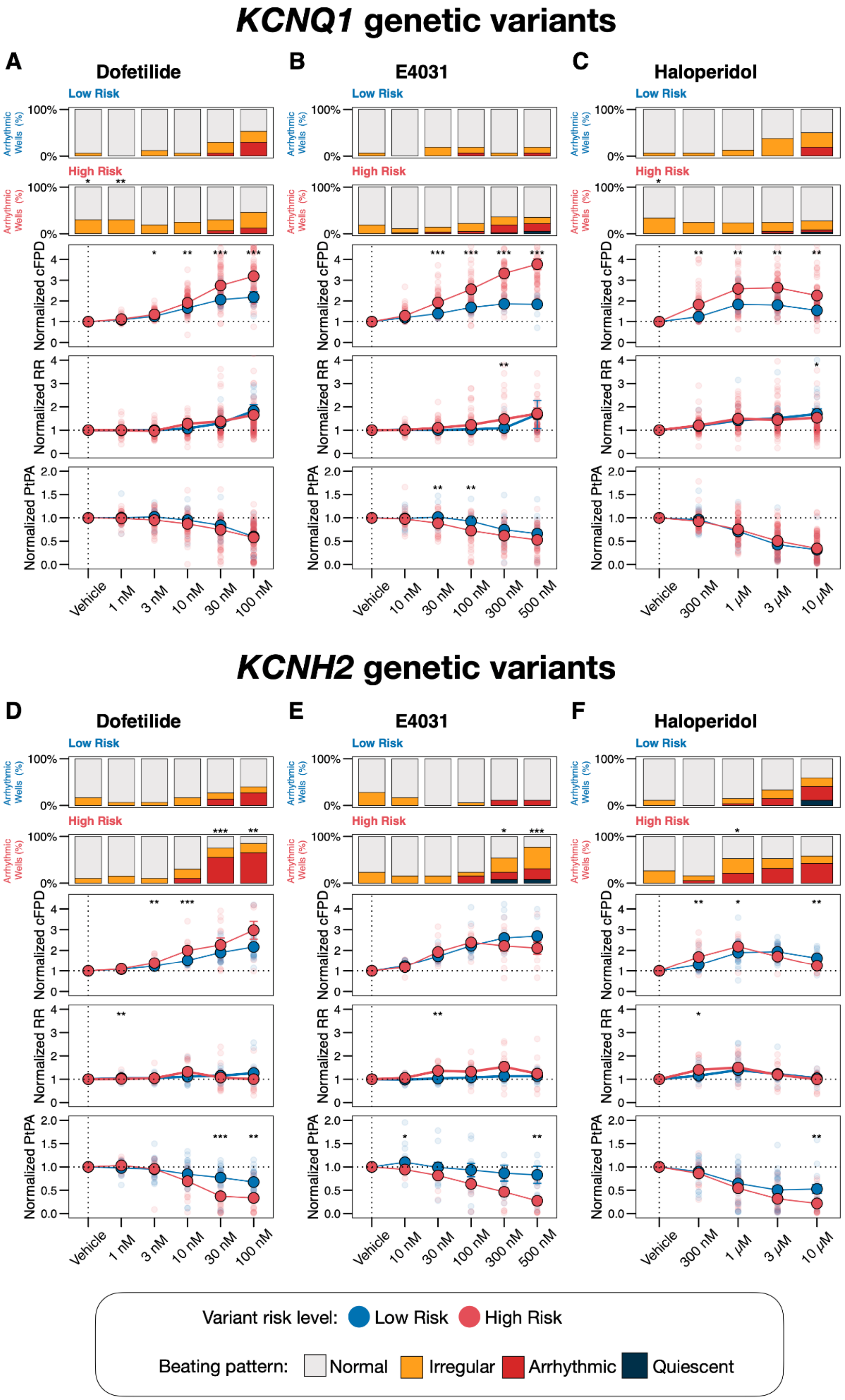
KCNQ1 genetic variants
A
Dofetilide
B
E4031
C
Haloperidol
Low Risk
High Risk
Arrhythmic Wells (%)
100%
0%
Normalized cFPD
Normalized RR
Normalized PtPA
0
1
2
3
4
0.0
0.5
1.0
1.5
2.0
*
**
***
Vehicle
1 nM
3 nM
10 nM
30 nM
100 nM
300 nM
500 nM
1 μM
3 μM
10 μM
KCNH2 genetic variants
D
Dofetilide
E
E4031
F
Haloperidol
Variant risk level: ● Low Risk ● High Risk
Beating pattern: ☐ Normal 🟧 Irregular 🟥 Arrhythmic ■ Quiescent

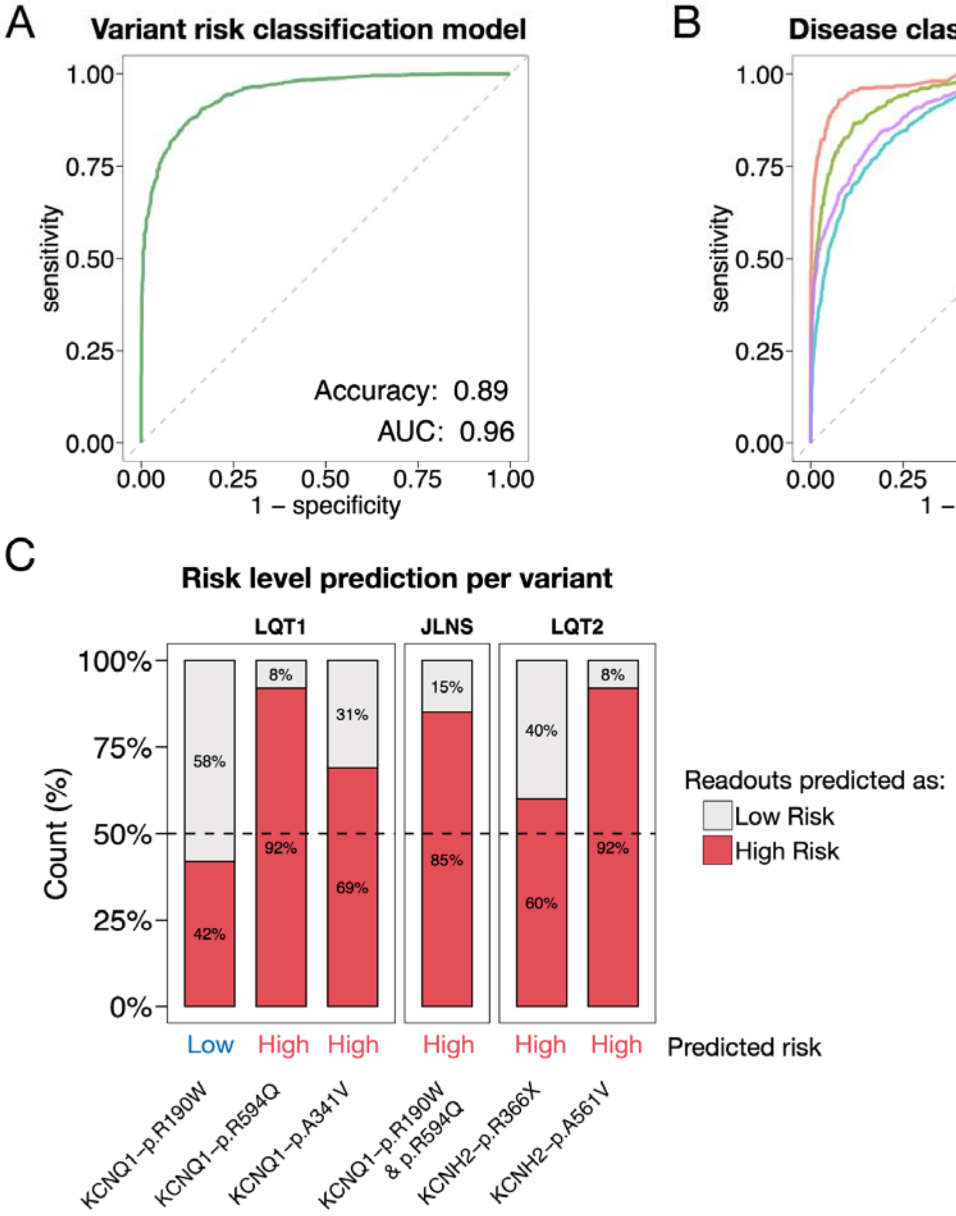
A
Variant risk classification model
1.00
0.75
0.50
0.25
0.00
sensitivity
0.00
0.25
0.50
0.75
1.00
1 – specificity
Accuracy: 0.89
AUC: 0.96
B
Disease classification model
1.00
0.75
0.50
0.25
0.00
sensitivity
0.00
0.25
0.50
0.75
1.00
1 – specificity
Disease
Healthy
JLNS
LQT1
LQT2
Accuracy: 0.79
AUC: 0.94
C
Risk level prediction per variant
LQT1
JLNS
LQT2
100%
75%
50%
25%
0%
Count (%)
58%
42%
8%
92%
31%
69%
15%
85%
40%
60%
8%
92%
Readouts predicted as:
Low Risk
High Risk
Low
High
High
High
High
High
Predicted risk
KCNQ1–p.R190W
KCNQ1–p.R594Q
KCNQ1–p.A341V
KCNQ1–p.R190W & p.R594Q
KCNH2–p.R366X
KCNH2–p.A561V

Discriminate High Risk vs Low Risk genetic variants in LQTS cohorts

High-throughput electrophysiological readouts on 11 patient-specific hiPSC-CMs

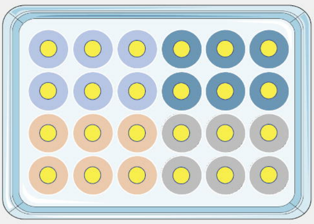

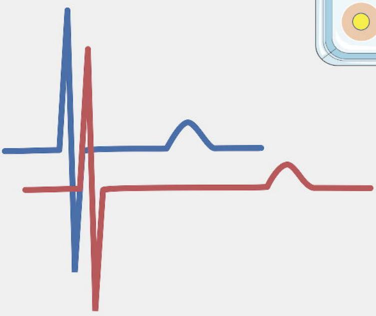

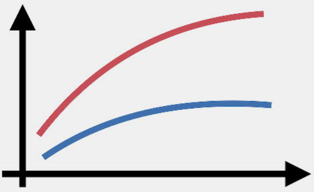

Variant-specific electrophysiological phenotype

Variant-specific drug responses

Machine Learning classifier

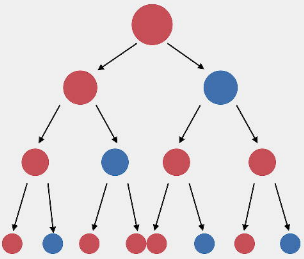

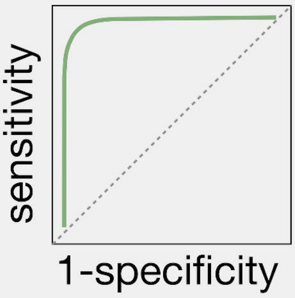

89% Accuracy
96% AUC

Variant Risk Classification Model

Low Risk variants

High Risk variants